THÈSE

Pour l'obtention du grade de
DOCTEUR DE L'UNIVERSITÉ DE POITIERS
UFR des sciences fondamentales et appliquées
Pôle poitevin de recherche pour l'ingénieur en mécanique, matériaux et énergétique - PPRIMME (Poitiers)
(Diplôme National - Arrêté du 25 mai 2016)

École doctorale : Sciences et Ingénierie des Matériaux, Mécanique, Énergétique (Poitiers)
Secteur de recherche : Milieux denses et Matériaux

Cotutelle : Université de Linköping

Présentée par :
Andreas Jamnig

Thin metal films on weakly-interacting substrates : Nanoscale growth dynamics, stress generation, and morphology manipulation

Directeur(s) de Thèse :
Grégory Abadias, Kostas Sarakinos

Soutenue le 05 novembre 2020 devant le jury

Jury :

Président	**Fredrik Eriksson**	Associate professor, Linköping University, Sweden
Rapporteur	**Gregory B. Thompson**	Professor, College of enginnering, University of Alabama
Rapporteur	**Frédéric Leroy**	Professeur, Université d'Aix-Marseille
Membre	**Grégory Abadias**	Professeur, Pprime, Université de Poitiers
Membre	**Kostas Sarakinos**	Professeur associé, Université de Linköping, Suède
Membre	**Sophie Camélio**	Professeur, Pprime, ENSIP, Université de Poitiers
Membre	**David Horwat**	Professeur, Université de Lorraine
Membre	**Rémi Lazzari**	Directeur de recherche CNRS, Sorbonne Université, Paris

Pour citer cette thèse :
Andreas Jamnig. *Thin metal films on weakly-interacting substrates : Nanoscale growth dynamics, stress generation, and morphology manipulation* [En ligne]. Thèse Milieux denses et Matériaux. Poitiers : Université de Poitiers, 2020. Disponible sur Internet <http://theses.univ-poitiers.fr>

Linköping Studies in Science and Technology
Dissertation No. 2084

Thin metal films on weakly-interacting substrates

Nanoscale growth dynamics, stress generation, and morphology manipulation

Andreas Jamnig

Nanoscale Engineering Division
Department of Physics, Chemistry and Biology (IFM)
Linköping University
SE-581 83 Linköping, Sweden
Linköping 2020

Cover image:
Lines: Evolution of stress-film thickness product with time during and post-deposition of thin silver films on weakly-interacting silicon oxide
Left: Coalescing silver islands, imaged by scanning electron microscopy
Top: Surface topography of a silver film, imaged by atomic force microscopy
Bottom: Microstructure of a silver film, imaged by cross-sectional transmission electron microscopy

Printed in Sweden by LiU-tryck, Linköping, SE, 2020

ISSN 0345-7524
ISBN 978-91-7929-820-3

THÈSE

Pour l'obtention du grade de

DOCTEUR DE L'UNIVERSITÉ DE POITIERS

Faculté des Sciences Fondamentales et Appliquées

École Doctorale : **SIMME**

Secteur de Recherche : **Milieux denses et matériaux**

Présentée par :

Andreas JAMNIG

****

Thin metal films on weakly-interacting substrates

Nanoscale growth dynamics, stress generation, and morphology manipulation

****

Directeurs de Thèse : Grégory **ABADIAS**, Kostas **SARAKINOS**

****

Soutenue le 5 Novembre 2020 devant la Commission d'Examen

****

JURY

Fredrik ERIKSSON	Docent, Linköping Univ., SE	Président
Gregory THOMPSON	Prof., Univ. of Alabama, USA	Rapporteur
Frédéric LEROY	Prof., Univ. Aix Marseille, FR	Rapporteur
David HORWAT	Prof., Univ. de Lorraine, FR	Examinateur
Sophie CAMÉLIO	Prof., Univ. de Poitiers, FR	Examinatrice
Rémi LAZZARI	Dr. CNRS, Sorbonne Univ., FR	Examinateur
Kostas SARAKINOS	Assoc. Prof., Linköping Univ., SE	Examinateur
Grégory ABADIAS	Prof., Univ. de Poitiers, FR	Examinateur

Abstract

Vapor-based growth of thin metal films with controlled morphology on weakly-interacting substrates (WIS), including oxides and van der Waals materials, is essential for the fabrication of multifunctional metal contacts in a wide array of optoelectronic devices. Achieving this entails a great challenge, since weak film/substrate interactions yield a pronounced and uncontrolled 3D morphology. Moreover, the far-from-equilibrium nature of vapor-based film growth often leads to generation of mechanical stress, which may further compromise device reliability and functionality. The objectives of this thesis are related to metal film growth on WIS and seek to: (i) contribute to the understanding of atomic-scale processes that control film morphological evolution; (ii) elucidate the dynamic competition between nanoscale processes that govern film stress generation and evolution; and (iii) develop methodologies for manipulating and controlling nanoscale film morphology between 2D and 3D. Investigations focus on magnetron sputter-deposited Ag and Cu films on SiO_2 and amorphous carbon (a-C) substrates. Research is conducted by strategically combining of *in situ* and real-time film growth monitoring, *ex situ* chemical and (micro)-structural analysis, optical modelling, and deterministic growth simulations.

In the first part, the scaling behavior of characteristic morphological transition thicknesses (i.e., percolation and continuous film formation thickness) during growth of Ag and Cu films on a-C are established as function of deposition rate and temperature. These data are interpreted using a theoretical framework based on the droplet growth theory and the kinetic freezing model for island coalescence, from which the diffusion rates of film forming species during Ag and Cu growth are estimated. By combining experimental data with *ab initio* molecular dynamics simulations, diffusion of multiatomic clusters, rather than monomers, is identified as the rate-limiting structure-forming process.

In the second part, the effect of minority metallic or gaseous species (Cu, N_2, O_2) on Ag film morphological evolution on SiO_2 is studied. By employing *in situ* spectroscopic ellipsometry, it is found that addition of minority species at the film growth front promotes 2D morphology, but also yields an increased continuous-layer resistivity. *Ex situ* analyses show that 2D morphology is favored because minority species hinder the rate of coalescence completion. Hence, a novel growth manipulation strategy is compiled in which minority species are deployed with high temporal precision to selectively target specific film growth stages and achieve 2D morphology, while retaining opto-electronic properties of pure Ag films.

In the third part, the evolution of stress during Ag and Cu film growth on a-C and its dependence on growth kinetics (as determined by deposition rate, substrate temperature) is systematically investigated. A general trend toward smaller compressive stress magnitudes with increasing temperature/deposition rate is found, related to increasing grain size/decreasing adatom diffusion length. Exception to this trend is found for Cu films, in which oxygen incorporation from the residual growth atmosphere at low deposition rates inhibits adatom diffusivity and decreases the magnitude of compressive stress. The effect of N_2 on stress type and magnitude in Ag films is also studied. While Ag grown in N_2-free atmosphere exhibits a typical compressive-tensile-compressive stress evolution as function of thickness, addition of a few percent of N_2 yields to a stress turnaround from compressive to tensile stress after film continuity which is attributed to giant grain growth and film roughening.

The overall results of the thesis provide the foundation to: (i) determine diffusion rates over a wide range of WIS film/substrates systems; (ii) design non-invasive strategies for multifunctional contacts in optoelectronic devices; (iii) complete important missing pieces in the fundamental understanding of stress, which can be used to expand theoretical descriptions for predicting and tuning stress magnitude.

Résumé

La morphologie de films minces métalliques polycristallins élaborés par condensation d'une phase vapeur sur des substrats à faible interaction (SFI) possède un caractère 3D intrinsèque. De plus, la nature hors équilibre de la croissance du film depuis une phase vapeur conduit souvent à la génération de contraintes mécaniques, ce qui peut compromettre davantage la fiabilité et la fonctionnalité des dispositifs optoélectroniques. Les objectifs de cette thèse sont liés à la croissance de films métalliques sur SFI et visent à : (i) contribuer à une meilleure compréhension des processus à l'échelle atomique qui contrôlent l'évolution morphologique des films ; (ii) élucider les processus dynamiques qui régissent la génération et l'évolution des contraintes en cours de croissance ; et (iii) développer des méthodologies pour manipuler et contrôler la morphologie des films à l'échelle nanométrique. L'originalité de l'approche mise en œuvre consiste à suivre la croissance des films *in situ* et en temps réel par couplage de plusieurs diagnostics, complété par des analyses microstructurales *ex situ*. Les grandeurs mesurées sont confrontées à des modèles optiques et des simulations atomistiques.

La première partie est consacrée à une étude de comportement d'échelonnement des épaisseurs de transition morphologiques caractéristiques, à savoir la percolation et la continuité du film, lors de la croissance de films polycristallins d'Ag et de Cu sur carbone amorphe (a-C). Ces grandeurs sont examinées de façon systématique en fonction de la vitesse de dépôt et de la température du substrat, et interprétées dans le cadre de la théorie de la croissance de gouttelettes suivant un modèle cinétique décrivant la coalescence d'îlots, à partir duquel les coefficients de diffusion des espèces métalliques sont estimés. En confrontant les données expérimentales à des simulations par dynamique moléculaire *ab initio*, la diffusion de clusters multiatomiques est identifiée comme l'étape limitante le processus de croissance.

Dans la seconde partie, l'incorporation, et l'impact sur la morphologie, d'espèces métalliques ou gazeuses minoritaires (Cu, N_2, O_2) lors de la croissance de film Ag sur SiO_2 est étudié. A partir de mesures ellipsométriques *in situ*, on constate que l'addition d'espèces minoritaires favorise une morphologie 2D, entravant le taux d'achèvement de la coalescence, mais donne également une résistivité accrue de la couche continue. Par conséquent, une stratégie de manipulation de la croissance est proposée dans laquelle des espèces minoritaires sont déployées avec une grande précision temporelle pour cibler sélectivement des stades de croissance de film spécifiques et obtenir une morphologie 2D, tout en conservant les propriétés optoélectroniques des films d'Ag pur.

Dans la troisième partie, l'évolution des contraintes résiduelles lors de la croissance des films d'Ag et de Cu sur a-C et leur dépendance à la cinétique de croissance est systématiquement étudiée. On observe une tendance générale vers des amplitudes de contrainte de compression plus faibles avec une augmentation de la température/vitesse de dépôt, liée à l'augmentation de la taille des grains/à la diminution de la longueur de diffusion des adatomes. Également, l'ajout dans le plasma de N_2 sur le type et l'amplitude des contraintes dans les films d'Ag est étudié. L'ajout de quelques pourcents de N_2 en phase gaz donne lieu à un renversement de la contrainte de compression et une évolution en tension au-delà de la continuité du film. Cet effet est attribué à une croissance anormale des grains géants et le développement de rugosité de surface.

L'ensemble des résultats obtenus dans cette thèse fournissent les bases pour : (i) déterminer les coefficients de diffusion sur une large gamme de systèmes films/SFI; (ii) concevoir des stratégies non invasives pour les contacts multifonctionnels dans les dispositifs optoélectroniques; (iii) apporter des éléments de compréhension à l'origine du développement de contrainte, qui permettent de prédire et contrôler le niveau de contrainte intrinsèque à la croissance de films minces polycristallins.

Populärvetenskaplig sammanfattning

Varje material är i ett ständigt samspel med sin omgivning och interaktionens natur bestäms till stor del av materialets yta. Genom att belägga material med en tunn film av ett annat ämne kan man påverka detta samspel, och på så sätt uppnå t.ex. nya optiska och elektriska egenskaper. Denna metod har visat sig ha flertalet nya tillämpningar, bland annat vid skapandet av elektroniska komponenter, solceller och energibesparande fönster. Som namnet antyder är tjockleken på tunna filmer försvinnande liten, och sträcker sig från några atomer till några mikrometer (1 mikrometer $= 0{,}001$ millimeter). Tunnfilm syntetiseras vanligtvis genom så kallade förångningstekniker, där en fast materialkälla omvandlas till ånga och atom för atom skapar en film på ytan (som kallas substrat). Denna process är dock svår att i detalj observera, och på grund av detta analyseras ofta filmbildningen indirekt via tekniker som mäter förändringar av filmens optiska, elektriska och mekaniska egenskaper i realtid.

Denna avhandling undersöker syntesen av och egenskaperna hos myntmetallsfilmer, (silver och koppar), på kiseldioxid- och grafitytor. Dock uppvisar dessa ytor endast mycket svaga kemiska bindningar med myntmetallatomerna, vilket medför att metallfilmerna tenderar att skapa en 3D nano struktur, dvs att metallatomerna hopar sig i isolerade öar. Denna tendens påverkar filmens optiska och elektriska egenskaper negativt och därför begränsas drastiskt möjligheterna att använda metallfilmer i flertalet tillämpningar. Därför fokuserar en del av avhandlingen på att förstå och kontrollera de atomistiska mekanismer som leder till 3D nano strukturbildning. En annan problematisk aspekt av tunnfilmsyntesen är uppbyggnaden av mekaniska spänningar, som kan leda till böjning av substrat, skapande av sprickor, och att filmen förstörs. Till följd av detta handlar andra delen av avhandlingen om sambandet mellan syntesparametrar och typ/storlek av mekaniska spänningar. Sammanfattningsvis: en bättre förståelse av de atomistiska processerna som styr filmbildning och uppbyggnaden av mekaniska spänningar samt strategier för deras manipulation möjliggör en mer riktad användning av metallfilmer i viktiga tekniska tillämpningar.

Preface

The present dissertation is the result of my doctoral studies carried out between 2016 and 2020 in the Physics and Properties of Nanostructures (PPNa) group at the Institut Pprime, University of Poitiers, France, and the Nanoscale Engineering Division (NADES) at the Department of Physics, Chemistry, and Biology, Linköping University, Sweden.

The first part provides an overview of the research field, and the employed research methods. In the second part, the results of the research performed in course of the doctoral studies are presented in form of appended papers.

My research has been financed by the French Government program "Investissements d'Avenir" (LABEX INTERACTIFS, reference ANR-11-LABX-0017-01) and the ÅForsk foundation (contract ÅF 19-137). I acknowledge travel support by the ÖMSE program of the French Institute of Sweden, and financing of inter-disciplinary collaboration within Linköping University by the Center of Nano Science and Technology.

Andreas Jamnig

Linköping, August 2020

Acknowledgements

The four years that I spent as a Ph.D. candidate were a wonderful time, full of new experiences, new countries, new languages, new people, new friends. Foremost, it was a time of learning, and I would like to dedicate this space to the people that were part of this learning curve.

I full-heartedly thank my two supervisors, Gregory Abadias and Kostas Sarakinos, for creating this opportunity of a joint degree, and welcoming me into their research groups in Poitiers and Linköping. Gregory and Kostas, it was amazing to have two such dedicated, motivated people backing my research, and showing me how to become a better scientist. Thank you both for encouraging me to spend as much time as possible in the lab—my favorite activity—and helping me to take a step back from experiments when you could see that the time for analysis and reflection had come, and I could not (the lab-ban of early 2019).

Much of the research presented here would not have been possible without collaborations with other research facilities. I would like to thank my fellow co-authors for sharing their expertise with me and joining in scientific discussion.

I would like to thank the research team in Poitiers, Anny, Cedric, Clarisse, Firat, Rubenson, and Thibaud, for taking me in and being patient with my French. At this point, I want to single out Clarisse, who was always there when I messed up an experimental setup or got lost in French bureaucracy. Thank you for your help. The deposition chamber was always prepared and ready-for-use on Monday mornings, for this and also for interesting conversations during the commute to work I thank Philippe (and after his retirement Marc).

I thank my office colleagues in Linköping, Nikos (thank you for joining the group and not leaving me alone with “those simulation people”) and Mohammad, and my fellow “hole-digger” Victor, for a fun work atmosphere and the opportunity to vent, when venting was due. Victor, even though we never managed to dig into the same direction, it was great to progress through the Ph.D. with you, and experience milestones, the first paper, the first conference talk, together and meet on Sundays at the lab while writing our theses. My thanks also go to Mattias and Viktor, who showed me how to operate MADAM, which was—I believe—a slow and painful experience. Thank you for your patience. I also want to mention “my” students Olle and Martin, whom I guided through their master’s projects. Introducing you to our research topic was very instructive for me, and I would like to thank you for this experience.

A Ph.D. student spends many hours at the university. Luckily for me, this is also the place where I met friends, so that coffee, lunch and fika breaks shortened the days, and afterwork prolonged them. Senda, you were the first person to welcome me into the Ph.D. student life and showed me that sometimes it is better not to take things too seriously, thank you for that. Our hikes with Damien and Julien were amazing, and evenings with Florian, Romain, Romuald were always fun. Benjamin and Maxime, thank you becoming good friends.

Arnaud, thank you for trying to convince me to play squash for six months, until I finally said yes and loved it, and being a person that I look up to. Johan, you were invited to my parents' house, so I guess I will not get rid of you anymore (I will not mention your corrections of the popular science abstract here, since you will probably see this many times in the following years). Julia, I am glad you moved to Linköping, even though you are not always. You guys are a great game night group (because you let me win sometimes)!

Marius, thanks for the motivation for regular sport, and practicing German. Rasmus, I apologize for forcing you into a (platonic?) relationship, but it was always nice to meet you at 7am in the corridor and discuss important cultural differences over a cup of coffee. All the best to you and your family and thank you for your input to the Swedish part of this document.

Alexandra, Claudia, Clio, Davide, Judit, Karina, Laurent, Lida, Max, Tim, I have fond memories with each and every one of you. Thank you for accepting me back into the group as if nothing happened after disappearing to France for a year, this gave me a huge boost when arriving back in Sweden.

Finally, there are the people that I left back home. Friends from back in the day, and from university that I only meet once a year, but when we meet, we can just talk as we used to do. Thank you for that, and for visiting me. Bei meiner Familie, Mama und Papa, Stefan und Bettina, Omas, Tanten und Onkels, entschuldige ich mich für die seltenen Heimatbesuche (und Anrufe). Danke, dass ihr meine Abenteuer- und Reiselust akzeptiert und unterstützt, oder sie zumindest als Ausrede für Urlaube nutzt.

Table of contents

1. Introduction

Thin metal films are critical components in many technologies that have become essential parts of modern life, including information storage systems, integrated circuits, sensors, and displays. [1] This is a direct result of the electronic, optical, magnetic, mechanical, and thermal properties that are unique to metallic materials. These properties are largely established during film synthesis, [2–4] and can often not be changed post-synthesis without losing unique film attributes. Thus, a fundamental understanding of nanoscale structure-forming processes that govern film growth is needed to effectively control performance and functionality of thin-film-based devices.

Noble-metal atoms interact weakly with the surface of oxides and van der Waals materials. [5,6] This weak interaction leads to a pronounced and uncontrolled three-dimensional (3D) film morphological evolution, which is characterized by discontinuous layers during the initial film growth stages, and rough surfaces upon formation of a continuous layer. [7] A 3D morphology is detrimental for applications that require flat film surfaces, e.g., in optoelectronic devices, biosensors, and low-emissivity energy-saving windows. [8–11] Since 3D growth is an intrinsic property of weakly-interacting film/substrate systems, special deposition strategies are required for manipulating growth toward two-dimensional (2D) morphology. While such strategies exist in the literature for epitaxial systems, e.g., via deployment of minority species (also referred to as surfactants) at the film growth front, [12] the way by which structure-forming processes in weakly-interacting systems are affected by the presence of surfactant atoms is not fully understood.

Vapor-based thin-film deposition is a far-from-equilibrium process, whereby structure formation is determined by the kinetic rates of atomic-scale mechanisms. [12] At such conditions, atoms often arrange themselves in metastable configurations, leading to the formation of mechanical stress, [13] which can be detrimental for the reliability and functionality of thin-film-based devices. Stress formation and evolution is strongly linked to the film morphology at various growth stages, during which a multitude of processes, including surface diffusion and grain growth, are active. [14,15] To date, it remains unclear how the complex interplay and the dynamic competition among these processes affect stress.

Research presented in this thesis focuses on the nanoscale growth dynamics, stress generation, and morphology manipulation in weakly-interacting film/substrate systems. Investigated films consist of silver and copper; a short introduction to the properties of these elements is given in Section 1.1. The research goal and strategy are presented in Section 1.2, and an outline of the thesis is given in Section 1.3.

1.1. Silver and copper

Silver and copper are members of group 11 in the periodic table of elements, and together with gold, are known as coinage metals. An overview of physical and chemical properties of silver and copper is given in Table 1. [16]

Silver has been known since ancient times because it exists in elemental form on earth's surface. Silver-based compounds that can be found naturally include sulfides and chlorides. Pure silver is stable in pure water and air, and has a brilliant white metallic luster that tarnishes when exposed to ozone, hydrogen sulfide, or air containing sulfur. It is used as mirror material, when deposited on glass or metals, since it is the best reflector in the visible-light spectral range, but it is a poor reflector in ultra-violet. Silver is ductile and malleable, and has the highest electrical and thermal conductivity of all elements, which is why it is used as ohmic contact material in microelectronics. Pure silver is not toxic, however, many of its salts are, and it is germicidal, i.e., lower organisms do not survive on silver surfaces.

Copper has been known since prehistoric times because it exists on the earth's surface with high purity. Naturally found compounds are oxides, sulfides, and carbonates. Pure copper has a reddish color and a metallic luster. Since pure copper is malleable and ductile, it is one of the first metallic materials that was used as tool by mankind (together with tin and lead). The recognition that a mixture of copper and tin, i.e., bronze, leads to a harder and stronger material than its constituents marks the invention of alloying, and the beginning of a new civilizational age–the bronze age. Copper is the best conductor of heat and electricity after silver, and therefore widely used in the electrical industry.

Thin silver and copper films in oxide/metal/oxide or dielectric/metal/dielectric heterostructures are used as low-emissivity coatings, e.g., on window glass. [11] Owing to the high corrosion resistance and flexibility, these structures are prime candidates to replace indium tin oxide as transparent conductive electrode material in optoelectronic devices including light-emitting diodes, thin-film solar cells, flat-panel displays, and touchscreens. [17] Silver is used in analytical sensors due to the plasmonic behavior of nanoscale silver films and particles, leading to surface enhanced Raman scattering (SERS), which increases sensitivity of biosensors. [18]

Table 1: Overview of physical and chemical properties of Cu and Ag as listed in Ref. [1].

	Cu	Ag
Atomic number	29	47
Electronic configuration	$[Ar]3d^{10}4s^1$	$[Kr]4d^{10}5s^1$
Molecular weight (g/mol)	63.546	107.868
Mass density (g/cm^3)	8.96	10.5
Crystal structure	Face centered cubic	
Lattice parameter (nm)	0.36150	0.40862
Melting temperature (K)	1358	1235
Homologous temperature at $300\ K$	0.22	0.24
Boiling temperature (K)	2835	2435
Gibbs energy of formation of gas at $298.15\ K$ (kJ/mol)	297.7	246.0
Bond dissociation energy (BDE) (kJ/mol)	201	162.9 ± 2.9
BDE with oxygen (kJ/mol)	287.4 ± 11.6	221 ± 21
BDE with sulfur (kJ/mol)	274.5 ± 14.6	216.7 ± 14.6
Electronegativity	1.90	1.93
Electrical resistivity at $298.15\ K$ ($\mu\Omega cm$)	1.543	1.467
Molar heat capacity ($J/(molK)$)	24.440	25.350
Thermal conductivity at $300\ K$ ($W/(cmK)$)	4.01	4.29

1.2. Research goal and strategy

The overall goal of the present thesis is to contribute to the understanding of fundamental aspects related to morphological evolution and stress generation during noble-metal film growth on weakly-interacting substrates. The specific objectives are to:

- Elucidate atomic-scale processes that control early film growth stages, and estimate the rates of such processes.
- Understand the way by which key deposition parameters (e.g., deposition rate and temperature) affect stress evolution, and establish the complex interplay among stress and film microstructure and morphology.
- Obtain atomistic insights with regards to the effect of gaseous and metallic surfactants on early stages of film growth, and leverage these insights for developing efficient non-invasive growth manipulation strategies.

Investigations focus on magnetron sputter-deposited silver and copper films on silicon dioxide and amorphous carbon substrates, which are archetypal weakly-interacting film/substrate systems. Research is conducted by strategically combining *in situ* and real-time film growth monitoring by means of multiple complementary diagnostic tools, *ex situ* chemical and (micro)-structural analyses, optical modelling, and deterministic growth simulations.

1.3. Outline of the thesis

This thesis work is divided into two parts. The first part (Chapters 1 through 7), is a topical, theoretical, and experimental introduction to the research performed throughout my Ph.D. studies. Concepts related to vapor-based thin film synthesis (i.e., vacuum science and technology, plasma physics, sputter-deposition) are described in Chapter 2. An overview of atomic-scale structure-forming processes during film growth is given in Chapter 3. Concepts that explain stress formation and evolution in thin films are presented in Chapter 4. Chapter 5 describes experimental devices and techniques that are employed in course of this thesis work, and Chapter 6 outlines employed simulation and theoretical techniques. Chapter 7 outlines contributions to the research field and provides an outlook for a potential continuation of the research conducted in the present work. In the second part, papers that present my main contributions to the research field are appended.

2. Vapor-based thin film deposition

Vapor-phase condensation is the most common method for synthesizing thin films for research and industrial purposes. In the present thesis, thin films are synthesized by magnetron sputtering, a deposition method in which vapor is generated by transferring momentum from energetic ions to a solid source. To be able to control the film synthesis environment, deposition experiments are routinely carried out in vacuum, hence a brief introduction to vacuum science and technology is provided in Section 2.1. The source of energetic ions required in sputter-deposition is a plasma; this state of matter is introduced in Section 2.2. Finally, the principle of magnetron sputter-deposition is presented in Section 2.3.

2.1. Vacuum science and technology

Vacuum is per definition space void of matter. To create vacuum from the atmosphere, gas molecules have to be removed from a closed isolated vessel (referred to as vacuum chamber). However, the complete removal of atoms is technologically not possible, such that in materials science the term “vacuum” refers to a volume with pressure lower than atmospheric pressure, [19] i.e., vacuum in thin film deposition chambers is a gas. Consequently, atom/molecule interactions with each other and with surfaces are described by the kinetic theory of gases. This theory predicts the speed distribution of gas atoms, from which the frequency of collisions in the gas phase and the flux of gas species toward the solid surface can be calculated (Section 2.1.1). These quantities are important for determining the energy and chemical nature of film forming species, as well as the incorporation of impurities in the film as explained in Section 2.1.2. Key technological aspects of vacuum science, i.e., principles and types of vacuum pumps and pressure gauges are outlined in Sections 2.1.3 and 2.1.4, respectively.

2.1.1. *Kinetics of atoms in gas phase*

The kinetic theory of gases describes the behavior of ideal gases in a confined volume, assuming random motion of gas molecules that are approximated as hard spheres with dimensions that are small compared to the mean molecule distance. Molecule-molecule and molecule-wall interactions are treated as elastic collisions, while no attractive or repulsive forces apply between gas molecules. With these approximations, the Maxwell-Boltzmann formula describes the steady-state distribution of molecular speeds v as [20,21]

$$f(v) = \frac{1}{n}\frac{dn}{dv} = \frac{4}{\sqrt{\pi}}\left(\frac{m}{2k_BT}\right)^{3/2} v^2 exp\left(-\frac{mv^2}{2k_BT}\right). \qquad (2.1)$$

In Eq. 2.1, $f(v)$ is the fractional number of molecules, n is the number of molecules per unit volume in the speed range v to $v + dv$, m is the molecular mass, k_B is the Boltzmann constant, and T is the absolute temperature. From this distribution function, we find that no molecules with zero or infinite speed exist. The root-mean-square speed $\sqrt{\overline{v^2}}$, which describes the collective behavior of the gas molecules, calculates as $\sqrt{\overline{v^2}} = \sqrt{3k_BT/m}$.

Speed distributions for He and Ar gas are presented in Fig. 2.1, and we find that $f(v)$ broadens and shifts toward larger speed values with decreasing m (e.g., $m_{He} = 4\,u$, and $m_{Ar} = 40\,u$), which is also reflected by the relation $\overline{v^2} \sim 1/m$ (indicated by vertical lines in Fig. 2.1). When comparing $f(v)$ of Ar at 300 and $1000\,K$, a shift of the distribution to larger speed and broadening is seen for increasing T; concurrently, $\overline{v^2}$ scales linearly with T. It is noted that while the speed distribution is dependent on m and T, the kinetic energy E_{kin} of a collection of gas molecules calculates as [20,21]

$$E_{kin} = \frac{1}{2}m\overline{v^2} = \frac{3}{2}k_BT\,, \tag{2.2}$$

and is only temperature dependent.

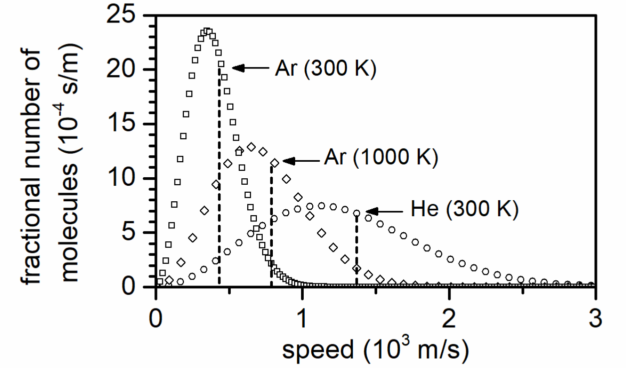

***Fig. 2.1:** Speed distributions of Ar and He gas calculated by the Maxwell-Boltzmann formalism for temperatures $300\,K$ (Ar and He), and $1000\,K$ (Ar). The root-mean-square speeds of the respective distributions are marked by vertical lines.*

2.1.2. *Gas/gas and gas/surface interactions*

As explained in Section 2.1.1, molecules in a contained volume interact with the walls that limit the volume, and apply a pressure $p = nm\overline{v^2}/3 = nk_BT$. [20,21] Vacuum systems are categorized by the lowest pressure they can reach, i.e., the base pressure. Low/intermediate-vacuum systems have base pressure between atmosphere ($10^5\ Pa$) and $10^{-1}\ Pa$, high-vacuum (HV) systems are in the range 10^{-1}

to $10^{-5}\,Pa$, while ultra-high-vacuum (UHV) is reached for $p < 10^{-5}\,Pa$. Ambient atmosphere consists mainly of nitrogen molecules, however, an artificially created HV contains predominantly water vapor, and hydrogen molecules are the most abundant species in UHV. This is a result of gas-dependent pumping rates in artificial vacuum systems.

From the Maxwell-Boltzmann speed distribution, the mean free path λ, i.e., the mean distance a gas molecule travels between collisions with other molecules, can be calculated as [20,21]

$$\lambda = \frac{k_B T}{\sqrt{2}\pi\, d_{mol}^2\, p}\,. \tag{2.3}$$

In Eq. 2.3, d_{mol} is the diameter of the gas molecule; a typical value of d_{mol} for gases used in thin film deposition is $3 \times 10^{-10}\,m$. [20] At $300\,K$, λ is in the range 10^{-1} to $10^{3}\,m$ in HV systems, and consequently comparable to typical vacuum chamber dimensions, i.e., gas molecules experience few/no collisions. However, during deposition of thin films, the working pressure is $\sim 1\,Pa$, and λ decreases to values $< 10^{-2}\,m$, and gas molecules collide often before they are pumped out of the chamber, or adsorb on a surface.

Another important quantity that can be derived from the Maxwell-Boltzmann speed distribution is the gas impingement flux Φ per unit time and area [20,21]

$$\Phi = n\sqrt{\frac{k_B T}{2\pi\, m}} = \frac{p}{\sqrt{2\pi\, m\, k_B T}}\,. \tag{2.4}$$

Equation 2.4 can be used to calculate the monolayer formation time t_{ML} of gas species on a surface. During film growth, background species arriving from the gas phase lead to contamination in the film, i.e., deposition of clean films is not possible if the arrival rates of film atoms and gas species from the background are comparable. From d_{mol}, the average area of a gas molecule can be estimated as $d_{mol}^2 \cong 10^{-19}\,m^2$, i.e., one monolayer of gas molecules consists of $\sim 10^{19}\,molecules/m^2$. For thin film growth in a system with base pressure $p = 10^{-5}\,Pa$, where water is the most abundant gas species ($m_{water} = 18\,u$), one monolayer (ML) forms in $\sim 30\,s$ at $T = 300\,K$. Comparing this time to t_{ML} of the film forming species, e.g., during deposition of Cu with deposition rate $0.1\,nm/s$, $t_{ML,Cu} \cong 2\,s$, a Cu/H_2O monolayer formation time ratio of $t_{ML,Cu}/t_{ML,water} \cong 0.07$ is calculated, i.e., a Cu film deposited at above-described conditions may contain up to $7\,at.\%$ of water. This value represents an upper theoretical limit since a sticking probability of 1 for gas molecules on the surface is assumed. In reality, the sticking probability of gases on surfaces is smaller than unity, so that a significantly smaller fraction of contaminants is incorporated in the growing films at typical vacuum conditions.

2.1.3. *Vacuum pumps*

To create sub-atmospheric pressure from the ambient atmosphere, air has to be removed from a closed volume (e.g., deposition chamber). For HV and UHV conditions, this is achieved using a pumping system rather than a single pump, which include a primary pump to create low vacuum down to $\sim 10^{-1}\,Pa$ that is connected in series to a second pump that is backed by the primary pump and allows reaching HV and UHV. Thin films discussed in this thesis are synthesized in two vacuum systems (HV and UHV). In the following, vacuum pump concepts that are used in the respective deposition chambers are outlined. A more detailed description of the pumping systems is given in Section 5.1.

Positive displacement pumps

Positive displacement pumps are used to create low/rough vacuum with pressure $\sim 10^{-1}\,Pa$, [20] or to back pumps that can create HV/UHV (see below). Their working principle is the isolation and compression of a volume from the to-be-pumped chamber that is then exhausted into the atmosphere; this volume displacement is usually performed by rotating parts. [22] If lubricant and pumped volume are isolated from each other, the pump is called dry positive displacement pump, which limits the risk of vacuum chamber contamination. [19]

An example of a rotary positive displacement pump is the Roots pump; the working principle is outlined in Fig. 2.2(a). Two lobed rotors spin in an oval housing with opposing directions driven by a motor. [19] When the two rotors are in a horizontal T-configuration, volume is isolated (e.g., right side during (iii) in Fig. 2.2(a)), which is subsequently exhausted in sequence (iv). The rotors touch neither each other nor the housing walls, i.e., no lubrication is needed, but due to the existence of small gaps between rotors and walls ($\sim 0.1\,mm$), HV cannot be reached with this pump. High rotation speeds (typically $3000\,rpm$) are used to compensate for the incomplete isolation of volume. When pumping against atmospheric pressure, the Roots pump has an ultimate pressure of $\sim 10^{3}\,Pa$, while for attaining backing pressure $\sim 10^{-1}\,Pa$, several Roots pumps are combined in series.

Another concept is the scroll pump, depicted in Fig. 2.2(b), which consists of two Archimedean spirals that are displaced along a horizontal line, and rotated by $45°$. This creates crescent-shaped closed volumes. One spiral is a stator, while the second one rotates, and transports gas from the chamber side toward the exhaust. Tip seals isolate the top of the spiral walls, i.e., no lubrication is needed. The ultimate pressure that can be attained with a scroll pump is $\sim 10^{-1}\,Pa$.

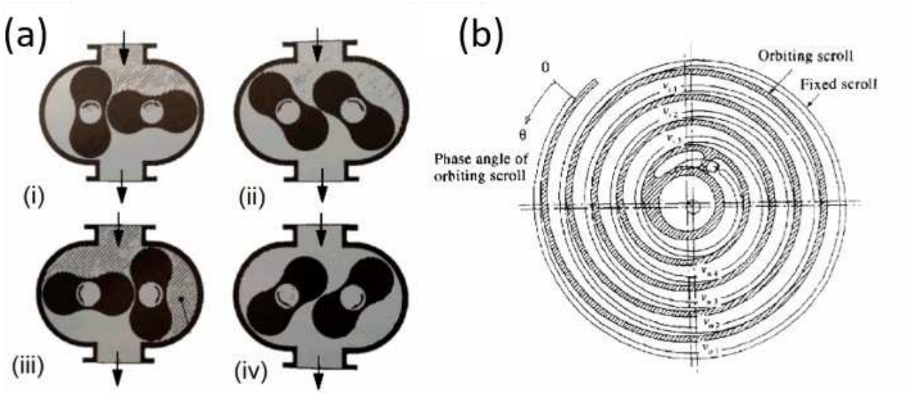

Fig. 2.2: Operation principle of (a) a Roots pump and (b) a scroll pump. Reprinted with permission from (a) Ref. [22] ***and (b) Ref.*** [23].

Cryogenic pumps

Cryogenic pumps trap gas species on surfaces that are cooled to temperatures $< 120\,K$. [20] At such temperatures, van der Waals forces inhibit the desorption of atoms from the surfaces, except for hydrogen, helium and neon that have too high vapor pressures, even at surfaces cooled to $20\,K$ in the innermost section of the pump. A schematic representation of a cryopump is given in Fig. 2.3(a). The pump is shielded from heating by thermal radiation from the surrounding atmosphere, and cryogenic temperatures are obtained by cooling the surfaces with liquid nitrogen. Cryogenic pumps are widely used in materials research due to their high pumping speed, and possibility to reach UHV. They cannot be operated from ambient pressure, since the influx of gas molecules would lead to heating of system, and formation of thick ice condensate, and are therefore coupled with primary pumps that create a pressure $\sim 10^{-1}\,Pa$. To limit the formation of thick condensate, gases are trapped at different stages, with decreasing temperature from the vacuum chamber to the innermost part of the pump.

Turbomolecular pumps

A turbomolecular pump consists of stator/rotor pairs; latter imparts a preferred orientation to the motion of gas molecules by impact, as schematically illustrated in Fig. 2.3(b). [4] While gas molecules are transferred through the pump, they are compressed from low pressures (on the chamber side) to higher pressure (on the backing line side). This compression ratio is proportional to the rotor speed ($> 20\,000\,rpm$), and the inverse of the molecular weight of the pumped species. Therefore, hydrogen is not efficiently captured and removed by this type of pumps. Nonetheless, base pressure in the $10^{-8}\,Pa$-range can be attained with a turbomolecular pump. Moreover, such a pump is not able to compress gases from the UHV regime to ambient pressure and is therefore coupled with a primary pump that creates a foreline pressure $\sim 10^{-1}\,Pa$.

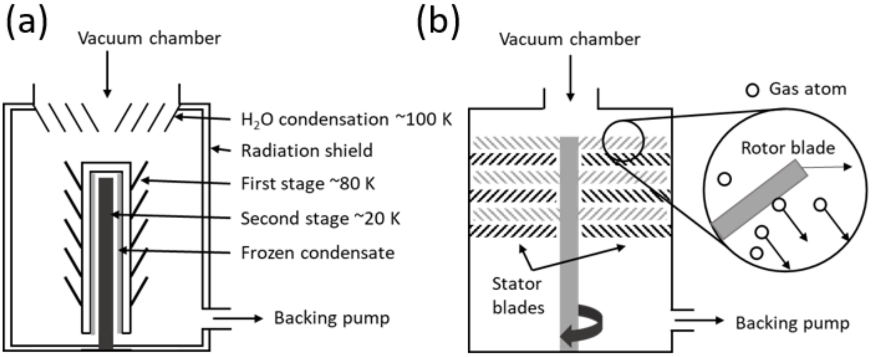

Fig. 2.3: (a) Schematic representation of a cryogenic pump that contains stages with different temperatures to condensate gas molecules. (b) Schematic representation of a turbomolecular pump. Rotor blades transfer momentum to gas atoms and compress them from the vacuum chamber to the backing line.

2.1.4. *Pressure gauges*

The discussion in Section 2.1.2 shows that pressure is an important quantity from which the behavior of gas molecules in a vacuum system can be determined, including mean free path and monolayer formation time. Depending on the vacuum type (HV, UHV), different gauges are used to determine the pressure in a vacuum system. In the following, the working principles of some pressure gauges that were used in course of the present thesis are outlined.

Capacitance manometer

Capacitance manometers are classified as direct-reading pressure gauges with a solid wall, and accurately measure pressure in the range 10^5 to $10^{-2}\ Pa$. [21] The gauge consists of two chambers (see Fig. 2.4(a)): a sealed chamber with reference pressure (typically $10^{-5}\ Pa$) and one with the to-be-determined pressure, separated by a diaphragm that acts as capacitator with a fixed counterelectrode. When the pressure changes in the measuring chamber, the deflection of the diaphragm changes, which is read as change in capacitance.

Pirani gauge

The Pirani gauge is an indirect pressure gauge (i.e., pressure is measured by the change in another physical property) that relates the heat transfer between a hot wire (filament) and its surrounding gaseous medium to the pressure. [21] In the low-pressure regime ($\sim 10^2$ to $10^{-2}\ Pa$), heat flow due to free molecules (i.e., conduction) increases linearly with temperature, i.e., the rate of temperature change can be related to the density of gas molecules. This linear relation is not valid at higher pressures, where convection is active, or at too low pressures, where radiation is the predominant heat-transfer mechanism. In the Pirani gauge, the temperature change is measured by temperature-induced resistivity change in an electrical circuit, i.e., a Wheatstone bridge schematically shown in Fig. 2.4(b). A decrease in electrical resistivity signifies that the wire temperature decreases owing to stronger gas molecule/wire interactions with increasing pressure. Pirani gauges are used in the pressure range 10^1 to $10^{-2}\ Pa$.

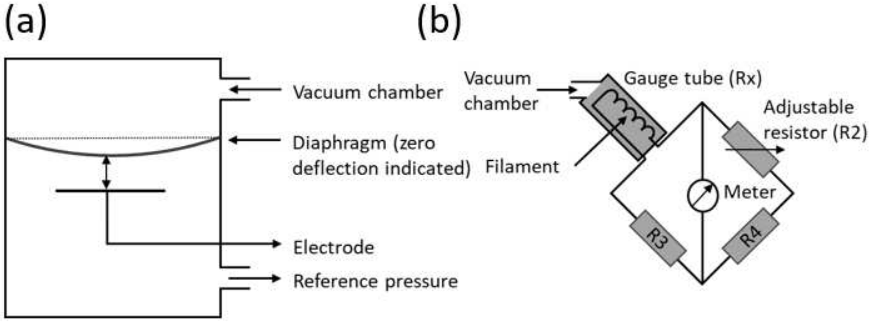

Fig. 2.4: (a) Schematic illustration of a capacitance manometer; when the pressure in the vacuum chamber is not equal to the reference pressure, the diaphragm deflects from its zero position, and the capacitance to a stationary electrode changes. (b) Schematic illustration of a Pirani gauge: the filament resistivity changes due to interaction with gases from the vacuum chamber. The filament is part of a Wheatstone bridge, and its resistivity R_x can be calculated to $R_x = R_2R_3/R_4$, when the resistor R_2 is adjusted so that no current flows through the Amperemeter.

Bayard-Alpert gauge

The Bayard-Alpert gauge is a hot filament ionization gauge that relates the current between a collector and a gas that has been ionized by electron impact to the pressure in the gas. [21] Fig. 2.5(a) illustrates this type of pressure gauge. The hot filament acts as electron emitter, while the positive ions are attracted by the collector. This pressure gauge is used in the pressure range 10^{-1} to $10^{-8}\ Pa$; ion/electron recombination limits the application in the high-pressure range, and x-ray photoemission leads to errors in the low-pressure range. Ionization gauges are not true pressure gauges, since the number of positive ions formed through impact ionization is proportional to their number density, but can be used to measure pressure if the temperature remains constant.

Cold cathode ionization gauge

In cold cathode ionization gauges, electrons are created between a cathode/anode pair, and forced into long spiral trajectories by a magnetic field (see illustration in Fig. 2.5(b)). [21] This increases the gas/electron interaction probability, which increases the ionization current, and eliminates the need of an additional electron source (i.e., the hot filament). Cold cathode ionization gauges are used in the pressure range 10^{-1} to $10^{-9}\,Pa$; the low-pressure limit is reached when no discharge is formed.

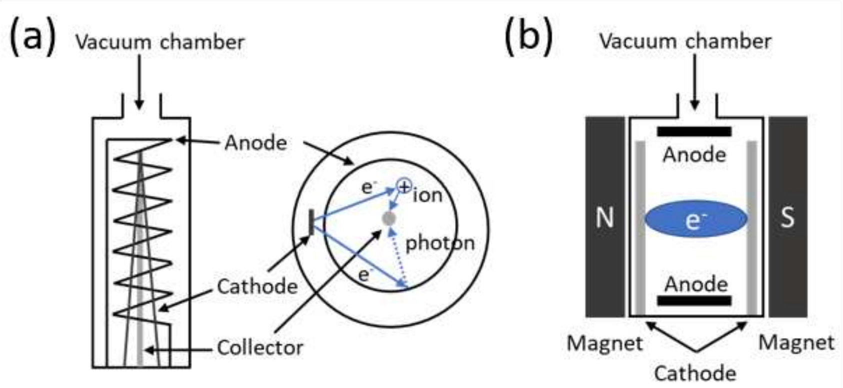

Fig. 2.5: (a) Schematic illustration of a hot filament ionization gauge, consisting of the electron (e^-) emitting cathode (i.e., hot filament), anode and collector. Electron/gas molecule interactions can lead to ionization; the ion is attracted by the collector. Impingement of electrons on the anode leads to x-ray emission. (b) Schematic illustration of a cold cathode ionization gauge, where electron density is locally increased by a magnetic field. This increases the interaction probability between electrons and gas molecules travelling from anode to cathode.

2.2. Confined plasma

During sputter-deposition of thin films, a vapor phase is created by bombarding the surface of a solid with ions. The source of these ions is a plasma that is created within the vacuum chamber. This state of matter is introduced in this section, before outlining sputtering and sputter-deposition in Section 2.3.

Most observable mass in the universe is in plasma-state, [4] i.e., it consists of a mixture of positively charged ions, negatively charged electrons, and neutral species, i.e., plasma is, on average, electrically neutral. [24] Plasmas can be categorized in terms of the number density of charged particles (typically $\sim 10^{16}\ m^{-3}$ in laboratory-scale plasmas) and the energy (i.e., temperature) of the species (typically, electron energies range between 1 to $10\ eV$, ion and neutral energies are in the meV regime). [4] If the plasma is in equilibrium, temperatures of all plasma species are equal to each other and to the temperature of the chamber walls. This condition is never met in the laboratory, i.e., nonequilibrium or *cold plasmas* are used in thin film synthesis experiments.

One important feature is that particles within a plasma move in random directions, but the plasma exhibits a collective behavior in the presence of an electric field, i.e., a particle flux is created which may be used in thin film deposition. Due to random movement within the plasma, particle interactions are common, e.g., electrons and ions (of species A and B) can recombine $e^- + A^+ \to A$, which leads to loss of charged particles. To maintain a stable plasma, additional processes are needed, e.g., ionization ($e^- + A \to A^+ + 2e^-$), attachment ($e^- + A \to A^-$), excitation ($e^- + A_2 \to\to A_2^* + e^-$), or dissociative attachment ($e^- + A_2 \to A^+ + A^- + e^-$). Atom-ion collisions are common, e.g., symmetric charge transfer ($A^+ + A \to A + A^+$), or metastable-neutral ionization ($A^* + B \to B^+ + A + e^-$), also known as Penning ionization. [4]

Due to the inequality of electron and ion temperatures in laboratory-scale plasmas, the net-neutrality is not sustained, and plasma interaction with the (electrically conductive) chamber wall leads to the creation of a *sheath* (see Fig. 2.6). Electrons have higher velocities than ions, and are therefore lost faster to the walls, i.e., the plasma has a positive potential with respect to the walls (plasma potential $V_p \cong 5\ V$). [4,24] Inserting an electrically isolated object into a plasma results initially in a negative charging due to arrival of fast electrons. The negative potential attracts ions, while it repels electrons, until a steady-state electron/ion flux is reached and a negative floating potential $V_f \cong -15\ V$ of the object is formed with respect to ground. [4,24]

If a negative potential is applied to the cathode (i.e., the target during sputter-deposition), electrons are accelerated away from the cathode surface, while ions are attracted. Close to the cathode surface, electron energies are too small to excite atoms/ions, therefore a dark region is formed close to the cathode surface. With increasing distance from the cathode surface, energies of primary and secondary electrons increase, leading to more excitation processes, and a typical *glow discharge* is seen when a plasma is ignited.

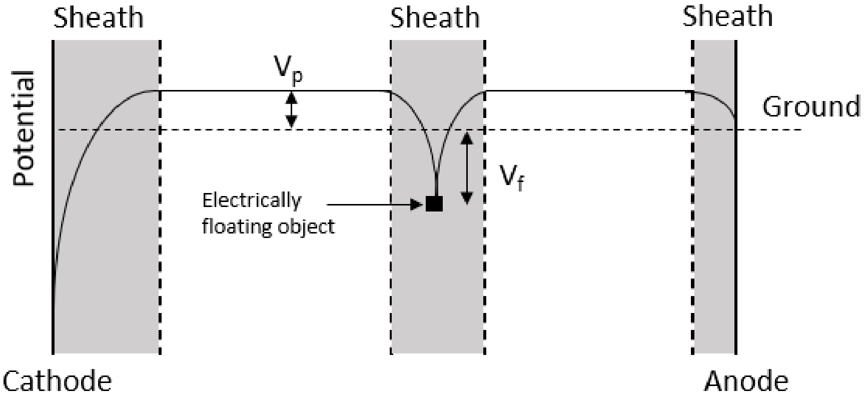

***Fig. 2.6:* Electrical potential distribution of a plasma between cathode on negative potential and anode on ground potential. The positive plasma potential V_p forms between cathode and anode, while an electrically floating object will be at negative floating potential V_f. Potential variations are only observed in sheaths close to walls/objects, while the plasma bulk exhibits a constant positive potential.**

2.3. Sputter-deposition

During *physical vapor deposition* (PVD), vapor is created from a solid source that condenses on a surface (i.e., the *substrate*) to form a thin film. PVD techniques are categorized by the way energy for vapor creation is provided: in *evaporation*, thermal energy is transferred, while in *sputtering*, momentum is transferred. Sputtering is extensively used in materials research and industry as it is easy to implement, works for a broad range of materials, and offers access to a wide parameter space for controlling film growth (e.g., temperature, deposition rate, energy of film-forming species). [25]

2.3.1. *Diode sputtering*

A sputtering device is implemented in vacuum systems by installing two electrodes with high potential difference (in kV-range), and introducing a working gas in the chamber. The potential difference leads to partial ionization of the gas and formation of a discharge/plasma. High negative potentials on the cathode lead to attraction of ions that impinge on the surface, hence, the cathode is called *target*. This impingement leads, among others, to target heating (i.e., active target cooling is required) and ejection of target atoms, i.e., the target is *sputtered*. Sputtered atoms are the most common species resulting from ion/target interactions; further species include diatoms, resputtered trapped gas atoms, single ions, reflected incident gas species (backscattered neutrals), and secondary electrons.

Three sputtering regimes exist depending on the energy of the ions impinging on the target (see Fig. 2.7 for schematic illustrations). In the first regime (see Fig. 2.7(a)), incident ions transfer enough energy to a target atom to break all bonds with its neighbors, i.e., single knock-on events occur. The minimum energy for this regime is the *threshold energy* E_{th} for atomic displacement in the target material (typically in the range 2 to $40\ eV$), [4,26] which depends strongly on the nature of the arriving ion, and mass and atomic number of the target atoms. [4] At higher ion energies (0.1 to $10\ keV$), [4] linear collision cascades are formed (see Fig. 2.7(b)), in which a series of atoms in the target transfer the projectile momentum until a surface atom is ejected. This regime is characterized by low collision number densities, so that on average only two particles are moving. [4] A third regime exists for very energetic (keV to MeV) heavy ions that sputter dense matter (see Fig. 2.7(c)). In this case, the collision number density is high, and many target atoms move at the same time, leading to a local heat spike, i.e., the target melts locally. [27]

The *sputter yield* is the ratio of number of sputtered atoms to incident particles, and is a measure for the efficiency of the sputtering process. Sputter yields vary with particle energy, incidence angle, as well as atomic number and molecular mass of sputtering/sputtered species. [28–30] Depending on these parameters, values for the sputter yield can change over orders of magnitudes, e.g., when argon ions impinge on silver with $500\ eV$, the sputter yield is 3.12, while it is 2.35 for copper targets, and only 0.12 for carbon targets. [4] While the dependence of the sputter yield on the energy of ions is complex (e.g., see Ref. [28]), it can be approximated by a linear function for small energy changes, which is seen in the linear dependency of deposition rate with cathode potential.

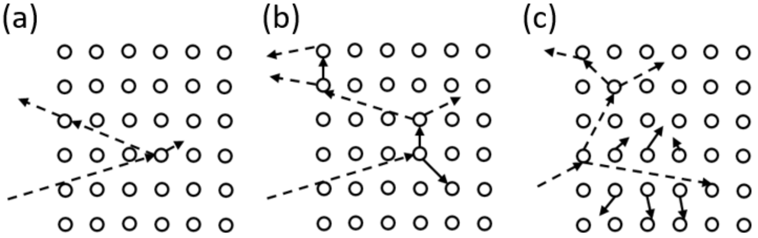

Fig. 2.7: Energy regimes of sputtering: (a) single knock-on (low energy), (b) linear cascade, (c) heat spike (high energy).

2.3.2. *Sputter gases*

Sputter-deposition refers to the synthesis of a film by condensation of sputtered species and is typically performed in argon plasma. Argon is inert (i.e., plasma/film chemical reactions do not have to be considered) and has a high sputter yield with the most common film elements compared to other gases, [30] while being reasonably priced (unlike krypton, xenon, which have higher sputter yields for heavy elements). Neon sputtering results in 20% higher sputter yields than argon for beryllium and carbon, while krypton has a 40% to 60% advantage for elements heavier than tantalum. [30] For compound film growth, reactive gases (e.g., nitrogen, oxygen) are added to the working atmosphere, in combination with elemental or compound targets. It is noted that compound films or multilayers can be also deposited from multiple targets installed in the deposition chamber at the same time.

2.3.3. *Magnetron sputter-deposition*

The efficiency of the sputtering process is increased by applying a magnetic field $\vec{B}$ perpendicular to the electric field $\vec{E}$ close to the target (i.e., *magnetron sputter-deposition*), as schematically presented in Fig. 2.8. Without magnetic field, electrons are accelerated away from the target, which reduces the occurrence frequency of electron-neutral ionizing collisions. In presence of a magnetic field, electrons (with charge q), are subject to the Lorentz force $\overrightarrow{F_L} = q\left(\vec{E} + \vec{v} \times \vec{B}\right)$, where $\vec{v}$ is the velocity of electrons. $\overrightarrow{F_L}$ forces electrons into a helical movement that traps them close to the target, and promotes electron/ion interactions, increasing the plasma density locally, and thus leading to more efficient sputtering of the target. $\vec{B}$ is typically not strong enough to affect ions that have a much higher mass than electrons. Compared to sputtering without magnetron, magnetized plasmas are stable at lower working pressures (0.1 to $1\ Pa$) and with lower potentials applied to targets (tens to hundreds of volts). The former leads to higher deposition rates, while the latter decreases substrate heating by energetic electrons.

Magnetron sputter-deposition is further characterized by the way potential (i.e., power) is applied to the target. Power can be applied continuously in a method that is known as direct-current magnetron sputtering. Alternatively, power can be supplied to the target in the form of electrical pulses, also known as pulsed magnetron sputtering. An advantage of the pulsed operation is that the average energy density on a target is not only dependent on the peak power, but also on the fraction of one period that the power is active (i.e., duty cycle). Hence, if the duty cycle is low, much higher power can be applied to targets without risking target overheating. In high power impulse magnetron sputtering, [31,32] very high voltages are applied to the target ($700\ V$ to $2\ kV$ for duty cycle up to 10%, with pulse duration in the μs-range), which substantially increases the degree of ionization of the sputtered species. Ionized film-forming species can be accelerated to the substrate by applying a potential (i.e., *substrate bias*), which allows setting the energy range and nature of species arriving at the substrate, i.e., ions offer an additional tool to engineer the morphology of growing films. [33]

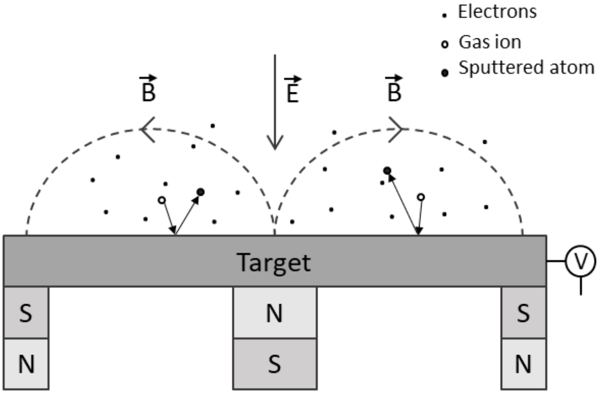

Fig. 2.8: Schematic representation of a magnetron sputtering source. Electric $\vec{E}$ and magnetic fields $\vec{B}$, created by applied potential (V) and magnets (N-S), respectively, are indicated by arrows.

3. Atomic-scale structure-forming processes and growth manipulation

The present chapter describes atomistic processes that lead to the formation of a thin film, and it discusses their manipulation for controlling film morphological evolution. As far as it concerns thin film growth, a distinction between near-equilibrium (i.e., atoms are arranged at minimum-energy configurations) and far-from-equilibrium growth (i.e., kinetic barriers impede thermodynamically favored configurations) has to be made (see Section 3.1). After condensation of atoms on the substrate, surface diffusion and adatom-adatom interactions lead to the formation of isolated islands; these concepts are presented in Sections 3.2 and 3.3, respectively. With continued deposition, islands become larger via processes that are described in Section 3.4. Section 3.5 outlines the film morphological evolution from isolated islands to percolation and continuous film formation, and introduces fundamental properties related to film structure and morphology (e.g., density, texture). By targeted manipulation of these processes, the thin film microstructure—and properties—can be tailored. Concepts for growth manipulation are presented in Section 3.6.

3.1. Near-equilibrium and far-from-equilibrium growth

Thin films are often deposited from the vapor phase, driven by the high supersaturation of atoms in the vapor phase compared to the substrate surface. Per definition, vapor is a gas that can condensate when pressure is increased because its temperature is lower than the critical temperature T_{crit} for gas/liquid phase transition (compared to real/fixed gases, for which the temperature is higher than T_{crit}, e.g., at $300\ K$, gaseous water is a vapor ($T_{crit,H_2O}\ \cong\ 647.1\ K$), and argon is a gas ($T_{crit,Ar}\ \cong\ 150.8\ K$)). Sputtering of metal targets at ambient temperature will always create vapors, since critical temperatures of metals range from $\sim 2\ 000\ K$ (lead) to $\sim 20\ 000\ K$ (rhenium). [34] The driving force for condensation/deposition emanates from the differences of partial pressure of the vapor phase and the vapor pressure created by the liquid/solid phase. Michely and Krug [12] illustrate this for the evaporation of platinum at partial pressure $\sim 10^{-3}\ Pa$ (created at temperature $T_{vapor} = 1900\ K$, resulting in deposition rate $\sim 4.4\ nm/s$) onto a solid platinum substrate at room temperature ($T_{solid} = 300\ K$), which creates a vapor pressure $\sim 10^{-88}\ Pa$. This results in a supersaturation σ_{sup} at the vapor/solid interface

$$\sigma_{sup} = ln\left(\frac{p(T_{vapor})}{p(T_{solid})}\right) = \ln\left(\frac{10^{-3}\ Pa}{10^{-88}\ Pa}\right) \cong 200\,. \tag{3.1}$$

Using the σ_{sup} value from Eq. 3.1, the difference in chemical potential of the vapor and solid phase calculates as $\Delta\mu = \sigma_{sup} k_B T \cong 5\ eV/atom$. This large driving force leads to film growth far from thermodynamic equilibrium, such that film formation is governed by the kinetic rates of atomic-scale processes. Despite the latter, equilibrium growth arguments are frequently used in the literature, as they provide a physically correct description of the asymptotic evolution of film morphology.

One of the most widely used near-equilibrium classifications of film morphology is that of Bauer, [35] which treats the case of epitaxial growth. According to Bauer, film morphology is governed by the interplay among the surface energies of the substrate γ_s and the film γ_f, and the film/substrate interface energy γ_i. When $\gamma_s \geq \gamma_f + \gamma_i$, which is typical for epitaxial growth, energy minimization arguments require that the film wets fully the substrate, and growth occurs in a layer-by-layer fashion (Frank-van der Merwe growth mode, Fig. 3.1(a)). This growth mode is also seen for homoepitaxy (i.e., film and substrate are chemically and crystallographically identical), where $\gamma_i = 0$, and thus $\gamma_s = \gamma_f$.

For $\gamma_s < \gamma_f + \gamma_i$, the energy of the film/substrate system is minimized by maximizing the exposed substrate surface, such that film material forms three-dimensional (3D) mounds/islands. This growth mode, depicted in Fig. 3.1(b), is called Volmer-Weber growth. If the lattice parameter of substrate and film differ, as commonly seen in heteroepitaxial growth (i.e., film and substrate differ both chemically and crystallographically), the film material grows pseudomorphically (i.e., with the lattice parameter imposed by the substrate), and strain builds up to accommodate the lattice mismatch. In this case, an additional energy component has to be considered, the elastic strain energy γ_{el}, which increases with film thickness. During Stranski-Krastanov growth (Fig. 3.1(c)), initially, $\gamma_s > \gamma_f + \gamma_i + \gamma_{el}$, and a wetting layer forms, but at a critical thickness $\gamma_f + \gamma_i + \gamma_{el}$ becomes larger than γ_s, and mounds form on the wetting layer to relieve the strain. Alternative strain-relief mechanisms include the formation of dislocations or surface undulations. [36,37]

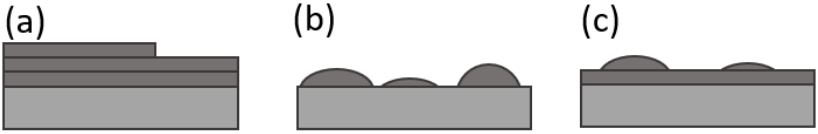

Fig. 3.1: Schematic representation of near-equilibrium film growth modes; (a) layer-by-layer growth (Frank-van der Merwe mode), (b) island formation (Volmer-Weber mode), and (c) island formation on wetting layer (Stranski-Krastanov mode).

Epitaxial growth necessitates that the substrate is a single crystal. The latter may not always be the case—e.g., during deposition on polycrystalline substrates, amorphous materials, and polymers—which yields polycrystalline films, i.e., films composed of grains with different crystallographic orientations, separated by grain boundaries. While the Bauer criteria were not derived for polycrystalline systems, they are still applicable for describing local epitaxial growth at the length scale of individual grains.

As explained at the outset of the present section, film growth proceeds far from equilibrium, such that film morphological evolution is largely governed by the kinetic rates of atomic migration (diffusion) processes. The occurrence rates of these processes are determined by the potential energy landscape that atoms encounter as they transverse on the film growth front. The following sections describe important atomic processes during non-equilibrium film growth and explain the way by which their kinetic rates affect film morphological evolution.

3.2. Adatom diffusion

During thin film deposition from the vapor phase, atoms arriving at the substrate surface have broad energy distributions, which they dissipate into the substrate lattice before being adsorbed, so that they become *adatoms*. Independent of the substrate surface (e.g., atomically flat, with (vicinal) steps, rough) different adsorption sites exist, distinguished by varying numbers of (next-) nearest neighbors (see Fig. 3.2(a)), and a net flux of adatoms to energetically favorable adsorption sites may form. To diffuse by hopping to low-energy sites on an atomically flat substrate, adatoms have to overcome energy barriers E_D separating surface sites, created by the periodic surface potential landscape formed by substrate atoms, which is illustrated in Fig. 3.2(b). Successful hopping events yield a two-dimensional (2D) adatom random walk on the surface, described by the surface diffusivity D,

$$D = D_0 exp\left(-\frac{E_D}{k_B T_S}\right), \tag{3.2}$$

where k_B and T_S are the Boltzmann constant and substrate temperature, respectively. The prefactor D_0 is approximated as $D_0 = a^2 v_0/4$, with the minimal adatom translational hopping distance a, the attempt frequency v_0 ($\sim 10^{12}\ Hz$). The factor $1/4$ is a convention used for 2D diffusion; generally, a prefactor $1/(2n)$ is used for n-dimensional diffusion. [12]

While E_D accounts for energy barriers for diffusion on flat surfaces, preexisting morphological features can lead to local variations of this value. A common feature on substrate surfaces are steps between terraces that add an additional barrier–called Ehrlich-Schwoebel barrier E_{ES}–for diffusion across the step. This additional barrier stems from the lower coordination number of adatoms during the step-edge crossing, and breaking of bonds, as indicated in Fig. 3.2(a) and (b). The total step-edge barrier E_{SE} calculates as $E_{SE} = E_D + E_{ES}$, and adatoms need higher energies to overcome it than for diffusion on a flat surface. Concurrently, the step represents a low-energy position on the lower terrace, where the coordination number is maximum; up-stepping is therefore associated with very high energy barrier and is an unlikely process in classical epitaxial growth theory.

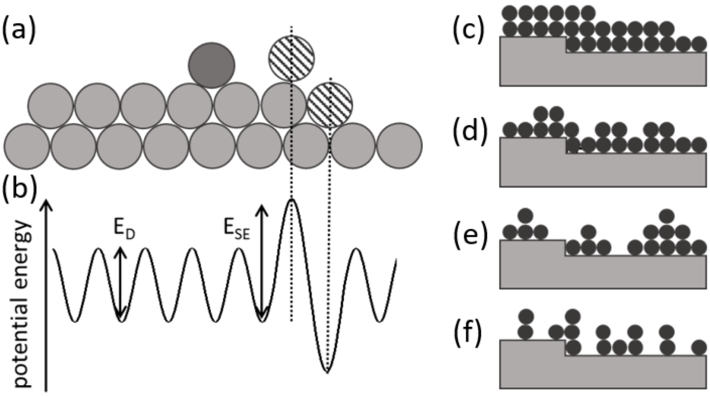

Fig. 3.2: (a) Adatom on top of a terrace (dark gray circle). Striped positions indicate high-energy position while down-stepping (left) and low-energy position at the kink site (right). (b) Potential energy landscape experienced by the adatom in (a) when diffusing. While on the flat terrace, the energy barrier E_D has to be overcome, when stepping over the edge, the adatom encounters a large step-edge barrier E_{SE}. (c)-(f) Illustrations of growth modes depending on surface diffusion and step-edge crossing rates, as determined by E_D and E_{SE}; (c) step flow growth, (d) layer-by-layer growth, (e) mound formation, and (f) self-affine growth.

The effect of atomic diffusion rates (mediated by the energy barriers) on the film morphology can be illustrated by homoepitaxial growth, for which thermodynamics (i.e., the Bauer classification) predicts layer-by-layer growth. If adatoms can migrate on the terraces and descend step-edges without restriction (i.e., unlimited *interlayer transport*), while the mean separation between islands (i.e., nucleation length) is longer than the average terrace length, adatoms diffuse and bond to the low-energy site at the terrace edge. This leads to *step flow* growth, where the terrace number density remains constant, as illustrated in Fig. 3.2(c). If the nucleation length is smaller than the average terrace length, nucleation of islands may occur on terraces (see Section 3.3 for a description of the nucleation process), but since step-descent is unlimited, the bottom layer will be completed before second-layer islands form, and *layer-by-layer* growth occurs (see Fig. 3.2(d)). In case of kinetically limited step-edge descent, the residence time of adatoms on terraces increases, such that second-layer nucleation occurs, leading to *formation of 3D mounds* (illustrated in Fig. 3.2(e)). When both terrace diffusion and, all the more, step-edge crossing are kinetically restricted, adatoms largely remain on their condensation site (see Fig. 3.2(f)). This yields to the so-called *self-affine* growth which is characterized by film porosity, surface roughness, and self-similar morphology.

3.3. Island nucleation

Residence times of adatoms on surfaces are limited by desorption (e.g., at high T_S), bonding to existing structures (e.g., steps, islands), or nucleating of new islands. [4] The latter is the principle adatom loss mechanism during initial growth stages on an atomically flat surface. In course of the random surface walk, adatoms can meet, and form *nuclei*. The size of a nucleus is equal to the number of atoms i in the nucleus. Clusters are thermally stable when $i > i^*$, while they dissolve if $i < i^*$. In many film/substrate systems, $i^* = 1$ has been found, [38] i.e., diatomic clusters are stable, and will, on average, grow in size as deposition continues. Stable clusters are referred to as *islands*, and the island number density N increases during the initial growth stages (i.e., transient nucleation regime). As N increases, adatom incorporation into islands becomes more probable, leading to a reduced number of adatoms on the surface that can nucleate new islands, and a steady-state island number density N_{sat} is reached that scales as

$$N_{sat} \sim \left(\frac{F}{\mathrm{D}}\right)^{\chi}. \tag{3.3}$$

In Eq. 3.3, F is the deposition rate, and χ is a scaling exponent that depends on i^* and the dimensionality of the growing islands. In weakly-interacting film/substrate systems, 3D islands form, [2,39,40] and for $i^* = 1$, $\chi = i^*/(i^* + 2.5) = 2/7$. [38] N_{sat} is a quantity that strongly impacts film growth at later growth stages, as it sets the frequency of islands-island interactions (see Section 3.4); for large values of N_{sat}, the average island spacing is small, and islands interact early, while for low values, islands are further apart and have to grow considerably in size before interacting. During growth manipulation studies, changes in N_{sat} are therefore investigated (see Section 3.6).

In Section 3.2, the concept of second layer nucleation was briefly mentioned, i.e., the nucleation of an island on an existing island. This process is responsible for the formation of 3D mounds on surfaces that lead to roughness build-up at the film growth front. Nucleation of islands occurs, if the adatom density is sufficiently high. For a discussion of second layer nucleation, the characteristic time of adatom arrival (i.e., condensation from the vapor phase) is compared to adatom residence times on an island (i.e., dependent on island size, E_{SE}). If the adatom residence time is much shorter than the time between consecutive adatom arrivals, second layer nucleation is not possible. This is the case for small island sizes (e.g., at early film formation), and low values of E_{SE}.

3.4. Island growth mechanisms

During initial film growth stages, islands grow through incorporation of adatoms on the substrate surface. As the substrate area coverage by film material increases, direct deposition onto islands becomes more probable, but does not play a major role, as surface coverages are low in general. When islands grow further, their average distance decreases, and island-island interactions become the dominant island growth mechanism, as explained in the following sections.

3.4.1. *Island coalescence*

Coalescence is an island growth mechanism that becomes active, once two islands are very close to each other (i.e., they are separated by a gap of several atom diameters). At this point, it becomes energetically favorable to form an island/island interface (i.e., grain boundary), and close the gap by elastically straining the islands. This process is called *impingement*, and initiates *coalescence* (i.e., reshaping of the island cluster until equilibrium shape is reestablished), which is driven by the minimization of the surface energy. The reshaping of the island cluster, schematically presented in Fig. 3.3, commences at the neck, which is a concave surface, offering a higher number of nearest neighbors to arriving atoms compared to convex surfaces. This results in a net flux of atoms toward the neck and closing thereof, while the mass centers of the two coalescing islands approach each other. Coalescence is completed, when an equilibrium shape is reestablished, the grain boundary has been eliminated, and a single crystallographic orientation is present in the island. In case of different island crystallographic orientations before impingement, islands may need to rotate for completing the process. Moreover, coalescence leads to a bimodal distribution of island sizes, as after coalescence completion, the substrate surrounding the newly formed island is void of material, which enables *secondary nucleation*.

According to the sintering theory, in the case of two hemispherical islands with radius R, the time τ_{coal} for coalescence completion is $\tau_{coal} \cong R^4/B,$ [41] where B is the coalescence-rate parameter that scales with the adatom surface self-diffusivity (i.e., is temperature dependent). Island coalescence is initially very fast (i.e., droplet-like coalescence), but becomes slow with increasing island size, and can eventually not be completed before another island impinges on the coalescing island pair. In this stage of *incomplete coalescence*, islands have elongated shapes, and may be polycrystalline. This is an important step toward continuous film formation, which is further discussed in Section 3.5. In the course of coalescence, the film morphology set during island nucleation is changed, and the newly formed morphology is largely dependent on τ_{coal}. Manipulation of coalescence rates is therefore a pathway to morphology tailoring.

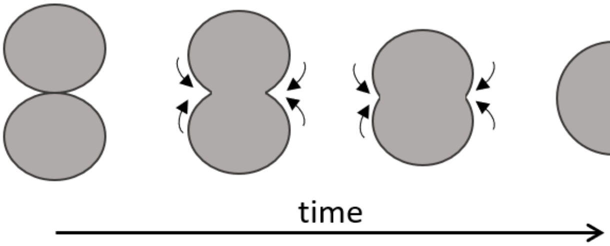

Fig. 3.3: Schematic representation of impingement and coalescence of two islands (top view). As coalescence progresses, the mass centers of the islands approach, and material is transported from convex to concave surfaces, indicated by arrows. Coalescence is completed when an equilibrium shape is reestablished.

3.4.2. *Ostwald ripening*

Atoms on island surfaces are weaker bonded than bulk atoms and can therefore detach from the islands. In case of stable islands, the ratio of detachment to reattachment processes is in favor of reattachment processes, i.e., on average, the island size does not decrease. The chemical potential $\mu = 2\Omega\gamma/R$, where Ω is the atomic volume, is associated with this "escaping tendency". [4] Comparing island sizes, μ is large for small islands, resulting in weaker bonded surface atoms (i.e., larger surface curvature, fewer nearest neighbors), and concurrently, small islands have a large adatom cloud surrounding them compared to larger islands (see Fig. 3.4). When two islands with different sizes are close to one another, the adatom clouds overlap, and adatoms that detach from the small island have a higher probability to attach to the larger island than reattaching to the smaller one. [42] This tendency can also be expressed as differences in adatom number densities surrounding the islands that lead to diffusion of adatoms from the high-number density region close to the small island to the low-adatom-density region surrounding the large island. Ostwald ripening is only active if adatom number density gradients are present, [43] it is therefore not active during film deposition from the vapor phase, where a constant influx of newly formed adatoms leads to a uniform high adatom density, and the gradient disappears. Ripening can be the dominant growth mechanism in non-continuous films after deposition has stopped.

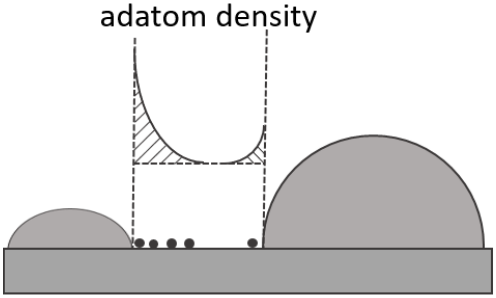

Fig. 3.4: Illustration of adatom number densities surrounding two islands of different size. The small island is surrounded by a larger adatom number density compared to the large island, resulting in a density gradient, and adatom diffusion.

3.4.3. *Smoluchowski ripening*

Islands are typically considered immobile, but at conditions of high atomic mobility, islands can execute concerted diffusive motion. This has been observed for small islands, islands with “magical numbers” in homoepitaxy, [44] and very large islands that support internal vibrations, and are therefore incommensurate with the substrate. [45–47] Mobile islands can impinge on stationary islands, and coalesce, leading to increased island size and decreased island number density. This process is referred to as Smoluchowski ripening.

3.5. Elongation, percolation, and continuous film formation

During initial growth stages, film morphology is characterized by isolated islands with (near-) equilibrium shape that grow in size via processes presented in Section 3.4, out of which island coalescence is the most prominent during deposition from the vapor phase. When coalescence of an island-pair cannot be completed before impingement of a third island, the equilibrium shape cannot be attained. Hence, islands obtain elongated shapes (which can be approximated by ellipses in top-view), characterized by an in-plane aspect ratio–the ratio of major to minor ellipse axis–larger than unity. This point in growth is called elongation transition.

The *elongation transition thickness* Θ_{elong} is a characteristic quantity that describes early film formation, and its scaling with deposition rate F and substrate temperature T_S gives valuable information about the dynamic competition of structure-forming processes (island nucleation vs. coalescence). [48–50] While Θ_{elong} is readily obtainable in simulations (i.e., thickness at which the average island cluster consists of two islands), experimental determination is difficult, as it does not have implications to measurable physical properties. While visual observation of film surfaces close to Θ_{elong}, e.g., with scanning tunnel microscopy, [51,52] is one option to study this transition, an indirect approach has been proposed by Lü *et al.,* [53] who determine Θ_{elong} by changing the adatom arrival rate during deposition and thus activating/freezing island coalescence.

Morphological transitions at higher film thicknesses can be determined experimentally easier because they impact film physical properties. With continued deposition beyond elongation transition, the rate of island impingement increases, and an interconnected array of film islands is formed on the substrate surface; this transition occurs at the *percolation thickness* Θ_{perc}. In case of conductor deposition on insulating substrates, the film becomes macroscopically conductive at Θ_{perc}, and film resistivity decreases several orders of magnitude. [54–56]

The formation of a continuous film requires the holes between interconnected islands in the percolated structure to be filled. With increasing amount of deposited material, the substrate coverage increases, such that direct deposition of film atoms into holes becomes less probable. For very narrow holes, atom trajectories are affected by the surrounding 3D islands, resulting in atom adsorption on the island facets (i.e., steering). [57] Concurrently, hole-filling requires adatom diffusion to the bottom of the hole via step-edge descent. In polycrystalline films, where grains are separated by grain boundaries (GB), the presence of the step-edge barrier E_{SE} (see Section 3.2) leads to mound formation as explained in the following (also known as Zeno effect): [57,58] Adatoms that are deposited onto a terrace diffuse to the ascending step, if they cannot cross the step-edge because of E_{SE}. Terrace growth is stopped at GBs; consequently, terrace length decreases as the ascending step approaches the GB, and the number of deposited adatoms decreases, which stops the step progression. For small terrace lengths (~ 5 atoms), the Ehrlich-Schwoebel barrier E_{ES} collapses, [57,59] and fast mass transport toward the GB (i.e., *downward funneling*) closes the remaining gaps.

Knowledge of the *continuous film formation thickness* Θ_{cont} of films is important to ensure that the substrate surface is covered completely by film material. Additionally, many of the morphological features and properties of the film are set by the time a film becomes continuous. In the following, the most important of these properties are listed and explained.

Mass density

The mass density ρ_m of a thin film is equal to the bulk density of the film material, if the chemistry is identical (i.e., no composition gradients) and no porosity has formed. Film porosity forms, when adatom mobility is not sufficient on the surface (compare self-affine growth in Fig. 3.2(f)), or shadowing effects occur, e.g., during deposition at glancing incidence. [4] Film density can be determined, e.g., via x-ray reflectometry (XRR, see Section 5.3.6). Density fluctuations are also visible in scanning electron microcopy (SEM, see Section 5.3.2) and transmission electron microscopy (TEM, see Section 5.3.3).

Grain size

The grain size determines opto-electronic properties, e.g., conductivity, and mechanical properties of a film (e.g., stress-state). Cross sectional SEM and TEM (Sections 5.3.2 and 5.3.3) can be used to determine if grains are columnar, V-shaped or globular, while x-ray diffractometry (XRD, see Section 5.3.5) and electron backscatter diffractometry (EBSD, see Section 5.3.4) give information about the out-of-plane and in-plane grain size, respectively.

Surface roughness

Knowledge of the surface properties of a thin film is essential to determine its interaction with its environment. It is largely determined by the surface mobility of adatoms. The root-mean-square roughness w is a quantity that can be determined from atomic force microscopy (AFM, see Section 5.3.1), and is a fitting parameter for XRR data (see Section 5.3.6)

Texture

In case of polycrystalline growth, initially, islands nucleate with random crystallographic orientations, which grow with different speed, due to thermodynamic reasons (surface energies of densely-packed atomic planes are lower than for loosely-packed planes), or kinetic reasons (planes with high diffusion barrier E_D host many adatoms that can nucleate into islands, while a low E_D leads to low adatom density, and concurrently, to few nucleation events). [60] Islands that grow fast can overgrow other islands that grow slower, and a texture develops, i.e., a crystallographic orientation is overrepresented in the polycrystalline film. Texture can continue to evolve as film thickness increases, and kinetic limitations arise (e.g., due to surface roughness). Texture analysis is performed by XRD (see Section 5.3.5) or EBSD (see Section 5.3.4).

3.6. Influence of process parameters on microstructural evolution

The nanoscale processes that lead to the formation of a thin film can be altered by changing process parameters. Concurrently, the morphology of a growing film is determined by these parameters, which are often interdependent. For use of thin films in applications, specific morphological features (e.g., low surface roughness, low level of contamination) may be required, and by understanding how process parameters affect the film growth, morphology manipulation methodologies can be devised to achieve them.

3.6.1. *Temperature*

Changes in the deposition temperature affect the mobility of (ad)atoms during film growth, e.g., the diffusivity increases (see Eq. 3.2) as energy barriers (E_D) can be overcome more easily. For many diffusion processes (e.g., lattice, grain boundary, or dislocation diffusion) and materials, the relation $E_D = c\,T_m$ is valid, [4] where c is a diffusion process dependent constant, and T_m is the bulk melting temperature of the film material. Substituting E_D in Eq. 3.2 leads to $D \sim \exp(-c\,T_m/(k_B T_S))$. Consequently, the homologous temperature $T_H = T_S/T_m$ (temperatures in Kelvin) is a parameter for a general comparison of mobilities among various film materials.

Common film morphological features can be found for similar values of T_H: [3] In the low mobility regime $T_H < 0.2$, neither bulk nor surface diffusion are active, and porous, columnar grains with small diameter (i.e., $\sim 1 - 10\,nm$) form. In the intermediate mobility regime $0.2 < T_H < 0.4$, surface diffusion is active, while energy barriers for bulk diffusion cannot be overcome. This leads to competitive grain growth, and fast-growing grains overgrow slow grains, which results in a V-shaped grain structure. For high mobility (i.e., $T_H > 0.4$), where surface and bulk diffusion are active, columnar grains form, with dense grain boundaries that are perpendicular to the substrate surface. With active bulk diffusion, grain growth throughout the whole film thickness is possible, leading to grain size that increases with increasing film thickness, and highly textured films.

This correlation between film morphology and homologous temperature led to the development of *structure zone diagrams,* [3,61] which allow for qualitative prediction of film morphology as a function of deposition parameters. Originally conceived for evaporated films, structure zone diagrams were expanded to account for the energy of arriving particles during sputter-deposition, [62–65] and the role of contamination on the morphological evolution. [66]

In Section 3.3, the scaling of the saturation island number density N_{sat} with deposition rate and diffusivity was presented (see Eq. 3.3). With increasing values of T_S, adatom diffusivity increases, and island nucleation events on a flat surface occur less often, i.e., N_{sat} decreases. Concurrently, a film deposited at high T_S can be expected to show a larger average grain size. This trend is independent of grain growth, activated by bulk diffusion.

Island coalescence is a surface self-diffusion dependent process, and therefore promoted by increased valued of T_S. Faster coalescence completion shifts the elongation transition, and consequently percolation and continuous film formation, to occur at larger thicknesses, leading to a strongly coalescence-controlled film morphology.

3.6.2. *Deposition rate*

The deposition rate F represents the vapor arrival rate at the substrate, and is set by the rate of plasma ions impinging on the target surface (i.e., determined by the electric potential on the target), the sputter yield of the target material (i.e., number of target atoms that are sputtered per impinging working gas ion), as well as working gas and pressure (see Chapter 2 for more details). A high value of F signifies that a high number of atoms arrive per substrate surface unit during a given time unit, and island nucleation events occur often, i.e., N_{sat} increases with increasing F. It is noted that the F-dependence of N_{sat} is much weaker than its T_S-dependence (see exponential function in Eq. 3.2), and F has to be decreased by orders of magnitudes to match the N_{sat} decrease set by increasing T_S few Kelvin.

Vacuum conditions in a film deposition chamber are not ideal, i.e., residual gases (e.g., oxygen, nitrogen, water) are present that contaminate the growing film. A comparison of F with the monolayer formation time τ_{ML} from the background pressure allows estimations of the contamination level of the growing film (see Section 2.1.2). For high values of F, contamination arrival becomes less significant, and cleaner films are grown. The most direct way to increase F is applying a higher power to the target to increase the number of arriving plasma ions. Concurrently, more energy is introduced to the target that needs to be removed via cooling, otherwise the target is overheated, leading to cracking, and/or melting.

3.6.3. *Working pressure*

A working gas is introduced into a deposition chamber to create a plasma, and initiate sputtering of the target. The pressure of the working gas largely determines the mean-free path of atoms in the chamber during the sputter-deposition process. At high working pressure, target atoms collide with working gas atoms often, and lose energy with every collision. Consequently, the average energy of atoms arriving at the substrate surface decreases with increasing working pressure.

The energy of arriving species on the substrate is instrumental in the texture evolution of the growing film, i.e., high-energy atoms promote surface rearrangement processes. [33,67] Deposition profile and rate, as well as energy and direction of sputtered particles can be simulated with the Simulation of the Metal Transport (SiMTra) Monte Carlo program. [68] It simulates the transport of sputtered particles through the working gas considering binary collisions, and the user can implement the experimental setup (e.g., chamber dimensions).

3.6.4. *Minority species*

Alloying is one of the oldest material engineering strategy that allows changing optical, mechanical, and electrical properties of a material. In thermodynamic equilibrium, the interaction of host material and minority species can be determined by calculating the Gibbs free energy of mixing $\Delta_{mix}G = \Delta_{mix}H - T\Delta_{mix}S$, where $\Delta_{mix}H$ and $\Delta_{mix}S$ are enthalpy of mixing and configurational entropy, respectively, and T is the system temperature. [53] $\Delta_{mix}S$ is strongly dependent on the composition of the compound, e.g., in a binary compound A_xB_{1-x}, the configurational entropy is $\Delta_{mix}S = -nR[x\ln(x) + (1-x)\ln(1-x)]$, where n is the total number of moles, R is the gas constant, and x is the mole fraction. From $0 < x < 1$ follows that $\ln(x)$ and $\ln(1-x)$ are always negative, consequently, $\Delta_{mix}S > 0$, and leads to a decrease in $\Delta_{mix}G$. For negative values of $\Delta_{mix}G$ in system consisting of elements A and B, the system is *miscible*, i.e., energy is minimized by forming a maximum of A-B bonds, and the species intermix spontaneously. An example for a miscible binary system is Ag-Au, which are miscible in the solid and liquid states. If $\Delta_{mix}G$ is positive, elements are *immiscible* and phase separation occurs below the miscibility gap, e.g., Ag is immiscible with Ni and Cu in the solid phase.

Thermodynamic equilibrium considerations alone cannot explain phase formation during thin film growth from the vapor phase, where metastable phases can form due to kinetic limitations of the structure-forming species (see Section 3.1). If the system is thermodynamically immiscible, phase separation occurs, if atoms have enough energy to diffuse, and one element *segregates*. In case of no chemical bonding to the film material, and efficient segregation of the minority species, such that it remains at the growth front at all times, the term *surfactant* is used. [12] Surfactants are used to manipulate film morphology as they affect both energetic and kinetic aspects of the film growth front. In the case of homoepitaxy, three different ways by which surfactants allow for growth manipulation have been identified in the literature:

(i) The surfactant changes the diffusion barrier E_D, e.g., exposing Pt(111) surfaces to oxygen increases E_D, and results in a larger island nucleation density in the Pt/Pt(111) system. [70] Concurrently, an increase in E_D promotes layer-by-layer growth.
(ii) The step-edge barrier E_{ES} is influenced by the presence of a surfactant, e.g., carbon monoxide preferentially adsorbs on step-edges of the Pt(111) surface, and thus increases E_{ES}. [71] This promotes mound formation in the Pt/Pt(111) system.

(iii) In a third scenario, the presence of surfactants changes the adatom diffusion along step-edges, and thus can lead to a change from compact to ramified island shapes. This increases the ratio of sites at the step-edge vs. terrace sites, and the attempt frequency of adatom step-edge crossing increases. Consequently, the lifetime of adatoms on the terrace and the second-layer island nucleation probability decrease. Sb surfactants have this effect on Ag/Ag(111) growth, [72] and shift the film growth mode from mound formation to layer-by-layer growth.

The film formation mechanisms in weakly-interacting film/substrate systems are different from those in strongly-interacting epitaxial systems, and depend strongly on the complex interplay of island nucleation, growth and coalescence. [3,5,7,73] Growth manipulation by surfactants is less well studied in these systems, however, empirical studies show that surfactants can suppress the uncontrolled formation of a 3D morphology, e.g., oxygen and nitrogen increase the island nucleation density, and improve wetting of Ag and Cu films on oxide substrates, promoting a 2D film morphology. [74–80]

4. Stress generation and evolution during thin film growth

During far-from-equilibrium thin film deposition, atoms often arrange themselves in metastable configurations, resulting in formation of mechanical stress that can lead to failure of thin film components and devices, e.g., via delamination, crack formation, buckling. The presence of a substrate upon which films are deposited yields different types of stresses (thermal stress, coherency stress, intrinsic stress), which are briefly explained in Section 4.1. The present thesis focuses on intrinsic stresses, which can, depending on deposition conditions, be tensile or compressive. Moreover, intrinsic stresses typically evolve with film thickness in a way that is related to the various formation stages discussed in Chapter 3: During island formation and growth, the Laplace-pressure-reduced lattice constant results in compressive stress (Section 4.2), while tensile stress emerges in coalescing island pairs (Section 4.3). The stress sign after continuous film formation depends on the mobility of adatoms on the film surface, as well as on the microstructural evolution (e.g. grain size, texture) of the continuous film during growth, as explained in Section 4.4. After deposition interruption, stress that has formed in the film can continue to evolve, which is discussed in Section 4.5. Finally, Section 4.6 summarizes some of the most established models that allow for calculation of stress formation and evolution during film growth.

Stress data discussed in this chapter are presented in film force per unit width (usually abbreviated as film force) vs. film thickness (h_f) diagrams, or stress-film thickness product ($\sigma \times h_f$) vs. h_f diagrams. Film force and $\sigma \times h_f$ are equivalent quantities and have the unit N/m. Data is interpreted as described in the following: The *average film stress* is tensile if the film force is positive; concurrently, the average stress is compressive for negative film force. The slope of film force vs. h_f data corresponds to the *incremental stress*, i.e., the stress that forms in the film due to growth of an additional layer of the film. Details about the generation of *in situ* stress data are given in Section 5.2.2.

4.1. Classification of stresses in thin films

Mechanical stress observed during far-from-equilibrium film growth may have different origins. This section outlines three stress generation mechanisms: (i) thermal stress σ_{th} due to the mismatch between thermal expansion coefficients of substrate and film; (ii) coherence stress σ_{coh} due to imposition of a crystal lattice constant different from the equilibrium value by the substrate in epitaxial film growth; and (iii) intrinsic stress σ_i that results from the film microstructural evolution during film growth.

4.1.1. *Thermal stress*

The temperature at which films are deposited may differ from their application temperature. For instance, transition metal nitride coatings—used to protect the surface of cutting tools—are grown at $\sim 600\ K$ to ensure sufficient atomic mobility for forming dense microstructures, they are stored at room temperature, and they are operated at temperatures exceeding $\sim 900\ K$. Upon such temperature variations ΔT_S, relative to the synthesis temperature, both film and substrate dimensions change (i.e., contract or expand), the magnitude of which depends on the respective thermal expansion coefficients of substrate ($\alpha_{th,s}$) and film ($\alpha_{th,f}$). Usually, a mismatch $\Delta\alpha_{th} = \alpha_{th,s} - \alpha_{th,f}$ exists, resulting in the buildup of thermal stress σ_{th}. For a homogeneous film on a rigid substrate, σ_{th} is calculated as $\sigma_{th} = Y_f \Delta\alpha_{th} \Delta T_S$, where Y_f is the biaxial modulus of the film. Thermal stress can be compressive or tensile, depending on the film/substrate system (i.e., the thermal expansion difference $\Delta\alpha_{th}$), and can reach higher values than the film's yield strength, leading to plastic deformation and/or film damage. [74,75]

In addition, even in the absence of intentional heating, the substrate temperature can rise during film growth due to the impingement of energetic particles from the arriving vapor flux. [4] This uncontrolled heating is pronounced for high deposition rates, long deposition times, and growth conditions for which species arriving at the substrate have high energies (e.g., when a bias voltage is applied on the substrate, and at low working pressure). Compared to intentional heating during film growth, the temperature induced by atom impingement is in most cases small (i.e., tens of Kelvin), but for precise analysis of stress evolution even such small temperature changes need to be considered.

4.1.2. *Coherency stress*

In heteroepitaxial growth, films are deposited onto structurally and chemically different single-crystalline substrates, which impose a crystal structure (substrate lattice constant a_s) on the film lattice (film lattice constant a_f). Hence, films may grow *pseudomorphically*, i.e., with a lattice constant that is different from their equilibrium lattice constant. The lattice misfit leads to formation of coherency strain defined as

$$\varepsilon_{coh} = \frac{a_s - a_f}{a_f}, \tag{4.1}$$

which manifests itself as coherency stress $\sigma_{coh} = \varepsilon_{coh} Y_f$, where Y_f is the film biaxial modulus. Following Eq. 4.1, σ_{coh} is compressive for $a_s < a_f$, and tensile for $a_s > a_f$.

An example of coherency stress formation is given in Fig. 4.1, where the evolution of film force per unit width vs. film thickness is presented for Fe evaporation onto MgO(100) substrates for various deposition temperatures. [83,84] Fe grows epitaxially on MgO (epitaxial relationship Fe(001) || MgO(001) and Fe[001] || MgO[110]), which leads to a lattice misfit of $\varepsilon_{coh} = 3.5\%$ at $500\ K$, and a theoretical $\sigma_{coh} = 6.8\ GPa$, as represented by the dashed line in Fig. 4.1. Koch *et al.* [83] found that for deposition at $500\ K$, the stress is close to the theoretical value σ_{coh} up to a film thickness of $\sim 8\ nm$, after which it levels off. At $500\ K$, the film grows in a layer-by-layer fashion, such that the maximum theoretical σ_{coh} is formed and strain energy is stored in the film until reaching a critical thickness, above which strain and stress are relieved, and the total energy of film/substrate system is minimized via nucleation of misfit dislocations. With decreasing deposition temperature to 465 and $440\ K$, nucleation of misfit dislocation and stress relief occur at smaller thicknesses. Further decrease of the temperature to $360\ K$ yields growth conditions during which atomic mobility is insufficient for nucleation of misfit dislocations, such that tensile stress that is lower than σ_{coh} builds up during film growth.

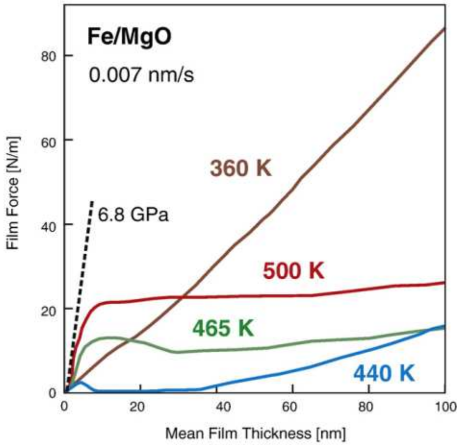

Fig. 4.1: Evolution of film force per unit width vs. film thickness during evaporation of Fe films onto MgO(001) substrates at different substrate temperatures. The dashed line indicates the maximum misfit stress for epitaxial growth. Reprinted with permission from Ref. [84].

Another example is the heteroepitaxial system Ge/Si(111), in which stress is partially relieved by creating three dimensional (3D) islands, i.e., via the Stranski-Krastanov growth mode (see film force vs. thickness measurements in Fig. 4.2). In this work by Koch *et al.* [78], Ge is grown on Si(111) substrates via molecular beam epitaxy (MBE), i.e., an evaporation technique that leads to epitaxial films with high purity, and the film force per unit width is measured *in situ*. The lattice misfit between film and substrate at $T_S = 915\ K$ leads to $\varepsilon_{coh} \cong -4\%$, and $\sigma_{coh} = -6.7\ GPa$. The data in Fig. 4.2 shows that a compressively strained film forms up to a film thickness $\sim 0.7\ nm$ on the Si substrate (stress regime I), which corresponds to $\sim 2.5\ monolayers\ (ML)$ of Ge(111) that wet pseudomorphically the substrate. At larger film thicknesses, less compressive stress forms in the Ge film (i.e., lower slope in regime II in Fig. 4.2), due to partial relief of stress by formation of 3D islands. [85] The observed stress in regime II stems from formation of misfit dislocations and stacking faults in the islands.

It is noted that the 3D structures that form in epitaxial semiconductor films are known as Asaro-Tiller-Grinfeld instabilities. [36,37,86] These instabilities form spontaneously on the surfaces of strained crystals to elastically relax stress on the additionally created surface.

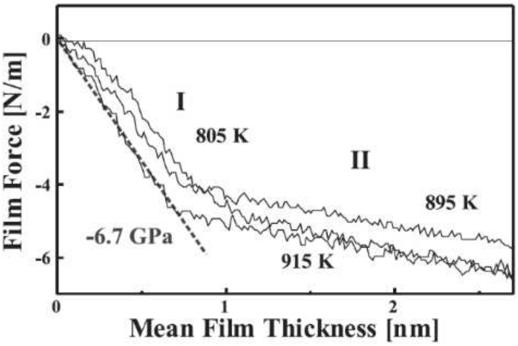

Fig. 4.2: Evolution of film force per unit width vs. film thickness during growth of Ge films on Si(111) substrates at different substrate temperatures. Regimes I and II correspond to formation of an epitaxial wetting layer and 3D island formation, respectively. The dashed line indicates the maximum misfit stress for epitaxial growth. Reprinted with permission from Ref. [85].

4.1.3. *Intrinsic stress*

Intrinsic stress forms due the microstructural evolution of thin films during growth, and it is a result of the far-from-equilibrium nature of vapor-based film deposition techniques. Like thermal and coherency stress, the nature of the substrate has influence on the intrinsic stress, as the interaction of film atoms and substrate surface largely governs the film morphology: While a flat surface morphology is expected for strongly-interacting film/substrate systems, 3D growth is seen in weakly-interacting systems. [7] For the latter case, film morphology develops from isolated islands, via coalescing island clusters, to a continuous film. These growth stages lead to a characteristic stress evolution that is discussed in greater detail in Sections 4.2 through 4.6.

4.2. Stress during island formation and growth

Stress formation during early film growth stages, where isolated islands populate the substrate (i.e., nano particles), results from two effects: the Laplace-pressure-reduced lattice parameter in nanoscale objects, and the decreasing atom mobility with increasing particle size. This section describes these two concepts briefly, and connects them to stress generation.

Film formation commences with the nucleation of islands on the substrate surface. These nano-sized structures can be approximated as hemispheres with radius r. The existence of stable islands dictates a balance between the force exerted by the curvature of the surface (i.e., the surface stress f) and the force due to the pressure p in the hemisphere, which can be expressed as [87,88]

$$\pi r f = \frac{1}{2}\pi r^2 p \, . \tag{4.2}$$

In general, the surface stress f_{ij} is a tensor, where j denotes the direction in which the force acts, and i denotes the direction of the surface normal. For metal surfaces with low Miller indices, $f \cong 1\ N/m$, i.e., f is positive and of the same order of magnitude as the surface energy γ. [89] For (incompressible) liquids, $f = \gamma$, and the expression "surface tension" is often used for both quantities. This is not true for solids, where f might be negative, depending on how atoms are rearranged on the surface. A distinction between surface stress and surface energy is therefore essential for solids.

Rewriting Eq. 4.2 gives $p = 2f/r$, where p is the Laplace pressure. Assuming that islands are crystalline with a cubic lattice (with lattice constant a) and using the compressibility $K = -\Delta V/(pV)$, we find

$$\frac{\Delta a}{a} = -\frac{2}{3}\frac{K}{r} f \, , \tag{4.3}$$

where Δa is the change in lattice constant due to the surface stress f. According to Eq. 4.3, the lattice constant in a nano particle decreases due to surface stress (if $f > 0$), and this decrease becomes less pronounced with increasing particle size, i.e., in a particle with infinite radius no surface stress-induced lattice decrease is expected. This dependency between particle size and lattice constants has been verified experimentally, see e.g., the work by Mays *et al.* [88] on lattice constant evolution of evaporated gold nano particles. Figures 4.3(a)-(c) present schematically the evolution the lattice constant of a metallic nano particle with increasing particle size (only one dimension indicated for clarity).

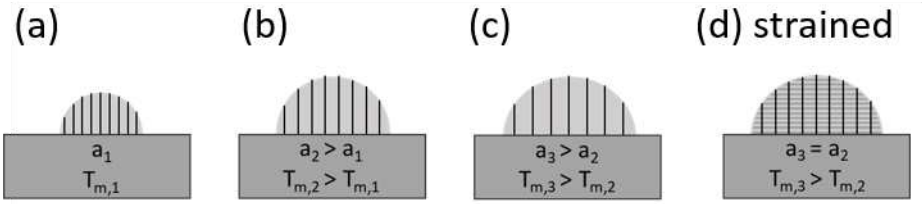

Fig. 4.3: Evolution of lattice constant a and melting temperature T_m of a supported nano particle with increasing particle size. Lattice constants in schematics (a) through (c) are equilibrium values, while in (d), atom mobility is too low and the smaller lattice constant a_2 is inherited, leading to compressive stress.

Nanoscale particles do not only have smaller-than-bulk lattice constants, but also a melting temperature T_m that is lower than the bulk value. [90] The latter results from the high surface-to-volume ratio of nano objects. Surface atoms spontaneously detach from and reattach to surfaces at all temperatures $> 0\ K$, and exert a pressure to the atmosphere surrounding the particle (i.e., the *vapor pressure* if the atmosphere is gaseous). This pressure increases with increasing temperature (i.e., detachment probability increases) and surface-to-volume ratio of the nanoscale object (i.e., the fraction of low-coordinated surface atoms increases). In a two-phase system (solid/gas or liquid/gas), a phase transition occurs, when the pressure exerted by two phases is equal, e.g., water boils in air when its vapor pressure reaches atmospheric pressure. Small particles create a higher pressure than large ones and, consequently, reach an equilibrium with its surrounding medium at lower temperatures, i.e., smaller objects exhibit lower values of T_m, [91] as illustrated in Fig. 4.3.

In Chapter 3, the temperature-dependence of the adatom diffusivity was discussed, and the homologous temperature $T_H = T_S/T_m$ was identified as proxy for adatom mobility, i.e., diffusion is promoted with increasing T_S and/or decreasing T_m. The rearrangement of atoms to accommodate the increasing lattice parameter in growing nano particles is diffusion-dependent, and it is thus facile in small particles with low T_m. Upon increasing particle size, atoms become less mobile, and the lattice parameter cannot further increase, i.e., a smaller-than-equilibrium lattice parameter is locked into the particle, and compressive stress forms. [89] The above-described scenario is illustrated in Fig. 4.3(b) through (d), where the equilibrium lattice constant increases from a_2 to a_3 as the particle since increases (Fig. 4.3(b) and (c)), but due to insufficient mobility, it is locked at the lower value a_2, and the particle is strained (Fig. 4.3(d)).

The island size at which the lattice parameter is locked into the island (i.e., the critical thickness t_o and the critical diameter d_o) is an essential quantity for determining the magnitude of the compressive stress that builds up during island growth, i.e., the earlier during growth the lattice constant is locked, the larger the induced compressive stress. A model by Cammarata *et al.* [89] predicts the stress σ of a cylindric island (thickness t, diameter d) which is given by

$$\sigma = (f + g)\left(\frac{1}{t} - \frac{1}{t_o}\right) + 2\beta h\left(\frac{1}{d} - \frac{1}{d_o}\right), \tag{4.4}$$

where f and h are the surface stresses of the round surface and curved surface, respectively, g is the film/substrate interface stress, and β is a function of the elastic compliances of the crystallite island. From Eq. 4.4 follows that σ increases with decreasing t_o and d_o (for $\beta > 0$).

Friesen and Thompson [92,93] studied stress evolution during island nucleation and growth, and found that the compressive stress relaxes during deposition interruptions, which they attribute to adatom/surface interactions. High adatom concentrations on the surface may lead to restructuring of surface atoms, which increases the surface stress. During interruptions, the adatom population decreases fast, and surface atoms move to equilibrium positions, i.e., surface stress relaxes.

4.3. Stress during island coalescence—grain boundary zipping

Coalescence is the reshaping of a pair (or cluster) of islands until near-equilibrium shape is reestablished, and it is the dominant island growth mechanism during sputter-deposition of thin films (see Chapter 3 for more details). The initial step of a coalescence process is the impingement of two neighboring islands. This energy-minimization process introduces tensile stress in the coalescing island pair: Just before impingement, two surfaces exist (island/vacuum interfaces), separated by a small gap, as indicated by the surface profile $y(z)$ in Fig. 4.4(a) (where z is the film growth direction).

Impingement leads to the formation of an interface (i.e., grain boundary GB), which has a lower energy than two surfaces. In this process, which can be seen as the inverse of crack formation and propagation, the driving force for energy-minimization is large enough to elastically deform the island lattice to form the interface, i.e., tensile stress is introduced into the coalescing island-pair. Once the first planes are zipped together, the gap between islands closes from bottom (substrate) to top, and it only stops when the energy needed for elastic straining of the crystal lattice becomes too large (note that the gap size increases with distance from substrate). The resulting reshaping of the surface profile, and generation of stress profile $\sigma(z)$, predicted by Nix and Clemens [94], are indicated in Fig. 4.4(b).

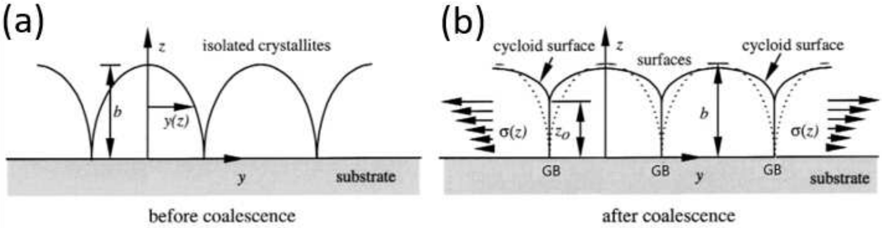

Fig. 4.4: (a) Surface profile $y(z)$ before coalescence, and (b) elastic displacement of $y(z)$ and stress profile $\sigma(z)$ accompanied by the coalescence of isolated crystallites. Grain boundaries (GB) are indicated after coalescence. Reprinted with permission from Ref. [94].

Seel *et al.* [95] observed that the Nix-Clemens model overestimates the tensile stress generation during coalescence, and found that the stress generated by island impingement and GB zipping is strongly dependent on the boundary conditions at the island/substrate interface. In their model, they investigate the effect of islands that are perfectly bound at the interface (i.e., *traction* in Fig. 4.5(a)) vs. islands that can accommodate strain by *sliding* at the interface. Furthermore, they compare the first impingement of an island (cases (i) and (iii) in Fig. 4.5(a)) to the impingement on an island that is part of a coalescing island pair (cases (ii) and (iv) in Fig. 4.5(a)). The resulting stresses as function of island radius are presented in Fig. 4.5(b). Smaller stress forms with increasing island radius, independent of the boundary conditions, however, while tensile stress is formed in an island that is bound firmly to the substrate (island (i)), the center of mass of an island that slides at the interface moves toward the GB (island (iii)), inhibiting tensile stress formation.

Furthermore, if perfect sliding occurs, no stress is transmitted to the substrate, and no stress generation can be measured via techniques that monitor the film stress-induced change of substrate curvature (see Section 5.2.2). This mechanism is a potential reason for the overestimation of the tensile stress formation with the Nix-Clemens model.

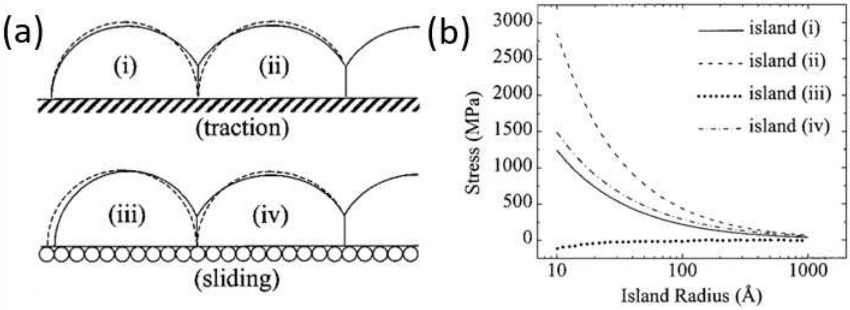

Fig. 4.5: (a) Surface profiles of islands before (dashed lines) and after (solid lines) impingement of (i) one and (ii) two islands with perfect traction at the island/substrate interface, and impingement of (iii) one and (iv) two islands that can freely slide at the island/substrate interface. (b) Evolution of stress due to island impingement and grain boundary zipping vs. island radius for plane strain conditions for islands illustrated in (a). Reprinted with permission from Ref. [95]**.**

Zhou *et al.* [96] investigated stress generation during island coalescence with molecular dynamics simulations, and found that the stress magnitude is strongly influenced by the shape of coalescing islands. In their simulations, atoms are deposited onto a pre-structured substrate with islands, which are separated by a gap that is too large for GB zipping to occur without deposition. In Fig. 4.6(a), the in-plane stress evolution with time during deposition of Fe onto two Fe islands is presented. For square island shapes that have flat and parallel island walls, and consequently a large contact area, tensile stress forms as islands coalesce via GB zipping, and a dense island is formed (see inset #1 in Fig. 4.6(a)). Concurrently, cylindrical and hemispherical islands, which have smaller contact areas than square islands, show no tensile stress formation, which the authors attribute to coalescence via gap filling by arriving Fe atoms, i.e., no GB zipping occurs since island walls are separated by too large gaps.

Simulations of the stress evolution due to coalescence in case of a polycrystalline film are presented in Fig. 4.6(b) for different surface morphologies, [96] where the contact area is decreased/the island gap increased by decreasing the island wall-to-substrate surface angle from $90°$ (perpendicular edge) to $58°$ (shallow groove). With decreasing angle, the maximum impingement tensile stress decreases, due to less pronounced GB zipping, e.g., compare maximum tensile stress $\sim 3\ GPa$ for perpendicular edge to $\sim 2\ GPa$ for deep surface grooves (i.e., angle $75°$). For deposition on a flat surface (not shown here), no tensile stress is observed. In reality, island shapes are more complex than those modelled in Ref. [96], e.g., convex surface profiles form between the island center and the substrate (see Figs. 4.4 and 4.5). Simulation of the stress evolution upon coalescence of such islands would result in stress magnitudes ranging between the values for perpendicular island walls and flat surfaces.

Coalescence is fully completed upon formation of a single-crystal island, which, per-definition, means that the GB and the resulting tensile stress have been eliminated, i.e., no permanent tensile stress is formed. Concurrently, stress from early film formation stages due to the Laplace pressure is annihilated during coalescence, as atoms are rearranged. With increasing island size (R), the coalescence-completion time t_{coal} increases ($t_{coal}{\sim}R^4$) [41,48], while the average island separation distance decreases, i.e., average time t_{imp} between impingement processes becomes shorter. When $t_{imp} < t_{coal}$, islands start impinging upon coalescing island-pairs, and coalescence cannot be completed. This leads to a net tensile stress in the films, which is a sign of incomplete coalescence.

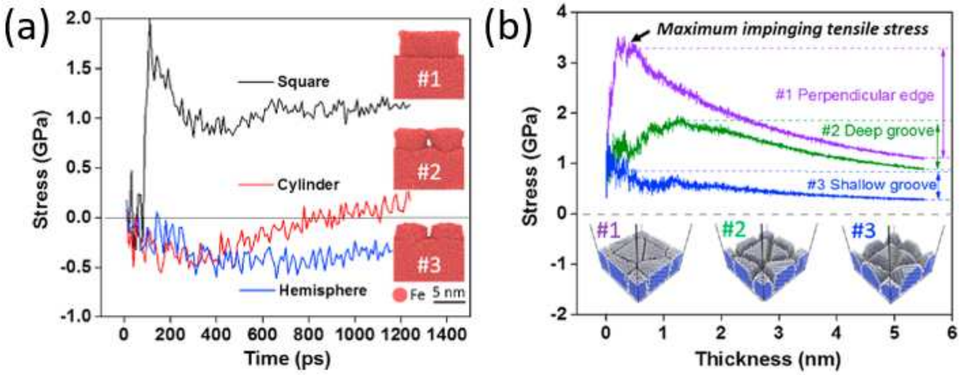

***Fig. 4.6:** (a) Simulated stress evolution as function of deposition time for Fe films with #1 square, #2 cylindrical, and #3 hemispherical island shapes. Insets show the island shape after deposition completion. (b) Simulated stress evolution vs, film thickness of W films with #1 perpendicular edge islands (island wall-to-substrate surface angle $90°$), #2 deep surface grooves (angle $75°$), #3 shallow surface grooves (angle $58°$). Insets show surface morphologies of #1 through #3 before deposition. Reprinted with permission from Ref.* [96].

4.4. Stress formation and evolution in continuous films

Application-relevant film thicknesses are typically much larger than those at which continuous layers are formed. Hence, it is important to understand stress formation beyond the stage of island coalescence. The discussion of the stress evolution in continuous films is complex, as the effect of several independent and inter-related mechanisms must be considered. Without knowledge of the film microstructural evolution, a discussion is not possible, as properties like grain size and texture, surface roughness, or film density are key to understanding which stress-contributing processes are active/dominant. In this section, studies on stress evolution in continuous films are presented phenomenologically; models that allow calculating stress during film growth are outlined in Section 4.6. Data presented in this section stems from growth of polycrystalline films that show no epitaxial relation to the substrate, i.e., stress formation mechanisms discussed in Section 4.1.2 are not relevant.

4.4.1. *Effect of atomic mobility on stress generation and evolution*

The stress evolution close to and after continuous film formation is strongly dependent on the adatom mobility, [97] i.e., the sign and magnitude of stress in continuous films are not material constants, but functions of deposition parameters and of the resulting film morphological evolution. [98]

Low atomic mobility conditions (i.e., obtained at T_H values below 0.2) may yield average adatom diffusion lengths that are shorter than the lateral grain size, such that adatom-GB interaction is inhibited. [90] In this case, adatoms contribute only to the out-of-plane propagation of the film growth front and the evolution of the surface roughness (columnar growth). At GB triple junctions (i.e., GB-vacuum interface), the GB height increases by elastic snapping of lattice planes, and thus tensile stress forms in the film (as described in Section 4.3). As in this case, the overall mobility of atoms is low (i.e., bulk diffusion is not active), the film microstructure does not evolve during deposition, and no additional stress contributions need to be considered. Consequently, a tensile steady-state is obtained, the magnitude of which is proportional to the GB number density at the surface.

Figure 4.7 presents Fe and Cu films that are grown at conditions of low atomic mobility, i.e., $300\,K$ for Fe on oxidized Si(001) substrates and $110\,K$ for Cu on mica(001). [84,99,100] These temperatures correspond to $T_H = 0.20$ and 0.08, respectively, where diffusion of atoms is expected to be kinetically limited (see Section 3.6.1), and a porous film with columnar grains forms. [50] From the film force evolution vs. film thickness, the onset of island coalescence and tensile stress formation can be seen (i.e., at $\sim 2\,nm$ for Fe and $\sim 8\,nm$ for Cu), however, no further morphological information can be deducted. We also note that the stress does not evolve after deposition interruption (marked by arrows in Fig. 4.7).

Stress evolutions during deposition at higher temperatures are also presented in Fig. 4.7, i.e., Fe film growth at $520\,K$ ($T_H = 0.34$), and Cu growth at $300\,K$ ($T_H = 0.22$) whereby surface diffusion is active. [3] A characteristic tensile film force maximum is found for both cases (at $\sim 10\,nm$ for Fe and $\sim 18\,nm$ for Cu); the thickness of this tensile peak has been shown to correspond to the continuous film formation thickness h_{cont}. [101] The tensile stress forming for mean film thickness $h_f < h_{cont}$ corresponds to stress owing to island coalescence, while the compressive stress observed for $h_f > h_{cont}$ is associated with atomic-scale processes occurring in continuous layers. We note that the magnitude of tensile stress for $h_f < h_{cont}$ is identical for low and high mobility conditions ($300\,K$ vs. $520\,K$ for Fe and $110\,K$ vs. $300\,K$ for Cu), which indicates that the island nucleation and coalescence stages are similar (i.e., island number densities, island sizes). Further increase of the temperature to $570\,K$ for Cu ($T_H = 0.42$), causes the tensile peak to shift to higher film thickness ($\sim 40\,nm$), which indicates that island coalescence is active to higher film thicknesses, due to lower island number density and larger islands resulting from increased surface diffusion at this temperature (and, thus, faster coalescence). [99] Another characteristic feature of the stress evolution in films deposited at high atomic mobility conditions is the tensile stress evolution upon deposition interruption (indicated by arrows in Fig. 4.7), which is revisited in Section 4.5.

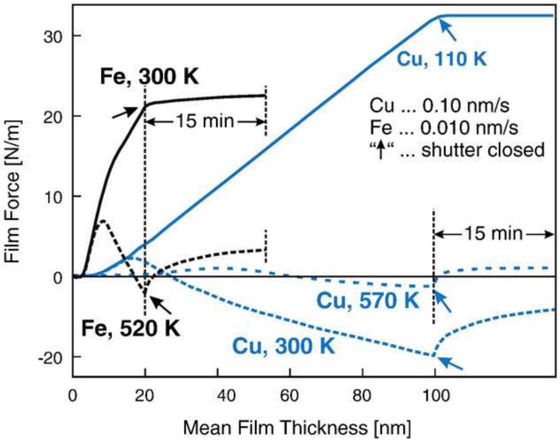

Fig. 4.7: Evolution of film force per unit width vs. film thickness for evaporated polycrystalline Fe films on oxidized Si(001) and Cu films on mica(001) for different deposition temperatures. The respective deposition rates are indicated in the figure. Arrows indicate the point at which deposition flux is terminated. Reprinted with permission from Ref. [84].

The most widely accepted theory with regards to the origin of compressive stress during deposition at high atomic mobility conditions suggests that a gradient of the chemical potential develops during film deposition between the surface and GBs, owing to the large difference in adatom number density. [102] This chemical potential difference is the driving force for flux of excess atoms into GBs, where they (i) decrease the tensile straining of the lattice induced via snapping, and (ii) increase the density at GBs, leading to compressive stress formation.

Consequently, the compressive stress formation is proportional to the GB number density, and a compressive steady-state stress (as seen for high atomic mobility conditions in Fig. 4.7) is formed, if the adatom/GB interaction is unchanged, i.e., no changes in GB number density and adatom mobility occur with continued film thickening. A detailed description of this model and other stress-generation mechanisms that are suggested in the literature are given in Section 4.6.

4.4.2. *Grain growth and stress*

When films are grown at conditions where surface and bulk atomic diffusion are active (i.e., for $T_H > 0.2$ and $T_H > 0.4$, respectively), the film morphology evolves with increasing film thickness. One key morphological feature of thin films is the grain size, the change of which (also referred to as grain growth) is a mechanism that is driven by a minimization of the total film energy. Energy minimization is achieved by elimination of GBs, which increase the interface energy, and by increasing volume fractions of low-energy crystallographic orientations. This growth can be mainly active close to the growth front, leading to V-shaped grains and to a continuous decrease of the GB number density at the film surface (i.e., when surface diffusion is active for $0.2 < T_H < 0.4$). [3] When bulk diffusion is active ($T_H > 0.4$), grain growth occurs throughout the film thickness, resulting in columnar grains with their grain size increasing along the film growth direction.

GBs are regions of low atomic density in thin films, i.e., the elimination of GBs during grain growth is accompanied by tensile stress formation, as the lattice of the growing grain has to accommodate the “missing volume” created when forming dense grains. Figure 4.8 presents film force evolution vs. film thickness during growth of Ni films at temperatures ranging from 300 to $473\,K$ (i.e., $T_H = 0.17$ to 0.27). [98] Initially, the film force evolves following the tensile-compressive evolution discussed in Section 4.4.1 for the high atomic mobility regime, however, with increasing film thickness, no compressive steady-state stress is observed, but a transition to tensile stress formation occurs (indicated by arrows). With increasing substrate temperature, the transition toward the tensile regime is shifted to larger film thicknesses.

Yu and Thompson [98] argued that the stress evolution seen in Fig. 4.8 is the result of the competition among tensile stress formation due to grain growth, and compressive stress formation due to adatom attachment to GBs. Initially, adatoms at the growth front diffuse to GBs and compensate the tensile stress forming due to grain growth, i.e., a net compressive stress forms in the film. With increasing film thickness, the average lateral grain size increases, while the diffusion length of adatoms remains constant, and fewer adatoms reach the GBs, leading to a net tensile stress formation. With increasing substrate temperature, the diffusion length of adatoms increases, and the compressive-to-tensile stress transition is shifted to larger film thicknesses. It is noted that the latter shift is seen in this system because the grain size of the Ni film does not increase with substrate temperature in the investigated temperature range.

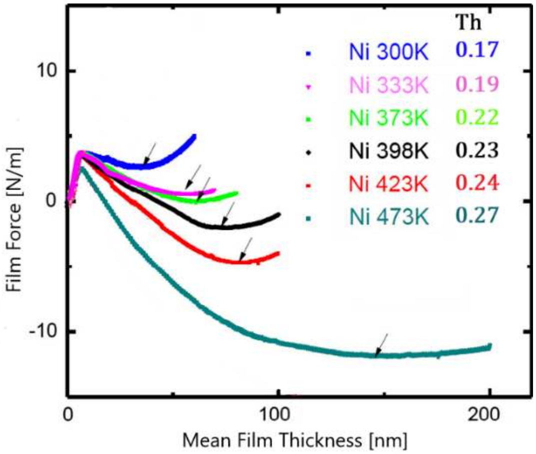

Fig. 4.8: Evolution of film force per unit width vs. film thickness for Ni films deposited at temperatures 300 to $473\,K$; the respective homologous temperatures T_h are indicated in the figure. Films are grown via electron-beam evaporation with deposition rate $0.05\,nm/s$. Arrows indicate the transition from compressive stress (i.e., negative slope) to tensile stress formation (i.e., positive slope). Reprinted with permission from Ref. [98]***.***

The question whether grain growth leads to a compressive-to-tensile stress transition is not easily answered, as the interplay among adatom diffusion length and lateral grain size determines which stress-state prevails. Comparing Cu growth at $300\,K$ ($T_H = 0.22$, Fig. 4.7), which was introduced as example for the high atomic mobility growth regime, to Ni growth at $373\,K$ ($T_H = 0.22$, Fig. 4.8), shows that knowledge of T_H is not sufficient to predict the stress evolution. Based on the data for Ni presented in Fig. 4.8, it can be expected that tensile stress will always prevail, if thick enough films are deposited, and grain size increases with film thickness. However, the viability of this hypothesis cannot be easily explored, as *in situ* stress studies usually focus on early film growth stages, therefore data for thick films is not readily available.

4.4.3. *Stress formation under energetic bombardment*

In Sections 4.4.1 and 4.4.2, stress data from films grown via evaporation have been presented. The general trends in stress formation in polycrystalline films discussed so far (high/low mobility, grain growth) are also valid for sputter-deposited films. However, an additional effect needs to be considered: interactions of hyperthermal noble gas and sputtered species with the growing film lead to *atomic peening*, i.e., a linear sputter cascade in the film that leads to film densification. [103] Atoms that are displaced via atomic peening can cause GB densification, which yields biaxial compressive stress in the film, or be implanted in grains, where they lead to a hydrostatic stress. [104–106]

Figure 4.9(a) presents the evolution of film force vs. film thickness for sputter-deposited Cu films on Si(100) for three working pressures. [84,107] All films show a tensile stress maximum during initial growth stages (see insert in Fig. 4.9(a)), indicating continuous film formation, and compressive stress formation thereafter. For low working pressures ($0.05\ Pa$), the compressive stress exhibits a steady-state in the observed thickness range, while a transition to tensile stress is observed for higher working pressures (0.5 and $2\ Pa$). After deposition interruption, stress changes are observed for all cases, indicating a high atomic mobility. Pletea *et al.* [107] found that the tensile stress evolution at high working pressure stems from a porous microstructure of Cu films with large surface roughness, while films are dense when compressive stress is observed. At low working pressure, film forming species experience few collisions while in the vapor phase and have a wide range of energies. Atoms that arrive with high kinetic energy can initiate sputtering of the film and promote atomic mobility by momentum transfer. With increasing working pressure, interatomic collisions in the vapor phase become more frequent, and the average energy distribution of vapor atoms is shifted to lower energies, i.e., film densification by collision-induced displacement is less common, and porous films form. [108]

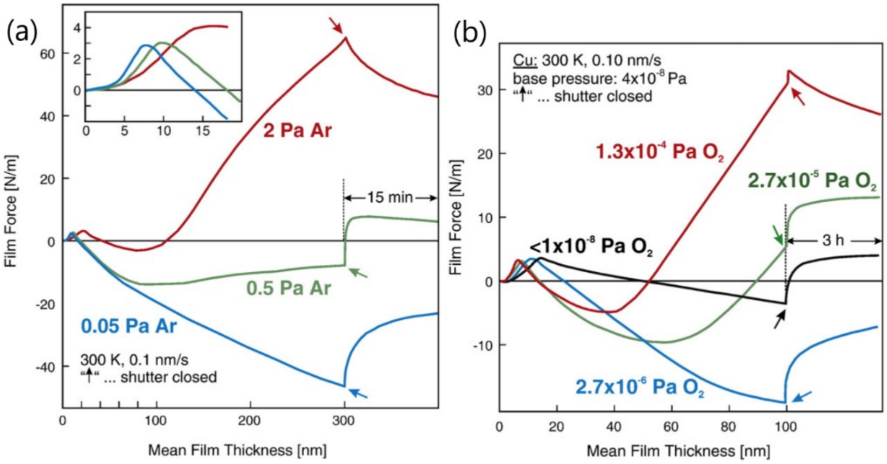

Fig. 4.9: Evolution of film force per unit width vs. film thickness for (a) sputter-deposited polycrystalline Cu films on Si(100) substrates for various working pressures, and (b) evaporated polycrystalline Cu films on MgF_2/glass substrates for various oxygen partial pressures. The inset in (a) shows the film force evolution during early growth stages. Essential deposition parameters (substrate temperature, deposition rate, base pressure in (b)) are indicated in the figures. Arrows indicate the point at which deposition flux is terminated. Reprinted with permission from Ref. [84].

Atomic peening has been studied more closely at low atomic mobility conditions (Mo and Ta, sputter-deposited at $300\ K$, i.e., $T_H = 0.10$ and 0.09, respectively). [109–111] While tensile stress forms in these films at conditions where no bombardment with energetic particle occurs (e.g., in evaporation), compressive stress with increasing magnitude has been observed in sputter-deposited films with (i) decreasing working pressure, (ii) increasing bias potential, and (iii) increasing deposition rate. This is understood in light of generation of point defects in the crystal lattice by collision-induced atom displacements when pressure is decreased and/or substrate bias potential is increased. Concurrently, defect annihilation by diffusion to the growth front is inhibited with increasing deposition rate. [106]

4.4.4. *Effect of impurities on stress formation*

Impurities can promote or inhibit fundamental structure-forming processes, and thus determine the film microstructural evolution during growth (see Section 3.6.4). [3] Consequently, the presence of impurities during film growth impacts the formation of intrinsic stress. Deposition of thin films in ultra-high vacuum (UHV) chambers (i.e., base pressure $< 10^{-5} Pa$) ensures that contamination of the growing film and impurity incorporation from the chamber background are minimized. During growth in high vacuum (HV) chambers, incorporation of oxygen-containing species might alter the film morphology and stress-state.

Abermann and Koch [112] investigated the effect of oxygen on the stress evolution in evaporated Cu films by introducing oxygen gas into an UHV chamber, to verify measurements performed in a HV chamber. [113] Figure 4.9(b) presents the evolution of film force with film thickness of Cu films deposited in various oxygen containing atmospheres. [84,112] For the lowest oxygen pressure ($< 1 \times 10^{-8} Pa$), a tensile-compressive stress evolution is found with a compressive steady-state in the continuous film regime. With increasing oxygen pressure, the tensile stress maximum is shifted to lower thicknesses, and a larger compressive stress is observed after continuous-layer formation. However, this compressive stress is not in a steady-state, and a transition to tensile stress is found; the thickness of the compressive-to-tensile stress transition decreases with increasing oxygen pressure. After deposition interruption (indicated by arrows in Fig. 4.9(b)), stress continuous to evolve for all deposition conditions.

The addition of oxygen in the atmosphere leads to the formation of copper-oxide nano particles at the film growth front, which stabilize smaller Cu islands during nucleation, thus leading to a decrease of the continuous film formation thickness (i.e., the tensile peak in Fig. 4.9(b)). [112] Presence of nano particles in the Cu matrix hinders GB migration (i.e., *solute drag*), [53] consequently, lateral grain growth is stopped during film deposition. The higher GB number density of films deposited in oxygen-containing atmospheres leads to increased compressive stress. Additionally, Cu adatom mobility is decreased due to the copper-oxygen interaction, and a porous columnar grain structure forms, leading to tensile stress formation.

4.5. Stress evolution after deposition interruption

During the discussion of stress data in Section 4.4, the stress evolution after deposition interruption has been mentioned several times. In Fig. 4.7, tensile stress formation is observed after deposition interruption for Cu and Fe film evaporation at high atomic mobility conditions (i.e., $300/570\,K$ and $520\,K$, respectively), while no stress evolution is observed for low mobility conditions (i.e., $110\,K$ and $300\,K$, respectively). During interruption of sputter-deposition of Cu films (see Fig. 4.9(a)), tensile stress formation is found for low working pressure (0.05 and $0.5\,Pa$), while compressive stress forms after deposition of porous Cu films at high working pressure ($2\,Pa$). Evaporation of Cu films in various oxygen-containing atmospheres (see Fig. 4.9(b)) leads to films that show a tensile stress behavior after deposition interruption below an oxygen pressure $2.7 \times 10^{-5} Pa$, and compressive stress at an oxygen pressure $1.3 \times 10^{-4} Pa$.

These results show that process parameters strongly affect the stress evolution after deposition interruption. In general, a stress evolution is observed for high mobility deposition conditions (i.e., high T_H). The fact that film stress during and after deposition are not the same underscores the necessity for *in situ* stress analysis since *ex situ* stress analyses cannot capture film stress variations upon deposition interruption. In addition, thermal stress must be considered when analyzing stress evolution, for the reasons explained in Section 4.1.1.

A systematic investigation of the stress evolution in the high atomic mobility regime after deposition interruption has been performed by Flötotto *et al.* [114]. Figure 4.10(a) presents the evolution of the film force per unit width vs. time after deposition interruption for evaporated Ag films with grain sizes in the range 63 to $436\,nm$. The magnitude of the tensile stress increases with decreasing grain size, which indicates that the GB number density is related to the post-deposition stress evolution. This is further strengthened by the lack of stress formation after deposition interruption in an epitaxial Ag film, which is single-crystalline, and therefore free of GBs. Furthermore, the authors show that the post-deposition tensile stress rise is linearly proportional to the inverse of the grain size (see Fig. 4.10(b)), while changes in the deposition rate and film thickness do not significantly influence the stress magnitude if the grain size remains constant.

Concurrently, increasing grain size and deposition rate lead to faster development of the post-deposition tensile stress rise. The can be seen in Fig. 4.10(a), where the stress evolution has stopped after $900\,s$ for grain size $436\,nm$, while a tendency for further tensile stress formation is observed for films with smaller grain sizes.

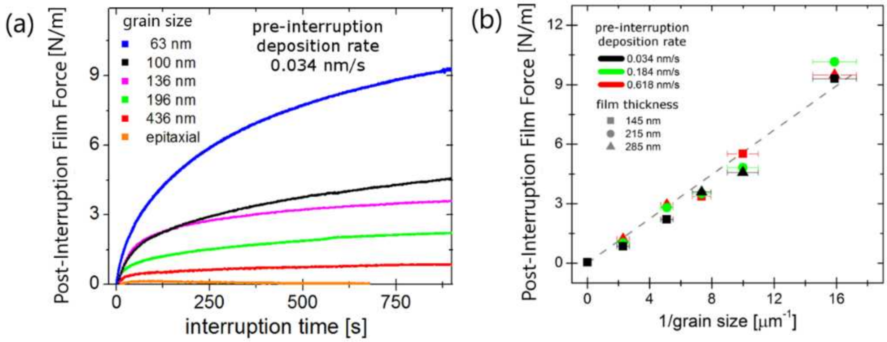

Fig. 4.10: (a) Evolution of the film force per unit width vs. time after growth interruption for evaporated Ag films on SiO$_2$ at $300\ K$ with lateral grain sizes in the range 63 to $436\ nm$, and an epitaxial Ag film on Si(100) (epitaxial relation Ag(100) || Si(100) and Ag[$1\bar{1}0$] || Si[$1\bar{1}0$]). Data is shifted to zero film force for convenience. (b) Dependence of the film force per unit width after $900\ s$ growth interruption (see final value in (a)) on the inverse lateral grain size for various deposition rates (colors) and film thicknesses (symbols). Reprinted with permission from Ref. [114].

Another aspect of the stress evolution upon deposition interruption is its reversibility if film growth is resumed. Figure 4.11 presents *in situ* stress data obtained during the evaporation of Au films, [115] which show a typical compressive-tensile-compressive stress evolution with increasing film thickness with a compressive steady-state, characteristic for the high atomic mobility regime. When film deposition is interrupted, a tensile rise is observed. The growth interruption is indicated by blue arrows in Fig. 4.11, while the stress evolution with time after deposition interruption is not presented here (see Ref. [115] for data). If film growth is resumed after $5\ min$ growth interruption (Fig. 4.11(a)), initially, very strong compressive stress is formed in the film (see large negative slope), which decreases within deposition of few nanometers of film until the stress magnitude of the compressive steady-state is reached (the film recovers the same stress value prior to interruption, indicated by red dashed line). This reversible stress evolution is reproducible, as seen for the three consecutive growth interruptions presented in Fig. 4.11(a). In a second set of depositions, presented in Fig. 4.11(b), growth interruptions are much longer (i.e., $24\ h$). While the general stress evolution with growth interruption is the same as for short growth interruptions, the post-interruption stress does not reach the compressive stress magnitude before interruption, but remains shifted to a less compressive/more tensile level (indicated by red arrow in Fig. 4.11(b)).

Yu *et al.* [115] found that the stress data during growth interruption is best fitted with an exponential decay function with two time constants ($\tau_1 \cong 10^2\ s$, $\tau_2 \cong 10^4\ s$). The fast process dominates the stress evolution during short growth interruptions and is reversible. Its time scale is comparable to surface diffusion-dependent changes of the surface morphology. [116,117] The slow process is irreversible and active in much longer time scales, indicating that its underlying process is a bulk effect, e.g., grain growth and recrystallisation that are active during growth interruptions.

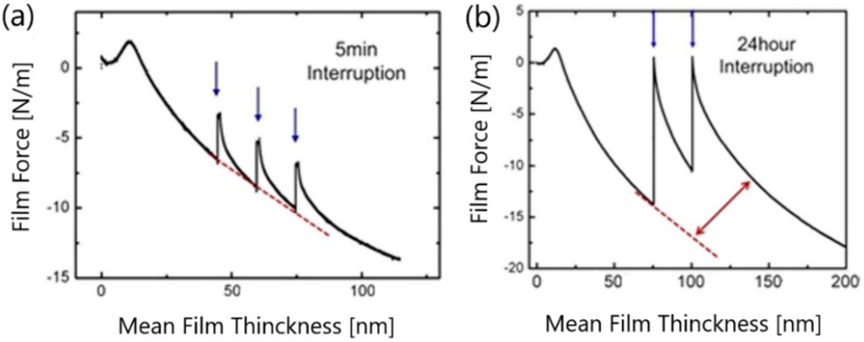

Fig. 4.11: Evolution of the film force vs. mean film thickness during evaporation of Au films on Si_3N_4/Si(100) at $300\ K$ with deposition rate $0.05\ nm/s$. Blue arrows mark (a) $5\ min$ and (b) $24\ h$ deposition interruptions, during which a tensile stress evolution is observed. While the pre-interruption stress evolution is retained in (a), a tensile shift occurs in (b). Reprinted with permission from Ref. [115]***.***

4.6. Models for stress formation and evolution in continuous films

Stress generation processes in discontinuous films (see Sections 4.2 and 4.3) are well understood and accepted within the research community. In contrast, no consensus exists with regards to mechanisms that govern stress in continuous layers. The literature survey presented in Sections 4.4 and 4.5 show common features that allows for drawing the following conclusions:

(i) Tensile stress prevails in continuous films deposited at low atomic mobility conditions.
(ii) Compressive stress forms in continuous films if atomic mobility is high.
(iii) The magnitude of stress in thin films is correlated with the GB number density.
(iv) Decrease of the GB number density (i.e., grain growth) during or after film growth, yields tensile stress.
(v) Porous microstructures are associated with tensile stress.
(vi) During growth interruptions at high atomic mobility conditions, a tensile stress evolution is observed that is reversible when deposition is resumed.

Based on the afore-mentioned conclusions and correlations, several mechanisms and models have been proposed in the literature that allow for calculating and predicting intrinsic stress σ_i during thin film growth as function of deposition parameters (e.g., substrate temperature, vapor arrival rate), morphological features (e.g., grain size), and material constants (e.g., lattice parameter, melting temperature). The following sections outline such models.

4.6.1. *Adatom/grain boundary interaction*

A kinetic model based on rate equations was developed by Chason *et al.* over the last two decades. [15,102,118–120] It is based on diffusion of adatoms from the film surface into GBs during film deposition. This diffusion is driven by differences of the chemical potential of adatoms at the film surface μ_S and within GBs μ_{GB}. During deposition, the vapor arrival rate leads to an increase of μ_S from the equilibrium value μ_S^0 to $\mu_S^0 + \delta\mu_S$. The chemical potential of adatoms in a GB is initially μ_{GB}^0 and changes to $\mu_{GB} = \mu_{GB}^0 - \sigma\Omega$ during deposition, i.e., it increases if compressive stress ($\sigma < 0$) forms in the film; Ω is the atomic volume of the film-forming species. At equilibrium, $\mu_S^0 \cong \mu_{GB}^0$, [118] and the difference in chemical potential $\Delta\mu$ during deposition is

$$\Delta\mu = \mu_S - \mu_{GB} \cong \delta\mu_S + \sigma\Omega = \left(\sigma - \sigma_{comp}\right)\Omega\,, \tag{4.5}$$

where $\sigma_{comp} = -\,\delta\mu_S/\Omega$. A driving force for adatom insertion into the GB exists if $\Delta\mu$ is positive, while adatoms in the GB diffuse toward the surface for $\Delta\mu < 0$ (see Fig. 4.12(a) for a schematic illustration).

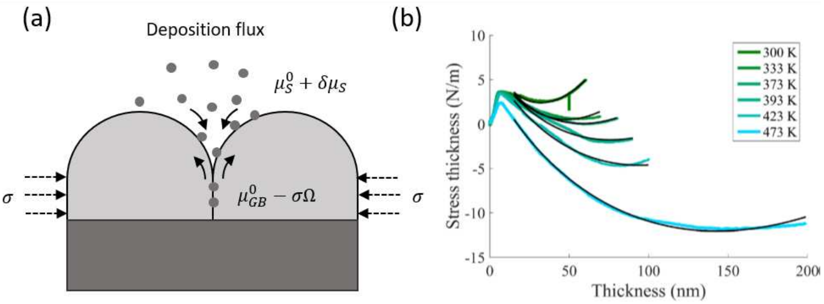

Fig. 4.12: (a) Schematic representation of the stress formation model based on adatom insertion into grain boundaries (GB). Equilibrium chemical potentials of adatoms at the surface and in GBs are μ_S^0 and μ_{GB}^0, respectively. The flux of atoms to the surface during deposition increases the surface chemical potential by $\delta\mu_S$, and stress σ changes the GB chemical potential by $\sigma\Omega$, where Ω is the atomic volume. (b) Evolution of stress-film thickness product vs. mean film thickness during electron-beam evaporation of Ni films at substrate temperatures 300 to $473\ K$ with deposition rate $0.05\ nm/s$. Colored lines represents experimental data (see Ref. [98]***) and black lines are stress predicted by the stress model on basis of adatom insertion into GBs. Reprinted with permission from Ref.*** [15]***.***

The change of the stress-film thickness product due to adatom insertion into the GB $(\sigma \times h_f)_{insert}$ as function of time t can be written as

$$\frac{d(\sigma \times h_f)_{insert}}{dt} = -\frac{Y_f \Omega^{2/3}}{L}\frac{dN}{dt}, \tag{4.6}$$

where Y_f is the film biaxial modulus, L is the lateral grain size, and N is the number of adatoms inserted into the GBs. The rate of adatom insertion into GBs, dN/dt, is given by

$$\frac{dN}{dt} \cong 4C_S \frac{D}{\Omega^{2/3}}\frac{\Delta\mu}{k_B T}, \tag{4.7}$$

where C_S is the concentration of mobile species on the surface, D is the effective diffusivity for adatom migration from the surface to the GB, k_B is the Boltzmann constant, and T is the absolute temperature. Combining Eqs. 4.5 through 4.7 gives

$$\frac{d(\sigma \times h_f)_{insert}}{dt} = -\frac{4C_S Y_f \Omega}{k_B T}\frac{D}{L}(\sigma - \sigma_{comp}) = -\frac{\beta D}{L}(\sigma - \sigma_{comp})\,. \tag{4.8}$$

The second mechanism that is considered in the model by Chason *et al.* is the stress that forms due to GB zipping at the growth front (see Section 4.3), which progresses with the same speed as the deposition rate F. Tensile stress σ_{tens} forming due to the elastic formation of the crystal lattice is proportional to $(\Delta\gamma/L)^{1/2}$, where $\Delta\gamma$ is the change of interfacial energy when a GB is formed at the cost of two film/vacuum interfaces. [94,118,121] The time derivative of the stress-thickness product change due to GB zipping $(\sigma \times h_f)_{zip}$ reads

$$\frac{d(\sigma \times h_f)_{zip}}{dt} = F\sigma_{tens}(L)\,. \tag{4.9}$$

Grain growth removes GBs and leads to tensile stress formation in the bulk of the film. If $L(z)$ is the grain size during the deposition of a layer at film thickness z, and $L(h_f)$ the grain size at the final film thickness h_f, the growth of the film from z to h_f has removed $1/L(z) - 1/L(h_f)$ GBs per unit length in the layer deposited at thickness z. If Δd is the excess volume per unit area that is removed during grain growth, the stress-thickness product due to grain growth $(\sigma \times h_f)_{gg}$ is

$$(\sigma \times h_f)_{gg} = Y_f \Delta d \int_0^{h_f} \left(\frac{1}{L(z)} - \frac{1}{L(h_f)} \right) dz\,. \tag{4.10}$$

Integration over the film thickness and calculation of the time derivative of Eq. 4.10 gives

$$\frac{d(\sigma \times h_f)_{gg}}{dt} = Y_f \Delta d h_f \left(\frac{1}{L(h_f)^2} \frac{\partial L(h_f)}{\partial t} \right). \tag{4.11}$$

Since grain size increases with time (i.e., $\partial L(h_f)/\partial t > 0$), this stress contribution will always lead to a tensile stress component. The summation of Eqs. 4.6, 4.9 and 4.11 gives the overall stress-thickness product evolution with time

$$\frac{d(\sigma \times h_f)}{dt} = F \sigma_{tens}(L) - \frac{\beta D}{L} (\sigma - \sigma_{comp}) + Y_f \Delta d h_f \left(\frac{1}{L(h_f)^2} \frac{\partial L(h_f)}{\partial t} \right). \tag{4.12}$$

Since stress data is usually presented as function of film thickness, the variable transformation $dh_f = F dt$ gives

$$\frac{d(\sigma \times h_f)}{dh_f} = \sigma_{tens}(L) - \frac{\beta D}{FL} \left(\frac{(\sigma \times h_f)}{h_f} - \sigma_{comp} \right) + Y_f \Delta d h_f \left(\frac{1}{L(h_f)^2} \frac{\partial L(h_f)}{\partial h_f} \right). \tag{4.13}$$

With this model, Chason *et al.* [15] were able to fit the stress evolution of Ni for various substrate temperatures, [98] where grain growth was found to be active and responsible for a compressive-to-tensile stress transition (see discussion of Fig. 4.8). The fitting of this data is presented in Fig. 4.12(b), and the authors found that fitting parameters ($\sigma_{tens}, \sigma_{comp}, \beta D, Y_f \Delta d$), which were obtained via non-linear least square fitting of the model to the experimental data, are physical, and reasonably close to reported values (for βD and $Y_f \Delta d$). We note that the fitting range is set to begin past continuous film formation, as stress generation and evolution in continuous films is the main focus.

In cases where the grain size does not increase with increasing film thickness, $\partial L(h_f)/\partial h_f = 0$, and Eqs. 4.12 and 4.13 can be simplified. In this case, a steady-state stress σ_{SS} forms in the film which is [118]

$$\sigma_{SS} = \frac{\sigma_{tens} + \frac{\beta D}{FL}\sigma_{comp}}{1 + \frac{\beta D}{FL}}. \tag{4.14}$$

This version of the stress model can be used to describe high mobility growth, e.g., during Cu growth at $300\ K$ (see Fig. 4.7), where a steady-state stress is found after continuous film formation. Equation 4.14 also captures the transition of a compressive σ_{SS} to tensile σ_{SS} for decreasing substrate temperature and increasing deposition rate. [119]

When the deposition flux is turned off during growth interruptions, the supersaturation of adatoms on the film surface decreases fast, and $\delta\mu_S$ becomes zero (i.e., $\sigma_{comp} = 0$). If σ_{SS} is the stress before growth interruption, a stress evolution

$$\sigma(t) = \sigma_{SS}\, exp\left(-\frac{\beta D}{h_f L}t\right) \tag{4.15}$$

is seen with time t thereafter. This stress evolution is in agreement with experiments (see Fig. 4.7, Fig. 4.9, Fig. 4.10), and captures some of the observed features, e.g., a faster tensile rise can be expected for increasing grain size (Fig. 4.10).

The model outlined above is only valid if atom mobility in GBs is high, i.e., the stress within the GB is constant throughout the film thickness. If this is not the case, stress gradients would have to be considered, leading to a more complex description.

An alternative description of the adatom/GB interaction model was presented by Yu and Thompson, [98] to better understand the observed stress regimes (compressive steady-state vs. compressive-to-tensile stress transition in continuous films). Again, stress that forms in the surface layer is distinguished from stress in the bulk of the film (e.g., due to grain growth). In their model, Yu and Thompson argue that the observed stress in continuous films is the result of a competition among adatom attachment to two-dimensional (2D) islands that form on grains and to the GB, where they lead to compressive stress. At low film thicknesses, the grain size L is relatively small, and, on average, only one island forms on top of each grain, because the entire island is the part of the GB capture zone (i.e., the area from which inserted adatoms come). Consequently, the number of adatoms that are inserted into the GB is high, but independent of L. When the grain size increases with film thickness, the grains become larger than the GB capture zones, and the number of adatoms that are inserted into the GB depends on the ratio of average island spacing to grain size, i.e., less adatoms are inserted with increasing grain size.

With this model, Yu and Thompson explain the stress evolution in Ni films (see Fig. 4.8) as follows: [98] Shortly after continuous film formation, the island size is small, and the compressive stress component due to adatom attachment to GBs is large, while tensile stress due to grain growth (similar to Eq. 4.11) is small, i.e., compressive stress forms in all films. With increasing grain size, the compressive stress component becomes smaller, while the tensile stress component increases, i.e., a compressive-to-tensile stress transition is seen when these two components are equivalent. Increasing substrate temperature leads to an increase of the adatom diffusion length, which increases the compressive stress component, and shifts the stress transition to larger film thicknesses.

The models described in this section are able to reproduce many stress features during and after film growth. Flötotto *et al.* [114] remark that several of the post-deposition stress features that are predicted by the models cannot be verified by experiments (e.g., increasing post-deposition stress rise magnitude and faster kinetics with increasing pre-interruption stress magnitude). Moreover, the models have been criticized because unphysically high GB-to-surface diffusion ratios have to be assumed in simulations to match compressive stress magnitudes observed experimentally. [122]

4.6.2. *Grain boundary grooving*

The fast character of stress evolution during growth interruptions, and the weak film-thickness-dependency of the stress rise indicate that surface processes are responsible for the stress evolution in high atomic mobility systems. Yu *et al.* [117] found in atomic force microscopic (AFM) surface studies that films show deep surface grooves long after deposition has been completed, while these grooves are not observed immediately after deposition. Grooving of surfaces at GB/surface intersections with a dihedral angle that is determined by the surface and interface free energies is described by Mullins. [116] During film growth from the vapor phase, the arriving vapor flux enables diffusion processes at the surface which are not active under equilibrium conditions, e.g., GB zipping leads to GB grooves that are flatter than in equilibrium, and the supersaturation of surface adatoms increases their chemical potential at the surface. Once film deposition is stopped, GB grooves will develop a shape that is closer to the equilibrium shape, i.e., grooves deepen when growth is interrupted. This is illustrated in Fig. 4.13(a).

Figures 4.13(b) and (c) show cross-sectional transmission electron microscopy images of evaporated Ni films, which were deposited at elevated temperature ($473\,K$), where Ni grows in the high-mobility stress regime (see Fig. 4.8), and then cooled to $300\,K$, where diffusivity is much slower and surface profile reshaping not expected (see Ref. [117] for more experimental details). For immediate cooling after deposition (Fig. 4.13(b)), GB grooves are very flat, while deep grooves are seen for cooling $60\,min$ after deposition interruption (Fig. 4.13(c)). The redistribution of atoms necessary for this reshaping is a surface diffusion process along GBs. For deepening of the GB groove by Δh, the stress-thickness product change is proportional to $\sigma^*\Delta h$, where σ^* is the compressive stress in the surface layers of the film due to trapped adatoms. When growth is resumed, the GB grooves become shallow again with a high number density of trapped atoms near the surface, leading to the apparent reversibility of the stress evolution during growth interruptions.

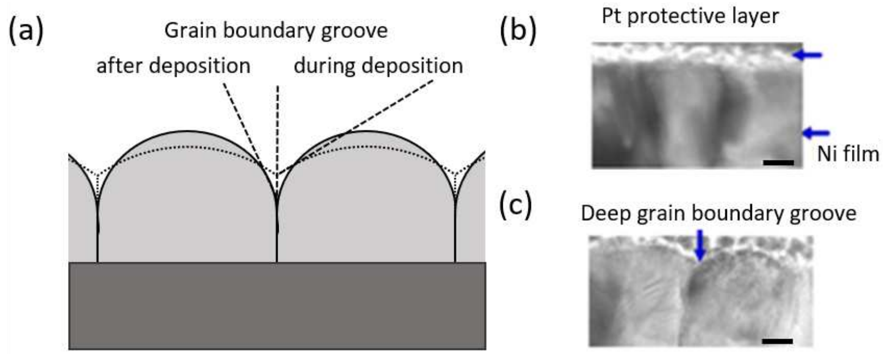

Fig. 4.13: (a) Schematic illustration of grain boundary grooves during (dotted line) and after (full line) deposition, where the dihedral angle steepens. Cross sectional transmission electron microscopy images of electron-beam evaporated Ni films (deposition rate $0.5\ nm/s$) (b) $0\ min$ and (c) $60\ min$ after growth interruption. Shallow grain boundary grooves can be seen in (b), while deep grooves are seen in (c). The scale bar is $10\ nm$. Reprinted with permission from Ref. [117].

GB grooving is able to explain the post-deposition stress evolution observed by Flötotto *et al.* [114] The post-deposition tensile rise magnitude depends on the stress before deposition interruption (σ^*) and Δh, i.e., even when σ^* increases, less post-deposition tensile stress can be formed, if Δh decreases. More shallow GB grooves can be expected to form with increasing deposition rate due to larger adatom flux to GBs and faster growth front progression. The kinetics of the stress evolution during growth interruptions depends on the kinetics of the GB groove deepening, which is proportional to $t^{1/4}$. [116]

Vasco and Polop [123] note that GBs observed with AFM do not correspond to the space between individual grains, but rather to bundles of grains that are separated by pseudo-coherent GBs. Other surface (e.g., scanning tunnel microscopy) or crystallographic techniques (e.g., selected area electron diffraction) are able to resolve these bundles. The GB grooving model outlined above does not distinguish between different types of GBs. Furthermore, Vasco and Polop argue that equilibrium GB profiles cannot be modified easily, unless certain regions grow preferentially (e.g., due to shadowing).

Advanced AFM techniques such as force modulation microscopy (FMM) [117] allow the mapping of the residual stress of the film surface, [118] and can therefore give valuable information on the local stress distribution. Vasco *et al.* have developed a stress model based on surface studies of polycrystalline Au films using FMM. [126,127] A residual stress map and corresponding surface topography and stress profiles are presented in Fig. 4.14(a) and (b), respectively. GB grooving is visible in the topographic profile in Fig. 4.14(b) (black line). Their experiments reveal that stress is concentrated close to GBs, with distinct compressive and tensile regions when approaching a GB from the grain center (see red lines in Fig. 4.14(b)). In Fig. 4.14(c) the evolution of calculated surface profiles during film growth (i.e., as a function of deposition time t) is presented; for easier comparison, the profiles are normalized to the GB groove depth h_{GB}.

Equilibrium surface profiles $h_e(r)$ before ($t = 0\ s$) and after deposition ($t = 10^4\ s$) are present as black and red lines, respectively. Close to the GB, an equilibrium slope m_0 forms due to GB grooving [116], while no surface slope is seen far from the GB. Between these boundaries, $h_e(r)$ follows [116]

$$h_e(r) = 1.77\ h_{GB}\ ierfc\left(\frac{m_0 r}{1.77\ h_{GB}}\right), \tag{4.16}$$

where $ierfc(x)$ is the integral of the error function of x.

During deposition, an adatom flux toward the GB exists, such that the GB groove approaches asymptotically a flat shape ($m_0 \rightarrow 0$). Since the slope of the surface profile at the GB is constrained, [123] the filling of the GB groove is slow compared to equilibrium conditions (compare GB groove depth of equilibrium (red) and steady-state (green) surface profile in Fig. 4.14(c)). Atoms that cannot diffuse into the GB groove accumulate close to the GB and form a ridge that increases in height with increasing deposition time (blue, teal and green lines in Fig. 4.14(c)). The resulting surface profile corresponds to Mullin's diffusive surface profile. [116]

From the surface profile $h(r)$, the surface curvature $\kappa(r)$ is calculated as

$$\kappa(r) = -\frac{\nabla^2 h(r)}{(1 + [\nabla h(r)]^2)^{3/2}}. \tag{4.17}$$

Equation 4.17 reduces to $\kappa(r) \approx -\nabla^2 h(r)$ for $\nabla h(r) \ll 1$. Where the curvature of the equilibrium surface profile $\kappa_{eq}(r,t)$ differs from the curvature of the diffusive surface profile $\kappa_d(r,t)$, a Laplace pressure

$$\sigma_N(r,t) = 2\gamma_S \left[\kappa_{eq}(r,t) - \kappa_d(r,t)\right] \tag{4.18}$$

forms, where γ_S is the surface free energy, and the index N indicates that the intrinsic stress is normal to the surface. The intrinsic stress profiles $\sigma_N(r,t)/2\gamma_S$ resulting from surface profiles presented in Fig. 4.14(c) are drawn in Fig. 4.14(d) and show a tensile stress maximum and a compressive minimum, which is dominant (i.e., compressive stress would be measured when measuring the average stress in the film). The arrows in Fig. 4.14(d) indicate that the stress maxima and minima increase in size and move toward the GB with increasing deposition time. Formation of surface stress in the ridges gives rise to a driving force for ridge-decay to minimize strain energy. [37] This driving force leads to diffusion of surface atoms from the strained GB toward the center of the grain, and thus to the stabilization of a steady-state surface profile.

When deposition it stopped, the driving force for adatom diffusion toward the GB disappears, and the ridge starts to decay driven by strain energy minimization. [37] When the driving force becomes smaller than the energy barrier for surface diffusion, the decay stops. While this decay leads to a decrease of the stress profile (not shown here, see Ref. [127] for details), parts of it persist and correspond to the stress profile measured in Fig. 4.14(b).

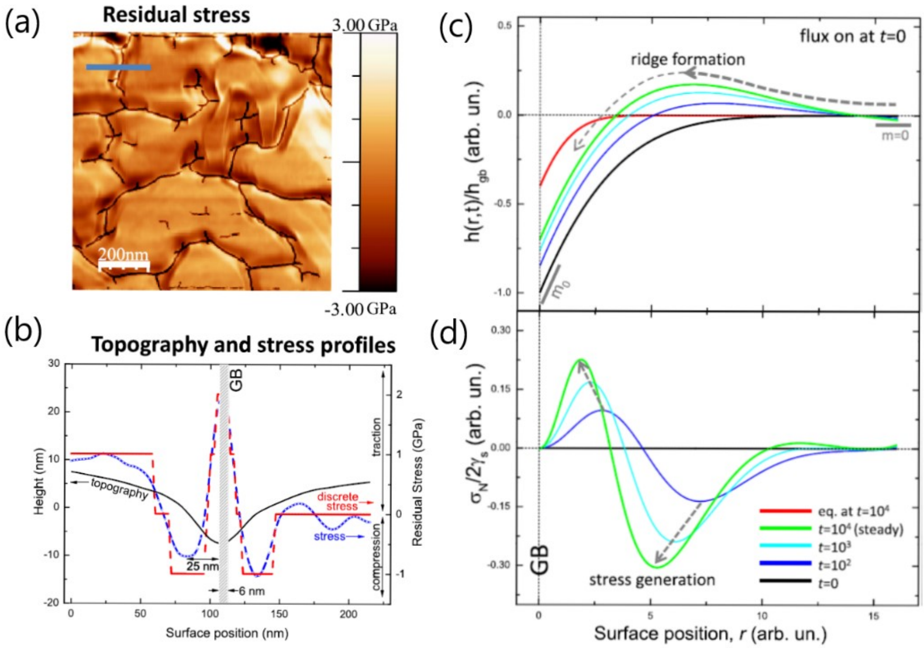

Fig. 4.14: (a) Residual stress map obtained from force modulation microscopy on the surface of evaporated Au/Si(111) films. (b) Topography (black line), residual stress (blue line), and discrete stress level (i.e., zero stress, tension, compression, red ine) profiles along a grain boundary (GB); location is indicated in (a). (c) Evolution of normalized surface profile $h(r,t)/h_{GB}$, and (d) corresponding intrinsic stress profiles σ_N/γ_S vs. distance r from GB and time t (indicated by colors). m and m_0 are the slopes of the surface profile far from the GB and at the GB, respectively. Arrows in (c) indicate the mass flow, and show the position of the stress maxima in (d). Reprinted with permission from Ref. [127].

With this stress model, stress generation and evolution during film growth can be described: (i) A steady-state surface profile develops during film deposition, which leads to compressive and tensile stress regions close to GBs. As the compressive stress is larger than the tensile stress, compressive stress is measured in the film, when stress is analyzed in average. (ii) Stress relaxation is seen when the deposition flux is stopped. (iii) Kinetics of surface diffusion driven by Mullins-type groove and ridge formation, and strain energy minimization lead to a time constant in the $10^2\ s$ range, which corresponds to experimentally observed values. This model only describes stress formation in the surface layer of a film and does not include bulk effects (e.g., grain growth), i.e., it cannot describe stress evolution in systems where grain growth is active. Additionally, GB/GB interactions are not considered at this stage, which might play an important role to explain effects of deposition temperature and flux. [127]

5. Thin film synthesis equipment and characterization techniques

The present chapter outlines the synthesis equipment and thin film characterization techniques (along with representative measurement data, when relevant) used in the thesis. For detailed experimental setup and measurement details, the reader is referred to appended papers. Section 5.1 describes deposition chambers used to grow thin films and analyze their growth *in situ* and in real-time. Section 5.2 presents *in situ* and real-time techniques to characterize optical, mechanical, and electric properties of films, as well as to determine the composition of the synthesis atmosphere in the chamber. *Ex situ* techniques are presented in Section 5.3, and include methods in which films are probed with electrons and x-rays, as well as real-space surface imaging.

5.1. Deposition chambers

Films were deposited in two magnetron sputter-deposition chambers, a high-vacuum (HV) chamber at the University of Poitiers (base pressure $\sim 8 \times 10^{-6}\ Pa$), and an ultra-high-vacuum (UHV) chamber at Linköping University (base pressure $< 10^{-8}\ Pa$).

The basic layout of the UHV chamber is presented in Fig. 5.1, but it is conceptually representative for both chambers. The deposition system consists of a main chamber (MC), and load-lock (LL) chamber used for loading samples. The LL chamber features a cassette with five samples positions with a lateral transfer arm for moving samples to the MC. The two compartments are connected through the LL-MC gate valve and separately pumped through their respective turbomolecular pumps (TMP), which are backed with (oil-free) scroll pumps.

The MC TMP is connected to the MC via a throttle valve (TV) that remains fully open when no deposition is running. Working gas (Ar, N_2, O_2) can be introduced i) through the MC wall, ii) close to the three targets, and/or iii) through a gas ring close to the substrate. The working pressure is then set by partially closing the TV, regulated by a loop between the TV motor and the MC Baratron (i.e., capacitance manometer). Pressures are measured with multiple additional pressure gauges (PG): i) MC cold ion gauge, ii) MC Pirani PG (when ion gauge is off), iii) LL and MC are equipped with full range PG, which are combined Bayard-Alpert Pirani gauges, and iv) foreline pressures are measured with Pirani PG.

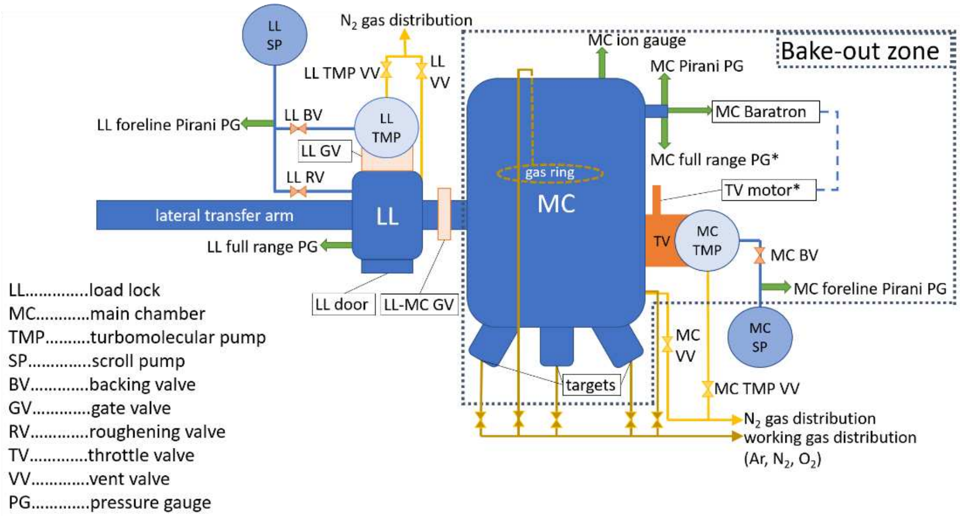

Fig. 5.1: Schematic illustration of the ultra-high-vacuum system used for thin film deposition in course of the present thesis.

For achieving pressures of $\sim 10^{-8}\ Pa$ or below in the MC, a bake-out procedure is implemented every time that the entire deposition system is pumped down after exposure to the atmosphere. Bake-out occurs in a specific zone (marked with dashed lines in Fig. 5.1) by heating the chamber to $\sim 420\ K$ for $\sim 48\ h$.

The main difference of the HV chamber compared to the UHV system is that a cryogenic pump sustains the vacuum in the MC that is backed by Roots pumps. UHV cannot be reached in this system, as it is not bakeable, i.e., non-metallic gaskets are used.

Film synthesis and *in situ* analysis are performed in the respective MCs of the two systems, which host three magnetron sources for circular targets that are water cooled, and substrate holders that are rotatable and can apply heating to the substrate (see schematic illustration in Fig. 5.2). For ignition of a plasma, working gas is added close to the targets. The MCs are equipped with several shutters that inhibit unwanted deposition of films on the substrate (substrate shutter), unused targets (target shutter), and view ports. Fused silica view ports allow observation of the film growth, e.g., for *in situ* analysis. Two of the *in situ* methods that are employed for growth analysis, i.e., spectroscopic ellipsometry and substrate curvature measurements, are schematically illustrated in Fig. 5.2, i.e., the substrate curvature technique (normal incidence), and spectroscopic ellipsometry ($70°$ angle of incidence with respect to substrate normal). *In situ* substrate curvature and four-point-probe measurements are performed in the HV chamber, while *in situ* spectroscopic ellipsometry is performed in the UHV chamber. More details about these techniques are given in Section 5.2. Thin films deposited for Papers I, II and VI are synthesized in the HV chamber, while Papers III through V are based on films grown in the UHV chamber.

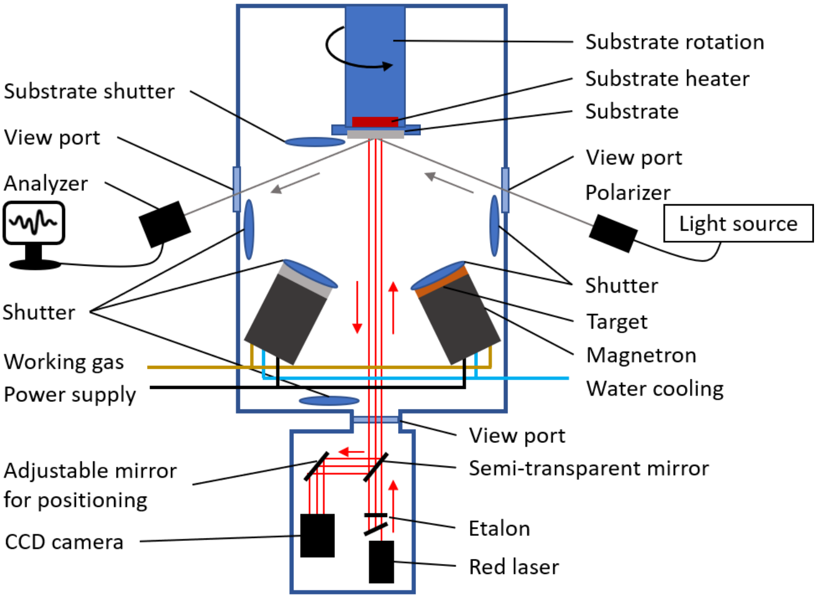

Fig. 5.2: Schematic illustration of the main chamber of a magnetron sputter-deposition system, equipped with in situ measurement techniques that allow analysis of film growth.

5.2. *In situ* characterization

For studying processes that govern film formation and stress evolution, *in situ* and real-time characterization techniques are used, i.e., properties of the film and substrate are monitored during deposition. This approach allows investigations without the sample being affected by atmospheric exposure (which causes, e.g., contamination, oxidation, surface restructuring, relaxation), and provides real-time information, such that kinetics of structure-forming processes can be studied.

5.2.1. *Spectroscopic ellipsometry*

In spectroscopic ellipsometry, the change of the polarization state of light after interaction with a sample surface is used to measure the real and imaginary part of the dielectric function of the probed material as function of incident light frequency. By modelling the dielectric function, information about electronic (e.g., electron number density) and microstructural (e.g., film thickness, surface roughness) properties of the sample can be obtained. Ellipsometry is a surface-sensitive technique, and is used in reflection-mode within this work, i.e., incident polarized light is reflected off the sample under investigation (see schematic setup of light source, polarizer and analyzer in Fig. 5.2).

In the presence of an electric field $\vec{E}$, bound charges (e.g., atomic nuclei, electrons) are displaced. This process is described by the electric displacement field $\vec{D} = \varepsilon_0\vec{E} + \vec{P}$, [128,129] where ε_0 is the vacuum permittivity, and $\vec{P}$ is the polarization. For homogeneous isotropic materials, $\vec{P} = \varepsilon_0\chi\vec{E}$, [128] where χ is the electric susceptibility. The material's response to $\vec{E}$ can therefore be written as

$$\vec{D} = \varepsilon_0\vec{E} + \vec{P} = \varepsilon_0\vec{E} + \varepsilon_0\chi\vec{E} = \varepsilon_0\varepsilon_r\vec{E}\,, \qquad (5.1)$$

where $\varepsilon_r = 1 + \chi$ is the relative dielectric function (for simplicity the subscript r is not used in the remainder of the text). The material's response is dependent on the frequency ω of the incident light, i.e., the complex dielectric function reads $\tilde{\varepsilon}(\omega) = \varepsilon_1 + i\varepsilon_2$, where ε_1 and ε_2 are the light dispersion and absorption, respectively. Light-matter interaction is also described by the complex index of refraction $\tilde{n} = n + ik = \sqrt{\tilde{\varepsilon}}$, [128] where n and k are the refractive index and extinction coefficient, respectively.

During an ellipsometric measurement in reflection mode, linearly polarized light is used, which becomes elliptically polarized after being reflected off the sample surface (Fig. 5.3(a)). To describe this change in polarization, the reflectance is analyzed in the orthogonal s-p system, where s and p denote planes that are parallel and perpendicular to the plane of incidence, respectively.

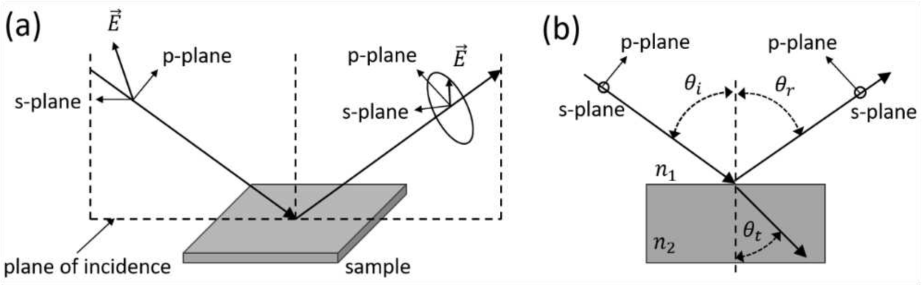

Fig. 5.3: (a) Schematic illustration of an ellipsometric measurement. Linearly polarized light (with electric field vector $\vec{E}$) is reflected at sample surface. The light-matter interactions change the polarization of the light to elliptically polarization. p-plane and s-plane indicate the planes that are parallel and perpendicular to the plane of incidence, respectively. (b) Light interactions at an interface between two media (materials with indices of refraction n_1, n_2). Angles of incident (θ_i), reflected (θ_r), and transmitted (θ_t) light with respect to the interface normal are indicated.

The simplest case of an ellipsometric measurement refers to a semi-infinite vacuum/sample system (also referred to as two-phase system), where light is either reflected or absorbed (see Fig. 5.3(b) for a schematic illustration). Reflection then occurs at the interface of two media with indices of refraction $\tilde{n}_1$ and $\tilde{n}_2$ ($\tilde{n}_1 = 1$ in case of vacuum), and incident and transmitted light have the angles θ_i and θ_t with reference to the interface normal, respectively. In this case, Snell's law is valid (i.e., $\tilde{n}_1 \sin(\theta_i) = \tilde{n}_2 \sin(\theta_t)$), and the Fresnel equations describe the reflection coefficients in the s-plane (r_s) and p-plane (r_p), [129]

$$r_s = \frac{\tilde{n}_1 \cos(\theta_i) - \tilde{n}_2 \cos(\theta_t)}{\tilde{n}_1 \cos(\theta_i) + \tilde{n}_2 \cos(\theta_t)}, \qquad r_p = \frac{\tilde{n}_1 \cos(\theta_t) - \tilde{n}_2 \cos(\theta_i)}{\tilde{n}_1 \cos(\theta_i) + \tilde{n}_2 \cos(\theta_t)}. \tag{5.2}$$

These quantities are complex numbers and define the complex reflectance ratio ρ_{ref} as [129]

$$\rho_{ref} \equiv \frac{r_p}{r_s} \equiv \tan(\Psi) \exp(-i\Delta) \,. \tag{5.3}$$

In Eq. 5.3, Ψ and Δ are the amplitude ratio and the phase difference of the reflection coefficients, respectively, which are the measured ellipsometric quantities. Recalling $\tilde{n} = \sqrt{\tilde{\varepsilon}}$ and Snell's law, the dielectric function $\tilde{\varepsilon}$ of medium 2 (i.e., the material under investigation) can be calculated:

$$\tilde{\varepsilon} = \tilde{\varepsilon}_1 \sin^2(\theta_i) + \frac{(1 - \rho_{ref})^2 \sin^2(\theta_i)/\tan^2(\theta_i)}{(1 + \rho_{ref})^2}, \tag{5.4}$$

where $\tilde{\varepsilon}_1$ is the dielectric function of medium 1 (i.e., vacuum).

If thin films are investigated via ellipsometry (i.e., a three-phase system comprising of vacuum, transparent film, and semi-infinite substrate), light that is transmitted through the film interacts with the film/substrate interface, and multiple reflections occur. For a single film with thickness h_f on a substrate that is probed with light with wavelength λ, the Fresnel reflection coefficients read

$$r_{123s} = \frac{r_{12s} + r_{23s}\exp(i2\beta)}{1 + r_{12s}r_{23s}\exp(i2\beta)}, \qquad r_{123p} = \frac{r_{12p} + r_{23p}\exp(i2\beta)}{1 + r_{12p}r_{23p}\exp(i2\beta)}, \tag{5.5}$$

where

$$\beta = \frac{2\pi h_f \tilde{n}_2 \cos(\theta_t)}{\lambda}. \tag{5.6}$$

In Eqs. 5.5 and 5.6, the subscripts 1,2,3 denote vacuum, transparent film, and semi-infinite substrate, respectively. Combining Eqs. 5.2 through 5.6 (note that here, $\rho_{ref} = r_{123p}/r_{123s}$), the pseudo-dielectric function $\langle\tilde{\varepsilon}\rangle$ that contains all optical information of the three media and the film thickness can be computed from Eq. 5.4.

Additional analysis and modelling of the measured pseudo-dielectric function is required to determine the optical response (i.e., dielectric function) and thereby intrinsic properties (e.g., electron density, and mean-free-path of electrons in a metal) of the film under investigation. This is done by using models that allow computing the optical response of the measured system, which may be purely mathematical with no physical meaning, or founded on classical/quantum mechanical descriptions of optoelectronic properties of materials. Within the present thesis work, two models are used for analysis of ellipsometric data, the Lorentz and Drude models that are outlined in the following.

Lorentz oscillator

The Lorentz oscillator describes the response of electrons (with effective electron mass m_e, and charge $-e$), which are bound to a positive ion core, to an electric field $\vec{E}(\omega) = \vec{E}_0 \exp(-i\omega t)$, where ω and t are frequency and time, respectively. The motion of electrons in one dimension (i.e., x) is described by [129]

$$m_e \frac{d^2x}{dt^2} = -m_e\Gamma_L \frac{dx}{dt} - m_e\omega_o^2 x - e\vec{E}_0 \exp(-i\omega t), \tag{5.7}$$

where the first term on the right hand side accounts for energy loss mechanisms in electronic transitions with the damping constant Γ_L (also called *broadening*), the second term represents the restoring force with the resonance frequency ω_0, and the third term is the electrostatic force due to the external electric field $\vec{E}$. Solving the differential equation gives

$$\vec{x}(\omega) = -\frac{e\vec{E}(\omega)}{m_e(\omega_o^2 - \omega^2 - i\Gamma_L\omega)}. \tag{5.8}$$

The induced polarization by this motion of charge carriers is $\vec{P}(\omega) = -ne\vec{x}(\omega)$, where n is the number of electrons per unit volume. Recalling $\varepsilon_0\vec{E} + \vec{P} = \varepsilon_0\tilde{\varepsilon}\vec{E}$ allows calculation of the dielectric function for a Lorentz oscillator

$$\tilde{\varepsilon}_L(\omega) = 1 + \frac{ne^2}{\varepsilon_0 m_e}\frac{1}{(\omega_o^2 - \omega^2 - i\Gamma_L\omega)}. \tag{5.9}$$

A derivation of the dielectric function from quantum mechanical point of view gives formally the same result; in this case ω_0 corresponds to the frequency of an electron transition between two states separated by the energy $\hbar\omega_0$. [130] In a real material, multiple electron transitions are possible, e.g., interband transitions in a material triggered by the energy of the incident light. In addition, experimental setups have a finite range of frequencies that are probed, while transitions that occur at higher frequencies lie outside the experimental range still influence the optical response of the material. These effects are included in the Lorentz model via the parameter ε_∞ and the dielectric function $\tilde{\varepsilon}_L(\omega)$ for the case of multiple oscillators reads

$$\tilde{\varepsilon}_L(\omega) = \varepsilon_\infty + \frac{ne^2}{\varepsilon_0 m_e}\sum_i \frac{f_i}{\omega_{o,i}^2 - \omega^2 - i\Gamma_{L,i}\omega}. \tag{5.10}$$

In Eq. 5.10, f_i is called oscillator strength, and accounts for the relative probability of quantum mechanical transition.

The Lorentz model is used to describe the optical response of metal films on insulators during initial growth stages. In the island-stage of film formation, the film supports *localized surface plasmon resonance* (LSPR), [40,129] i.e., electrons in the isolated islands are in-phase with the externally applied electric field, and move collectively. This induces an electric dipole locally that is opposing the external field. Owing to the dipole, a restoring force exits, and the resulting electron oscillation has a resonance frequency. The presence of the island surface and ions leads to damping of the oscillations. This resonance effect can be modelled with one Lorentz oscillator, with ω_0 and Γ. LSPR is described with a single oscillator as long as the island shape can be approximated by hemisphere, and island-island interactions are negligible, i.e., when the island spacing is larger than the interaction distance between the electric dipoles. [129]

Drude oscillator

The Drude model is based on Drude's free electron theory that describes ideal metals, i.e., metals in which the optoelectronic response is only determined by unbounded electrons. In the Drude model, conduction band electrons are free, i.e., no restoring force exists, and Eq. 5.7 is reduced to

$$m_e\frac{d^2x}{dt^2} = -m_e\Gamma_D\frac{dx}{dt} - e\vec{E}_0\exp(-i\omega t)\,. \tag{5.11}$$

The solution of Eq. 5.11 and treatment as for the Lorentz model give the dielectric function for the Drude model

$$\tilde{\varepsilon}_D(\omega) = \varepsilon_\infty - \frac{\omega_p^2}{\omega^2 + i\Gamma_D\omega}, \tag{5.12}$$

where $\omega_p = \sqrt{ne^2/(\varepsilon_0 m_e)}$ is the plasma frequency. [128] From ω_p and Γ_D, the film resistivity can be calculated as $\rho_{res} = \Gamma_D\varepsilon_0^{-1}\omega_p^{-2}$. A description of film growth with the Drude model is valid for percolated and continuous metal films. The time evolution of ρ_{res} can also be used to determine the continuous film formation thickness, since ρ_{res} is in a steady-state for continuous films, as illustrated in Fig. 5.4. [131]

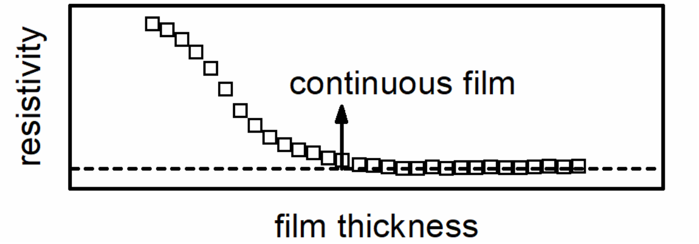

Fig. 5.4: Evolution of film resistivity vs. film thickness as determined from in situ spectroscopic ellipsometry using a Drude model to simulate a metal film. The continuous film formation thickness is indicated with a vertical solid arrow.

Spectroscopic ellipsometry measurements performed in course of this thesis work are performed and analyzed as follows:

- Loading of Si substrates (thickness $625\,\mu m$, i.e., semi-infinite) covered with thermally grown SiO_2, and measurement of Ψ and Δ as function of incident-light photon energy $\hbar\omega$.
- Fitting of $\Psi(\omega)$ and $\Delta(\omega)$ to three-phase model (i.e., vacuum/SiO_2/Si stack), in which the dielectric functions of SiO_2 and Si are taken from databases, [132] and incidence angle θ_i and SiO_2 layer thickness are fitting parameters. θ_i is fitted since it can vary from nominal incidence angle defined by the chamber geometry due to sample mounting and sample holder loading.
- Real-time measurement of $\Psi(\omega, t)$ and $\Delta(\omega, t)$ during film growth.
- Fitting of *in situ* data to model (i.e., vacuum/film/SiO_2/Si) where the film is simulated by a single Lorentz oscillator (accounting for LSPR in the island stage of film formation), and a Drude oscillator (accounting for ideal metal behavior in percolated and continuous films). Fitting parameters are f, ω_0, and Γ_L from the Lorentz term, ω_p and Γ_D from the Drude term, as well as ε_∞ and h_f.
- From the film thickness h_f vs. time t evolution, the deposition rate is determined as dh_f/dt, which is constant in continuous films.

In situ spectroscopic ellipsometry is employed in Papers III and IV, where the microstructural evolution of Ag films on SiO_2/Si substrate is investigated during growth in various Ag-N_2 and Ag-O_2 atmospheres, respectively. In Paper V, growth of AgCu films with various compositions is observed with *in situ* spectroscopic ellipsometry.

5.2.2. *Substrate curvature measurement*

Stress generation mechanisms during thin film growth are discussed in Chapter 4. The investigation of stress during growth is based on the substrate curvature technique, which measures changes in the curvature of a film-substrate system in real-time. When stress forms in the film, the stress is transferred to the substrate, which bends if the transferred force is large enough. Figures 5.5(a) and (b) show the conventional description of the substrate curvature: If the film is under compression, the substrate curvature κ is negative, and for tensile stress in the film, κ is positive.

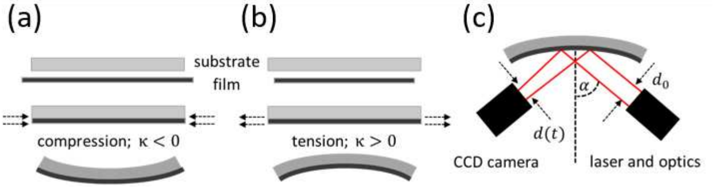

Fig. 5.5: Schematic illustration of the curvature (κ) change of the substrate (light grey) when the film (dark grey) is (a) under compressive stress and (b) under tension. (c) Schematic illustration of the substrate curvature technique; laser spots with spacing d_0 are reflected on the curved substrate (incidence angle α) and observed with a camera. If during film deposition stress forms in the film, the substrate curvature changes, and the measured spacing changes with time $d(t)$.

The substrate curvature is measured by tracing the spacing of a 3×3 array of laser spots (wavelength $658\,nm$), which are reflected off the substrate surface, with a CCD camera. A schematic illustration of the substrate curvature setup is presented in Fig. 5.5(c), where d_0 is the initial spacing, α is the incidence angle, and $d(t)$ indicates that the spacing changes with time t (i.e., during film deposition). The change in substrate curvature with time $\Delta\kappa(t)$ is calculated as

$$\Delta\kappa(t) = \frac{\Delta d(t)\cos(\alpha)}{d_0\,2L}, \tag{5.13}$$

where $\Delta d(t) = d(t) - d_0$, and L is the distance between substrate and camera.

For a correct application of the substrate curvature technique, the lateral dimensions of the substrate have to be large compared to substrate and film thickness, and the film thickness must be small ($< 1\%$) compared to the substrate thickness h_S. This is ensured by using $1 \times 1\,cm^2$ substrates, compared to $h_S \cong 100\,\mu m$ and film thicknesses in the nm range. Moreover, several hypotheses about the mechanical state of the film/substrate system apply: [133,134]

(i) The system has a neutral plane that is not deformed during bending of the substrate.
(ii) Only biaxial stress is observed, transversal stress is negligible.
(iii) The substrate is homogeneous and isotropic, and the film material is isotropic.
(iv) Linear elasticity can be applied.
(v) The observed curvatures are small.

As deposited films are very thin, transversal stresses are negligible, satisfying hypothesis (ii). Point (iii) is ensured by using Si(100) single-crystal substrates. Investigated films are pure metal films (Ag, Cu), which do not support large enough stresses to lead to conditions dissatisfying points (iv) and (v).

The relation between the change of the substrate curvature to film stress was developed by Stoney [135] and reads

$$\Delta\kappa = \frac{6\,\Delta(\bar{\sigma} \times h_f)}{Y_S h_S^2}, \tag{5.14}$$

where $\bar{\sigma}$ is the average film stress, h_f is the film thickness, and Y_S is the substrate biaxial modulus. In the original Stoney equation, the elastic modulus is used, which was later corrected by Hoffman. [136] This equation allows the determination of the change of the stress-thickness product $\Delta(\bar{\sigma} \times h_f)$, when the substrate properties Y_S and h_S are known. It is noted that $\Delta(\bar{\sigma} \times h_f)$ is equivalent to the force per unit width, which is used in figures in Chapter 4.

Equation 5.14 implies that only the average in-plane film stress is measured via the substrate curvature technique, i.e., no information about the lateral stress distribution is given. By defining $\bar{\sigma}$ as

$$\bar{\sigma} = \frac{1}{h_f}\int_0^{h_f} \sigma_{xx}(z)dz, \tag{5.15}$$

where σ_{xx} is the in-plane stress, the evolution of the stress with film thickness can be computed. Since the substrate curvature technique is used *in situ*, the stress evolution with time is given as

$$\frac{d(\bar{\sigma} \times h_f)}{dt} = \sigma_{xx}(h_f)\frac{dh_f}{dt} + \int_0^{h_f} \frac{\delta\sigma_{xx}(z)}{\delta t}dz. \tag{5.16}$$

The first term in Eq. 5.16 represents the stress formed in the topmost layer of the film, i.e., the *incremental* or *instantaneous* stress, while the second accounts for stress changes in the bulk of the film. When interpreting stress data that is acquired with the substrate curvature technique, Eq. 5.16 must always be considered, since changes in the stress state can result both from the top layer or the bulk of the film.

In practice, an *in situ* substrate curvature measurement gives $\Delta\kappa$ vs. t data. Former quantity is used to calculate the stress-thickness product with Eq. 5.14 (h_S is determined for each substrate after deposition), while the (nominal) film thickness is calculated from t with the deposition rate. This gives $\bar{\sigma} \times h_f$ vs. h_f data that is discussed in detail in Chapter 4.

The substrate curvature technique is used in Paper I to determine continuous film formation thicknesses of Ag and Cu films on amorphous carbon, as function of deposition rate and substrate temperature. The stress evolution of these film/substrate systems, determined from substrate curvature measurements, is discussed in Paper II. Paper VI presents the evolution of stress during the growth of Ag films in mixed Ar-N_2 atmospheres.

5.2.3. *Four-point-probe measurement*

The four-point-probe (4PP) measurement allows for determining the resistivity of a film/substrate system by measuring the voltage drop V between two probes on the sample surface, when applying an electric current I to two additional probes. If the placement of the four contacts is symmetric, and the sample is homogeneous and without holes, the van der Pauw theorem can be applied [137] and the film sample resistivity ρ is calculated as

$$\rho = \frac{\pi h_f}{\ln(2)} \frac{V}{I}. \tag{5.17}$$

The term $\pi/\ln(2)$ in Eq. 5.17 is a geometric correction factor that accounts for the finite sample thickness, the probe position with respect to the sample edge, and the finite lateral size of the sample. [137] Forming the sheet resistance $R_S = \rho/h_f$, a sample-independent parameter is provided, i.e., sheet resistance data of samples with the same geometry can be easily compared.

Measuring the electrical resistivity of a growing film allows for obtaining information about the film morphological evolution, e.g., when depositing a conductive material onto insulating substrates, a characteristic resistivity drop can be seen when the film becomes macroscopically conductive, i.e., at the *percolation thickness*. For such investigations, a load-lock compatible system for 4PP measurements was developed by Colin *et al*. [56] (see Fig. 5.6(a)) that measures the sheet resistance of the film/substrate system *in situ* and in real-time. The sample holder of the system is presented in Fig. 5.6(b), which also shows the mask that protects electric contacts from film deposition. Prior to sample mounting, gold contacts are deposited onto the silicon substrate with a titanium adhesion layer, to ensure a uniform contact during measurement. These contacts can be square ($2.5 \times 2.5\ mm^2$) or rectangular ($2.5 \times 10\ mm^2$), which does not affect the quality of the measurement (in case of rectangular contacts, one voltage and one current probe is placed on each contact). [56]

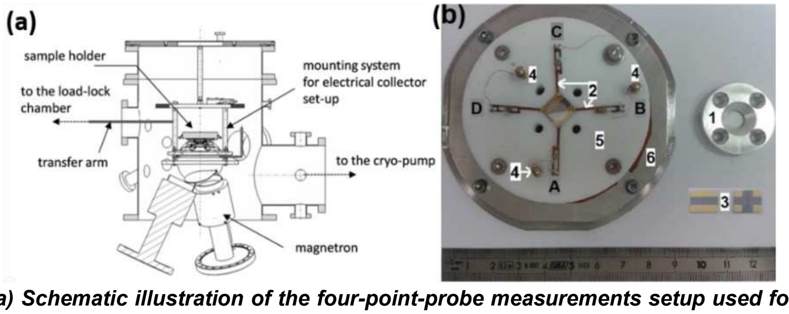

Fig. 5.6: (a) Schematic illustration of the four-point-probe measurements setup used for in situ resistivity measurement in a high-vacuum deposition chamber. (b) Sample holder used for the four-point-probe measurement. A mask (1) protects the copper contacts (2) that hold the substrate in place. Four squares or two gold stripes (3) are deposited onto substrates prior to film deposition that act as ohmic contacts. Copper contacts are connected to vertical silver rods on springs (4) that transfer current/voltage to the mounting system. The sample holder is mounted on a Teflon insulating plate (5) that is fixed onto the base (6). Reprinted with permission from Ref. [56]***.***

Figure 5.7 presents data obtained from *in situ* 4PP measurements during Ag film growth on SiO2 substrates, where h_f is calculated by multiplying time with the deposition rate. Plotting R_S vs. h_f in logarithmic scale (see Fig. 5.7(a)) shows a sudden drop by several orders of magnitude from high R_S, which corresponds to the percolation of the film. This characteristic thickness is obtained more accurately from $R_S \times h_f$ vs. h_f data (see Fig. 5.7(b)), which starts at zero for $h_f = 0\,nm$. [56] Furthermore, the thickness at which a continuous film is formed can be, theoretically, determined from the minimum of the R_S vs. h_f data (compare to resistivity vs. film thickness data in Fig. 5.4, obtain from *in situ* spectroscopic ellipsometry). However, this is not possible with the setup used in the present work due to insufficient signal-to-noise ratio.

In situ 4PP measurements are presented in Paper I, where they are used to determine percolation thicknesses of Ag and Cu films on amorphous carbon, as function of deposition rate and substrate temperature.

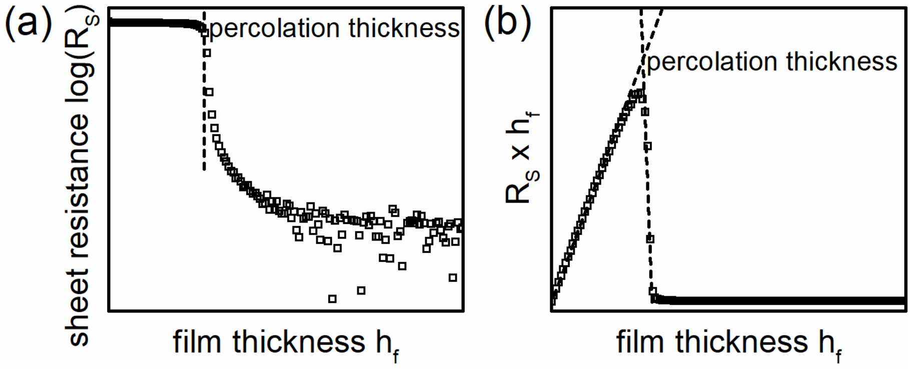

Fig. 5.7: Evolution of (a) sheet resistance R_S and (b) sheet resistance-film thickness product $R_S \times h_f$ vs. film thickness h_f for deposition of Ag on amorphous carbon/SiO2 substrate. The percolation thickness is indicated with vertical lines.

5.2.4. *Residual gas analysis*

Residual gas analysis is a technique that allows the determination of the composition of the chamber atmosphere at base pressure or during film deposition. Former measurement is of interest, as contamination from the background pressure can lead to changes in the film morphology, and latter is used to determine the species in the plasma, and the ratios of working gases, if several gases are used (e.g., argon and nitrogen, argon and oxygen).

Every residual gas analyzer (RGA) consists of three parts, the ionization unit, the mass filter, and the detector. Ionization of gas molecules is needed, since mass filtering is performed in electric fields (i.e., neutral species cannot be distinguished), as well as increasing the sensitivity of the measurement. [21] Gas molecules are typically ionized via collision with electrons that are created in a cathode (ionization process $e^- + A \rightarrow A^+ + 2e^-$). This ionization process is one source for measurement errors, since collision cross-sections of gas molecules and electrons depend on the gas species, [21] i.e., ionization of species with small cross-sections is less probable, which leads to an under-representation of these species in the detected signal.

The positive ions are then accelerated toward the mass filter, which filters ions with respect to their mass-to-electric charge ratio M/z. Figure 5.8(a) illustrates a quadrupole mass filter. When passing through the positively charged electrodes (direct current (DC) potential $U > 0$), a positive ion has a stable trajectory (Fig. 5.8(b)); this trajectory is destabilized when applying an additional radio frequency (RF) potential $Vcos(\omega t)$, with $V > U$, to the electrodes (Fig. 5.8(c)). Ions with small M/z values are deflected by the Lorentz force created due to the resulting potential $U + Vcos(\omega t)$ and do no pass the filter (i.e., ions collide with electrodes), while ions with large M/z values pass, i.e., the positively charged electrodes act as high-pass filter (Fig. 5.8(d)).

A positive ion is attracted by the negatively charged electrodes (DC potential $-U$) and does not pass the quadrupole filter (Fig. 5.8(e)). When superposing the RF potential $Vcos(\omega t)$, ions with small M/z values pass the filter (Fig. 5.8(f)), i.e., the negatively charged electrodes act as low-pass filter. As only ions that pass both filters are detected, the quadrupole is a band-pass filter. Ions that pass the mass filter are detected in an ion current detector (comparable to ion gauges described in Chapter 2). Different M/z are probed by sweeping the DC and RF potentials linearly in time. Trajectories in Fig. 5.8 are simplified, in reality, the superposition of the electric fields leads to helical trajectories. [21]

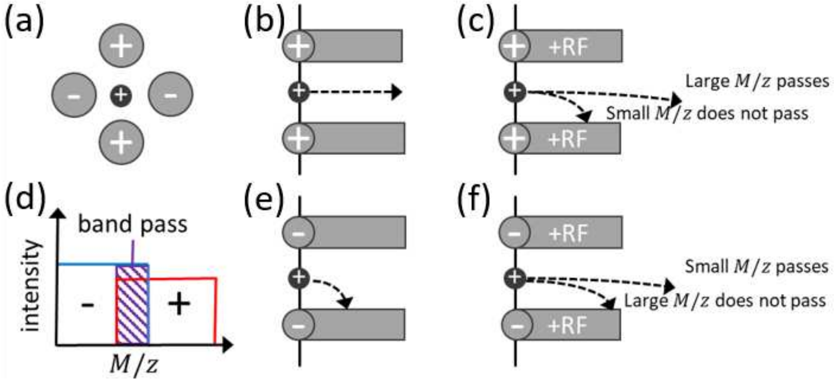

Fig. 5.8: Schematic illustration of a quadrupole mass filter, (a) that consists of two pairs of electrodes at positive and negative direct current (DC) potential. Trajectories of positive ions due to (b) positive DC potential and (c) superposed radio frequency (RF) potential, which depend on mass-to-electric charge ratio M/z. (d) Signal measured at the detector as function of M/z; the positive electrodes act as low-pass filter and the negative electrodes act as high-pass filter. Trajectories of positive ions due to (e) negative DC potential and (f) superposed RF potential.

Residual gas analysis was performed to determine the composition of the atmosphere at base pressure in both deposition chambers, an example for the species present in the UHV chamber at base pressure is presented in Fig. 5.9. The background pressure is created by hydrogen (H_2), carbo-hydrides (CH_x), traces of water (H_2O), carbon monoxide (CO), and dioxide (CO_2). Analysis in the HV-regime gives a similar result, with water as the most prominent constituent of the gas. In paper VI, this technique is used to determine the partial pressure of N_2 in a mixed Ar-N_2 working gas.

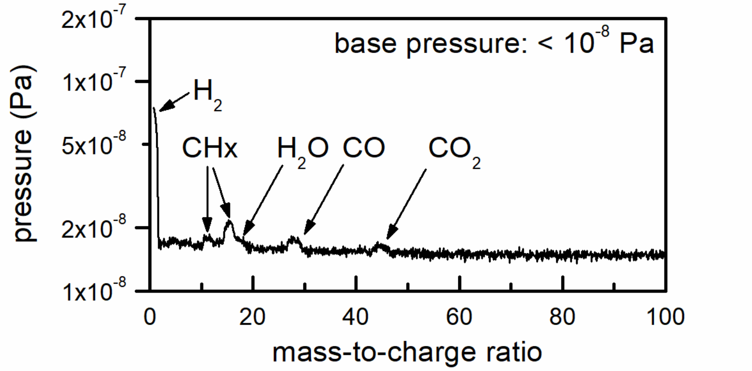

Fig. 5.9: Gas species detected in the ultra-high vacuum chamber at base pressure via residual gas analysis.

5.3. *Ex situ* characterization

Ex situ techniques described in this section were used for characterizing films with respect to their surface morphology, crystallography, and chemical composition, to better understand and analyze *in situ* obtained data. This is achieved by probing films with ultra-sharp tips (Section 5.3.1), electrons (Sections 5.3.2 through 5.3.4), x-rays (Sections 5.3.5 through 5.3.8), and ions (Section 5.3.9).

Prior to *ex situ* characterization, great care was taken to minimize changes in the film due to interaction with the atmosphere (e.g., oxidation, surface restructuring). This was obtained by depositing amorphous carbon capping layers onto films, before subjecting them to the atmosphere, and by performing measurements shortly after unloading, where possible. Carbon was chosen, because it does not have any chemical affinity to investigated silver and copper films, while its amorphous nature does not interfere with characterization techniques that investigate the film crystallography.

5.3.1. *Atomic force microscopy*

Atomic force microscopy (AFM), which belongs to the family of scanning probe microscopies, allows for real-space investigation of the surface topography of condensed matter. [138] Its principle setup is illustrated in Fig. 5.10(a). The electrostatic and van der Waals forces between the surface atoms of the probed material and a sharp tip lead to a deflection of the cantilever on which the tip is mounted. A laser is reflected on the backside of the cantilever, for measuring its deflection. Cantilever and tip are typically micromachined from silicon. [4] A surface topographical map is acquired by moving the cantilever over the sample surface with the help of piezoelectric crystals that are connected with the cantilever. The surface topography is typically presented in color maps (see Fig. 5.10(b)), and used to image the surface in real space.

Three measuring methodologies exist for AFM: [4] In contact-mode AFM, the tip is in close proximity to the surface, such that electrostatic repulsive forces from overlapping electron clouds lead to cantilever deflection. In non-contact-mode, the tip oscillates $1-10\ nm$ from the sample surface. At such distances, van-der Waals forces attract the tip, which leads to changes in vibrational amplitude and resonance frequency. Tapping-mode is a combination of these two modes, where the amplitude of the cantilever oscillation leads to surface contact. AFM measurements presented in this work were performed in tapping-mode. The surface profile is obtained by keeping the tip-surface distance, the force on the tip, or the oscillation amplitude/frequency constant, which performed via a control loop between detector and piezo crystals.

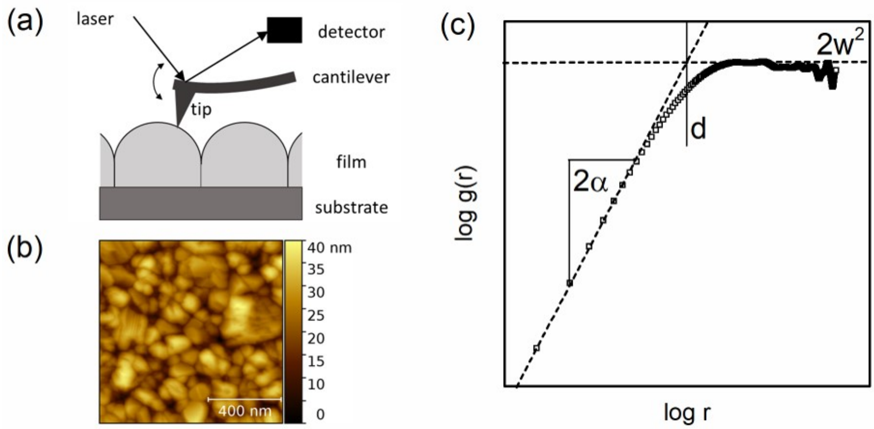

Fig. 5.10: (a)Schematic illustration of an atomic force microscopic measurement in tapping-mode. A sharp tip is mounted on a cantilever and interacts with the film surface. This leads to bending of the cantilever, which is detected by tracing the position of a laser spot that is reflected on the cantilever. (b) Surface profile of a silver thin film, height is represented in false color scale. (c) Evolution of height-height-correlation function $g(r)$ vs. lateral distance r. From this data, the roughness scaling factor α, lateral feature size d and root-mean-square surface roughness w can be determined.

For quantitative analysis of AFM images, the height-height correlation function $g(\vec{r}) = \langle [h(\vec{x}+\vec{r}) - h(\vec{x})]^2 \rangle$ is determined, [139] where $h(\vec{x})$ is the surface height at a position $\vec{x} = (x, y)$ on the surface, $\vec{r}$ is a displacement vector, and $\langle \ldots \rangle$ denotes the statistical average over the entire surface. In Fig. 5.10(c), $g(\vec{r})$ vs. $\vec{r}$ data of the AFM image in Fig. 5.10(b) is presented. For small values of $\vec{r}$, $g(\vec{r}) \sim r^{2\alpha}$, where α is the roughness scaling exponent, while $g(\vec{r}) = 2w^2$ for large values of $\vec{r}$, where $w = \langle [h(\vec{x}) - \bar{h}]^2 \rangle^{1/2}$ is the root-mean-square surface roughness ($\bar{h}$ is the average surface height). These limits are indicated in Fig. 5.10(c); at the intersection of the limit functions, the correlation length d is defined, which corresponds to the average lateral feature size of objects present at the surface. Analysis of α, w and d with respect to growth time (i.e., film thickness), allows drawing conclusions about the evolution of the growth front, e.g., whether in-plane of out-of-plane growth is prominent. [140]

Surface topography images and analysis thereof of Ag and Cu films deposited at various deposition rates and substrate temperatures are presented in Papers I and II. Analysis of Ag films deposited in various working gas atmospheres (Ar and Ar-N_2) is presented in Paper VI.

5.3.2. *Scanning electron microscopy*

Scanning electron microscopy (SEM) is used for imaging the surface of a sample by probing it with an electron beam that is moved over the sample (i.e., the sample is scanned). Primary (i.e., beam) electrons have energies in the range of a few to tens of keV, i.e., the primary electron beam is created by accelerating electrons toward the sample in a kV-potential difference. Electron-matter interactions lead to emission of electrons and x-rays from the sample, which can be detected, and give information about the sample chemistry and topography. Figure 5.11(a) presents the teardrop-shaped volume from which emission stems. [4] The emission volume has a lateral size of $\sim 10\,nm$ (i.e., the lateral resolution of SEM) and is larger than the primary electron beam ($\sim 1\,nm$ diameter).

Secondary electrons are created by inelastic scattering when primary electrons interact with the sample electrons in the near-surface region ($\sim 1\,nm$ depth), and have low energies in the eV-range (see Fig. 5.11(b)). As secondary electrons stem from the near-surface region, their intensity is strongly influenced by the surface topography of the sample, as illustrated by Fig. 5.11(c). If the primary electron beam hits the surface with a high incidence angle, a larger portion of the interaction volume is close to the surface, and more secondary electrons are emitted. Backscattered electrons are created by elastic scattering and have energies that are close to primary electrons. The probability of backscattering increases with the atomic number of the sample material, i.e., a compositional contrast can be observed from backscattered electron images, however, quantitative chemical analysis is not possible. Diffraction of backscattered electrons is used for microstructural analysis (see Section 5.3.4).

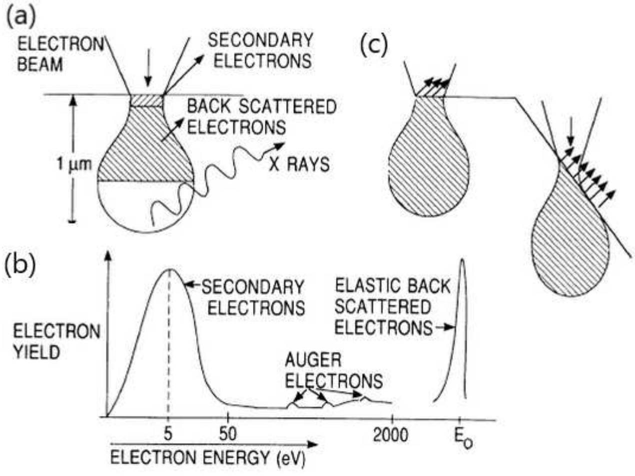

Fig. 5.11: (a) Interaction volume of matter with electron beam from which electrons and x-rays are emitted. (b) Energy distribution of emitted electrons as function of emission process. (c) Effect of surface topography on the emission of electrons. Reprinted with permission from Ref. **[4].**

Electron-matter interactions lead to further emission processes that are not used for imaging purposes, and they are briefly outlined in the following: The collision of primary electrons in the sample can cause vacant electronic states in the inner electron shells, which outer-shell electrons can occupy. The energy that is released by this relaxation is emitted in form of x-rays that have characteristic energies for the relaxation process, i.e., these x-rays can be used for chemical analysis (see Section 5.3.8 for more details). In some cases, the relaxation can instead lead to the emission of an outer-shell electron (i.e., *Auger* electron), which can be used for compositional analysis due to characteristic energy levels.

SEM imaging is performed on discontinuous Ag and AgCu films on SiO_2/Si substrates to determine lateral island sizes, island size distribution and substrate area coverage in Papers IV and V, respectively.

5.3.3. *Transmission electron microscopy*

If an electron beam interacts with a thin sample, the attenuation by the sample is weak, and the electron beam is partially transmitted. In transmission electron microscopy (TEM) the transmitted electron beam is analyzed. Compared to SEM, higher acceleration voltages are applied in TEM (hundreds of kV), and sample preparation is essential (sample thickness $< 100\,nm$). [4,141] Electrons can be scattered elastically by the ion cores of the sample, which gives information about the film thickness, elemental composition, and crystal structure. Latter stems from diffraction of electrons at crystallographic planes. Inelastic scattering occurs on microstructural features on the sample (e.g., grain boundaries, pores, dislocations., and defects), which leads to local intensity fluctuations.

During *bright field imaging,* the central electron beam is observed, while all diffracted beams are excluded by placing apertures in the back focal plane of the objective lens. With this imaging mode, the sample microstructure can be investigated. *Dark field imaging* is better suited to observe local crystallographic features (e.g., dislocations), as the intensity of one diffracted electron beam is analyzed. When analyzing the electron intensities at the back focal plane, microdiffraction patterns are observed (i.e., *selected area electron diffraction* SAED), which give information about the local structural features (e.g., lattice orientation). In this case, TEM is used as an analytical instrument.

TEM is a powerful tool for analysis at the nanoscale, since it has a lateral resolution in the sub-nm range. Limitations are caused by the quality of electron lenses, which cause aberration; modern electron microscopes are aberration-corrected. [141] For the analysis of thin films, cross-sectional TEM (XTEM) can be performed, i.e., the film is imaged perpendicular to its growth direction. This gives information about the film morphology as function of the film thickness, e.g., close to the film/substrate interface, and the surface.

Plan-view TEM images of discontinuous Ag films deposited onto electron-transparent SiO_2 grids are presented in Paper III, from which island size and distance distributions are determined. XTEM and SAED are used to analyze continuous Ag films deposited in Ar and Ar-N_2 atmospheres in Papers III and VI.

5.3.4. *Electron backscatter diffractometry*

Electron-matter interactions lead to incoherent scattering of an electron beam in the sample. These incoherent scattering processes are sources of electrons within the sample, and electrons that are scattered toward the sample surface (i.e., backscattered), may be scattered coherently by the crystal lattice before reaching the surface, carrying information about the sample crystal structure. Electron backscatter diffractometry (ESBD) is a technique that analyses the resulting diffraction patterns. [142] Electrons that are elastically scattered in a three-dimensional crystal lattice travel along trajectories that form a pair of cones (i.e., Kikuchi or Kossel cones) with an axis that is perpendicular to the diffracting plane, and an opening angle that is related to the Bragg diffraction angle (see Fig. 5.12(a) for geometry, and Section 5.3.5 for more detailed information about diffraction). Imaging of this electron beam on a planar detector leads to hyperbolical bands of intensity known as *Kikuchi bands*. Each crystallographic orientation leads to specific bands (i.e., defined by cone axis and opening angle), and the intersection of Kikuchi bands on the detector is used for the analysis on the EBSD data (Fig. 5.12(b)). By comparing Kikuchi band widths and intersections to computed data for ideal crystal lattices, the crystal orientation of the probed volume can be attributed. By scanning the primary electron beam over the sample surface, grain orientation maps can be created, from which grain sizes can be determined.

EBSD maps of Ag and Cu films deposited at various deposition rates and substrate temperatures are presented in Paper II, where they are used to determine lateral grain sizes and orientations. In Paper VI, EBDS maps of Ar- and Ar-N_2-grown Ag films are presented for grain size and orientation analysis.

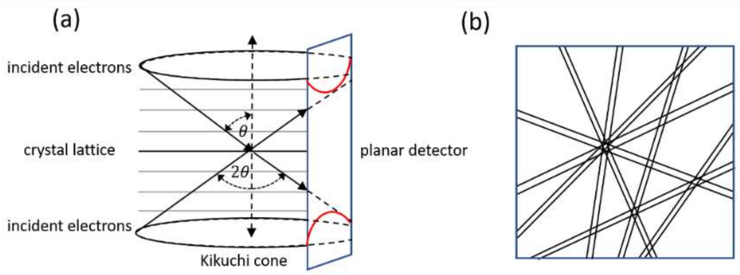

Fig. 5.12: (a) Creation of Kikuchi cone (with opening angle θ) during electron diffraction in a three-dimensional crystal lattice, and formation of Kikuchi bands on a planar detector. (b) Schematic illustration of signal detected via electron backscatter diffractometry of a polycrystalline sample. Bands do not appear hyperbolical due to small detector size.

5.3.5. *X-ray diffractometry*

Diffraction is a phenomenon that occurs when photons interact with structures that have sizes comparable to the photon wavelength λ. Microstructural features of condensed matter (e.g., the lattice parameter in crystals) are typically in the sub-nm range and can therefore be analyzed by photons with wave lengths in this range, i.e., x-rays. In x-ray diffractometry (XRD) photons are created in metal anodes (typically copper anode; $\lambda = 0.154\,nm$), interact with a sample, and are detected after scattering. Elastic scattering of x-rays in randomly ordered matter, or matter with only short-range order (i.e., amorphous materials), leads to destructive interference. Concurrently, in materials with long-range order, scattering on parallel planes of atoms can lead to constructive interference.

The long-range order in crystalline materials can be described by unit cells, which are defined by the lengths a, b, c of the unit cell axes, and angles α, β, γ between the b and c, a and c, and a and b axes, respectively. The complete crystal lattice is formed by translating the unit cell in all three dimensions. For cubic lattices that are discussed in this work, $a = b = c$, and $\alpha = \beta = \gamma = 90°$. Miller indices hkl define planes and positions in the unit cell; in a cubic lattice with the lattice parameter a, the spacing d_{hkl} of the plane (hkl) is calculated as

$$d_{hkl} = \frac{a}{\sqrt{h^2 + k^2 + l^2}}. \tag{5.18}$$

The crystal symmetry can also be described in the reciprocal space, where each plane corresponds to a reciprocal vector with norm $2\pi d_{hkl}^{-1}$ that is orthogonal to the real-space plane. [142,143]

Let $\vec{k}$ and $\vec{k}'$ be the wave vectors of incident and scattered photons, respectively, where $|\vec{k}| = |\vec{k}'| = 2\pi\lambda^{-1}$, and θ the angle between the wave vectors and the surface of the reflecting sample (see Fig. 5.13). Then, the scattering vector $\vec{Q} = \vec{k}' - \vec{k}$ has the norm $4\pi\lambda^{-1}\sin(\theta)$ and is orthogonal to the plane. Scattering occurs on a plane, when the scattering vector is equal to the reciprocal vector, i.e., $4\pi\lambda^{-1}\sin(\theta) = 2\pi d_{hkl}^{-1}$. Rearranging this equation gives the condition for Bragg diffraction $2d_{hkl}\sin(\theta_B) = \lambda$, where θ_B is the Bragg diffraction angle. [142,143]

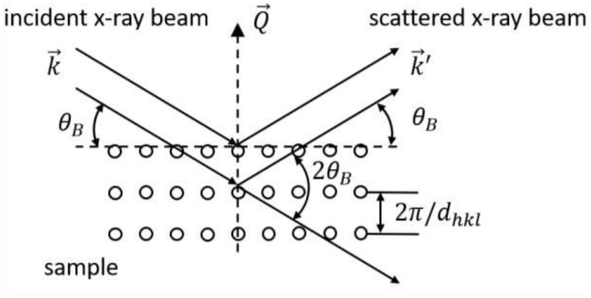

Fig. 5.13: Bragg diffraction of an incident x-ray beam on a crystalline sample in the reciprocal space.

Bragg's law describes at which angles diffraction peaks can be expected. The intensity of peaks depends on further parameters, most importantly on the structure factor F that depends on the position of atoms within the unit cell. If the unit cell contains multiple atoms, scattering of photons on different atoms in the unit cell can lead to destructive interference. The structure factor for the (hkl) plane is calculated as

$$F_{hkl} = \sum_j f_j \exp(2\pi i [hu_j + kv_j + lw_j]), \tag{5.19}$$

where j is the number of atoms in the unit cell, f_j are atomic scattering factors, and u_j, v_j, w_j denote the position of the atom j in the unit cell. The effect of F can be illustrated by the face-centered cubic (fcc) lattice of silver (or copper), where $j = 4$, and $f_j = f$ for all atoms. Atom positions are $\langle 0,0,0 \rangle$, $\left[\frac{1}{2}, 0, \frac{1}{2}\right]$, $\left[\frac{1}{2}, \frac{1}{2}, 0\right]$, and $\left[0, \frac{1}{2}, \frac{1}{2}\right]$, i.e.,

$$F_{hkl} = f \times [1 + \exp(\pi i [h + l]) + \exp(\pi i [h + k]) + \exp(\pi i [k + l])]. \tag{5.20}$$

Equation 5.20 gives $F_{hkl} = 4f$ for planes in which h, k, and l are all even (including 0) or uneven, and $F_{hkl} = 0$ for planes with mixed h, k, l, e.g., the 100 reflection is forbidden, while the 111 can be measured.

In a powder sample, the Bragg condition can be fulfilled by planes with different (hkl) at the same time; for cubic crystals this is the case as long as $h^2 + k^2 + l^2$ gives the same result, e.g., (111) and (-111) planes. Not all planes have the same representation within the unit cell, e.g., in the fcc lattice, eight planes of the $\{111\}$ family exist, while the $\{100\}$ family only has six, i.e., the intensity the 111 peak will be higher. The multiplicity factor accounts for this difference.

The derivation of the diffraction condition is only valid in an infinite crystal lattice. If the crystal size is finite, intensity peak broadening can be observed, i.e., with decreasing crystal size, the width of diffraction peaks increases. Peak broadening is also affected by microstrain in the crystallites. Determining the full-width-at-half-maximum ($FWHM$) of diffraction peaks allows estimating the size L of coherently diffracting domains in the sample via $FWHM = K\lambda/(L\cos(\theta_B))$. [144] K is a constant that accounts for the crystallite shape, and is close to unity (typically $K = 0.9$ is chosen). Note that this equation (known as Scherrer's equation) neglects microstrain, so it gives a lower limit of crystallite size.

For determination of the $FWHM$, experimental data can be fitted to mathematical models. [145,146] The Cauchy-Lorentz distribution function describes peak broadening due to the finite crystallite size well, while the Gauss distribution function is well suited to describe peak broadening due to local lattice parameter changes (i.e., microstrain). A convolution of these two functions is used in the Voigt distribution function; the Pseudo-Voigt function is a linear combination of Cauchy-Lorentz and Gauss distribution, which is easier to implement mathematically. [145]

XRD measurements presented in publications related to this thesis are performed in Bragg-Brentano geometry, i.e., x-ray source and detector are at fixed distance from the sample (see Fig. 5.14(a)). In $\theta/2\theta$ measurements, the scattering vector is always perpendicular to the sample surface, i.e., only crystal planes that are parallel to the substrate surface are probed. This is achieved by rotating source and detector by angles θ and $-\theta$, respectively, while the sample position is fixed, or by rotating sample and detector by θ and 2θ, respectively, while the x-ray source remains at fixed position.

A typical x-ray diffractogram of a silver thin film is presented in Fig. 5.14(b). Within the experimentally probed diffraction angles 2θ, two intensity maxima are observed, while the intensity is small for other angles (i.e., instrumental background). If peak positions correspond to reference peak positions obtained from powder diffraction samples, [147] the diffraction pattern can be attributed to a phase. Comparison of the integrated intensities I_{hkl} of measured peaks to the intensities $I_{hkl.0}$ of the reference data gives information of *texture* in the film, i.e., an overpopulation of certain crystallographic orientations with respect to the measurement geometry. The texture coefficient $TC(hkl)$ is calculated as

$$TC(hkl) = \frac{I_{hkl}/I_{0,hkl}}{\frac{1}{N}\sum_N I_{hkl}/I_{0,hkl}}, \tag{5.21}$$

where N is the number of considered diffraction peaks. $TC(hkl) = 1$ if the hkl orientation is represented as in a powder sample, $TC(hkl) > 1$ signifies an overpopulation, and $TC(hkl) < 1$ an underpopulation.

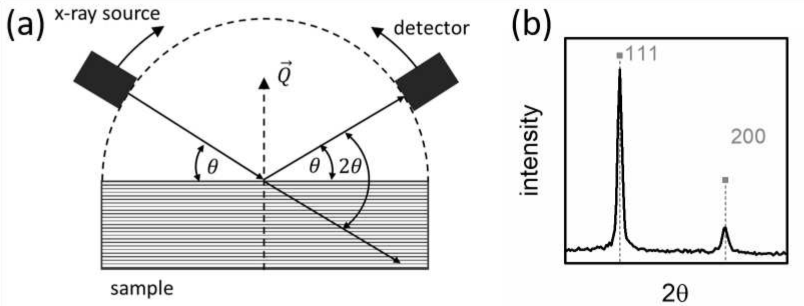

Fig. 5.14: (a) X-ray diffraction measurement in Bragg-Brentano geometry. In a $\theta/2\theta$ measurement, the scattering vector $\vec{Q}$ is perpendicular to sample surface, while x-ray source and detector rotate. (b) Schematic x-ray diffractogram of a silver thin film. The peak positions and relative intensities of 111 and 200 planes in a reference powder sample are indicated.

XRD measurements are performed on Ag thin films to determine texture and crystallite sizes in papers III through VI.

5.3.6. *X-ray reflectometry*

X-ray reflectometry (XRR) is an x-ray based characterization technique that allows determination of sample density and surface roughness, and, in case of supported thin films, also film thickness and interface roughness, by fitting reflectivity vs. scattering angle data to a mathematical model. [148] Figure 5.15 outlines schematically the geometry during an XRR measurement: The incident beam is reflected on the sample surface and partially transmitted into the sample. In case of a homogeneous sample, the transmitted photons are absorbed by the sample and lost for analysis. If a film/substrate system is measured, photons are reflected at the film/substrate interface and can be detected. The nature of interference between directly reflected photons and photons that were reflected at the interface depends on the film thickness h_f and the scattering angle θ. [148]

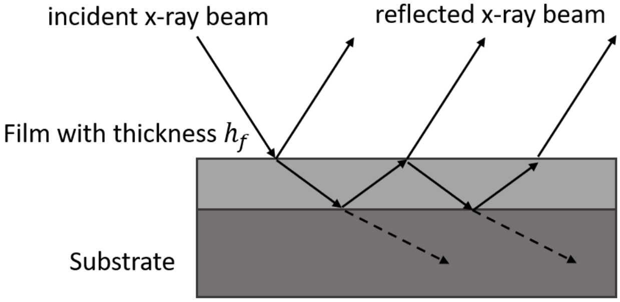

Fig. 5.15: Reflection of an x-ray beam from the surface of a thin film and from the film/substrate interface.

Figure 5.16 presents reflectivity vs. scattering data for bulk and thin film samples that was modeled. Three general regimes can be observed in the bulk model (see Fig. 5.16(a); bulk material is silver): (i) For $\theta < \theta_{crit}$, where θ_{crit} is the critical angle, total external reflection occurs, (ii) for $\theta > \theta_{crit}$, a decrease in intensity is observed, and (iii) for $\theta \gg \theta_{crit}$, a constant, very small reflectivity is measured, which corresponds to the background signal of the instrument. The critical angle is proportional to the square-root of the sample mass density. With increasing surface roughness, the intensity of the reflected beam decreases faster with scattering angle since more photons are lost to random scattering (compare surface roughness $w = 2\,nm$ vs. $1\,nm$ Fig. 5.16(a)).

The presence of a film and the resulting multiple reflections at the film/substrate interface alters the XRR signal considerably. Figures 5.16(b) and (c) present reflectivity curves for Ag/SiO$_2$ stacks. We note that the θ_{crit} strongly depends on the film material, while the substrate has a weaker influence (compare positions of θ_{crit} in Fig. 5.16(a) and (b)). Fringes in the reflectivity data are a result of the constructive (local maxima) and destructive (local minima) interference of photons that are reflected at the surface and interface. Surface roughness leads to loss of coherency of photons, and fringes are not visible at high scattering angles; with increasing surface roughness, this fringe-diminution appears at lower scattering angles (Fig. 5.16(b)). From the distance of the local maxima, the film thickness can be determined, i.e., fringes are closer to one another for thicker films (Fig. 5.16(c)).

For multilayer systems, intensity fluctuations of multiple interfaces overlap and create a complex pattern, however, data can be modelled with film density, film thickness, and interface roughness as fitting parameters. [149] This allows non-destructive measurement of these parameters, which is of great interest in materials research and quality control.

XRR is used in all papers related to this thesis. In Papers I, II and VI film thicknesses determined by XRR are used to calculated/verify deposition rates. In Papers III through V, XRR is used to verify film thicknesses determined by spectroscopic ellipsometry and calculate film densities and surface/interface roughness.

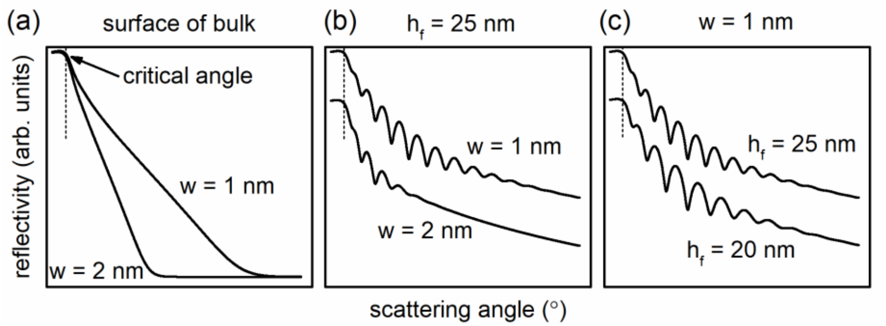

Fig. 5.16: Evolution of the reflectivity with scattering angle for (a) a bulk silver surface with surface roughness w, (b) a silver thin film with film thickness $h_f = 25\ nm$ and varying values of w, and (c) a silver thin film with $w = 1\ nm$ and varying values of h_f. Films are modeled on silicon dioxide substrate ($w = 0.1\ nm$), the critical angle of the models is indicated. Curves in (b) and (c) are shifted vertically for clarity.

5.3.7. *X-ray photoelectron spectroscopy*

The interaction of photons with matter can lead to emission of electrons (i.e., *photoelectrons*). X-ray photoelectron spectroscopy (XPS) analyses the kinetic energies of the emitted electrons, gaining information about the electron bonding state, i.e., XPS is a spectroscopic technique for chemical analysis (see schematics in Fig. 5.17). [150,151] Since only electrons from the near-surface region can leave the probed sample, it is a surface-sensitive technique (analysis depth in the nm-range).

The kinetic energy E_k of the photoelectron is the quantity that is measured in XPS, and it relates to the energy of the incident x-ray photon $\hbar\omega$ as [151]

$$E_k = \hbar\omega - E_B - \phi - \delta E. \tag{5.22}$$

In Eq. 5.22, the binding energy E_B is the quantity of interest in an XPS measurement, as it gives information about the local surrounding of the atom that the photoelectron was emitted from. ϕ is the spectrometer work function, an instrument constant that is known, and δE accounts for electrostatic charging of the sample surface, which is of importance for analysis of electrically insulating samples. Charging can be observed in the XPS data, since it affects all XPS peak uniformly, i.e. it is corrected by comparing the position of a known peak to its reference position found in databases.

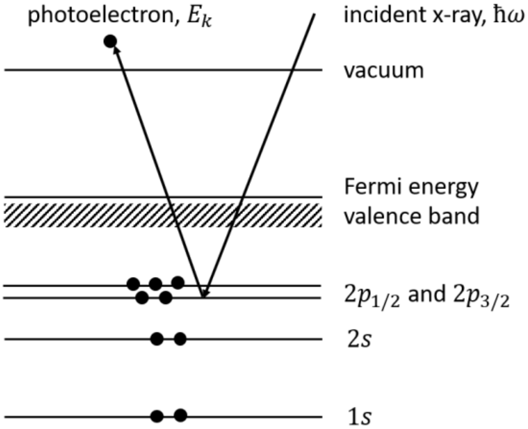

Fig. 5.17: Schematic illustration of the photoelectron emission process: Interaction of a photon with energy $\hbar\omega$ with the sample leads to emission of an electron with kinetic energy E_k. Note spin orbital splitting in the p orbital.

Binding energies of electrons depend on the attraction of the positive ion cores in their vicinity. Compared to the elemental binding state, E_B increases if a stable compound is formed, and it decreases if the compound is metastable. If binding states are mixed (i.e., elemental and compound, or different compounds), XPS peak positions of these binding states overlap, and peaks have to be deconvoluted.

Interpretation of compound binding states is facilitated, since the change in E_B must be observable in XPS peaks of all elements that constitute the compound. When using XPS for chemical analysis, a detection limit of $\sim 0.1 - 1\,at.\%$ can be expected, where the upper limit is valid for light elements with few electrons. [4]

Spin orbital splitting occurs in all electron orbits except the s electrons. The spin states $+1/2$ and $-1/2$ lead to differences in E_B, i.e., XPS peak doublets are observed for these orbitals. For analysis, this is important when XPS peak broadening is larger than the E_B difference due to spin orbital splitting, and the doublet peaks overlap. A secondary loss feature of photoelectrons is plasmon losses induced by the collective movement of the electron cloud in the conduction band. Plasmon loss peaks are observed at energies higher than E_B.

XPS is used in Paper II to determine the concentration of contamination from the background pressure in the deposition chamber. In Papers III, IV and VI, concentration of gaseous species that are employed as surfactants is measured, and in Paper V, the composition of AgCu films that was determined from EDS measurements is verified.

5.3.8. *Energy-dispersive x-ray spectroscopy*

As mentioned in Section 5.3.2, x-rays are emitted from a sample when electrons from an outer shell fall into inner shells. The energy of the emitted photons is a fingerprint for the emitting atoms, i.e., by detecting the x-rays, chemical analysis is possible. Energy-dispersive x-ray spectroscopy (EDS) is often integrated in SEM, since the interaction of primary electrons with the sample, which is usually used for imaging, also creates x-rays, i.e., no additional instrument is needed. X-rays are detected in a Si(Li) photodetector, where they create electron-hole pairs in the depleted area of the reverse biased Si diode, which is detected as a voltage pulse. [4] Si(Li) detectors have an energy resolution of $\sim 150\ eV$, which leads to the overlap of peaks in EDS spectra. The detection limit of elements is $\sim 0.1\ at.\%$. [4] X-rays stem from $\sim 1\ \mu m$ depth of the probed sample (see Fig. 5.11(a)), i.e., EDS is not very suitable for the analysis of thin films, however, it is used for qualitative analysis of the film composition.

EDS is used in Paper V to estimate the composition of AgCu films.

5.3.9. *Secondary ion mass spectrometry*

The principle of mass spectrometry was described in Section 5.2.4 for residual gas analysis. In secondary ion mass spectrometry (SIMS), an ion beam bombards the surface of a sample, which leads to the emission of neutrals and ions via sputtering processes, and once in the gas phase, ions are analyzed with respect to their mass-to-electric charge ratio M/z. [4] In time-of-flight SIMS (ToF-SIMS), M/z is determined by measuring the time that ions need to travel a defined distance. Since only sputtered ions are detected, SIMS is a surface sensitive technique with an analytical depth in the nm-range.

SIMS has an extremely low detection limit of $\sim 10^{-4}\ at.\%$, and is the most powerful characterization tool utilized within this thesis. A quantitative analysis of SIMS data is however only possible if a reference with known composition, and same morphological features (grain size, orientation, roughness) as the studied sample is available. This limitation arises from the sputtering process that is the source of ions that are analyzed, and highly dependent on the sample morphology.

SIMS measurements are presented in Paper III, where it is used to detect very low concentrations of nitrogen-containing species in Ag films that are deposited in Ar-N_2 atmosphere.

6. Computer simulations

Computer simulations are used in materials science to better understand the correlation among atomic-scale processes (i.e., processes stipulated by theoretical models) and macroscopic attributes (i.e., experimentally-measured properties). This chapter introduces three computational methods that are used in the present thesis: density functional theory (Section 6.1), *ab initio* molecular dynamics (Section 6.2), and finite-difference time-domain calculations (Section 6.3).

6.1. Density functional theory

Density functional theory (DFT) is a quantum mechanical method used for calculating physical properties of materials, based on their electronic structure. [152] Due to the large number of atoms and electrons in a solid, exact solutions to the Schrödinger equation cannot be found. By reducing the many-body problem to a single-body problem, it becomes possible to find solutions computationally. In DFT, this is achieved using the theorems of Hohenberg and Kohn, [153] which postulate that the total energy of a system is a unique functional of the electron charge density $\rho_{el}(\vec{r})$, and that a minimization of the total energy of the system is obtained for the ground-state of $\rho_{el}(\vec{r})$. The ground state is described by a system of non-interacting electrons in an effective potential field $V_{eff}(\vec{r}) = f(\rho_{el}(\vec{r}))$, which is computed from the attractive nuclear potential and the electronic interaction potential. The single-body Schrödinger equation is then solved in an iterative scheme procedure until convergence of the total energy is achieved.

DFT calculations are performed at temperature $0\,K$, i.e., molecular and lattice vibrations are not considered, and dynamic phenomena cannot be described. In thin film physics, DFT calculations are primarily used for determining surface formation energies, adsorption energies, and static potential energy landscapes.

DFT calculations are used in Paper I to calculate Ag and Cu adatom adsorption energies, as well as Ag_2 and Cu_2 addimer binding energies on amorphous carbon substrates.

6.2. *Ab initio* molecular dynamics

Molecular dynamics (MD) is a method for calculating the trajectories $\vec{r}(t)$ of particles (e.g., atoms) that interact in gaseous, liquid, or solid phase at finite temperatures (i.e., above 0 K). This is done by solving Newton's equations of motion for the system of interacting particles. In the most common MD approach (also referred to as classical MD), the forces between particles are modelled using semi-empirical mathematical models, the interatomic potentials, the choice of which is a key aspect for the physical accuracy of the simulation results. [152]

The utilization of semi-empirical interatomic potentials leads to limitations in MD simulations, e.g., charges appear as static parameters, and atom-connectivity is implicit (i.e., bond breaking and forming cannot be described). [154] *Ab initio* molecular dynamics (AIMD) combines MD simulations with DFT, such that interatomic forces needed for MD are calculated from electronic structure calculations in DFT after each time step. [154,155]

AIMD simulations are performed to study diffusion of Ag and Cu adatoms on amorphous carbon, and determine surface diffusivities as a function of temperature in Paper I.

6.3. Finite-difference time-domain calculations

The finite-difference time-domain (FDTD) method is a computational approach used for solving electrodynamical problems, which discretizes differential equations via approximation with difference equations in the time-domain (as opposed to the frequency-domain). [156] As FDTD is a time-domain technique, it can be used to treat problems in a wide range of frequencies. The calculations are performed by dividing the investigated system into domains and, subsequently, time-integrating the Maxwell's equations (see Eqs. 6.1 and 6.2) on the computational grid [156–158]:

$$\nabla \times \boldsymbol{E} = -\mu \frac{\delta \boldsymbol{H}}{\delta t} \tag{6.1}$$

$$\nabla \times \boldsymbol{H} = \varepsilon_0 \frac{\delta \boldsymbol{E}}{\delta t} + \frac{\delta \boldsymbol{P_0}}{\delta t} + \sum_{j=1}^{N} \frac{\delta \boldsymbol{P_j}}{\delta t} \tag{6.2}$$

In Eq. 6.1, $\boldsymbol{E}$ and $\boldsymbol{H}$ denote the electric and magnetic field, respectively, and μ is the relative permittivity. In Eq. 6.2, ε_0 is the permittivity of free space, and $\boldsymbol{P_0}$ and $\boldsymbol{P_j}$ stand for the polarization of the free and bound electrons, respectively.

Expressions for the polarization terms are introduced to Eq. 6.2, in accordance with the treated material system, e.g., $\boldsymbol{P_0}$ and $\boldsymbol{P_j}$ can be expressed with help of Drude and Lorentz oscillators, respectively (see Section 5.2.1). Subsequently, Eqs. 6.1 and 6.2 are solved computationally, giving the $\boldsymbol{E}$ and $\boldsymbol{H}$ fields at every point in the computational grid in the time domain, from which other optoelectronic properties can be calculated. [157].

FDTD is used in Paper III to calculate the localized surface resonance frequency LSPR of isolated Ag islands on insulating SiO_2 substrates as functions of island size and inter-island spacing.

7. Contribution to the field and outlook

The present thesis focuses on the nanoscale growth dynamics, stress generation, and morphology manipulation of thin metal films on weakly-interacting substrates. My contributions to these topics are outlined in the following.

In **Paper I**, the scaling behavior of characteristic morphological transition thicknesses (i.e., percolation and continuous film formation thickness) during growth of Ag and Cu films on amorphous carbon (a-C) are established as function of deposition rate and temperature. These data are interpreted using a theoretical framework based on the droplet growth theory and the kinetic freezing model for island coalescence, from which the diffusion rates of film forming species during Ag and Cu growth are estimated. By combining experimental data with *ab initio* molecular dynamics simulations, diffusion of multiatomic clusters, rather than monomers, is identified as the rate-limiting structure-forming process during island nucleation.

In **Paper II**, the evolution of stress during Ag and Cu film growth on a-C, and its dependence on growth kinetics (as determined by deposition rate, substrate temperature) are systematically investigated. A general trend toward smaller compressive stress magnitudes with increasing temperature/deposition rate is found, related to increasing grain size/decreasing adatom diffusion length. Exception to this trend is found for Cu films, in which oxygen incorporation from the residual growth atmosphere at low deposition rates inhibits adatom diffusivity and decreases the magnitude of compressive stress.

In **Papers III through V**, the effect of minority metallic and gaseous species (Cu, N_2, O_2) on Ag film morphological evolution on SiO_2 is studied. By employing *in situ* spectroscopic ellipsometry, it is found that addition of minority species at the film growth front promotes 2D morphology, but also yields an increased continuous-layer resistivity. *Ex situ* analyses show that 2D morphology is favored because minority species hinder the rate of coalescence completion. Hence, a novel growth manipulation strategy is devised in which minority species are deployed with high temporal precision to target the initial stages of island nucleation, growth, and coalescence, and thereby achieve 2D morphology, while retaining opto-electronic properties of pure Ag films.

The effect of N_2 on stress type and magnitude in Ag films is studied in **Paper VI**. Ag films grown in N_2-free atmosphere exhibit a typical compressive-tensile-compressive stress evolution as function of thickness, whereby a steady-state stress is reached in the second compressive regime. Addition of N_2 yields (i) onset of island-coalescence—and consequently tensile stress formation—at lower film thicknesses, (ii) higher compressive stress upon continuous film formation, and (iii) a compressive-to-tensile stress transition in the continuous film regime. These stress changes are attributed to strain-energy-minimization driven giant grain growth of grains with soft crystallographic orientation, and film roughening, owing to decreased surface diffusivity of film-forming species in the presence of nitrogen at the growth front.

The overall results of the thesis provide the foundation to: (i) determine diffusion rates over a wide range of weakly-interacting film/substrate systems; (ii) design non-invasive strategies for morphology manipulation of multifunctional contacts in optoelectronic devices; (iii) complete important missing pieces in the fundamental understanding of stress, which can be used to expand theoretical descriptions for predicting and tuning stress magnitude in thin films.

Research on weakly-interacting film/substrate systems is an emerging topic in the thin film physics community, and it is driven by the increasing demand of components containing such material pairings (e.g., in microelectronics, sensors, etc.). The growth manipulation strategies presented in Papers III through V is a promising concept that can allow a more efficient use of thin films on weakly-interacting substrates such as oxides and van der Waals materials. A next step would be the implementation of these deposition strategies in thin metal film-based applications, where the effects of present gas and metal species on device performance and functionalities need to be further investigated. Although not included in this work, preliminary experiments showed that the presence of minority species with low mobility (e.g., Ti, Cr, Mo) can lead to a delayed continuous film formation in Ag films, implying more pronounced 3D morphology during the island nucleation and growth stage. This effect could be leveraged in the synthesis of nano particles from the vapor phase.

Stress data presented in Paper II is consistent with stress generation models that are widely accepted, stipulating the reversible insertion of adatoms into grain boundaries during film growth. The experimental proof for this mechanism does not exist so far. Only if a conclusive model exists, can *in situ* stress measurements be used to verify the quality of the deposited film, or used for studying new effects, e.g., the stress evolution in films that react chemically during growth.

A specific future research question is related to Paper VI, where tensile stress is formed in Ag films deposited in N_2-containing atmospheres that show giant grain growth, in course of which soft crystallographic orientations overgrow the energetically and kinetically favored (111) oriented grains. Combining *in situ* x-ray diffractometry and substrate curvature measurements in a synchrotron facility would allow unambiguously determine how tensile stress formation and texture selection are connected.

In conclusion, it should be stated that the present work is experimental at its core, and simulations are only used to better understand experimental results and their trends. I expect that further validation of the mechanisms proposed by the present thesis will be obtained in the following years by combining advanced *in situ* and *in operando* imaging and spectroscopic tools with new computational approaches (e.g., artificial intelligence-based simulation tools) that enable atom-by-atom modelling of multicomponent film formation.

References

[1] K. Seshan, ed., Handbook of thin film deposition : techniques, processes, and technologies, 3rd ed., William Andrew, Oxford, UK, 2012.

[2] J.E. Greene, Thin Film Nucleation, Growth, and Microstructural Evolution - An Atomic Scale View, in: P.M. Martin (Ed.), Handb. Depos. Technol. Film. Coatings Sci. Appl. Technol., 3rd ed, Oxford, U.K. ; Burlington, Mass. : William Andrew/Elsevier, Oxford, 2010: pp. 554–618.

[3] P.B. Barna, M. Adamik, Fundamental structure forming phenomena of polycrystalline films and the structure zone models, Thin Solid Films. 317 (1998) 27–33. https://doi.org/10.1016/S0040-6090(97)00503-8.

[4] M. Ohring, Materials Science of Thin Films. Deposition and Structure., 2nd ed., Academic Press, San Diego, 2002.

[5] C.T. Campbell, Metal films and particles on oxide surfaces: structural, electronic and chemisorptive properties, J. Chem. Soc. Faraday Trans. 92 (1996) 1435. https://doi.org/10.1039/ft9969201435.

[6] X. Liu, Y. Han, J.W. Evans, A.K. Engstfeld, R.J. Behm, M.C. Tringides, M. Hupalo, H.-Q. Lin, L. Huang, K.-M. Ho, D. Appy, P.A. Thiel, C.-Z. Wang, Growth morphology and properties of metals on graphene, Prog. Surf. Sci. 90 (2015) 397–443. https://doi.org/10.1016/j.progsurf.2015.07.001.

[7] K. Sarakinos, A review on morphological evolution of thin metal films on weakly-interacting substrates, Thin Solid Films. 688 (2019) 137312. https://doi.org/10.1016/j.tsf.2019.05.031.

[8] T.J. Echtermeyer, S. Milana, U. Sassi, A. Eiden, M. Wu, E. Lidorikis, A.C. Ferrari, Surface Plasmon Polariton Graphene Photodetectors, Nano Lett. 16 (2016) 8–20. https://doi.org/10.1021/acs.nanolett.5b02051.

[9] T. Mueller, F. Xia, P. Avouris, Graphene photodetectors for high-speed optical communications, Nat. Photonics. 4 (2010) 297–301. https://doi.org/10.1038/nphoton.2010.40.

[10] Y. Xu, C.-Y. Hsieh, L. Wu, L.K. Ang, Two-dimensional transition metal dichalcogenides mediated long range surface plasmon resonance biosensors, J. Phys. D. Appl. Phys. 52 (2019) 065101. https://doi.org/10.1088/1361-6463/aaf0f7.

[11] C. Schaefer, G. Bräuer, J. Szczyrbowski, Low emissivity coatings on architectural glass, Surf. Coatings Technol. 93 (1997) 37–45. https://doi.org/10.1016/S0257-8972(97)00034-0.

[12] T. Michely, J. Krug, Islands, Mounds and Atoms, Springer Berlin Heidelberg, Berlin, Heidelberg, 2004. http://link.springer.com/10.1007/978-3-642-18672-1.

[13] G. Abadias, E. Chason, J. Keckes, M. Sebastiani, G.B. Thompson, E. Barthel, G.L. Doll, C.E. Murray, C.H. Stoessel, L. Martinu, Review Article: Stress in thin films and coatings: Current status, challenges, and prospects, J. Vac. Sci. Technol. A Vacuum, Surfaces, Film. 36 (2018) 020801. https://doi.org/10.1116/1.5011790.

[14] E. Chason, P.R. Guduru, Tutorial: Understanding residual stress in polycrystalline thin films through real-time measurements and physical models, J. Appl. Phys. 119 (2016) 191101. https://doi.org/10.1063/1.4949263.

[15] E. Chason, A.M. Engwall, Z. Rao, T. Nishimura, Kinetic model for thin film stress including the effect of grain growth, J. Appl. Phys. 123 (2018) 185305. https://doi.org/10.1063/1.5030740.

[16] D.R. Lide, ed., CRC Handbook of Chemistry and Physics: A Ready-Reference Book for Chemical and Physical Data, 88th ed., CRC Press, Boca Raton, Fl, 2008.

[17] J. Yun, Ultrathin Metal films for Transparent Electrodes of Flexible Optoelectronic Devices, Adv. Funct. Mater. 27 (2017) 1606641. https://doi.org/10.1002/adfm.201606641.

[18] H.K. Park, J.K. Yoon, K. Kim, Novel Fabrication of Ag Thin Film on Glass for Efficient Surface-Enhanced Raman Scattering, Langmuir. 22 (2006) 1626–1629. https://doi.org/10.1021/la052559o.

[19] A. Chambers, Modern vacuum physics, CRC Press, Boca Raton, Fl, 2005.

[20] W.M. Haynes, CRC Handbook of chemistry and physics: a ready-reference book for chemical and physical data, ed. 58, CRC Press, Cleveland, Ohio, 1977.

[21] J.F. O'Hanlon, A User's Guide to Vacuum Technology, Third Edit, John Wiley & Sons Inc., Hoboken, NJ, USA, 2003.

[22] K. Jousten, Handbook of Vacuum Technology, WILEY-VCH Verlag GmbH & co. KGaA, Weinheim, 2008.

[23] Y. Su, T. Sawada, J. Takemoto, S. Haga, Theoretical study on the pumping mechanism of a dry scroll vacuum pump, Vacuum. 47 (1996) 815–818. https://doi.org/10.1016/0042-207X(96)00073-5.

[24] M.A. Lieberman, A.J. Lichtenberg, Principles of Plasma Discharges and Materials Processing, Second Edi, John Wiley & Sons, Inc., Hoboken, NJ, USA, 2005. https://doi.org/10.1002/0471724254.

[25] K. Wasa, I. Kanno, H. Kotera, Handbook of Sputter Deposition Technology: Fundamentals and Applications for Functional Thin Films, Nanomaterials, and MEMS, Second edi, William Andrew, Oxford, 2012.

[26] A.Y. Konobeyev, U. Fischer, Y.A. Korovin, S.P. Simakov, Evaluation of effective threshold displacement energies and other data required for the calculation of advanced atomic displacement cross-sections, Nucl. Energy Technol. 3 (2017) 169–175. https://doi.org/10.1016/j.nucet.2017.08.007.

[27] M. Ghaly, R.S. Averback, Effect of viscous flow on ion damage near solid surfaces, Phys. Rev. Lett. 72 (1994) 364–367. https://doi.org/10.1103/PhysRevLett.72.364.

[28] P. Sigmund, Theory of Sputtering. I. Sputtering Yield of Amorphous and Polycrystalline Targets, Phys. Rev. 184 (1969) 383–416. https://doi.org/10.1103/PhysRev.184.383.

[29] Y. Yamamura, N. Matsunami, N. Itoh, Theoretical studies on an empirical formula for sputtering yield at normal incidence, Radiat. Eff. 71 (1983) 65–86. https://doi.org/10.1080/00337578308218604.

[30] I. Petrov, V. Orlinov, S. Grudeva, On the energy efficiency of sputtering, Bulg. J. Phys. 18 (1991).

[31] V. Kouznetsov, K. Macák, J.M. Schneider, U. Helmersson, I. Petrov, A novel pulsed magnetron sputter technique utilizing very high target power densities, Surf. Coatings Technol. 122 (1999) 290–293. https://doi.org/10.1016/S0257-8972(99)00292-3.

[32] I.K. Fetisov, A.A. Filippov, G.V. Khodachenko, D.V. Mozgrin, A.A. Pisarev, Impulse irradiation plasma technology for film deposition, Vacuum. 53 (1999) 133–136. https://doi.org/10.1016/S0042-207X(98)00408-4.

[33] F. Cemin, G. Abadias, T. Minea, C. Furgeaud, F. Brisset, D. Solas, D. Lundin, Benefits of energetic ion bombardment for tailoring stress and microstructural evolution during growth of Cu thin films, Acta Mater. 141 (2017) 120–130. https://doi.org/10.1016/j.actamat.2017.09.007.

[34] A.L. Horvath, Critical temperature of elements and the periodic system, J. Chem. Educ. 50 (1973) 335. https://doi.org/10.1021/ed050p335.

[35] E. Bauer, Phänomenologische Theorie der Kristallabscheidung an Oberflächen. I, Zeitschrift Für Krist. - Cryst. Mater. 110 (1958). https://doi.org/10.1524/zkri.1958.110.16.372.

[36] R.J. Asaro, W.A. Tiller, Interface morphology development during stress corrosion cracking: Part I. Via surface diffusion, Metall. Mater. Trans. B. 3 (1972) 1789–1796. https://doi.org/10.1007/BF02642562.

[37] D.J. Srolovitz, On the stability of surfaces of stressed solids, Acta Metall. 37 (1989) 621–625. https://doi.org/10.1016/0001-6160(89)90246-0.

[38] J.A. Venables, G.D.T. Spiller, Nucleation and Growth of Thin Films, in: Surf. Mobilities Solid Mater., Springer US, Boston, MA, 1983: pp. 341–404. https://doi.org/10.1007/978-1-4684-4343-1_16.

[39] B. Lü, G.A. Almyras, V. Gervilla, J.E. Greene, K. Sarakinos, Formation and morphological evolution of self-similar 3D nanostructures on weakly interacting substrates, Phys. Rev. Mater. 2 (2018) 063401. https://doi.org/10.1103/PhysRevMaterials.2.063401.

[40] T.W.H. Oates, A. Mücklich, Evolution of plasmon resonances during plasma deposition of silver nanoparticles, Nanotechnology. 16 (2005) 2606–2611. https://doi.org/10.1088/0957-4484/16/11/023.

[41] F.A. Nichols, Coalescence of Two Spheres by Surface Diffusion, J. Appl. Phys. 37 (1966) 2805–2808. https://doi.org/10.1063/1.1782127.

[42] W. Ostwald, Über die vermeintliche Isomerie des roten und gelben Quecksilberoxyds und die Oberflächenspannung fester Körper, Zeitschrift Für Phys. Chemie. 34U (1900) 495–503. https://doi.org/10.1515/zpch-1900-3431.

[43] Z. Zhang, Atomistic Processes in the Early Stages of Thin-Film Growth, Science (80-.). 276 (1997) 377–383. https://doi.org/10.1126/science.276.5311.377.

[44] S.C. Wang, U. Kürpick, G. Ehrlich, Surface diffusion of compact and other clusters: Ir-x on Ir(111), Phys. Rev. Lett. 81 (1998) 4923–4926. https://doi.org/10.1103/PhysRevLett.81.4923.

[45] L. Bardotti, P. Jensen, A. Hoareau, M. Treilleux, B. Cabaud, A. Perez, F.C.S. Aires, Diffusion and aggregation of large antimony and gold clusters deposited on graphite, Surf. Sci. 367 (1996) 276–292. https://doi.org/10.1016/S0039-6028(96)00875-8.

[46] P. Deltour, J.-L. Barrat, P. Jensen, Fast Diffusion of a Lennard-Jones Cluster on a Crystalline Surface, Phys. Rev. Lett. 78 (1997) 4597–4600. https://doi.org/10.1103/PhysRevLett.78.4597.

[47] S.Y. Krylov, Surface Gliding of Large Low-Dimensional Clusters, Phys. Rev. Lett. 83 (1999) 4602–4605. https://doi.org/10.1103/PhysRevLett.83.4602.

[48] G. Jeffers, M.A. Dubson, P.M. Duxbury, Island-to-percolation transition during growth of metal films, J. Appl. Phys. 75 (1994) 5016–5020. https://doi.org/10.1063/1.355742.

[49] J.M. Warrender, M.J. Aziz, Effect of deposition rate on morphology evolution of metal-on-insulator films grown by pulsed laser deposition, Phys. Rev. B. 76 (2007) 045414. https://doi.org/10.1103/PhysRevB.76.045414.

[50] J. Carrey, J.-L. Maurice, Transition from droplet growth to percolation: Monte Carlo simulations and an analytical model, Phys. Rev. B. 63 (2001) 245408. https://doi.org/10.1103/PhysRevB.63.245408.

[51] C. Polop, C. Rosiepen, S. Bleikamp, R. Drese, J. Mayer, A. Dimyati, T. Michely, The STM view of the initial stages of polycrystalline Ag film formation, New J. Phys. 9 (2007) 74–74. https://doi.org/10.1088/1367-2630/9/3/074.

[52] O. Dulub, L.A. Boatner, U. Diebold, STM study of the geometric and electronic structure of ZnO(0001)-Zn, (000-1)-O, (10-10), and (11-20) surfaces, Surf. Sci. 519 (2002) 201–217. https://doi.org/10.1016/S0039-6028(02)02211-2.

[53] B. Lü, L. Souqui, V. Elofsson, K. Sarakinos, Scaling of elongation transition thickness during thin-film growth on weakly interacting substrates, Appl. Phys. Lett. 111 (2017) 084101. https://doi.org/10.1063/1.4993252.

[54] A.S. Ingason, F. Magnus, J.S. Agustsson, S. Olafsson, J.T. Gudmundsson, In-situ electrical characterization of ultrathin TiN films grown by reactive dc magnetron sputtering on SiO2, Thin Solid Films. 517 (2009) 6731–6736. https://doi.org/10.1016/j.tsf.2009.05.028.

[55] A.I. Maaroof, B.L. Evans, Onset of electrical conduction in Pt and Ni films, J. Appl. Phys. 76 (1994) 1047–1054. https://doi.org/10.1063/1.357822.

[56] J.J. Colin, Y. Diot, P. Guerin, B. Lamongie, F. Berneau, A. Michel, C. Jaouen, G. Abadias, A load-lock compatible system for in situ electrical resistivity measurements during thin film growth, Rev. Sci. Instrum. 87 (2016) 023902. https://doi.org/10.1063/1.4940933.

[57] M.J. Rost, In Situ Real-Time Observation of Thin Film Deposition: Roughening, Zeno Effect, Grain Boundary Crossing Barrier, and Steering, Phys. Rev. Lett. 99 (2007) 266101. https://doi.org/10.1103/PhysRevLett.99.266101.

[58] I. Elkinani, J. Villain, Growth roughness and instabilities due to the Schwoebel effect : a one-dimensional model, J. Phys. I. 4 (1994) 947–973. https://doi.org/10.1051/jp1:1994238.

[59] M. Giesen, G. Schulze Icking-Konert, H. Ibach, Fast Decay of Adatom Islands and Mounds on Cu(111): A New Effective Channel for Interlayer Mass Transport, Phys. Rev. Lett. 80 (1998) 552–555. https://doi.org/10.1103/PhysRevLett.80.552.

[60] S. Mahieu, P. Ghekiere, D. Depla, R. De Gryse, Biaxial alignment in sputter deposited thin films, Thin Solid Films. 515 (2006) 1229–1249. https://doi.org/10.1016/j.tsf.2006.06.027.

[61] B.A. Movchan, A. V. Demchishin, Structure and properties of thick condensates of nickel, titanium, tungsten, aluminum oxides, and zirconium dioxide in vacuum, Fiz. Met. Met. 28 (1969) 653–660.

[62] J.A. Thornton, Influence of apparatus geometry and deposition conditions on the structure and topography of thick sputtered coatings, J. Vac. Sci. Technol. 11 (1974) 666–670. https://doi.org/10.1116/1.1312732.

[63] J.A. Thornton, High Rate Thick Film Growth, Annu. Rev. Mater. Sci. 7 (1977) 239–260. https://doi.org/10.1146/annurev.ms.07.080177.001323.

[64] R. Messier, A.P. Giri, R.A. Roy, Revised structure zone model for thin film physical structure, J. Vac. Sci. Technol. A Vacuum, Surfaces, Film. 2 (1984) 500–503. https://doi.org/10.1116/1.572604.

[65] A. Anders, A structure zone diagram including plasma-based deposition and ion etching, Thin Solid Films. 518 (2010) 4087–4090. https://doi.org/10.1016/j.tsf.2009.10.145.

[66] I. Petrov, P.B. Barna, L. Hultman, J.E. Greene, Microstructural evolution during film growth, J. Vac. Sci. Technol. A Vacuum, Surfaces, Film. 21 (2003) S117–S128. https://doi.org/10.1116/1.1601610.

[67] I. Petrov, L. Hultman, U. Helmersson, J.-E. Sundgren, J.E. Greene, Microstructure modification of TiN by ion bombardment during reactive sputter deposition, Thin Solid Films. 169 (1989) 299–314. https://doi.org/10.1016/0040-6090(89)90713-X.

[68] K. Van Aeken, S. Mahieu, D. Depla, The metal flux from a rotating cylindrical magnetron: a Monte Carlo simulation, J. Phys. D. Appl. Phys. 41 (2008) 205307. https://doi.org/10.1088/0022-3727/41/20/205307.

[69] D.A. Porter, K.E. Easterling, M.Y. Sherif, Phase Transformations in Metals and Alloys, 3rd Ed., CRC Press, Boca Raton, 2009. https://doi.org/10.1201/9781439883570.

[70] S. Esch, M. Hohage, T. Michely, G. Comsa, Origin of oxygen induced layer-by-layer growth in homoepitaxy on Pt(111), Phys. Rev. Lett. 72 (1994) 518–521. https://doi.org/10.1103/PhysRevLett.72.518.

[71] M. Kalff, G. Comsa, T. Michely, How Sensitive is Epitaxial Growth to Adsorbates?, Phys. Rev. Lett. 81 (1998) 1255–1258. https://doi.org/10.1103/PhysRevLett.81.1255.

[72] J. Vrijmoeth, H.A. van der Vegt, J.A. Meyer, E. Vlieg, R.J. Behm, Surfactant-Induced Layer-by-Layer Growth of Ag on Ag(111): Origins and Side Effects, Phys. Rev. Lett. 72 (1994) 3843–3846. https://doi.org/10.1103/PhysRevLett.72.3843.

[73] V. Gervilla, G.A. Almyras, F. Thunström, J.E. Greene, K. Sarakinos, Dynamics of 3D-island growth on weakly-interacting substrates, Appl. Surf. Sci. 488 (2019) 383–390. https://doi.org/10.1016/j.apsusc.2019.05.208.

[74] G. Zhao, W. Wang, T.-S. Bae, S.-G. Lee, C. Mun, S. Lee, H. Yu, G.-H. Lee, M. Song, J. Yun, Stable ultrathin partially oxidized copper film electrode for highly efficient flexible solar cells, Nat. Commun. 6 (2015) 8830. https://doi.org/10.1038/ncomms9830.

[75] W. Wang, M. Song, T.-S. Bae, Y.H. Park, Y.-C. Kang, S.-G. Lee, S.-Y. Kim, D.H. Kim, S. Lee, G. Min, G.-H. Lee, J.-W. Kang, J. Yun, Transparent Ultrathin Oxygen-Doped Silver Electrodes for Flexible Organic Solar Cells, Adv. Funct. Mater. 24 (2014) 1551–1561. https://doi.org/10.1002/adfm.201301359.

[76] J.M. Riveiro, P.S. Normile, J.P. Andrés, J.A. González, J.A. De Toro, T. Muñoz, P. Muñiz, Oxygen-assisted control of surface morphology in nonepitaxial sputter growth of Ag, Appl. Phys. Lett. 89 (2006) 201902. https://doi.org/10.1063/1.2388140.

[77] A.J. Birnbaum, C. V. Thompson, J.C. Steuben, A.P. Iliopoulos, J.G. Michopoulos, Oxygen-induced giant grain growth in Ag films, Appl. Phys. Lett. 111 (2017) 163107. https://doi.org/10.1063/1.4998741.

[78] J. Bulíř, M. Novotný, J. Lančok, L. Fekete, J. Drahokoupil, J. Musil, Nucleation of ultrathin silver layer by magnetron sputtering in Ar/N2 plasma, Surf. Coatings Technol. 228 (2013) S86–S90. https://doi.org/10.1016/j.surfcoat.2012.08.021.

[79] R.H.H. Ko, A. Khalatpour, J.K.D. Clark, N.P. Kherani, Ultrasmooth ultrathin Ag films by AlN seeding and Ar/N 2 sputtering for transparent conductive and heating applications, APL Mater. 6 (2018) 121112. https://doi.org/10.1063/1.5052261.

[80] J. Yun, H.-S. Chung, S.-G. Lee, J.-S. Bae, T.E. Hong, K. Takahashi, S.M. Yu, J. Park, Q. Guo, G.-H. Lee, S.Z. Han, Y. Ikoma, E.-A. Choi, An unexpected surfactant role of immiscible nitrogen in the structural development of silver nanoparticles: an experimental and numerical investigation, Nanoscale. 12 (2020) 1749–1758. https://doi.org/10.1039/C9NR08076G.

[81] I. Dutta, M.W. Chen, K. Peterson, T. Shultz, Plastic deformation and interfacial sliding in Al and Cu thin film: Si substrate systems due to thermal cycling, J. Electron. Mater. 30 (2001) 1537–1548. https://doi.org/10.1007/s11664-001-0171-3.

[82] S. Bigl, W. Heinz, M. Kahn, H. Schoenherr, M.J. Cordill, High-Temperature Characterization of Silicon Dioxide Films with Wafer Curvature, JOM. 67 (2015) 2902–2907. https://doi.org/10.1007/s11837-015-1600-8.

[83] R. Koch, M. Weber, K. Thürmer, K.H. Rieder, Magnetoelastic coupling of Fe at high stress investigated by means of epitaxial Fe(001) films, J. Magn. Magn. Mater. 159 (1996) L11–L16. https://doi.org/10.1016/0304-8853(96)00291-0.

[84] R. Koch, Stress in Evaporated and Sputtered Thin Films – A Comparison, Surf. Coatings Technol. 204 (2010) 1973–1982. https://doi.org/10.1016/j.surfcoat.2009.09.047.

[85] R. Koch, Intrinsic stress of ultrathin epitaxial films, Appl. Phys. A Mater. Sci. Process. 69 (1999) 529–536. https://doi.org/10.1007/s003390051462.

[86] M.A. Grinfeld, The stress driven instability in elastic crystals: Mathematical models and physical manifestations, J. Nonlinear Sci. 3 (1993) 35–83. https://doi.org/10.1007/BF02429859.

[87] J.S. Vermaak, C.W. Mays, D. Kuhlmann-Wilsdorf, On surface stress and surface tension, Surf. Sci. 12 (1968) 128–133. https://doi.org/10.1016/0039-6028(68)90118-0.

[88] C.W. Mays, J.S. Vermaak, D. Kuhlmann-Wilsdorf, On surface stress and surface tension, Surf. Sci. 12 (1968) 134–140. https://doi.org/10.1016/0039-6028(68)90119-2.

[89] R.C. Cammarata, T.M. Trimble, D.J. Srolovitz, Surface stress model for intrinsic stresses in thin films, J. Mater. Res. 15 (2000) 2468–2474. https://doi.org/10.1557/JMR.2000.0354.

[90] M. Takagi, Electron-Diffraction Study of Liquid-Solid Transition of Thin Metal Films, J. Phys. Soc. Japan. 9 (1954) 359–363. https://doi.org/10.1143/JPSJ.9.359.

[91] W.H. Qi, M.P. Wang, Size and shape dependent melting temperature of metallic nanoparticles, Mater. Chem. Phys. 88 (2004) 280–284. https://doi.org/10.1016/j.matchemphys.2004.04.026.

[92] C. Friesen, C. V Thompson, Reversible Stress Relaxation during Precoalescence Interruptions of Volmer-Weber Thin Film Growth, Phys. Rev. Lett. 89 (2002) 126103. https://doi.org/10.1103/PhysRevLett.89.126103.

[93] C. Friesen, S.C. Seel, C. V Thompson, Reversible stress changes at all stages of Volmer–Weber film growth, J. Appl. Phys. 95 (2004) 1011–1020. https://doi.org/10.1063/1.1637728.

[94] W.D. Nix, B.M. Clemens, Crystallite coalescence: A mechanism for intrinsic tensile stresses in thin films, J. Mater. Res. 14 (1999) 3467–3473. https://doi.org/10.1557/JMR.1999.0468.

[95] S.C. Seel, C. V. Thompson, S.J. Hearne, J.A. Floro, Tensile stress evolution during deposition of Volmer–Weber thin films, J. Appl. Phys. 88 (2000) 7079–7088. https://doi.org/10.1063/1.1325379.

[96] X. Zhou, X. Yu, D. Jacobson, G.B. Thompson, A molecular dynamics study on stress generation during thin film growth, Appl. Surf. Sci. 469 (2019) 537–552. https://doi.org/10.1016/j.apsusc.2018.09.253.

[97] R. Abermann, Measurements of the intrinsic stress in thin metal films, Vacuum. 41 (1990) 1279–1282. https://doi.org/10.1016/0042-207X(90)93933-A.

[98] H.Z. Yu, C. V Thompson, Grain growth and complex stress evolution during Volmer–Weber growth of polycrystalline thin films, Acta Mater. 67 (2014) 189–198. https://doi.org/10.1016/j.actamat.2013.12.031.

[99] D. Winau, R. Koch, A. Führmann, K.H. Rieder, Film growth studies with intrinsic stress measurement: Polycrystalline and epitaxial Ag, Cu, and Au films on mica(001), J. Appl. Phys. 70 (1991) 3081–3087. https://doi.org/10.1063/1.349313.

[100] R. Koch, D. Hu, A.K. Das, Compressive Stress in Polycrystalline Volmer-Weber Films, Phys. Rev. Lett. 94 (2005) 146101. https://doi.org/10.1103/PhysRevLett.94.146101.

[101] G. Abadias, L. Simonot, J.J. Colin, A. Michel, S. Camelio, D. Babonneau, Volmer-Weber growth stages of polycrystalline metal films probed by in situ and real-time optical diagnostics, Appl. Phys. Lett. 107 (2015) 183105. https://doi.org/10.1063/1.4935034.

[102] E. Chason, B.W. Sheldon, L.B. Freund, J.A. Floro, S.J. Hearne, Origin of Compressive Residual Stress in Polycrystalline Thin Films, Phys. Rev. Lett. 88 (2002) 156103. https://doi.org/10.1103/PhysRevLett.88.156103.

[103] H. Windischmann, Intrinsic stress in sputtered thin films, J. Vac. Sci. Technol. A Vacuum, Surfaces, Film. 9 (1991) 2431–2436. https://doi.org/10.1116/1.577295.

[104] J.-D. Kamminga, T.H. de Keijser, R. Delhez, E.J. Mittemeijer, On the origin of stress in magnetron sputtered TiN layers, J. Appl. Phys. 88 (2000) 6332–6345. https://doi.org/10.1063/1.1319973.

[105] A. Debelle, G. Abadias, A. Michel, C. Jaouen, Stress field in sputtered thin films: Ion irradiation as a tool to induce relaxation and investigate the origin of growth stress, Appl. Phys. Lett. 84 (2004) 5034–5036. https://doi.org/10.1063/1.1763637.

[106] E. Chason, M. Karlson, J.J. Colin, D. Magnfält, K. Sarakinos, G. Abadias, A kinetic model for stress generation in thin films grown from energetic vapor fluxes, J. Appl. Phys. 119 (2016) 145307. https://doi.org/10.1063/1.4946039.

[107] M. Pletea, W. Brückner, H. Wendrock, R. Kaltofen, Stress evolution during and after sputter deposition of Cu thin films onto Si (100) substrates under various sputtering pressures, J. Appl. Phys. 97 (2005) 054908. https://doi.org/10.1063/1.1858062.

[108] S.Y. Grachev, F.D. Tichelaar, G.C.A.M. Janssen, Stress in sputter-deposited Cr films: Influence of Ar pressure, J. Appl. Phys. 97 (2005) 073508. https://doi.org/10.1063/1.1876579.

[109] A. Fillon, G. Abadias, A. Michel, C. Jaouen, Stress and microstructure evolution during growth of magnetron-sputtered low-mobility metal films: Influence of the nucleation conditions, Thin Solid Films. 519 (2010) 1655–1661. https://doi.org/10.1016/j.tsf.2010.07.091.

[110] D. Magnfält, V. Elofsson, G. Abadias, U. Helmersson, K. Sarakinos, Time-domain and energetic bombardment effects on the nucleation and coalescence of thin metal films on amorphous substrates, J. Phys. D. Appl. Phys. 46 (2013) 215303. https://doi.org/10.1088/0022-3727/46/21/215303.

[111] J.J. Colin, G. Abadias, A. Michel, C. Jaouen, On the origin of the metastable β-Ta phase stabilization in tantalum sputtered thin films, Acta Mater. 126 (2017) 481–493. https://doi.org/10.1016/j.actamat.2016.12.030.

[112] R. Abermann, R. Koch, In situ study of thin film growth by internal stress measurement under ultrahigh vacuum conditions: Silver and copper under the influence of oxygen, Thin Solid Films. 142 (1986) 65–76. https://doi.org/10.1016/0040-6090(86)90303-2.

[113] R. Abermann, R. Koch, In situ determination of the structure of thin metal films by internal stress measurements: Structure dependence of silver and copper films on oxygen pressure during deposition, Thin Solid Films. 66 (1980) 217–232. https://doi.org/10.1016/0040-6090(80)90225-4.

[114] D. Flötotto, Z.M. Wang, L.P.H. Jeurgens, E.J. Mittemeijer, Kinetics and magnitude of the reversible stress evolution during polycrystalline film growth interruptions, J. Appl. Phys. 118 (2015) 055305. https://doi.org/10.1063/1.4928162.

[115] H.Z. Yu, J.S. Leib, S.T. Boles, C. V Thompson, Fast and slow stress evolution mechanisms during interruptions of Volmer-Weber growth, J. Appl. Phys. 115 (2014) 043521. https://doi.org/10.1063/1.4863600.

[116] W.W. Mullins, Theory of Thermal Grooving, J. Appl. Phys. 28 (1957) 333–339. https://doi.org/10.1063/1.1722742.

[117] H.Z. Yu, C. V Thompson, Correlation of shape changes of grain surfaces and reversible stress evolution during interruptions of polycrystalline film growth, Appl. Phys. Lett. 104 (2014) 141913. https://doi.org/10.1063/1.4871214.

[118] E. Chason, A kinetic analysis of residual stress evolution in polycrystalline thin films, Thin Solid Films. 526 (2012) 1–14. https://doi.org/10.1016/j.tsf.2012.11.001.

[119] E. Chason, J.W. Shin, S.J. Hearne, L.B. Freund, Kinetic model for dependence of thin film stress on growth rate, temperature, and microstructure, J. Appl. Phys. 111 (2012) 083520. https://doi.org/10.1063/1.4704683.

[120] P. Jagtap, E. Chason, A unified kinetic model for stress relaxation and recovery during and after growth interruptions in polycrystalline thin films, Acta Mater. 193 (2020) 202–209. https://doi.org/10.1016/j.actamat.2020.04.013.

[121] C.-H. Chiu, H. Gao, Stress singularities along a cycloid rough surface, Int. J. Solids Struct. 30 (1993) 2983–3012. https://doi.org/https://doi.org/10.1016/0020-7683(93)90208-O.

[122] J.S. Tello, A.F. Bower, Numerical simulations of stress generation and evolution in Volmer-Weber thin films, J. Mech. Phys. Solids. 56 (2008) 2727–2747. https://doi.org/10.1016/j.jmps.2008.02.008.

[123] E. Vasco, C. Polop, Comment on “Correlation of shape changes of grain surfaces and reversible stress evolution during interruptions of polycrystalline film growth” [Appl. Phys. Lett. 104 , 141913 (2014)], Appl. Phys. Lett. 105 (2014) 246101. https://doi.org/10.1063/1.4903863.

[124] P. Maivald, H.J. Butt, S.A.C. Gould, C.B. Prater, B. Drake, J.A. Gurley, V.B. Elings, P.K. Hansma, Using force modulation to image surface elasticities with the atomic force microscope, Nanotechnology. 2 (1991) 103–106. https://doi.org/10.1088/0957-4484/2/2/004.

[125] C. Polop, E. Vasco, A.P. Perrino, R. Garcia, Mapping stress in polycrystals with sub-10 nm spatial resolution, Nanoscale. 9 (2017) 13938–13946. https://doi.org/10.1039/C7NR00800G.

[126] E. Vasco, C. Polop, Intrinsic Compressive Stress in Polycrystalline Films is Localized at Edges of the Grain Boundaries, Phys. Rev. Lett. 119 (2017) 256102. https://doi.org/10.1103/PhysRevLett.119.256102.

[127] E. Vasco, E.G. Michel, C. Polop, Disclosing the origin of the postcoalescence compressive stress in polycrystalline films by nanoscale stress mapping, Phys. Rev. B. 98 (2018) 195428. https://doi.org/10.1103/PhysRevB.98.195428.

[128] C. Kittel, Introduction to solid state physics, 8. ed., Hoboken, NJ, USA, 2005.

[129] T.W.H. Oates, H. Wormeester, H. Arwin, Characterization of plasmonic effects in thin films and metamaterials using spectroscopic ellipsometry, Prog. Surf. Sci. 86 (2011) 328–376. https://doi.org/10.1016/j.progsurf.2011.08.004.

[130] F. Wooten, Optical Properties of Solids, Academic Press, New York, 1972.

[131] V. Elofsson, B. Lü, D. Magnfält, E.P. Münger, K. Sarakinos, Unravelling the physical mechanisms that determine microstructural evolution of ultrathin Volmer-Weber films, J. Appl. Phys. 116 (2014) 044302. https://doi.org/10.1063/1.4890522.

[132] C.M. Herzinger, B. Johs, W.A. McGahan, J.A. Woollam, W. Paulson, Ellipsometric determination of optical constants for silicon and thermally grown silicon dioxide via a multi-sample, multi-wavelength, multi-angle investigation, J. Appl. Phys. 83 (1998) 3323–3336. https://doi.org/10.1063/1.367101.

[133] L.B. Freund, J.A. Floro, E. Chason, Extensions of the Stoney formula for substrate curvature to configurations with thin substrates or large deformations, Appl. Phys. Lett. 74 (1999) 1987–1989. https://doi.org/10.1063/1.123722.

[134] L.B. Freund, Some elementary connections between curvature and mismatch strain in compositionally graded thin films, J. Mech. Phys. Solids. 44 (1996) 723–736. https://doi.org/10.1016/0022-5096(96)00008-7.

[135] G.G. Stoney, The Tension of Metallic Films Deposited by Electrolysis, Proc. R. Soc. London A. 82 (1909) 172–175. https://doi.org/10.1098/rspa.1909.0021.

[136] R.W. Hoffman, Stresses in thin films: The relevance of grain boundaries and impurities, Thin Solid Films. 34 (1976) 185–190. https://doi.org/10.1016/0040-6090(76)90453-3.

[137] I. Miccoli, F. Edler, H. Pfnür, C. Tegenkamp, The 100th anniversary of the four-point probe technique: The role of probe geometries in isotropic and anisotropic systems, J. Phys. Condens. Matter. 27 (2015) 223201. https://doi.org/10.1088/0953-8984/27/22/223201.

[138] G. Binnig, C.F. Quate, C. Gerber, Atomic Force Microscope, Phys. Rev. Lett. 56 (1986) 930–933. https://doi.org/10.1103/PhysRevLett.56.930.

[139] P. Meakin, Fractals, scaling and growth far from equilibrium, Cambridge University Press, Cambridge, 1998.

[140] S.M. Obaidulla, P.K. Giri, Surface roughening and scaling behavior of vacuum-deposited SnCl2Pc organic thin films on different substrates, Appl. Phys. Lett. 107 (2015) 221910. https://doi.org/10.1063/1.4936937.

[141] D.B. Williams, C.B. Carter, Transmission electron microscopy, 2. ed., Springer, New York, London, 2009.

[142] K. Barmak, K. Coffey, Metallic films for electronic, optical and magnetic applications. Structure, processing and properties, Woohead Publishing Limited, Cambridge, UK, 2014.

[143] B.D. Cullity, Elements of x-ray diffraction, Addison-Wesley Publishing Company, Inc, Reading, MA, USA, 1956.

[144] A.L. Patterson, The Scherrer Formula for X-Ray Particle Size Determination, Phys. Rev. 56 (1939) 978–982. https://doi.org/10.1103/PhysRev.56.978.

[145] T. de Keijser, E.J. Mittemeijer, H.C.F. Rozendaal, The determination of crystallite-size and lattice-strain parameters in conjunction with the profile-refinement method for the determination of crystal structures, J. Appl. Crystallogr. 16 (1983) 309–316. https://doi.org/10.1107/S0021889883010493.

[146] A.. Hindeleh, D.. Johnson, Crystallinity and crystallite size measurement in cellulose fibres: 1. Ramie and Fortisan, Polymer (Guildf). 13 (1972) 423–430. https://doi.org/10.1016/0032-3861(72)90107-3.

[147] ICDD powder diffraction file no. 00-004-0787; silver, (n.d.).

[148] J. Als-Nielsen, D. McMorrow, Elements of Modern X-ray Physics, 2. ed., John Wiley & Sons, Ltd., Chichester, UK, 2011.

[149] E.E. Fullerton, I.K. Schuller, H. Vanderstraeten, Y. Bruynseraede, Structural refinement of superlattices from x-ray diffraction, Phys. Rev. B. 45 (1992) 9292–9310. https://doi.org/10.1103/PhysRevB.45.9292.

[150] D. Briggs, M.P. Seah, eds., Practical surface analysis. Vol. 1, Auger and X-ray photoelectron spectroscopy, John Wiley & Sons, Ltd., Chichester, UK, 1990.

[151] J.F. Watts, X-ray photoelectron spectroscopy, Vacuum. 45 (1994) 653–671. https://doi.org/10.1016/0042-207X(94)90107-4.

[152] D.G. Sangiovanni, Transition Metal Nitrides. Alloy Design and Surface Transport Properties using Ab-initio and Classical Computational Models, Linköping University, Sweden, 2013.

[153] P. Hohenberg, W. Kohn, Inhomogeneous Electron Gas, Phys. Rev. 136 (1964) B864–B871. https://doi.org/10.1103/PhysRev.136.B864.

[154] M.E. Tuckerman, Ab initio molecular dynamics: basic concepts, current trends and novel applications, J. Phys. Condens. Matter. 14 (2002) R1297–R1355. https://doi.org/10.1088/0953-8984/14/50/202.

[155] R. Car, M. Parrinello, Unified Approach for Molecular Dynamics and Density-Functional Theory, Phys. Rev. Lett. 55 (1985) 2471–2474. https://doi.org/10.1103/PhysRevLett.55.2471.

[156] J.D. Jackson, Classical electrodynamics, 3rd ed., John Wiley & Sons Inc., New York, 1998.

[157] E. Lidorikis, S. Egusa, J.D. Joannopoulos, Effective medium properties and photonic crystal superstructures of metallic nanoparticle arrays, J. Appl. Phys. 101 (2007) 054304. https://doi.org/10.1063/1.2709863.

[158] A. Taflove, S.C. Hagness, Computational electrodynamics : the finite-difference time-domain method, 3rd ed., Boston, MA, 2005.

List of appended papers and contributions

Paper I

Atomic-Scale Diffusion Rates during Growth of Thin Metal Films on Weakly-Interacting Substrates.
Jamnig, A.; Sangiovanni, D. G.; Abadias, G.; Sarakinos, K.
Scientific Reports 9 (2019), 6640.

I planned and performed all experimental work (film depositions, *in situ* measurements, *ex situ* film characterization) and analyzed all resulting data. I wrote major parts of the article, and act as corresponding author.

Paper II

The Effect of Kinetics on Intrinsic Stress Generation and Evolution in Sputter-Deposited Films at Conditions of High Atomic Mobility.
Jamnig, A.; Pliatsikas, N.; Sarakinos, K.; Abadias, G.
Journal of Applied Physics 127 (2020), 045302.

I planned and performed the majority of the experimental work (film depositions, *in situ* measurements, *ex situ* film characterization with AFM, XRR) and analyzed all resulting data. I wrote major parts of the article, and act as corresponding author.

Paper III

3D-to-2D Morphology Manipulation of Sputter-Deposited Nanoscale Silver Films on Weakly-Interacting Substrates via Selective Nitrogen Deployment for Multifunctional Metal Contacts.
Jamnig, A.; Pliatsikas, N.; Konpan, M.; Lu, J.; Kehagias, T.; Kotanidis, A. N.; Kalfagiannis, N.; Bellas, D. V.; Lidorikis, E.; Kovač, J.; Abadias, G.; Petrov, I. G.; Greene, J. E.; Sarakinos, K.
ACS Applied Nano Materials 3 (2020), acsanm.0c00736.

I was part of the research strategy development, and performed/supervised experimental work (film depositions, *in situ* measurements, *ex situ* film characterization with XRD, XRR) and analysis of resulting data. I was part of writing the article (introduction, relevant experimental sections, discussion).

Paper IV

Manipulation of thin silver film growth on weakly-interacting silicon dioxide substrates using oxygen as a surfactant.
Pliatsikas, N.; Jamnig, A.; Konpan, M.; Delimitis, A.; Abadias, G.; Sarakinos, K.
Journal of Vacuum Science & Technology A 38 (2020), 043406

I was part of the research strategy development, and supervised experimental work (film depositions, *in situ* measurements, *ex situ* film characterization with XRD, XRR) and analysis of resulting data. I took part in writing the article (introduction, discussion).

Paper V

On the effect of copper on the morphological evolution of thin silver films on weakly-interacting silicon dioxide substrates.
Jamnig, A.; Pliatsikas, N.; A.; Abadias, G.; Sarakinos, K.
(Submitted)

I was part of the research strategy development, and performed experimental work (film depositions, *in situ* measurements, *ex situ* film characterization with XRD, XRR, AFM) and analysis of resulting data. I wrote major parts of the article.

Paper VI

The effect of nitrogen on the stress and morphology evolution during growth of thin silver films.
Jamnig, A.; Pliatsikas, N.; Bahsoun, H.; Sarakinos, K.; Barna, P.; Radnóczi, G.; Abadias, G.
(Manuscript in final preparation)

I developed the research strategy, and performed experimental work (film depositions, *in situ* measurements, *ex situ* film characterization with XRD, XRR, AFM) and analysis of resulting data. I wrote major parts of the article.

List of related but not included work

Paper

Probing the uniformity of silver-doped epitaxial graphene by micro-Raman mapping
Shtepliuk, I.; Ivanov, I. G.;Pliatsikas, N.; Iakimov, T.; Jamnig, A.; Sarakinos, K.; Yakimova, R.
Physica B: Condensed Matter 580 (2020), 411751.

Paper

Interplay between thin silver films and epitaxial graphene
Shtepliuk, I.; Ivanov, I. G.; Pliatsikas, N.; Ben Sedrine, N.; Andersson, O.; Iakimov, T.; Jamnig, A.; Sarakinos, K.; Yakimova, R.
Surface and Coatings Technology 381 (2020), 125200.

Paper I

Atomic-scale diffusion rates during growth of thin metal films on weakly-interacting substrates

A. Jamnig[1,2,*], D.G. Sangiovanni[3,4], G. Abadias[1], and K. Sarakinos[2]

*Corresponding author

[1]Institut Pprime, Département Physique et Mécanique des Matériaux, UPR 3346 CNRS, Université de Poitiers, SP2MI, 11 Bvd M. et P. Curie, BP 30179, F86962 Chasseneuil-Futuroscope Cedex, France

[2]Nanoscale Engineering Division, Department of Physics, Chemistry, and Biology, Linköping University, SE 581 83, Linköping, Sweden

[3]Atomistic Modelling and Simulation, ICAMS, Ruhr-Universität Bochum, D-44801 Bochum, Germany

[4]Theoretical Physics Division, Department of Physics, Chemistry, and Biology, Linköping University, SE 581 83, Linköping, Sweden

Scientific Reports 9 (2019), 6640.

https://doi.org/10.1038/s41598-019-43107-8

SCIENTIFIC REPORTS

Atomic-scale diffusion rates during growth of thin metal films on weakly-interacting substrates

Received: 13 November 2018
Accepted: 16 April 2019

A. Jamnig[1,2], D. G. Sangiovanni[3,4], G. Abadias[1] & K. Sarakinos[2]

We use a combined experimental and theoretical approach to study the rates of surface diffusion processes that govern early stages of thin Ag and Cu film morphological evolution on weakly-interacting amorphous carbon substrates. Films are deposited by magnetron sputtering, at temperatures T_S between 298 and 413 *K*, and vapor arrival rates *F* in the range 0.08 to 5.38 *monolayers/s*. By employing *in situ* and real-time sheet-resistance and wafer-curvature measurements, we determine the nominal film thickness Θ at percolation (Θ_{perc}) and continuous film formation (Θ_{cont}) transition. Subsequently, we use the scaling behavior of Θ_{perc} and Θ_{cont} as a function of *F* and T_s, to estimate, experimentally, the temperature-dependent diffusivity on the substrate surface, from which we calculate Ag and Cu surface migration energy barriers E_D^{exp} and attempt frequencies ν_0^{exp}. By critically comparing E_D^{exp} and ν_0^{exp} with literature data, as well as with results from our *ab initio* molecular dynamics simulations for single Ag and Cu adatom diffusion on graphite surfaces, we suggest that: (i) E_D^{exp} and ν_0^{exp} correspond to diffusion of multiatomic clusters, rather than to diffusion of monomers; and (ii) the mean size of mobile clusters during Ag growth is larger compared to that of Cu. The overall results of this work pave the way for studying growth dynamics in a wide range of technologically-relevant weakly-interacting film/substrate systems—including metals on 2D materials and oxides—which are building blocks in next-generation nanoelectronic, optoelectronic, and catalytic devices.

The fabrication of heterostructure devices founded upon weakly-interacting 2D-material (e.g., graphene and MoS_2) and oxide (e.g., TiO_2 and ZnO) substrates largely relies on the essential step of growing thin metal films with controlled morphology, to serve as electrical contacts, or active optical and catalytic layers[1–4]. Such films are typically synthesized via condensation from the vapor phase, and their morphology is, predominantly, governed by the occurrence rates of atomic-scale surface diffusion processes during early growth stages[5]. These rates are not well-established in the literature—as opposed to the case of metal-on-metal homoepitaxial growth[6–9]—and they are estimated indirectly, either by post-deposition *ex situ* analyses of island densities and sizes using electron and atomic force microscopies[10–12], or by studying de-wetting of continuous metal layers upon annealing[12,13].

Lü *et al.*[14] have recently suggested a method for determining, *in situ* and in real time, the effective atomic-scale surface diffusivity during metal film growth on weakly-interacting substrates, by using scaling relations of the nominal film thickness Θ at characteristic morphological transitions (elongation, percolation and continuous film formation) with respect to the deposition rate *F*. They also argued that the accuracy of this method can be further improved by studying the way by which the deposition temperature T_S affects film morphological evolution, as this would allow to gauge the effect of surface vibrations on diffusion dynamics.

In the present work, we use the method originally presented in ref.[14] to study growth of sputter-deposited Ag and Cu films on weakly-interacting amorphous carbon (a-C) substrates, for T_S between 298 and 413 *K*, and *F* in the range 0.08 to 5.38 *monolayers*/*s*(*ML*/*s*). We determine Θ at percolation (Θ_{perc}) and continuous film formation (Θ_{cont}) transitions by means of *in situ* and real-time sheet-resistance and wafer-curvature measurements, respectively. Using the scaling behavior of Θ_{perc} and Θ_{cont} as function of *F* and T_S, we estimate a temperature-dependent Ag diffusivity on the substrate surface $D_{Ag}(T_S)$, which is up to three orders of magnitude larger than the diffusivity

[1]Institut Pprime, Département Physique et Mécanique des Matériaux, UPR 3346 CNRS, Université de Poitiers, SP2MI, 11 Bvd M. et P. Curie, F 86073, Poitiers Cedex 9, France. [2]Nanoscale Engineering Division, Department of Physics, Chemistry, and Biology, Linköping University, SE 581 83, Linköping, Sweden. [3]Atomistic Modelling and Simulation, ICAMS, Ruhr-Universität Bochum, D-44801, Bochum, Germany. [4]Theoretical Physics Division, Department of Physics, Chemistry, and Biology, Linköping University, SE 581 83, Linköping, Sweden. Correspondence and requests for materials should be addressed to A.J. (email: andreas.jamnig@liu.se)

of Cu $D_{Cu}(T_S)$. Linear regression analysis of $\ln(D_{Ag}(T_S))$ and $\ln(D_{Cu}(T_S))$ vs. $1/T_S$ data enables us to extract Ag and Cu surface diffusion energy barriers E_D^{exp} and attempt frequencies ν_0^{exp}. We also perform *ab initio* molecular dynamics (AIMD) simulations—within the framework of density functional theory (DFT)—of single Ag and Cu adatom diffusion on graphite surface for $T_S = 300–1000\,K$, from which we compute adatom surface migration energy barriers and attempt frequencies. By critically comparing E_D^{AIMD} and ν_0^{AIMD} with their respective experimental values, as well as with literature data, we suggest that: (i) E_D^{exp} and ν_0^{exp} correspond to metal cluster diffusion on a-C substrates, which is the rate limiting process for determining the early-stage Ag and Cu film morphology, and (ii) the mean size of mobile Ag clusters is larger than that of Cu clusters. The overall results of this work are the first step toward determining diffusion rates in film/substrate systems which are relevant for device fabrication in the areas of nanoelectronics, catalysis, and architectural glazing[3,15].

The paper is organized as follows: First, we present a brief theoretical background concerning the scaling laws of Θ at characteristic morphological transitions during growth of metals on weakly-interacting substrates and we discuss the way by which these laws are used to calculate atomic surface diffusion rates. Then, experimental and simulation results are presented and discussed. Finally, the overall study is summarized. The section "Methods" outlines the experimental procedures employed in this study and provides a description of the methodology used for DFT-based calculations and simulations.

Morphological Transitions and their Scaling Behavior

Thin film growth starts with nucleation of isolated islands, which grow in size, until they impinge on each other and start to coalesce. As island size increases further, with continued deposition and coalescence, material redistribution among islands becomes progressively slow, which eventually stops the process of coalescence and leads to the formation of a percolated network of interconnected islands separated by voids. Further deposition fills the inter-island space until a continuous film is formed.

Metal islands deposited on weakly-interacting substrates typically exhibit a pronounced 3D shape[16–18]. The time τ_{coal} required for completion of coalescence of a pair of such islands—i.e., the time from island impingement until the equilibrium shape of the island pair is established—can be approximated by the classical expression developed by Nichols[19] for sintering as $\tau_{coal} = \frac{R^4}{B}$; where R is the radius of the smaller island in the coalescing pair, and B is the coalescence-rate parameter that scales with the adatom self-diffusivity D_s. According to the expression $\tau_{coal} = \frac{R^4}{B}$, as R increases, τ_{coal} increases as well, and there is a critical R value at which τ_{coal} becomes longer than the time required for a third island to impinge on a coalescing island pair. This point during growth corresponds to the so-called *elongation transition*, beyond which the film surface consists predominantly of elongated non-coalesced groups of islands.

Analytical modelling, based on the droplet growth theory[20,21], and kinetic Monte Carlo simulations[22–26] suggest that, for film materials and deposition parameters for which coalescence is the dominant process during early stages of film growth (*coalescence-controlled regime*), the nominal film thickness at the elongation transition Θ_{elong} scales with F as

$$\Theta_{elong} \sim \left(\frac{B}{F}\right)^{\frac{1}{3}}. \tag{1}$$

This expression encodes the effect of dynamic competition among island growth and coalescence on film morphological evolution. For a constant coalescence-rate parameter B, increase of F yields a larger island growth rate, so that an elongated surface morphology is attained at smaller nominal thicknesses. Conversely, increase of B, at a constant F, promotes coalescence completion relative to island growth, thereby delaying the occurrence of elongation transition.

For a given film/substrate system, one can determine deposition conditions in terms of F and T_S, for which coalescence is not completed throughout all stages of growth (*coalescence-free regime*)[23,27]. In this case, Θ_{elong} becomes proportional to the island-island separation distance when island density reaches saturation N_{sat}[22,28], i.e., $\Theta_{elong} \sim \mathrm{N}_{sat}^{-\frac{1}{2}}$. From the atomistic nucleation theory[29], N_{sat} for 3D growth is calculated by the expression $\mathrm{N}_{sat} \sim \left(\frac{F}{D}\right)^{\frac{2}{7}}$, which yields

$$\Theta_{elong} \sim \left(\frac{D}{F}\right)^{\frac{1}{7}}. \tag{2}$$

We note here that the expression $\mathrm{N}_{sat} \sim \left(\frac{F}{D}\right)^{\frac{2}{7}}$ holds for a critical cluster size $i^* = 1$ (i^* is expressed in number of atoms)—i.e., for the case of a dimer being the smallest stable island on the substrate surface—and for immobile clusters[30]. The validity of the condition $i^* = 1$ and the implications of cluster mobility for the conclusions drawn in the present study are elaborated upon in the "Discussion" section.

The adatom surface diffusivity D in Eq. (2) is equal to

$$D = D_0 \exp\left(-\frac{E_D}{k_B T_S}\right). \tag{3}$$

The prefactor D_0 can be approximated as $D_0 = \frac{1}{4}\nu_0 a^2$, where ν_0 is the attempt frequency for adatom migration and a is the minimum adatom translational hopping distance on the substrate surface. E_D is the surface diffusion

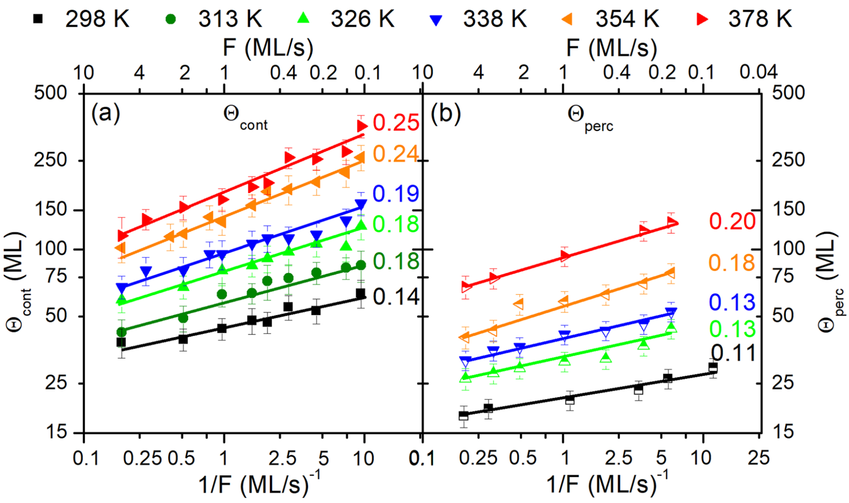

Figure 1. Evolution of (**a**) continuous film formation thickness Θ_{cont} and (**b**) percolation thickness Θ_{perc} during growth of Ag on amorphous carbon as a function of inverse deposition rate $1/F$ at various growth temperatures T_S. F values are presented in the top axis for clarity. Error bars correspond to the standard error during acquisition of the (**a**) $\sigma \times \Theta$, (**b**) R_S vs. Θ data and the graphical determination of Θ_{cont} and Θ_{perc} values, respectively. The numbers next to each T_S set are the slopes of linear fits to the data points in log-log scale.

activation barrier. It should be noted that D_S, which largely determines B, is also calculated from Eq. (3), by using the E_D, ν_0, and a values for the surface of the deposited film material. In analogy to coalescence-controlled growth (Eq. (1)), Eq. (2) reflects the way by which the interplay among island nucleation and growth affects the early-stage film morphology. Increase of D, for a given F, favors growth of existing islands, at the expense of nucleation of new ones, resulting in an increase of the nominal thickness required for the onset of island-island impingement. In the opposite case, larger F, for a constant D, promotes nucleation, and pushes elongation to occur at smaller nominal thicknesses.

The growth regimes with respect to coalescence can be identified experimentally using the following procedure: (i) establish the existence of a linear relationship between Θ_{elong} and $1/F$ in logarithmic scale; (ii) determine the slope of the linear function that describes Θ_{elong} vs. $1/F$ data; and (iii) compare this slope with the scaling exponents in Eqs (1) and (2). By repeating steps (i) through (iii) for various T_S values in the *coalescence-free* (*coalescence-controlled*) growth regime, temperature-dependent $D(T_S)$ ($B(T_S)$) values can be calculated. From this, surface diffusion (self-diffusion) energy barriers and attempt frequencies can be extracted via linear regression on $\ln(D(T_S))$ ($\ln(B(T_S))$) vs. $1/T_S$ data. It should be noted that the elongation transition is an intrinsically abstract concept, i.e., Θ_{elong} is difficult to determine experimentally[14]. Hence, the scaling behavior in view of Eqs (1) and (2) is, typically, studied using later morphological transition thicknesses, i.e., Θ_{perc} and Θ_{cont}[23,24], which have been shown to scale linearly with Θ_{elong}[14,23,31]. In the present study, we implement the above-explained procedure for determining surface migration energy barriers and attempt frequencies during film growth of Ag and Cu on a-C. We employ sputter deposition to access multiple growth regimes and establish the Θ_{perc} and Θ_{cont} vs. $1/F$ relationships at multiple T_S values.

Results

Film morphological transitions and evolution.

The evolution of Θ_{cont} vs. $1/F$ (in logarithmic scale), for the Ag/a-C film/substrate system, at $T_S = 298$–$378\,K$, is plotted in Fig. 1(a). Representative curves of the film stress-thickness product ($\sigma \times \Theta$) vs. Θ, from which Θ_{cont} is determined, are shown in Fig. S1 in the Supplemental Material[32]. Details on the stress measurement methodology can be found in the "Methods" section. We see in Fig. 1(a) that Θ_{cont} varies linearly with $1/F$, for all T_S values, with the slope χ (i.e., the exponent of the $\Theta_{cont} \sim (1/F)^{\chi}$ function in linear scale) indicated next to each set of data. For $T_S = 298\,K$, an exponent χ of 0.14 is obtained, which matches the theoretical value for *coalescence-free* growth (1/7, see Eq. (2)). Furthermore, this result is in excellent agreement with the scaling exponent found by Lü *et al.*[25]—using *in situ* spectroscopic ellipsometry—for room-temperature sputter-deposition of Ag films on SiO_2.

Increase of the growth temperature to the two largest values of 354 and 378 K, yields $\chi = 0.24$–0.25, which is smaller than the theoretical value of 1/3 for *coalescence-controlled* growth (see Eq. (1)). Lü *et al.*[25] have suggested that Θ_{cont} values which scale as a function of $1/F$ with an exponent χ in the range 0.25 to 0.28 are associated with a broad transition region (spanning up to two orders of magnitude in F) between *coalescence-controlled* and *coalescence-free* growth regimes. In addition, Fig. 1(a) shows that $\chi = 0.18$–0.19 for $313 \le T_S \le 338\,K$, which is also an indication that the transition between the two growth regimes occurs gradually. Finally, we note that it

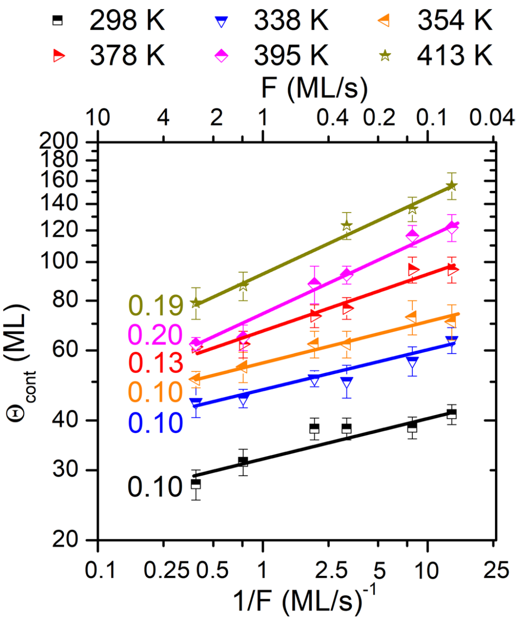

Figure 2. Evolution of continuous film formation thickness Θ_{cont} during growth of Cu on amorphous carbon as a function of inverse deposition rate $1/F$ at various growth temperatures T_S. F values are presented in the top axis for clarity. Error bars correspond to the standard error during acquisition of the $\sigma \times \Theta$ vs. Θ data and the graphical determination of the Θ_{cont} values. The numbers next to each T_S set are the slopes of linear fits to the data points in log-log scale.

was not possible to determine Θ_{cont} for $T_S > 378\,K$, as the intrinsic stress in the film becomes too small and the *in situ* curvature measurements unreliable.

The dependence of Θ_{perc} on $1/F$ is presented in Fig. 1(b) in logarithmic scale, while typical film resistivity (R_S) vs. Θ curves, which are used for determining Θ_{perc}, are provided in Fig. S2 in the Supplemental Material[32]. Details on the film resistivity measurement methodology can be found in the "Methods" section. For each set of F and T_S values in Fig. 1(b), Θ_{perc} is smaller than the corresponding Θ_{cont}, and the two thicknesses exhibit a nearly constant $\frac{\Theta_{perc}}{\Theta_{cont}}$ ratio $\kappa \sim 0.5$ at all deposition conditions. The relationship $\Theta_{perc} < \Theta_{cont}$ is consistent with the growth evolution stages explained in the "Morphological transitions and their scaling" section; a continuous layer is formed when deposited material fills the inter-island space of a percolated film.

Analysis of the scaling behavior $\Theta_{perc} \sim (1/F)^{\chi}$ shows that, at $T_S = 298\,K$, a χ value of 0.11 is obtained, which gradually increases to $\chi = 0.2$ upon increasing temperature to $T_S = 378\,K$. Moreover, we see that the χ values for Θ_{perc} are slightly smaller than the corresponding exponents for Θ_{cont}. Despite the small quantitative differences in the scaling exponents of Θ_{perc} and Θ_{cont} vs. $1/F$, the overall asymptotic qualitative trends in Fig. 1 indicate a transition from *coalescence-free* toward *coalescence-controlled* growth with increasing T_S.

In situ and real-time wafer-curvature measurements were also employed during Cu growth on a-C (see Fig. S3 in Supplemental Material[32] for representative $\sigma \times \Theta$ vs. Θ curves), from which Θ_{cont} was determined. Θ_{cont} vs. $1/F$ data are plotted in Fig. 2 for T_S in the range 298 to 413 K. As in the Ag/a-C system, a linear relationship between Θ_{cont} and $1/F$ is observed, and the corresponding slopes χ are given next to each dataset. The scaling exponent χ equals 0.10 for $T_S = 298$–$354\,K$, and increases slightly to 0.13 for $T_S = 378\,K$. For temperatures above 378 K, χ takes a value of 0.19–0.20. The evolution of χ vs. T_S described above is qualitatively similar to that of Ag, and supports the fact that an increase in T_S favors *coalescence-controlled* growth.

Comparison between Figs 1(a) and 2 shows that Θ_{cont} for Cu lies in the range 25 to 150 ML, which is smaller than the corresponding values determined for Ag ($40\,ML < \Theta_{cont} < 360\,ML$). These differences imply that, at the deposition conditions used in the present work, nucleation (coalescence) rates are smaller (larger) for Ag compared to Cu, leading to a more pronounced 3D morphology in the Ag/a-C system.

We also determined Θ_{perc} from *in situ* and real-time sheet-resistance measurements for Cu, for selected F values and $T_S \leq 354\,K$. The results (not presented here) reveal that $\Theta_{perc} < \Theta_{cont}$ with $\kappa = \frac{\Theta_{perc}}{\Theta_{cont}} \sim 0.3$, while the $\Theta_{perc} \sim (1/F)^{\chi}$ scaling exponent χ is equal to 0.07–0.08. These values are qualitatively consistent with the results for the Ag/a-C system, where χ for Θ_{perc} was found to be lower than the corresponding value for Θ_{cont}. The overall results for Θ_{perc} and Θ_{cont} indicate that the morphological evolution of Cu films on a-C proceeds in the *coalescence-free* growth regime for $T_S \leq 378\,K$.

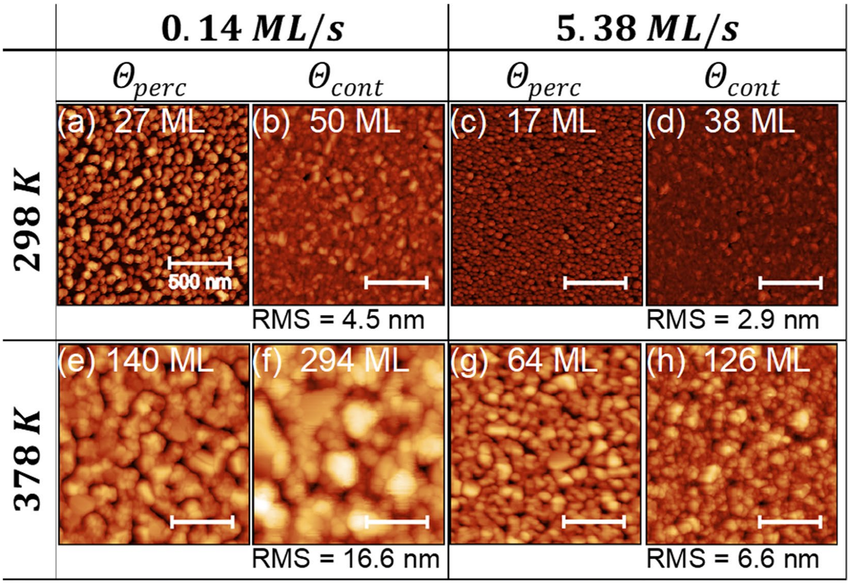

Figure 3. Atomic force microscopy images of the surface morphology of Ag grown on amorphous carbon at deposition temperatures T_S of 298 K ((**a**–**d**)) and 378 K ((**e**–**h**)) and deposition rates F of 0.14 ML/s ((**a**,**b**,**e**,**f**)) and 5.38 ML/s ((**c**,**d**,**g**,**h**)). For each pair of deposition parameters T_S and F, images of films at percolation Θ_{perc} ((**a**,**c**,**e**,**g**)) and continuous film formation Θ_{cont} thicknesses ((**b**,**d**,**f**,**h**)) are presented. The nominal thickness is indicated in the respective figures, and root-mean-square roughness (RMS) values are given for the continuous films. The height scale is 60 nm for images (**a**–**d**), (**g**,**h**), and 120 nm for images (**e**,**f**).

In order to confirm the film morphological transitions and evolution inferred by the *in situ* data in Figs 1 and 2, we studied *ex situ* the film surface topography by atomic force microscopy (AFM). Figure 3 presents AFM images recorded for Ag films grown on a-C at Θ_{perc} and Θ_{cont}, and at the following sets of conditions: (i) $T_S = 298\,K$ and $F = 0.14\,ML/s$ (Fig. 3(a,b)), (ii) $T_S = 298\,K$ and $F = 5.38\,ML/s$ (Fig. 3(c,d)), (iii) $T_S = 378\,K$ and $F = 0.14\,ML/s$ (Fig. 3(e,f)), and (iv) $T_S = 378\,K$ and $F = 5.38\,ML/s$ (Fig. 3(g,h)). At all conditions imaged in Fig. 3, the fraction of the substrate area covered by the Ag films is larger at Θ_{cont}, as compared to Θ_{perc}, which provides further support to the fact that the experimentally determined values of Θ_{perc} and Θ_{cont} in Figs 1 and 2 are consistent with the different stages of film morphological evolution.

Moreover, Fig. 3 shows that, for a given deposition rate, increase of T_S from 298 K to 378 K leads to an increase of the size of the features (i.e., islands) on the film surface, compare, e.g., Fig. 3(b) vs. (f) and Fig. 3(d) vs. (h). These differences in morphology translate into changes of the surface roughness, e.g., the root-mean-square roughness (RMS) value of a Ag film at Θ_{cont}, grown with $F = 0.14\,ML/s$, increases from 4.5 to 16.6 nm when T_S is increased from 298 to 378 K (Fig. 3(b) vs. (f)). Conversely, increase of F for a given growth temperature leads to smoother films. As an example, the RMS roughness value of 16.6 nm of a Ag film at Θ_{cont}, grown with $F = 0.14\,ML/s$ and at $T_S = 378\,K$ (Fig. 3(f)) decreases to 6.6 nm, when increasing F to 5.38 ML/s for the same growth temperature (Fig. 3(h)).

AFM measurements were also performed for Cu films grown on a-C, and the results were again found consistent with the *in situ* analysis data. Cu shows a smoother surface morphology, as compared to Ag, for similar deposition conditions, (see Fig. S4 in the Supplemental Material[32]). At Θ_{cont}, the RMS roughness of Ag (6.6 nm) is higher than that of Cu (1.7 nm), and this trend persists for nominal thicknesses of $\Theta \cong 450\,ML$, where Ag films (10.9 nm) remain rougher than Cu films (6.2 nm).

Atomic-scale diffusion rates. As discussed in the previous section, the results in Figs 1 and 2 indicate that increase of T_S causes a transition toward *coalescence-controlled* growth, which is in agreement with previously reported data by Warrender and Aziz[24] and Lü *et al.*[25]. However, there is no set of Θ_{perc} and Θ_{cont} vs. $1/F$ data that can be clearly associated with this growth regime. Concurrently, the scaling exponent χ for Ag ($T_S \leq 338\,K$) and Cu ($T_S \leq 378\,K$) matches, or is in close agreement with the theoretically-predicted value of 1/7 for *coalescence-free* growth for $i^* = 1$. Based on the arguments presented above, in the remainder of the manuscript we use data in the *coalescence-free* growth regime to determine the surface diffusivity D.

Previous studies in homoepitaxial Ag/Ag(100)[33] and Cu/Cu(100)[34] systems report $i^* = 1$ for $T_S = 295$ and 213 K, respectively, but also emphasize the tendency toward larger i^* values for higher deposition temperatures (Ag, Cu) and deposition rates below $2 \times 10^{-4}\,ML/s$ (Cu). This tendency is significantly reduced in

	$E_{ads,Ag(Cu)}$ (eV)			
	Atop	**Bridge**	**Hollow**	$E_{b,Ag_2(Cu_2)}$ (eV)
Ag	−0.21	−0.21	−0.20	1.89
Cu	−0.49	−0.49	−0.33	2.21

Table 1. Values of Ag and Cu adatom adsorption energies $E_{ads,Ag(Cu)}$ (atop, bridge, and hollow sites) and Ag_2 and Cu_2 addimer binding energies $E_{b,Ag_2(Cu_2)}$ on the graphene surface calculated via DFT at $0\,K$.

weakly-interacting film/substrate systems, including Ag and Cu on graphite, for which early STM studies[35–37] show that dimers are stable at room temperature. This behavior is consistent with the binding energies of ~2 eV for Ag and Cu addimers on graphite, obtained by our DFT calculations (see Table 1; details on the DFT calculation methodology are provided in the "Methods" section) and reported in the literature[38]. Thus, we conclude that the condition $i^* = 1$ is a realistic scenario for the film/substrate systems studied and the growth conditions employed in the present work.

For a mathematically rigorous calculation of D, we take $\mathrm{N}_{sat} = \eta\left(\frac{F}{D}\right)^{\frac{2}{7}}$[39], so that Eq. (2) becomes,

$$\Theta_{elong} = \eta^{-\frac{1}{2}}\left(\frac{D}{F}\right)^{\frac{1}{7}}. \tag{4}$$

In Eq. (4), η is a proportionality factor that accounts for the dimensionality of the growing islands and i^*[39]. $\eta(i^* = 1) = 0.13$, for 3D island growth, and when island saturation density is reached (at $\Theta \sim 0.4\,ML$ according to growth simulation data from ref.[31]). We convert Θ_{cont} to Θ_{elong} using the ratios $\kappa = \Theta_{perc}/\Theta_{cont} = 0.5$ and 0.3 for Ag and Cu, respectively (see section "Film morphological transitions and evolution"), and the relationship $\Theta_{perc}/\Theta_{elong} = 1.9$, as suggested by Carrey and Maurice for *coalescence-free* growth[23]. By substituting the above ratios to Eq. (4) and solving for D, we obtain

$$D(T_S, F) = F\eta^{\frac{7}{2}}\left(\frac{\kappa}{1.9}\Theta_{cont}\right)^{7}. \tag{5}$$

We then calculate $D(T_S)$ from Eq. (5), by averaging diffusivities for all F values for a given T_S.

$\ln(D(T_S))$ vs. $1/T_S$ data for Ag (black squares) and Cu (red circles) are plotted in Fig. 4. We find that $D_{Ag}^{exp}(T_S)$ lies in the range 10^4 to 10^7 a^2/s, with the corresponding values for Cu being between 10^1 and 10^4 a^2/s. In addition, for both Ag and Cu, $\ln(D(T_S))$ scales linearly with $1/T_S$, which enables us to calculate the following experimental values for E_D and ν_0: $E_{D,Ag}^{exp} = 1.28 \pm 0.02\ eV$, $E_{D,Cu}^{exp} = 0.64 \pm 0.03\ eV$, $\nu_{0,Ag}^{exp} = 2.3\ (\times 2.4^{\pm 1}) \times 10^{25}\ Hz$, and $\nu_{0,Cu}^{exp} = 8.2\ (\times 2.3^{\pm 1}) \times 10^{11}\ Hz$. Besides the experimental data, Fig. 4 also presents $\ln(D(T_S))$ vs. $1/T_S$ values for Ag (hollow black squares) and Cu (hollow red circles) single adatom diffusion on graphite, as determined by AIMD simulations. $D^{AIMD}(T_S)$ ranges from 10^{11} to $10^{13} a^2/s$ for both Ag and Cu for T_S between 300 and $1000\,K$, which yields $E_{D,Ag(Cu)}^{AIMD}$ values of $0.10 \pm 0.02 (0.09 \pm 0.04)\ eV$, and attempt frequencies $\nu_{0,Ag}^{AIMD}$ and $\nu_{0,Cu}^{AIMD}$ of 1.4 $(\times 1.5^{\pm 1}) \times 10^{12}$ and 8.3 $(\times 2.6^{\pm 1}) \times 10^{11}\,Hz$, respectively. These ν_0^{AIMD} values correspond to $D_{0,Ag}^{AIMD}$ and $D_{0,Cu}^{AIMD}$ of 3.17 $(\times 1.5^{\pm 1}) \times 10^{-3}$ and 1.44 $(\times 2.6^{\pm 1}) \times 10^{-3}\ cm^2/s$, respectively.

Discussion

The up to ten orders of magnitude larger AIMD diffusivities, in comparison to the experimentally-determined values, and the considerably larger E_D^{exp} vs. E_D^{AIMD} values, indicate that the rate-limiting atomic-scale process that controls early film growth stages and sets Θ_{elong} for Ag and Cu on a-C, at the growth conditions employed in the present work, is diffusion of multi-atomic clusters. This is consistent with experimental data showing that Ag clusters are mobile on C-based substrates[40], even at room temperature It should be noted that in case clusters are mobile, the scaling exponent y in the relation $N_{sat} \sim \left(\frac{F}{D}\right)^{y}$ is expected to be larger than the value 2/7 for immobile clusters[30]. This would yield a $D \sim {\Theta_{cont}}^{2/y}$ power law with $\frac{2}{y} < 7$ compared to the value $\frac{2}{y} = 7$ in Eq. (5). Hence, the diffusivity values plotted in Fig. 4 are to be seen as an upper limit, which means that the conclusions drawn based on the result $D^{AIMD}(T_S) \gg D^{exp}(T_S)$ still hold.

Attempt frequencies for metal adatom surface diffusion are typically of the order of 10^{12}–$10^{13}\,Hz$[41], with our ν_0^{AIMD} values being within this range for both Ag and Cu. Compared to single adatoms, clusters may exhibit considerably larger attempt frequencies. For example, Wang *et al.*[42] have encountered values of ~$10^{16}\,Hz$ for diffusion of *compact* Ir clusters consisting of 19 atoms on Ir(111), while Bardotti *et al.*[43] found that Au_N and Sb_N clusters ($N = 100$–1000 atoms) diffuse on graphite surfaces with attempt frequencies of the of the order of ~$10^{20}\,Hz$. The considerably larger, with respect to adatoms, ν_0 values for clusters reported in refs. [42,43]. have been interpreted as an effect originating from multiple vibrational degrees of freedom within the cluster, augmented by dynamical mismatch (i.e., the substrate internal vibrations are decoupled from those within the cluster) and weak interactions between the cluster and the substrate[44–46]. Deltour *et al.*[46] suggested that the propensity of clusters to support internal vibrational states increases with the cluster size. Krylov[45] used an analytical kinetic model of particle-on-substrate diffusion and showed that surface gliding attempt frequency of an one-dimensional cluster consisting of N atoms increases as $\sim N^{\alpha}$, where $\alpha \gg 1$, while the activation energy increases as $\sim N^{\beta}$, with $\beta < 1$. In view of the arguments outlined above, the fact that $\nu_{0,Cu}^{exp} < \nu_{0,Ag}^{exp}$ may be attributed to differences in cluster size

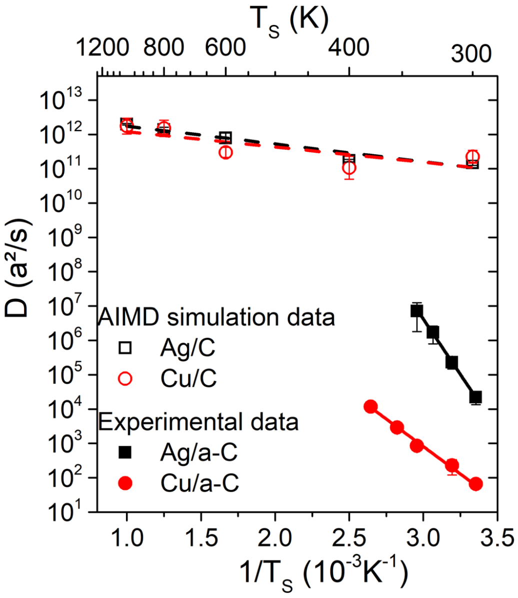

Figure 4. Surface diffusivity D as function of temperature T_S, as calculated from Eq. (5) from continuous film formation thickness Θ_{cont} for Ag and Cu diffusion on amorphous carboon (a-C). Hollow symbols correspond to single adatom diffusivity calculated from *ab initio* molecular dynamics (AIMD) simulations (black squares for Ag, red circles for Cu) for diffusion on single-layer graphite. Error bars of the experimental data correspond to the standard deviation after averaging $D(F, T_S)$ over deposition rate F, and error bars of AIMD data correspond to the standard deviation of the slopes of adatom mean-square displacements vs. time. Lines represent linear fits of the experimental (full lines) and simulation (dashed lines) data points in the Arrhenius plot.

between the two metals, whereby Ag forms larger mobile clusters than Cu. It is also noteworthy that, even though $E_{D,Ag}^{exp} > E_{D,Cu}^{exp}$, surface diffusivity for the Ag/a-C system is up to three orders of magnitude larger than that for Cu on a-C. This highlights the importance of knowledge of both diffusion barrier and attempt frequency, in order to determine rates of atomic-scale structure-forming processes. This is particularly relevant for film/substrate systems in which adatom diffusion is not the rate limiting step that governs morphological evolution.

Summary and Outlook

The rates of atomic-scale processes that control the early stages of thin metal film growth on weakly-interacting substrates are not well established in the literature. In the present work, we contributed to the afore-mentioned gap in knowledge by implementing a method suggested recently by Lü *et al.*[14],—this method utilizes scaling relations of the nominal film thickness Θ at characteristic morphological transitions as a function of deposition temperature T_S and rate F—to determine atomic-scale surface diffusion rates during sputter-deposition of Ag and Cu films on a-C substrates.

We determined Θ at percolation (Θ_{perc}) and continuous film formation (Θ_{cont}) transition for T_s between 298 and 413 K, F in the range 0.08 to 5.38 *monolayers/s*, from which we estimated the temperature-dependent atomic diffusivity $D_{Ag}(T_S)$ and $D_{Cu}(T_S)$ on the substrate surface and calculated, experimentally, the following migration energy barriers E_D^{exp} and attempt frequencies ν_0^{exp}: $E_{D,Ag}^{exp} = 1.28 \pm 0.02\ eV$, $E_{D,Cu}^{exp} = 0.64 \pm 0.03\ eV$, $\nu_{0,Ag}^{exp} = 2.3\ (\times 2.4^{\pm 1}) \times 10^{25}\ Hz$, and $\nu_{0,Cu}^{exp} = 8.2(\times 2.3^{\pm 1}) \times 10^{11}\ Hz$. We also performed *ab initio* molecular dynamics (AIMD) simulations, within the framework of density functional theory, and studied diffusion of Ag and Cu adatoms on graphite for $T_S = 300\text{–}1000\ K$. Analysis of AIMD results yielded adatom migration energy barriers $E_{D,Ag(Cu)}^{AIMD} = 0.10 \pm 0.02\ (0.09 \pm 0.04)\ eV$, and attempt frequencies $\nu_{0,Ag}^{AIMD}$ and $\nu_{0,Cu}^{AIMD}$ of $1.4\ (\times 1.5^{\pm 1}) \times 10^{12}$ and $8.3\ (\times 2.6^{\pm 1}) \times 10^{11}\ Hz$, respectively. By critically comparing experiments, simulations and literature data we suggest that: (i) the experimentally-determined diffusivities of Ag and Cu correspond to cluster diffusion, rather than to diffusion of isolated monomers; and (ii) Ag forms larger mobile clusters than Cu on a-C.

The overall results of this work open the way for determining diffusion rates during growth of metals on a wide range of weakly-interacting film/substrate systems. Knowledge of these rates can be used to develop strategies for selectively manipulating atomic processes that drive film morphological evolution, by e.g., use of surfactants[47–49] or temporally modulated fluxes[9]. Such approaches may, for example, be relevant for directed growth of metals on 2D-material (e.g., graphene and MoS_2) and oxide (e.g., TiO_2 and ZnO) substrates, and thereby fabricate high-performance nanoelectronic, catalytic, and optical devices[3,15].

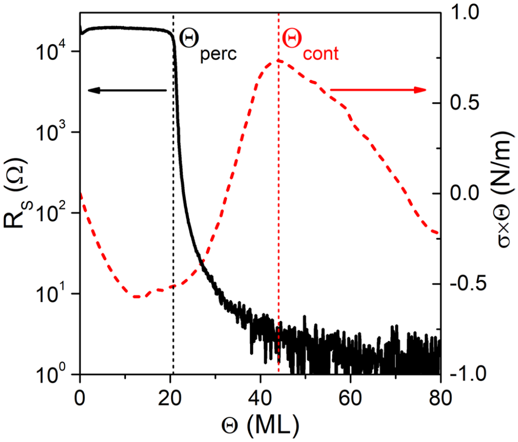

Figure 5. *In situ* and real-time measured evolution of sheet resistance R_S (left axis, black solid line) and stress-thickness product $\sigma \times \Theta$ (right axis, red dashed line) as function of the nominal film thickness Θ, for Ag grown on amorphous carbon with deposition rate $F = 1\,ML/s$ and at growth temperature $T_S = 298\,K$. The abrupt drop in the R_S vs. Θ curve at ~20 *ML* marks the percolation transition thickness Θ_{perc}, while the position of the tensile-to-compressive peak in the $\sigma \times \Theta$ vs. Θ curve at ~42 *ML* corresponds to the continuous film formation thickness Θ_{cont}.

Methods

Film growth. Ag and Cu films were deposited by direct current magnetron sputtering in a high-vacuum chamber (base pressure ~$8 \times 10^{-6}\,Pa$). Ar gas (purity 99.999%) at a pressure of 0.25 *Pa* was used to generate plasma and sputter magnetron sources were equipped with Ag (diameter 7.62 *cm*, purity 99.99%) and Cu (diameter 7.62 *cm*, purity 99.999%) targets. The target-to-substrate distance was 180 *mm*, to minimize radiative heating and energetic bombardment of the film by backscattered Ar atoms, while the angle between substrate and target normal was 25°. Films were grown on Si (100) substrates covered by a 6.5 *nm* thick a-C layer grown *in situ*, prior to Ag and Cu deposition, by sputtering a graphite target (7.62 *cm*, purity 99.995%), with a power of 150 *W*, at an Ar pressure of 0.25 *Pa*. Ag and Cu films were then deposited with growth rates in the respective ranges 0.11 to 5.38 *ML/s* and 0.08 to 2.5 *ML/s*, set by changing the power applied to the two targets from 5 to 300 *W*. We note that 1 ML corresponds to the distance between (111) crystallographic planes (0.2359 and 0.2089 *nm* for Ag and Cu, respectively). The growth temperature T_S was varied using a resistive heater in the range 298 to 378 *K* for Ag, while the corresponding range for Cu was 298 to 413 *K*. The substrates were heated to T_S and held at this temperature for a period of 1 *h* prior to deposition start. T_S values were confirmed using vacuum-compatible temperature indicators (NiGK Corp.) which change their color irreversibly upon reaching specific temperature (accuracy $\pm 2\,K$ below 410 *K* and $\pm 4\,K$ above 410 *K*). Deposition rates were determined by *ex situ* x-ray reflectometry (XRR) in an XRD 3000 Seifert diffractometer (line focus Cu source, Ge (220) monochromator selecting $K_{\alpha 1}$ Cu radiation). XRR measurements also verified that changing T_S had only minor effects on F for a given target power (<4% variation in the T_S range used in the present study).

Film characterization. Θ_{perc} was determined, *in situ* and in real-time, by measuring the evolution of the film sheet-resistance R_S vs. Θ with a custom-built four-point probe setup[50,51] during deposition on a Si (100) substrate (dimension $1 \times 1\,cm^2$, substrate thickness $d_s = 350\,\mu m$, resistivity ~20 *k*Ω) covered with a 6.5 *nm* a-C layer. Prior to the film growth, two Au stripes (film nominal thickness $\Theta = 100\,nm$, width $w = 2.5\,mm$) were sputter deposited with a Ti adhesion layer ($\Theta = 40\,nm$, $w = 2.5\,mm$) onto the a-C layer to ensure a uniform electrical contact. Figure 5 shows a characteristic example of the R_S vs. Θ evolution during Ag deposition on a-C at $F = 1\,ML/s$ and $T_S = 298\,K$ (left axis, black solid line). R_S exhibits a sharp drop at $\Theta \sim 20\,ML$; this indicates the formation of an electrically conducting film and corresponds to Θ_{perc}.

Θ_{cont} was determined by *in situ* and in real-time measurements of the change of the substrate curvature $\Delta\kappa$ with a multi-beam optical stress sensor (MOSS, k-Space Associates), described in-detail in refs.[52,53]. Stress measurements were performed for samples grown on Si(100) substrates ($d_s = 100 \pm 2\,\mu m$), also covered with a 6.5 *nm* a-C layer. The use of ultra-thin Si(100) wafers allows for a measurement sensitivy of 0.05 N/m[52]. These measurements enable us to monitor the evolution of the film residual stress σ; the film stress-thickness product $\sigma \times \Theta$ is proportional to $\Delta\kappa$ via the Stoney equation $\sigma \times \Theta = \frac{1}{6} Y_s d_s^2 \Delta\kappa$ ($Y_s = 180.5\,GPa$ is the Si(100) substrate biaxial modulus)[54]. The slope of the $\sigma \times \Theta$ vs. Θ curve corresponds to the stress forming in the film, which exhibits a tensile-to-compressive transition (i.e., transition from positive to negative slope) upon reaching Θ_{cont} for films with 3D morphological evolution[55–57]. An example for such measurement is given in Fig. 5 (right axis, red dashed line) for Ag deposited on a-C ($F = 1\,ML/s$ and $T_S = 298\,K$), where the tensile-to-compressive transition is seen at

$\Theta_{cont} \sim 42\,ML$. No abrupt curvature change could be detected in the very early stage of metal film growth, confirming the weak interaction between the metal deposit and a-C layer, which is associated with insignificant surface stress evolution. Additional *in situ* R_S and $\sigma \times \Theta$ vs. Θ curves are presented in the Supplemental Material[32].

In situ characterization was complemented by *ex situ* imaging of film surfaces using Atomic Force Microscopy (AFM) in tapping mode (Nanoscope III Multimode, Digital Instruments). Surface topography was studied at various film growth stages, and the effect of deposition conditions on film morphology was quantified by calculating the RMS surface roughness. AFM data were processed and analyzed using the WSxM software[58].

Density functional theory calculations and molecular dynamics simulations. We used static (i.e., 0 K) DFT to calculate Ag and Cu adatom adsorption energies, as well as Ag_2 and Cu_2 addimer binding energies on a-C, i.e., the energy required to dissociate a diatomic (Ag_2 or Cu_2) cluster residing on an a-C surface. We approximated the a-C substrate used in the experiments with a 72-atom single-layer graphite (i.e., graphene) sheet. Such choice is motivated by the need of simplifying the computational model and by the fact that short-range order of amorphous carbon surface has been shown to be close to that of graphite, with nearest-neighbor distances of 0.147 and 0.146 *nm* for a-C and graphite, respectively[59]. This length-scale describes the surface that an adatom encounters in its immediate environment. Hence, a similar adatom and addimer adsorption and diffusivity behavior is expected on the two types of surfaces.

DFT calculations were carried out with the VASP code[60], using the Perdew-Burke-Ernzerhof generalized gradient approximation[61], and the projector augmented wave method[62]. The approximation proposed by Grimme[63] was adopted to model the non-locality of electron correlation. $3 \times 3 \times 1$ **k**-point integration of the reciprocal space and 500 eV plane-wave cutoff energies were employed to converge ground-state energies to within an accuracy of $10^{-5}\,eV/supercell$ and minimize forces to less than 0.01 eV/Å. First, we determined the equilibrium lattice parameter and energy E_{graph} of a 6×6 unit cell (72 atoms) graphene sheet. Thus, the adsorption energies E_{ads} of Ag and Cu adatoms in hollow, atop-C, and bridge (above C–C bond center) positions were evaluated as $E_{ads,Ag(Cu)} = E_{graph+Ag(Cu)} - (E_{graph} + E_{Ag(Cu)})$. The energy $E_{graph+Ag(Cu)}$ is obtained by adatom vertical relaxation (on the adsorption site) together with full relaxation of C positions. The energies $E_{Ag(Cu)}$ of isolated Ag and Cu atoms were calculated accounting for electronic spin degrees of freedom, using cutoff energies of 870 and 1000 eV, respectively. Ag_2 and Cu_2 addimer binding energies E_b, determined after full relaxation of two vicinal adatoms in different initial positions on the graphene surface, were calculated as $E_{b,Ag_2(Cu_2)} = E_{graph} + 2(E_{ads,Ag(Cu)} + E_{Ag(Cu)}) - E_{graph+Ag_2(Cu_2)}$. DFT results of adsorption and binding energies are summarized in Table 1.

We also used AIMD simulations, within the framework of DFT[64], to study diffusion of Ag and Cu adatoms. AIMD simulations were based on canonical *NVT* sampling of the phase space, performed by coupling the system with the Nosé-Hoover thermostat, integrating the equations of motion at 1 *fs* timesteps. The dynamics of individual Ag and Cu adatoms on single graphite layers consisting of 72 carbon atoms was modeled at temperatures $T_S = 300$, 400, 600, 800 and 1000 *K* with total simulation times of ~0.77 *ns* for Ag and ~0.66 *ns* for Cu. Γ-point sampling of the Brillouin-zone and 300 *eV* cutoff energy for the planewave basis set were used for all simulations. Temperature-dependent diffusivities $D(T_S)$ of Ag and Cu adatoms were computed from the slope of the adatom mean square displacement vs. time according to the methodology suggested by Saxton[65], from which adatom surface diffusion activation barriers and attempt frequencies were determined via linear regression on $ln(D(T_S))$ vs. $1/T_S$ data.

References

1. Ernst, K. H., Ludviksson, A., Zhang, R., Yoshihara, J. & Campbell, C. T. Growth model for metal films on oxide surfaces: Cu on ZnO(0001)-O. *Phys. Rev. B* **47**, 13782–13796 (1993).
2. Sclafani, A. & Herrmann, J. M. Influence of metallic silver and of platinum-silver bimetallic deposits on the photocatalytic activity of titania (anatase and rutile) in organic and aqueous media. *J. Photochem. Photobiol. A Chem.* **113**, 181–188 (1998).
3. Gong, C. *et al*. Metal contacts on physical vapor deposited monolayer MoS2. *ACS Nano* **7**, 11350–11357 (2013).
4. Appy, D. *et al*. Transition metals on the (0 0 0 1) surface of graphite: Fundamental aspects of adsorption, diffusion, and morphology. *Prog. Surf. Sci.* **89**, 219–238 (2014).
5. Petrov, I., Barna, P. B., Hultman, L. & Greene, J. E. Microstructural evolution during film growth. *J. Vac. Sci. Technol. A Vacuum, Surfaces, Film.* **21**, S117–S128 (2003).
6. Brune, H. *et al*. Effect of strain on surface diffusion and nucleation. *Phys. Rev. B* **52**, R14380 (1995).
7. Kim, S. Y., Lee, I.-H. & Jun, S. Transition-pathway models of atomic diffusion on fcc metal surfaces. I. Flat surfaces. *Phys. Rev. B* **76**, 245407 (2007).
8. Kim, S. Y., Lee, I.-H. & Jun, S. Transition-pathway models of atomic diffusion on fcc metal surfaces. II. Stepped surfaces. *Phys. Rev. B* **76**, 245408 (2007).
9. Krug, J., Politi, P. & Michely, T. Island nucleation in the presence of step-edge barriers: Theory and applications. *Phys. Rev. B* **61**, 14037 (2000).
10. Stroud, P. T. Nucleation and critical condensation phenomena of silver on silicon oxide. *J. Phys. C Solid State Phys.* **4**, 577–583 (1971).
11. Jeffers, G., Dubson, M. A. & Duxbury, P. M. Island-to-percolation transition during growth of metal films. *J. Appl. Phys.* **75**, 5016–5020 (1994).
12. Bréchignac, C. *et al*. Instability driven fragmentation of nanoscale fractal islands. *Phys. Rev. Lett.* **88**, 196103 (2002).
13. Thompson, C. V. Solid-State Dewetting of Thin Films. *Annu. Rev. Mater. Res.* **42**, 399–434 (2012).
14. Lü, B., Souqui, L., Elofsson, V. & Sarakinos, K. Scaling of elongation transition thickness during thin-film growth on weakly interacting substrates. *Appl. Phys. Lett.* **111**, 084101 (2017).
15. Liu, X. *et al*. Growth morphology and properties of metals on graphene. *Prog. Surf. Sci.* **90**, 397–443 (2015).
16. Lü, B., Almyras, G. A., Gervilla, V., Greene, J. E. & Sarakinos, K. Formation and morphological evolution of self-similar 3D nanostructures on weakly interacting substrates. *Phys. Rev. Mater.* **2**, 063401 (2018).
17. Greene, J. E. Thin Film Nucleation, Growth, and Microstructural Evolution - An Atomic Scale View. in *Handbook of Deposition Technologies for Films and Coatings: Science, Applications and Technology* (ed. Martin, P. M.) 554–618 (Oxford, U.K.; Burlington, Mass.: William Andrew/Elsevier, 2010).
18. Oates, T. W. H. & Mücklich, A. Evolution of plasmon resonances during plasma deposition of silver nanoparticles. *Nanotechnology* **16**, 2606–2611 (2005).
19. Nichols, F. A. Coalescence of two spheres by surface diffusion. *J. Appl. Phys.* **37**, 2805–2808 (1966).

20. Family, F. & Meakin, P. Scaling of the droplet-size distribution in vapor-deposited thin films. *Phys. Rev. Lett.* **61**, 428 (1988).
21. Jensen, P. Growth of nanostructures by cluster deposition: Experiments and simple models. *Rev. Mod. Phys.* **71**, 1695–1735 (1999).
22. Carrey, J. & Maurice, J.-L. Transition from droplet growth to percolation: Monte Carlo simulations and an analytical model. *Phys. Rev. B* **63**, 245408 (2001).
23. Carrey, J. & Maurice, J.-L. Scaling laws near percolation during three-dimensional cluster growth: A Monte Carlo study. *Phys. Rev. B* **65**, 205401 (2002).
24. Warrender, J. M. & Aziz, M. J. Effect of deposition rate on morphology evolution of metal-on-insulator films grown by pulsed laser deposition. *Phys. Rev. B* **76**, 045414 (2007).
25. Lü, B., Elofsson, V., Münger, E. P. & Sarakinos, K. Dynamic competition between island growth and coalescence in metal-on-insulator deposition. *Appl. Phys. Lett.* **105**, 163107 (2014).
26. Lü, B., Münger, E. P. & Sarakinos, K. Coalescence-controlled and coalescence-free growth regimes during deposition of pulsed metal vapor fluxes on insulating surfaces. *J. Appl. Phys.* **117**, 134304 (2015).
27. Jensen, P. *et al*. Kinetics of shape equilibration for two dimensional islands. *Eur. Phys. J. B* **11**, 497–504 (1999).
28. Jensen, P., Larralde, H., Meunier, M. & Pimpinelli, A. Growth of three-dimensional structures by atomic deposition on surfaces containing defects: simulations and theory. *Surf. Sci.* **412**, 458–476 (1998).
29. Kryukov, Y. A. & Amar, J. G. Scaling of the island density and island-size distribution in irreversible submonolayer growth of three-dimensional islands. *Phys. Rev. B* **81**, 165435 (2010).
30. Michely, T. & Krug, J. *Islands, Mounds and Atoms* (Springer Berlin Heidelberg, 2004).
31. Elofsson, V., Lü, B., Magnfält, D., Münger, E. P. & Sarakinos, K. Unravelling the physical mechanisms that determine microstructural evolution of ultrathin Volmer-Weber films. *J. Appl. Phys.* **116**, 44302 (2014).
32. Supplemental material. *Suppl. Mater*.
33. Zhang, C.-M. *et al*. Submonolayer island formation and the onset of multilayer growth during Ag/Ag(100) homoepitaxy. *Surf. Sci.* **406**, 178–193 (1998).
34. Swan, A., Shi, Z.-P., Wendelken, J. F. & Zhang, Z. Flux-dependent scaling behavior in Cu(100) submonolayer homoepitaxy. *Surf. Sci.* **391**, L1205–L1211 (1997).
35. Dumont, J., Wiame, F., Ghijsen, J. & Sporken, R. Growth of atomically flat Ag on mica. *Surf. Sci.* **572**, 459–466 (2004).
36. Ganz, E., Sattler, K. & Clarke, J. Scanning tunneling microscopy of Cu, Ag, Au and Al adatoms, small clusters, and islands on graphite. *Surf. Sci.* **219**, 33–67 (1989).
37. Francis, G. M., Goldby, I. M., Kuipers, L., von Issendorff, B. & Palmer, R. E. Deposition and growth of noble metal clusters on graphite. *J. Chem. Soc. Dalt. Trans*. 665–671 (1996).
38. Duffy, D. M. & Blackman, J. A. The energy of Ag adatoms and dimers on graphite. *Surf. Sci.* **415**, L1016–L1019 (1998).
39. Venables, J. A., Spiller, G. D. T. & Hanbucken, M. Nucleation and growth of thin films. *Reports Prog. Phys.* **47**, 399 (1984).
40. Goldby, I. M., Kuipers, L., Von Issendorff, B. & Palmer, R. E. Diffusion and aggregation of size-selected silver clusters on a graphite surface. *Appl. Phys. Lett.* **69**, 2819–2821 (1996).
41. Ibach, H. *Physics of Surfaces and Interfaces* (Springer-Verlag, 2006).
42. Wang, S. C., Kürpick, U. & Ehrlich, G. Surface diffusion of compact and other clusters: Ir-x on Ir(111). *Phys. Rev. Lett.* **81**, 4923–4926 (1998).
43. Bardotti, L. *et al*. Diffusion and aggregation of large antimony and gold clusters deposited on graphite. *Surf. Sci.* **367**, 276–292 (1996).
44. Kürpick, U., Fricke, B. & Ehrlich, G. Diffusion mechanisms of compact surface clusters: Ir7 on Ir(111). *Surf. Sci.* **470**, L45–L51 (2000).
45. Krylov, S. Y. Surface Gliding of Large Low-Dimensional Clusters. *Phys. Rev. Lett.* **83**, 4602–4605 (1999).
46. Deltour, P., Barrat, J.-L. & Jensen, P. Fast Diffusion of a Lennard-Jones Cluster on a Crystalline Surface. *Phys. Rev. Lett.* **78**, 4597–4600 (1997).
47. Tonkikh, A. A. & Werner, P. Surfactant-mediated Stranski-Krastanov islands. *Phys. status solidi b* **250**, 1795–1798 (2013).
48. Lewis, R. B. *et al*. Quantum Dot Self-Assembly Driven by a Surfactant-Induced Morphological Instability. *Phys. Rev. Lett.* **119**, 086101 (2017).
49. Furgeaud, C., Simonot, L., Michel, A., Mastail, C. & Abadias, G. Impact of Ge alloying on the early growth stages, microstructure and stress evolution of sputter-deposited Cu-Ge thin films. *Acta Mater.* **159**, 286–295 (2018).
50. Miccoli, I., Edler, F., Pfnür, H. & Tegenkamp, C. The 100th anniversary of the four-point probe technique: The role of probe geometries in isotropic and anisotropic systems. *J. Phys. Condens. Matter* **27**, 223201 (2015).
51. Colin, J. J. *et al*. A load-lock compatible system for *in situ* electrical resistivity measurements during thin film growth. *Rev. Sci. Instrum.* **87**, 23902 (2016).
52. Floro, J. A. *et al*. Real-time stress evolution during Si1-xGex Heteroepitaxy: Dislocations, islanding, and segregation. *J. Electron. Mater.* **26**, 969–979 (1997).
53. Fillon, A., Abadias, G., Michel, A. & Jaouen, C. Stress and microstructure evolution during growth of magnetron-sputtered low-mobility metal films: Influence of the nucleation conditions. *Thin Solid Films* **519**, 1655–1661 (2010).
54. Stoney, G. G. The Tension of Metallic Films Deposited by Electrolysis. *Proc. R. Soc. London A* **82**, 172–175 (1909).
55. Abadias, G. *et al*. Volmer-Weber growth stages of polycrystalline metal films probed by *in situ* and real-time optical diagnostics. *Appl. Phys. Lett.* **107**, 183105 (2015).
56. Chason, E. & Guduru, P. R. Tutorial: Understanding residual stress in polycrystalline thin films through real-time measurements and physical models. *J. Appl. Phys.* **119**, 191101 (2016).
57. Seel, S. C., Thompson, C. V., Hearne, S. J. & Floro, J. A. Tensile stress evolution during deposition of Volmer–Weber thin films. *J. Appl. Phys.* **88**, 7079–7088 (2000).
58. Horcas, I. *et al*. WSXM: A software for scanning probe microscopy and a tool for nanotechnology. *Rev. Sci. Instrum.* **78**, 013705 (2007).
59. Tersoff, J. Empirical Interatomic Potential for Carbon, with Applications to Amorphous Carbon. *Phys. Rev. Lett.* **61**, 2879–2882 (1988).
60. Kresse, G. & Hafner, J. Ab initio molecular dynamics for liquid metals. *Phys. Rev. B* **47**, 558–561 (1993).
61. Perdew, J. P., Burke, K. & Ernzerhof, M. Generalized Gradient Approximation Made Simple. *Phys. Rev. Lett.* **77**, 3865–3868 (1996).
62. Blöchl, P. E. Projector augmented-wave method. *Phys. Rev. B* **50**, 17953–17979 (1994).
63. Grimme, S. Semiempirical GGA-type density functional constructed with a long-range dispersion correction. *J. Comput. Chem.* **27**, 1787–1799 (2006).
64. Car, R. & Parrinello, M. Unified Approach for Molecular Dynamics and Density-Functional Theory. *Phys. Rev. Lett.* **55**, 2471–2474 (1985).
65. Saxton, M. J. Single-particle tracking: the distribution of diffusion coefficients. *Biophys. J.* **72**, 1744–1753 (1997).

Acknowledgements

A.J. and G.A. wish to thank Ph. Guérin for his technical assistance during sample deposition. A.J. and G.A. acknowledge the financial support of the French Government program "Investissements d'Avenir" (LABEX INTERACTIFS, reference ANR-11-LABX-0017-01). KS acknowledges Linköping University ("LiU Career Contract, Dnr-LiU-2015-01510, 2015–2020"), the Swedish research council (contract VR-2015-04630), and the

Olle Engkvist foundation (contract SOEB 190-312) for financial support. D.G.S. gratefully acknowledges financial support from the Olle Engkvist Foundation. Simulations were performed using supercomputer resources provided by the Swedish National Infrastructure for Computing (SNIC) on: (i) the Gamma and Triolith Clusters located at the National Supercomputer Centre (NSC) at Linköping University, Sweden, (ii) the Beskow cluster located at the Center for High Performance Computing (PDC) at Royal Institute of Technology, Stockholm, Sweden, and (iii) the Kebnekaise cluster located at the High Performance Computing Center North (HPC2N) at Umeå University, Sweden.

Author Contributions

A.J. performed all experimental work and analyzed the data. K.S. and A.J. wrote the manuscript. D.S. performed the AIMD simulations and wrote the respective section of the manuscript. G.A. and K.S. are responsible for the development of experiments and analysis, respectively. All authors were involved in the interpretation/discussion of the results and have approved the final version of the manuscript.

Additional Information

Supplementary information accompanies this paper at https://doi.org/10.1038/s41598-019-43107-8.

Competing Interests: The authors declare no competing interests.

Supplemental material: “Atomic-scale diffusion rates during growth of thin metal films on weakly-interacting substrates”

A. Jamnig[1,2,*], D.G. Sangiovanni[3,4], G. Abadias[1], and K. Sarakinos[2]

*Corresponding author, email: andreas.jamnig@liu.se

[1]*Institut Pprime, Département Physique et Mécanique des Matériaux, UPR 3346 CNRS, Université de Poitiers, SP2MI, 11 Bvd M. et P. Curie, F 86073 Cedex 9, France*

[2]*Nanoscale Engineering Division, Department of Physics, Chemistry, and Biology, Linköping University, SE 581 83, Linköping, Sweden*

[3]*Atomistic Modelling and Simulation, ICAMS, Ruhr-Universität Bochum, D-44801 Bochum, Germany*

[4]*Theoretical Physics Division, Department of Physics, Chemistry, and Biology, Linköping University, SE 581 83, Linköping, Sweden*

We employed *in situ* and real-time sheet-resistance[1] and wafer-curvature measurements[2,3], from which we determined the nominal film thickness Θ at percolation (Θ_{perc}) and continuous film formation (Θ_{cont}) transition, respectively. Θ_{cont} is determined by the nominal thickness at which the slope of the stress-thickness product $\sigma \times \Theta$ undergoes a tensile to compressive transition (i.e., transition from positive to negative slope), while Θ_{perc} corresponds to the thickness at which the film sheet-resistance R_S exhibits a sharp drop indicating the formation of a macroscopically conductive film.

Figure S1 shows representative $\sigma \times \Theta$ vs. Θ curves during growth of Ag on amorphous carbon (a-C) for deposition rates F (a) $0.14\ monolayers/s\ (ML/s)$, (b) $0.63\ ML/s$, (c) $5.38\ ML/s$ and temperatures T_S of $298, 313, 354$ and 378 K. We observe that Θ_{cont} increases with increasing T_S, e.g., at $F = 0.14\ ML/s$ (Fig. S1(a)) Θ_{cont} increases from 50 to $276\ ML$, when T_S is increased from 298 to $378\ K$. For constant values of T_S, Θ_{cont} shifts to lower values with increasing F; this effect is more pronounced at the highest temperature $\mathrm{T}_S = 378\ K$ (red dash-dotted line in Fig. S1), where Θ_{cont} decreases from 276 to 115 ML, when increasing F from 0.14 to $5.38\ ML/s$.

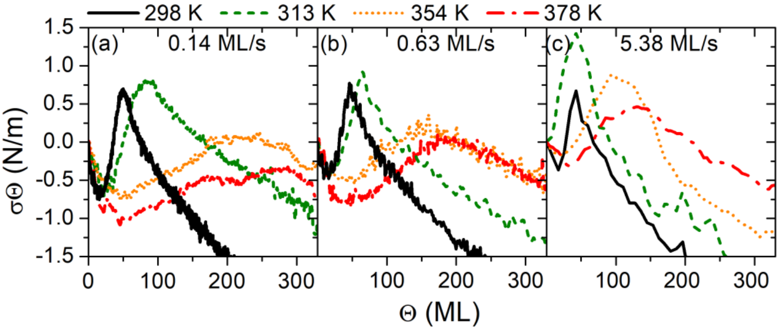

Figure S1. *In situ measured evolution of stress-thickness $\sigma \times \Theta$ as function of the nominal film thickness Θ for Ag grown on a-C/Si with deposition rate (a) $0.14\ ML/s$, (b) $0.63\ ML/s$, (c) $5.28\ ML/s$ and temperatures in the range 298 to $378\ K$. The position of the tensile-to-compressive peak in the $\sigma\Theta$ vs. Θ curves corresponds to the continuous film formation thickness Θ_{cont}.*

Representative R_S vs. Θ curves during Ag growth on a-C are shown in Fig. S2 for $298\ K \leq \mathrm{T}_S \leq 378\ K$ and F equal to (a) $0.27\ ML/s$, (b) $1\ ML/s$, (c) $5\ ML/s$. The onset of macroscopic conductivity, i.e., Θ_{perc}, shifts from 26 to 121 ML, when increasing T_S from 298 to 378 K at $\mathrm{F} = 0.27\ ML/s$.(Fig. S2(a)) With increasing values of F, Θ_{perc} shifts to lower thicknesses, e.g., increasing F from 0.27 to $5\ ML/s$, for $\mathrm{T}_S = 378\,K$ (red, short-dotted line in Fig. S2), leads to a decrease of Θ_{perc} from 121 to 77 ML. We note that the R_S values at $\Theta = 0\,ML$ differ among the various measurements. This value primarily depends on the doping of the Si substrate, and for the measurements presented in Fig.S2, different substrate batches were used, which exhibited sheet resistance values spreading over an order of magnitude. These differences, however, do not influence of the quality of the measurements and the resulting Θ_{perc} value.

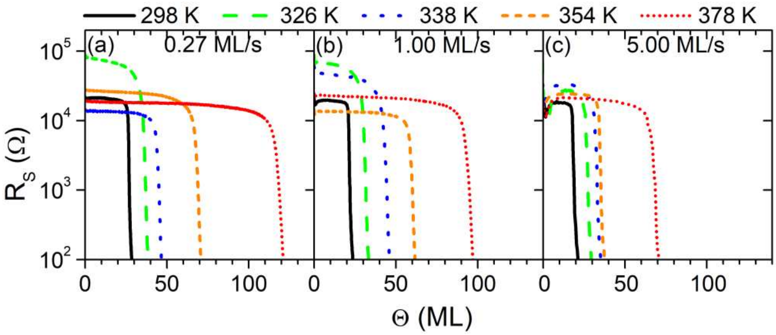

Figure S2. *In situ measured evolution of sheet resistance R_S as function of the nominal film thickness Θ for Ag grown on a-C/Si with deposition rate (a) $0.27\ ML/s$, (b) $1\ ML/s$, (c) $5\ ML/s$ and temperatures in the range 298 to $378\,K$. The position of the sharp drop in the R_S vs. Θ curves corresponds to the percolation transition thickness Θ_{perc}.*

Figure S3 presents $\sigma \times \Theta$ vs. Θ curves during growth of Cu on a-C, for deposition rates F equal to (a) $0.07\ ML/s$, (b) $0.49\ ML/s$, and (c) $2.55\ ML/s$, and T_S values in the range 298 to 413 K. Similar to the results for Ag, we find that Θ_{cont} increases with increasing T_S, e.g., for $\mathrm{F} = 0.07\ ML/s$, $\Theta_{cont}(298\,K) = 42\,ML$ and

$\Theta_{cont}(413\ K) = 156\ ML$ (see solid black and dashed-dotted purple lines in Fig. S3(a)). Conversely, Θ_{cont} shifts to lower values for increasing F, e.g., $\Theta_{cont}(0.07\ ML/s) = 156\ ML$ and $\Theta_{cont}(2.55\ ML/s) = 79\ ML$ for $T_S = 413\ \mathrm{K}$ (see dashed-dotted purple line in Figs. S3 (a) and (c)).

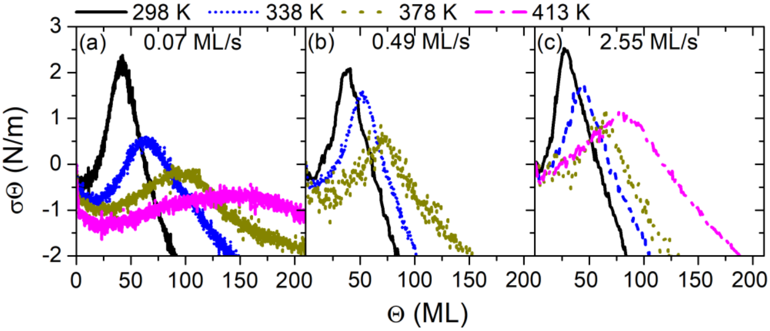

Figure S3. *In situ measured evolution of stress-thickness $\sigma \times \Theta$ as function of the nominal film thickness Θ for Cu grown on a-C with deposition rate (a) $0.07\ ML/s$, (b) $0.49\ ML/s$, (c) $2.55\ ML/s$ and temperatures in the range 298 to $413\ K$. The position of the tensile-to-compressive peak in the $\sigma\Theta$ vs. Θ curves corresponds to the continuous film formation thickness Θ_{cont}.*

Figure S4 presents *ex situ* AFM images for Ag ($T_S = 378\ K,\ F = 5.38\ ML/s$) and Cu ($T_S = 413\ K,\ F = 2.55\ ML/s$) films grown on a-C, at their respective Θ_{cont} values (Figs. 4 (a) and (b)) and for $\Theta \sim 450\ \mathrm{ML}$ (Figs. 4 (c) and (d)). For both thicknesses, Ag surface appears rougher with larger features as compared to Cu. At Θ_{cont}, the root mean-square (RMS) roughness for Ag is $6.55\ nm$, while the value for Cu is $1.66\ nm$. When increasing Θ to $\sim 450\ ML$, the RMS roughness increases to $10.93\ nm$ and $6.22\ nm$ for Ag/a-C and Cu/a-C, respectively, with the value for Cu remaining lower than the respective value for Ag growth. These trends are consistent with the *in situ* data presented in Figs. S1 and S3, showing that Cu has the tendency to grow flatter and, thus, form continuous layers at lower nominal thicknesses than Ag.

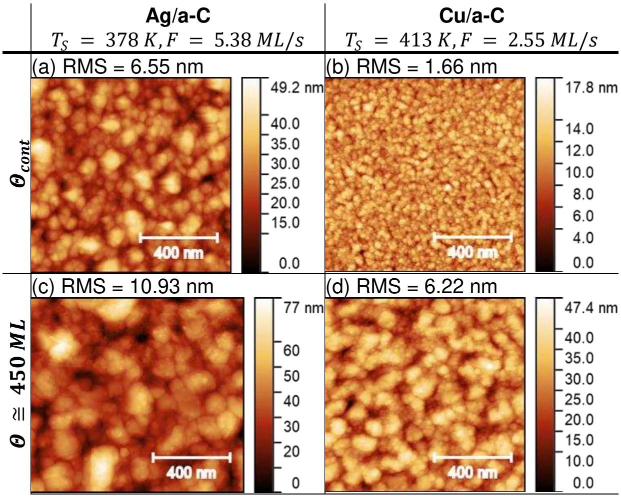

Figure S4. *Atomic force microscopy images of the surface morphology of Ag and Cu grown on amorphous carbon (a-C) with deposition temperature* T_S *and rate* F *indicated. Morphologies are compared for nominal film thickness* Θ *equal to* Θ_{cont} *((a) and (b)) and* $\Theta \cong 450\,ML$ *((c) and (d)). The root mean-square roughness values (RMS) are indicated for the respective films.*

REFERENCES

1. Colin, J. J. *et al.* A load-lock compatible system for in situ electrical resistivity measurements during thin film growth. *Rev. Sci. Instrum.* **87,** 23902 (2016).
2. Chason, E. & Guduru, P. R. Tutorial: Understanding residual stress in polycrystalline thin films through real-time measurements and physical models. *J. Appl. Phys.* **119,** 191101 (2016).
3. Abadias, G. *et al.* Volmer-Weber growth stages of polycrystalline metal films probed by in situ and real-time optical diagnostics. *Appl. Phys. Lett.* **107,** 183105 (2015).

Paper II

The effect of kinetics on intrinsic stress generation and evolution in sputter-deposited films at conditions of high atomic mobility

A. Jamnig[1,2,*], N. Pliatsikas[2], K. Sarakinos[2], and G. Abadias[1]

*Corresponding author

[1]Institut Pprime, Département Physique et Mécanique des Matériaux, UPR 3346 CNRS, Université de Poitiers, SP2MI, 11 Bvd M. et P. Curie, F86073 Poitiers Cedex 9, France

[2]Nanoscale Engineering Division, Department of Physics, Chemistry, and Biology, Linköping University, SE 581 83, Linköping, Sweden

Journal of Applied Physics 127 (2020), 045302.

https://doi.org/10.1063/1.5130148

Journal of Applied Physics

The effect of kinetics on intrinsic stress generation and evolution in sputter-deposited films at conditions of high atomic mobility

Cite as: J. Appl. Phys. **127**, 045302 (2020); https://doi.org/10.1063/1.5130148
Submitted: 05 October 2019 . Accepted: 11 January 2020 . Published Online: 27 January 2020

A. Jamnig, N. Pliatsikas, K. Sarakinos, and G. Abadias

Journal of Applied Physics ARTICLE scitation.org/journal/jap

The effect of kinetics on intrinsic stress generation and evolution in sputter-deposited films at conditions of high atomic mobility

Cite as: J. Appl. Phys. **127**, 045302 (2020); doi: 10.1063/1.5130148
Submitted: 5 October 2019 · Accepted: 11 January 2020 ·
Published Online: 27 January 2020

A. Jamnig,[1,2,a)] N. Pliatsikas,[2] K. Sarakinos,[2] and G. Abadias[1]

AFFILIATIONS

[1]Département Physique et Mécanique des Matériaux, Institut Pprime, UPR 3346 CNRS, Université de Poitiers, SP2MI, 11 Bvd M. et P. Curie, F86073 Poitiers Cedex 9, France
[2]Nanoscale Engineering Division, Department of Physics, Chemistry, and Biology, Linköping University, SE 581 83 Linköping, Sweden

[a)]**Author to whom correspondence should be addressed:** andreas.jamnig@liu.se

ABSTRACT

Vapor-based metal film growth at conditions that promote high atomic mobility is typically accompanied by compressive stress formation after completion of island coalescence, while an apparent stress relaxation is observed upon deposition interruption. Despite numerous experimental studies confirming these trends, the way by which growth kinetics affect postcoalescence stress magnitude and evolution is not well understood, in particular, for sputter-deposited films. In this work, we study *in situ* and in real-time stress evolution during sputter-deposition of Ag and Cu films on amorphous carbon. In order to probe different conditions with respect to growth kinetics, we vary the deposition rate F from 0.015 to 1.27 nm/s, and the substrate temperature T_S from 298 to 413 K. We find a general trend toward smaller compressive stress magnitudes with increasing T_S for both film/substrate systems. The stress-dependence on F is more complex: (i) for Ag, smaller compressive stress is observed when increasing F; (ii) while for Cu, a nonmonotonic evolution with F is seen, with a compressive stress maximum for $F = 0.102$ nm/s. Studies of postdeposition stress evolution show the occurrence of a tensile rise that becomes less pronounced with increasing T_S and decreasing F, whereas a faster tensile rise is seen by increasing F and T_S. We critically discuss these results in view of *ex situ* obtained film morphology which show that deposition-parameter-induced changes in film grain size and surface roughness are intimately linked with the stress evolution.

I. INTRODUCTION

The evolution of stress—with respect to its type and magnitude—in vapor-deposited films is closely linked with the various film growth stages.[1–4] Isolated islands that form initially on the substrate surface exhibit a smaller-than-equilibrium lattice parameter due to the Laplace pressure they are subjected to.[5] An increase of the island size with continued deposition causes a reduction of the Laplace pressure, while the islands become less mobile and less prone to reshape. As a result, their lattice cannot expand following the decrease of the Laplace pressure, and compressive stress emerges. Further vapor deposition causes islands to impinge on each other, which initiates the process of coalescence.[4,6,7] The energy of the coalescing island cluster is minimized by creating a grain boundary (GB), leading to island reshaping and tensile straining of the lattice.[8]

As the deposited layer approaches the point at which it becomes continuous, the stress evolution depends strongly on atomic mobility. For conditions that yield low mobility, new segments of GBs that form at triple junctions (i.e., the intersection of surface and GB[9]) induce tensile stress.[10,11] Moreover, energetic particle bombardment of the growing layer (as, e.g., during sputter-deposition) may lead to point-defect generation, hydrostatic lattice expansion, and compressive stress.[12] The net effect of these two independently operating processes is a steady-state stress (σ_{SS}), the sign of which (i.e., compressive or tensile) is determined by the dominant mechanism.[13,14]

At high-mobility conditions, compressive stress is commonly observed in the continuous film formation regime, with its origin still being a matter of debate. In the most widely accepted explanation, Chason *et al.*[15,16] have attributed the compressive stress to adatom insertion into GBs, which are areas with a lower concentration of mobile atoms compared to the surface of the growing film. The effectiveness of this mechanism, and thereby the magnitude of the generated compressive stress, depends on film topography (i.e., terrace length) and adatom diffusivity.[16,17] The model proposed by Chason *et al.* also includes the effect of grain growth,[18] which causes removal of GBs and tensile stress generation.[19] In the case of negligible grain growth and effectively unimpeded insertion of adatoms into the GBs, a compressive σ_{SS} is reached.

Since GBs seemingly play a key role for stress generation,[18,20,21] researchers have been striving to establish and understand stress-kinetics relations—kinetics is primarily governed by the substrate temperature T_S and the film growth rate F—using films with well-controlled grain sizes (i.e., GB length) that are independent of film thickness and deposition conditions. It has been observed that stress becomes less compressive (more tensile) with increasing F in the case of deposition conditions in which energetic bombardment has no appreciable effect on film growth.[22,23] However, this trend has been shown to reverse for sputter-deposited Cu films grown at conditions for which interactions between energetic particles and films have to be considered as well.[24] Studies on the effects of deposition temperature have mostly focused on the change from low- to high-mobility growth regimes showing a transition from compressive-tensile to compressive-tensile-compressive (CTC) stress vs film thickness evolution with increasing T_S.[9,25,26]

The studies highlighted above have provided data for benchmarking the predictions of theoretical models which describe stress evolution in films grown using thermalized vapor fluxes.[27,28] However, in realistic sputter-deposition scenarios grain sizes change as a function of growth conditions, while the interaction of hyperthermal species with the film surface and near-surface layers may modify stress evolution.[24,28,29] Hence, systematic investigations on the effect of kinetics on the stress generation and evolution at application-relevant sputter-deposition conditions are required. Such investigations should also address postdeposition stress evolution, as a tensile stress rise is observed at conditions of high atomic mobility, but the way by which the magnitude and time scale of this rise are affected by kinetics is not well understood. In one study, Flötotto *et al.*[30] found little influence of F on the postdeposition tensile rise magnitude (for fixed grain size) and a weaker but faster tensile rise with increasing grain size. Moreover, Leib and Thompson[31] reported a linear dependence of the tensile stress rise on the compressive stress accumulated in the film before interruption but no T_S-dependence of the initial tensile rise.

Here, we study—using *in situ* wafer curvature measurements and *ex situ* morphology characterization tools—stress evolution during and after magnetron-sputter-deposition of Ag and Cu films on amorphous carbon (a-C) substrates. To systematically probe the effect of kinetics at conditions of high atomic mobility, we vary T_S in the range 298–413 K, while F is altered from 0.015 to 1.27 nm/s . In all cases, we observe CTC stress evolution as a function of film thickness and tensile stress rise after deposition interruption. We find that for both film/substrate systems the increase of T_S leads to smaller compressive stress after continuous-layer formation and larger grain sizes (i.e., the GB length decreases). For Ag deposition over the entire probed F range and for Cu deposition with $F > 0.102$ nm/s, smaller compressive stress is observed when increasing F. These trends are consistent with models that explain compressive stress generation as a result of adatom incorporation into GBs. However, smaller compressive stress is formed in Cu films when decreasing F below 0.102 nm/s. We argue, based on chemical analysis, that adsorption of gas molecules from the background pressure (e.g., H_2O), impeding atomic surface-diffusion and incorporation into GBs, is the reason for this behavior. The postdeposition tensile stress rise becomes faster with increasing T_S and F and smaller in magnitude with increasing T_S and decreasing F. We attribute the change in magnitude of the tensile rise to the decreasing grain size.

II. FILM GROWTH AND CHARACTERIZATION

Films were sputter-deposited using Ar (purity 99.999%) plasma discharges at a working pressure of $p = 0.25$ Pa in a multisource high-vacuum chamber (base pressure $\sim 8 \times 10^{-6}$ Pa). Si wafers, covered with native oxide, were used as substrates, with substrate thickness $h_s = 100 \pm 2$ μm for *in situ* stress measurements and $h_s = 675 \pm 20$ μm for *ex situ* characterization. The magnetron sources were equipped with Ag (purity 99.99%), Cu (purity 99.99%), and graphite (purity 99.995%) targets (diameter 7.62 cm), installed in a confocal configuration, with a target-to-substrate-normal angle of 25° and a target-to-substrate distance of 180 mm. A 6.5 nm thick a-C diffusion barrier layer was grown *in situ*, prior to Ag and Cu film deposition, by sputtering the graphite target at a power of 150 W (i.e., growth rate $F = 0.01$ nm/s). For Ag and Cu films, growth rates F in the range $0.025 - 1.27$ nm/s (Ag) and $0.015 - 0.535$ nm/s (Cu) were employed, by changing the power applied to the respective magnetrons from 5 to 300 W. Moreover, the substrate temperatures T_S for Ag and Cu deposition were varied in the respective ranges $298 - 378$ K and $298 - 413$ K. T_S was set by a resistive heater 1 h before deposition start and held constant during and after deposition. Vacuum-compatible temperature indicators (NiGK Corp.) that change their color irreversibly upon reaching specific T_S (accuracy ± 2 K for $T_S < 410$ K and ± 4 K for $T_S \geq 410$ K) were used to confirm the temperature settings. *Ex situ* x-ray reflectivity measurements [XRD 3000 Seifert diffractometer, line focus Cu source, Ge (220) monochromator selecting $K_{\alpha 1}$ Cu radiation] were performed to determine the film thickness and F, as a function of applied power and T_S; varying T_S had only minor effects on F (variation $<$ 4% in the used T_S range).

Immediately after metal film growth, a 6.5 nm thick a-C capping layer was deposited on samples that were used for *ex situ* characterization, in order to minimize the interaction between film and atmospheric ambient and suppress postdeposition changes of the film morphology. More details on the *ex situ* film analysis are provided later in the present section.

The evolution of the substrate curvature change $\Delta\kappa$ during deposition on Si(100) substrates was monitored *in situ* and in real-time with a multibeam optical stress sensor (MOSS, k-Space Associates).[32,33] The stress-film thickness product $\sigma \times h_f$ was then calculated from $\Delta(\sigma \times h_f) = \frac{1}{6} Y_s h_s^2 \Delta\kappa$,[34] where $Y_s = 180.5$ GPa is the Si(100) substrate biaxial modulus. Being subject to the flux of arriving vapor atoms, the film/substrate system heats up during deposition, leading to expansion of the crystal lattices according to their thermal expansion coefficients α_{th}. Once the deposition is completed, the sample temperature returns to the set T_S value and thermal stress σ_{th} builds up due to the mismatch of film and substrate $\Delta\alpha_{th}$ according to $\sigma_{th} = Y_{\text{Ag,Cu}}\Delta\alpha_{th}\Delta T_S$, where $Y_{\text{Ag,Cu}}$ are the biaxial moduli of Ag (130 GPa) and Cu (200 GPa), respectively, and ΔT_S is the deposition-induced temperature increase. The heating of the substrate due to the deposition flux and its cooling after deposition stop were measured with thermocouples placed close to the substrate on the substrate holder for depositions at $T_S = 298$ and 413 K; we find that ΔT_S is independent of T_S. The evolution of temperature vs time $T_S(t)$ after deposition can be described with an exponential decay function $T_S(t) = T_S + \Delta T_S \times \exp(-t/\tau)$, whereby all sets are fitted using the decay time constant $\tau = 2470 \pm 3$ s. The stress evolution after growth interrupt was corrected by subtracting the time-dependent thermal stress $\sigma_{th}(t) = \sigma_{th} \times (1 - \exp(-t/\tau))$; the values of ΔT_S, σ_{th}, and $\sigma_{th} \times h_f$ for various values of F are listed in Table S1 in the supplementary material.

All results presented in Secs. III A–III D are obtained by monitoring $\Delta\kappa$ in a four-stage process, see Fig. 1 that shows data recorded during the growth of a Cu film at $T_S = 298$ K and $F = 0.276$ nm/s: (a) Deposition of a-C layer ($h_{f,a-C} = 7$ nm); (b) presputtering of metal target; (c) deposition of metal film; and (d) postdeposition stress monitoring. $\Delta\kappa$—and by extension $\sigma \times h_f$—shows a first maximum at $h_{f,a-C} = 0.5$ nm [marked by an arrow in Fig. 1(a)], indicating that a continuous a-C film is formed early during deposition. During stage (b), $\Delta\kappa$ does not change, i.e., relaxation in the a-C film does not have an appreciable effect in the metal-layer stress evolution. Moreover, we found that stress-evolution during the deposition of a-C has not been influenced by T_S (data not shown here). For comparison purposes, all results corresponding to stages (c) and (d) in Fig. 1 have been shifted in Figs. 2, 3, 7, and 9 to start at the same $\sigma \times h_f = 0$ N/m value.

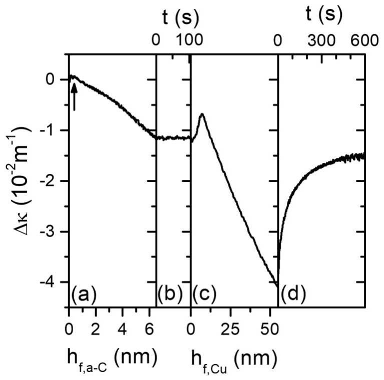

FIG. 1. Evolution of substrate curvature $\Delta\kappa$ during (a) deposition of amorphous carbon (a-C); (b) presputtering of Cu target; (c) Cu layer deposition at substrate temperature $T_S = 298$ K and deposition rate $F = 0.276$ nm/s; and (d) after Cu-layer deposition completion. The change in κ is plotted as a function of film thickness h_f in (a) and (c) and time t in (b) and (d). The arrow in (a) indicates the position of a peak in $\Delta\kappa$ during a-C deposition.

In situ characterization was complemented by *ex situ* imaging of the surface morphology of films grown at various T_S and F with a Nanoscope III Multimode Digital Instruments atomic force microscope (AFM) operating in tapping mode. Observations were made at film thicknesses of 65 nm and 105 nm for Cu/a-C and Ag/a--C, respectively. The acquired images can be found in the supplementary material (Fig. S1) and were analyzed with the Gwyddion software package.[35] Statistical quantities that are used to describe thin film morphology include the root-mean square surface roughness $w = \langle [h(\vec{x}) - \bar{h}]^2 \rangle$ and height–height correlation function $g(r) = \langle [h(\vec{x} + \vec{r}) - h(\vec{x})]^2 \rangle$, where $h(\vec{x})$ is the surface height at a position $\vec{x} = (x, y)$ on the surface, $\bar{h}$ is the average surface height, $\langle \ldots \rangle$ denotes the statistical average over the entire surface, and $\vec{r}$ is a displacement vector.

Grain size and orientation were analyzed via electron backscatter diffraction (EBSD) with a FEI-Helios Nanolab G3 Dual Beam microscope operated at 15 kV with 11 nA and a step size of 25 nm. The acquired maps were treated with the OIM Analysis™ software, using Neighbor Confidence Index Correlation (minimum Confidence Index 0.05) and Grain Dilatation cleanup (tolerance angle 2°, minimum grain size 3 points).

X-ray photoelectron spectroscopy (XPS) was used to determine the chemical composition of Ag and Cu films. The measurements were carried out in a Kratos AXIS Ultra DLD UHV system (base pressure 5×10^{-8} Pa), equipped with a monochromatic Al-K$_\alpha$ x-ray beam, a hemispherical sector analyzer, and a multichannel detector. The pass energy was 20 eV. Surface-cleaning and depth-etching were performed using a 4 keV Ar$^+$ ion-beam, and the shift of the Ar-2p peak was used for correcting charge-induced shifts of the binding energies owing to Ar$^+$ ions. Elemental analysis was performed with the Kratos Vision software and its sensitivity factor database.

III. RESULTS AND DISCUSSION

We start the presentation and discussion of the results with regard to *in situ* stress evolution before formation of a continuous layer (Sec. III A). Data for *in situ* stress after continuous film formation are presented in Sec. III B and discussed in light of the *ex situ* film morphological characterization in Sec. III C. The final part, Sec. III D, is devoted to description and discussion of *in situ* data concerning postdeposition stress evolution. In order to establish a unified and material-independent picture of the effect of process parameters on the stress generation and evolution during growth of Ag and Cu films, we rescale all deposition temperatures using the homologous temperature $T_h = T_S/T_m$, where T_m is the melting point of Ag or Cu given in *K*.

A. Stress evolution before continuous film formation

Figure 2 presents the evolution of $\sigma \times h_f$ vs film thickness h_f during growth of Ag films on a-C, for T_h between 0.24 and 0.31

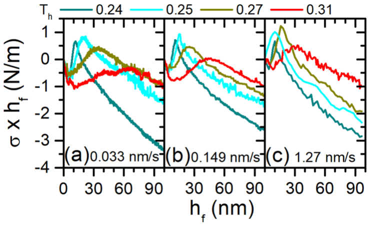

FIG. 2. Evolution of stress-thickness $\sigma \times h_f$ vs film thickness h_f during deposition of Ag thin films on amorphous carbon with deposition rates (a) $F = 0.033\,\mathrm{nm/s}$, (b) $F = 0.149\,\mathrm{nm/s}$, and (c) $F = 1.27\,\mathrm{nm/s}$ and homologous temperatures $T_h = 0.24$, 0.25, 0.27, and 0.31 (i.e., substrate temperatures $T_S = 298$, 313, 338 and 378 K). Curves in (a) and (b) have been smoothed by averaging over five consecutive points.

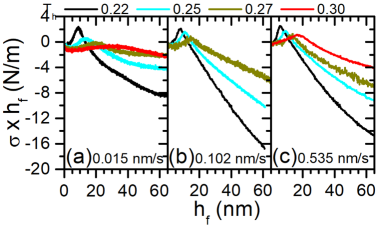

FIG. 3. Evolution of stress-thickness $\sigma \times h_f$ vs film thickness h_f during deposition of Cu thin films on amorphous carbon at deposition rates (a) $F = 0.015$ nm/s, (b) $F = 0.102$ nm/s, and (c) $F = 0.535$ nm/s and homologous temperatures $T_h = 0.22$, 0.25, 0.27, and 0.30 (i.e., substrate temperatures $T_S = 298$, 338, 378, and 413 K).

(i.e., $T_S = 298 - 378$ K) and for three different deposition rates: (a) $F = 0.033$ nm/s; (b) $F = 0.149$ nm/s; and (c) $F = 1.27$ nm/s. For all films, a pronounced CTC stress evolution is observed. With increasing T_h, the magnitude of the initially formed (i.e., for $h_f = 0 - 10$ nm) incremental compressive stress ($\sigma_{c,init}$) increases, and the magnitude of the incremental tensile stress ($\sigma_{t,init}$) that appears thereafter (i.e., for $h_f = 10 - 65$ nm) decreases. For instance, $\sigma_{c,init}$ evolves from ~ -21 to ~ -74 MPa, and $\sigma_{t,init}$ varies from ~ 150 to ~ 19 MPa when increasing T_h from 0.25 to 0.31 for $F = 0.033$ nm/s [see Fig. 2(a)]. Additionally, the onset of the tensile rise and the subsequent tensile-to-compressive stress peak are shifted to higher h_f values, e.g., the thickness of the tensile-to-compressive stress peak in Fig. 2(a) changes from 12 to 65 nm at $F = 0.033$ nm/s, when increasing T_h from 0.24 to 0.31. Conversely, increasing F results in a smaller $\sigma_{c,init}$ [see, e.g., change from ~ -74 to ~ -44 MPa when increasing F from 0.033 to 1.27 nm/s for $T_h = 0.31$ in Figs. 2(a) and 2(c)], and in a smaller h_f value at which the tensile-to-compressive stress transition occurs [see, e.g., the tensile-to-compressive peak position shift from 65 to 30 nm, for $T_h = 0.31$ when increasing F from 0.033 to 1.27 nm/s in Figs. 2(a) and 2(c)]. $\sigma_{c,init}$ and $\sigma_{t,init}$ values for representative samples are listed in Table S2 in the supplementary material.

The CTC evolution of $\sigma \times h_f$ vs h_f curves during growth of Cu thin films on a-C is presented in Fig. 3 for $T_h = 0.22 - 0.30$ (i.e., $T_S = 298 - 413$ K) and (a) $F = 0.015$ nm/s, (b) $F = 0.102$ nm/s, and (c) $F = 0.535$ nm/s. In qualitative agreement with the results for Ag in Fig. 2, increasing T_h (decreasing F) leads to larger $\sigma_{c,init}$ values (see also Table S2 in the supplementary material), while the tensile rise onset is shifted to higher h_f values, accompanied by an increase of the tensile-to-compressive stress transition thickness. For instance, for $F = 0.015$ nm/s, the tensile-to-compressive transition thickness increases from 9 to 33 nm when increasing T_h from 0.22 to 0.30 [Fig. 3(a)], and decreases from 33 to 17 nm when increasing F from 0.015 to 0.535 nm/s for $T_h = 0.30$ [compare Figs. 3(a) and 3(c)].

The magnitude of $\sigma_{c,init}$ depends on the island size at which the Laplace-pressure-reduced lattice constant is locked into the island, which may increase with increasing T_h,[36] yielding a smaller compressive stress. In addition, $\sigma_{c,init}$ scales with the size of islands formed during the early film growth stages.[37] The latter is determined by the dynamic competition between island nucleation and growth,[38] whereby an increase of T_h and/or a decrease of F enhances the effective adatom diffusivity on the substrate surface and favors formation of fewer and larger islands.[39–44] Our measurements show larger values of $\sigma_{c,init}$ for both Ag (Fig. 2) and Cu (Fig. 3) with increasing (decreasing) $T_h(F)$, which suggests that in our experiments the mechanical load is transferred to the substrate by larger islands and that the change of the island size at which the lattice parameter becomes locked into the island is not very pronounced.

The subsequent tensile stress is caused by island coalescence and, as such, the stress magnitude is proportional to the number of island-impingement occurrences. The latter increases with increasing island number density, which can explain the larger values of $\sigma_{t,init}$ with decreasing T_h. This $\sigma_{t,init}$ vs T_h trend has also been found by Seel *et al.*,[8] who showed, using a model based on finite element methods, that the increasing atomic mobility at the island-substrate interface with increasing T_h leads to island-sliding and reduced tensile stress formation. Figures 2 and 3 also show that the tensile stress regime extends over a larger h_f range with increasing T_h. This is because higher temperatures promote coalescence of islands with increasingly larger sizes[44,45] so that cluster reshaping and coarsening is facilitated over longer periods of time during deposition.

The interplay among tensile stress from island-impingement and compressive stress from insertion of atoms into GBs leads to a tensile-to-compressive peak,[4] which has been shown to coincide with formation of a continuous film.[2] We find a trend toward a larger continuous film formation thickness with increasing T_h and decreasing F for both Ag and Cu films, which is a direct consequence of the larger island size and promoted coalescence,[44] i.e., the films exhibit a more pronounced three-dimensional growth morphology, as discussed in detail in our previous work.[44]

B. Stress evolution after continuous film formation

All curves presented in Fig. 2 exhibit a constant $\sigma \times h_f$ vs h_f slope for $h_f \gtrsim 70$ nm, indicating that a compressive steady-state stress (σ_{SS}) regime is reached for Ag films. Figure 4(a) plots σ_{SS} vs F for $T_h = 0.24 - 0.31$ (i.e., $T_S = 298 - 378$ K). At $T_h = 0.24$, the largest compressive σ_{SS}($\sim\!-44$ MPa) is obtained at $F = 0.025$ nm/s, while increasing F causes σ_{SS} to decrease and reach a plateau value ($\sim\!-25$ MPa) for $F > 0.05$ nm/s. For $T_h = 0.27$, the compressive σ_{SS} values are smaller ($\sim\!-20$ MPa) than those for $T_h = 0.24$ with less pronounced dependence on F; further increase of T_h to 0.31 does not decrease σ_{SS} further, and no F-dependence of σ_{SS} is observed.

In contrast to Ag, no compressive steady-state stress regime is seen during Cu film growth in Fig. 3, which is consistent with previous reports.[29,46,47] Hence, in Fig. 4(b), we present the compressive incremental stress σ_{incr}—calculated from the slope of the $\sigma \times h_f$ vs h_f curves in the film thickness range $h_f = 50 - 65$ nm—as a function of the deposition conditions. The σ_{incr} vs F evolution at $T_h = 0.22$ (i.e., $T_S = 298$ K) is nonmonotonic; the compressive stress initially increases from $\sim\!-85$ MPa, reaching its maximum value (~ -320 MPa) at $F = 0.102$ nm/s, above which it decreases to $\sim\!-220$ MPa for $F = 0.535$ nm/s. With increasing T_h, the dependency of σ_{incr} on F becomes less pronounced, and at the highest $T_h = 0.30$ (i.e., $T_S = 413$ K), σ_{incr} is almost independent of F.

Qualitative comparison of the results presented in Figs. 4(a) and 4(b) shows that for the deposition parameters used in this study, larger compressive stress builds up in Cu films compared to Ag films. Moreover, for both film/substrate systems, the dependence of the stress magnitude on F is pronounced for $T_h = 0.22 - 0.24$ and it is diminished with increasing T_h. To better understand these trends, we study film morphology and correlate it with the stress magnitude and evolution, as discussed in Sec. III C.

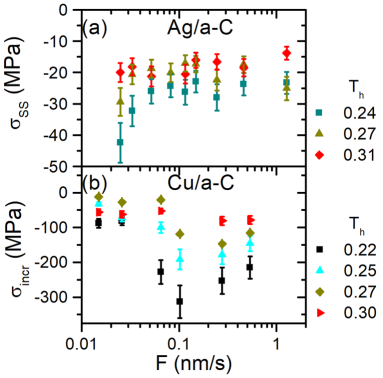

FIG. 4. (a) Evolution of compressive steady-state stress σ_{SS} as a function of deposition rate F during growth of Ag thin films on amorphous carbon (a-C) at homologous temperatures $T_h = 0.24$, 0.27, and 0.31 (i.e., substrate temperatures $T_S = 298$, 338, and 378 K). (b) Evolution of compressive incremental stress σ_{incr} with F during deposition of Cu thin films on a-C at $T_h = 0.22$, 0.25, 0.27, and 0.30 (i.e., $T_S = 298$, 338, 378, and 413 K). More details in the definition of σ_{incr} are provided in the text.

C. Correlation of continuous-layer stress with film morphology

AFM was used to study the morphology of Ag and Cu films deposited at various T_h and F values (images are provided in the supplementary material), and the respective height–height correlation functions $g(r)$ were calculated, as explained in Sec. II. Due to the nonequilibrium character of vapor-based growth, deposited films have self-affine surfaces,[48] for which $g(r)$ converges to steady-state value $g_{SS}(r)$ that is related to the root-mean square surface roughness w via the expression $g_{SS}^{1/2}(r) = \sqrt{2}\,w$.[49] Figure 5 plots $g^{1/2}(r)$ vs r for Cu [Fig. 5(a)] and Ag [Fig. 5(b)] films grown at various F and T_h values. We see that $g_{SS}(r)$ (indicated by horizontal arrows) and thereby w increases with increasing T_h [e.g., for Ag deposited with $F = 0.033$ nm/s, $w_{Ag}(T_h = 0.24) = 3.2$ nm, and $w_{Ag}(T_h = 0.31) = 14.5$ nm] and decreasing F for both film/substrate systems [e.g., for $F = 1.27$ nm/s, $w_{Ag}(T_h = 0.24) = 1.8$ nm]. We also notice that for comparable values of T_h and F, $w_{Cu} < w_{Ag}$, e.g., for $T_h = 0.30$ and $F = 0.015$ nm/s, $w_{Cu} = 7.6$ nm, compared to $w_{Ag} = 14.5$ nm for $T_h = 0.31$ and $F = 0.033$ nm/s.

A closer analysis of $g^{1/2}(r)$ vs r curves reveals local minima in the $30 - 350$ nm r-range. The position of the first local minimum (indicated by vertical arrows in Fig. 5) corresponds to the average mound separation distance d on the film surface,[50–52] which provides information on the lateral surface corrugation that is not included in the root-mean square roughness w. For Ag films [see Fig. 5(b)] and Cu films deposited at $T_h = 0.30$ [see Fig. 5(a)], d follows the trend of w (i.e., increases with increasing T_h and

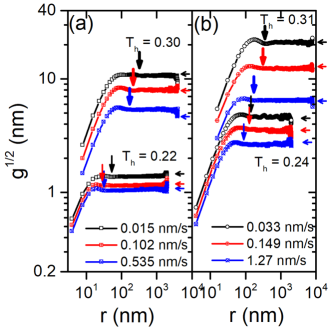

FIG. 5. Square root of the height–height correlation function $g^{1/2}(r)$ of (a) Cu (thickness 65 nm) and (b) Ag (thickness 105 nm) thin films grown at different deposition rates (indicated by symbols) and homologous temperatures T_h (indicated by line thickness and text in the figure). Vertical arrows mark local minima of $g^{1/2}(r)$, indicating the average mound separation on the surface, and horizontal arrows mark the steady-state value $g_{ss}^{1/2}(r)$, i.e., an indicator for the film surface roughness.

decreasing F), which means that the surface is characterized by laterally larger mounds separated by deeper trenches. This trend does not hold for Cu deposited at $T_h = 0.22$, where the highest value of $d = 53$ nm is found for $F = 0.015$ nm/s, but no substantial change is seen (28 and 32 nm) when increasing F from 0.102 to 0.535 nm/s.

EBSD maps indicating the grain size and orientation (color code presented by inverse pole figures) of 105 nm thick Ag films are presented in Fig. 6. For deposition at $T_h = 0.24$ (i.e., $T_S = 298$ K), the average grain size decreases slightly from ∼130 to ∼120 nm when increasing F from 0.033 to 1.27 nm/s, which stems from a smaller population of grains with sizes larger than 200 nm for high F. In addition, a strong preferred $\langle 111 \rangle$ orientation of the grains can be found for deposition for $F = 1.27$ nm/s. For higher $T_h = 0.31$ (i.e., $T_S = 378$ K), the grain size of Ag films deposited at 0.033 nm/s increases to ∼200 nm, while the grain size remains at ∼120 nm for $F = 1.27$ nm/s. Independent of F, no preferred crystal orientation can be detected for $T_h = 0.31$. EBSD measurements for Cu films were not successful, as the lateral grain size approaches the resolution of the instrument (25 nm). This is consistent with the low value of lateral mound separation d ($d \leq 53$ nm) extracted from AFM for Cu films deposited at $T_h = 0.22$ [i.e., $T_S = 298$ K, see Fig. 5(a)].

In the literature, the following mechanisms have been suggested to explain stress evolution of continuous films: (i) Formation of **new GB segments** at triple junctions that causes tensile stress;[10,11] (ii) **grain growth** that may occur at high-mobility conditions and leads to tensile stress;[18,27] (iii) **adatom-insertion into GBs** at high-mobility conditions driven by chemical potential gradient between surface and GB resulting in compressive stress;[15,18] and (iv) incorporation of **point defects** in the grains and/or in GBs, due to energetic bombardment (i.e., "atomic peening"), yielding compressive stress.[12] The final magnitude and type of film stress is the result of the superposition of these stress contributions and their respective dependence on the film morphology. With the microstructural information provided earlier in the present section, we can now discuss our experimental results in view of the interplay and interdependence of these stress-contributing processes.

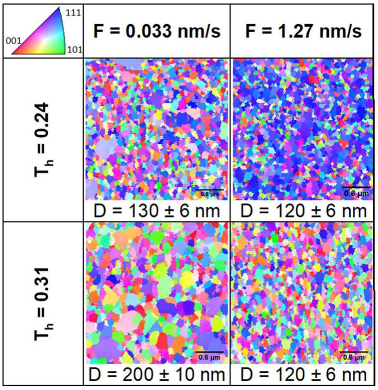

FIG. 6. EBSD maps ($3 \times 3\,\mu m^2$) for Ag films grown on amorphous carbon with deposition rates $F = 0.033$ and 1.27 nm/s at homologous temperatures $T_h = 0.24$ (i.e., substrate temperature $T_S = 298$ K) and 0.31 (i.e., $T_S = 378$ K). The color code of the grains corresponds to their orientation in an inverse pole figure, and the average grain size D is indicated for the respective maps.

The results for Ag films presented in Fig. 2 show that compressive stress develops after continuous-layer formation, which reaches a compressive steady-state. For depositions at $T_h = 0.24$, grain size does not change significantly as a function of F, while σ_{SS} becomes less compressive with increasing F before reaching a plateau. This trend is consistent with the model proposed by Chason *et al.*[9] The model explains the compressive σ_{SS} decrease in light of a reduced number of adatoms that can reach the GBs, owing to the higher density of adatoms and shorter adatom diffusion length with increasing F. A similar trend is also observed for Cu films at $T_h = 0.22$ for F values larger than 0.102 nm/s [see Fig. 4(b)]. This is opposite to data by Kaub *et al.*,[24] who reported an increase in compressive σ_{SS} values for Cu grown at $T_h = 0.22$ for F increasing in the range $1.2 - 2.4$ nm/s. This behavior has been attributed to bombardment-induced point-defect formation and trapping due to the faster progressing growth front at larger F values. Our largest $F = 0.535$ nm/s lies well outside the range in the work of Kaub *et al.*,[24] which indicates that defect-induced stress formation is not a dominant process at our growth conditions. In contrast to low-mobility metals (as, e.g., Mo deposited at $T_h \sim 0.1$),[12] the effect of energetic particle bombardment is less significant for high-mobility systems, whereby high values of T_h promote defect annihilation.

Increasing T_h from 0.24 to 0.31 causes the magnitude of compressive stress in Ag to decrease, most notably for $F \leq 0.033$ nm/s [see Fig. 4(a)], while the grain size increases from ∼130 to ∼200 nm (see Fig. 6). In a film with larger grains, fewer new GB segments form on the surface, which results in smaller tensile stress. Concurrently, fewer GBs exist into which atoms can be inserted yielding a smaller compressive stress. Figure 5(b) shows that w increases with T_h, which has been suggested to inhibit the formation of new GB segments on the surface.[28] Hence, we attribute the decrease of the magnitude of σ_{SS} as a function of T_h to reduction of the compressive stress component caused by elimination of GBs.

At $T_h = 0.31$, σ_{SS} reaches its smallest value of ∼20 MPa and it becomes practically independent of F for Ag films, despite changes in the film microstructure (the grain size decreases from ∼200 nm for $F = 0.033$ nm/s to ∼ 120 nm for $F = 1.27$ nm/s, and the roughness decreases from 14.9 to 4.6 nm in the same F range). This indicates that adatom surface diffusion and incorporation into GBs is not the limiting factor that determines the magnitude of σ_{SS} at these high temperature conditions. A similar behavior is also observed for Cu films at $T_h = 0.30$ [see Fig. 4(b)].

Comparison of Figs. 4(a) and 4(b) reveals a noticeable difference between the stress evolutions of Ag and Cu films at low deposition rates: contrary to Ag film growth, a smaller compressive stress is formed when decreasing F from 0.102 to 0.015 nm/s for $T_h = 0.22$. This is also reflected in the $\sigma \times h_f$ vs h_f curves for $F = 0.015$ nm/s, which show that the incremental stress tends to turn tensile for $h_f = 65$ nm (see Fig. 3). This is a known behavior for films that exhibit grain growth (e.g., Ni in Ref. 53) or under-dense morphology (e.g., Cu during deposition at high Ar pressure > 0.5 Pa[29]). XRR measurements show that Cu films deposited at $F = 0.015$ nm/s have a mass density equal to the bulk value (8.92 g/cm^3), i.e., the emergence of tensile stress cannot be ascribed to the formation of under-dense films. Concurrently, the average mound separation distance increases from 28 to 53 nm for $T_h = 0.22$ when changing F from 0.102 to 0.015 nm/s [compare data in Fig. 5(a)], suggesting that the grain size increases with decreasing F. The thickness of the tensile-to-compressive transition in Fig. 3 can be used as an approximation for the grain size upon continuous film formation. The transition thickness marginally increases from 8 to 9 nm, when decreasing F from 0.102 to 0.015 nm/s, indicating similar grain sizes at continuity. Hence, the larger grain size indicated for low F from AFM measurements for 65 nm thick films may be the result of grain growth at larger thicknesses.

Yu and Thompson reported that incorporation of impurities, including O_2, in Ni films is another factor that affects the steady-state stress magnitude.[54] They performed experiments at various oxygen partial pressures p_{O_2} in the deposition chamber and showed that an increase of p_{O_2} leads to more tensile stress formation, due to reduced adatom-GB interaction and thus less pronounced adatom insertion into GBs. In our experiments, we do not deliberately introduce impurity species during film growth. However, depositions are performed in a high-vacuum chamber, which has a residual atmosphere at a base pressure of $\sim 8 \times 10^{-6}$ Pa consisting mainly of H_2O, toward which Cu has a high affinity.[55] In order to explore the relevance of impurities for the stress formation in our films, XPS measurements and depth-profile analysis were performed on capped Ag and Cu films; an overview of the results is presented in Table I, while x-ray photoelectron spectra are presented in the supplementary material. For the chemical analysis, O-1s and Cu-2p/Ag-3d binding energies were used, other elements were not detected. After surface cleaning (i.e., ~1 nm ion-beam etching), the O/Cu ratio in Cu films deposited at $F = 0.015$ nm/s is 0.246; this value decreases with increasing deposition rate and O/Cu = 0.091 for $F = 0.535$ nm/s. The relative oxygen concentration decreases with increasing etching depth but remains nonzero for all deposition rates (e.g., O/Cu = 0.014 for $F = 0.015$ nm/s after ~7 nm etching) and decreases with increasing values of F (e.g., O/Cu = 0.006 for $F = 0.535$ nm/s) for constant etching depth. For comparable values of F, Ag films contain no oxygen after ~5 nm ion-beam etching, which is consistent with considerably weaker affinity Ag to background gaseous impurities.[55] Hence, the nonmonotonic behavior of σ_{incr} vs F for Cu may also be explained by gaseous impurities incorporation in the Cu films from the background atmosphere in the deposition chamber. The increased propensity for impurity incorporation with decreasing deposition rate can be understood in light of the interplay between the monolayer (ML) formation times of impurities $\tau_{ML}^{impurities}$ and film τ_{ML}^{film}. $\tau_{ML}^{impurities}$ is dependent on the impurity partial pressure in the growth atmosphere, and thus constant for all F values, while τ_{ML}^{film} decreases with increasing F. Consequently, the ratio $\tau_{ML}^{film}/\tau_{ML}^{impurities}$, which is a measure for the impurity-incorporation in the film, decreases with increasing deposition rate. An increase of T_h leads to smaller sticking coefficient of impurity species (i.e., $\tau_{ML}^{impurities}$ increases),[56] while adatoms have higher diffusivities.[44] This can explain the decrease of σ_{incr} with decreasing F is less pronounced at $T_h = 0.25$ and that almost no variation is observed at $T_h = 0.30$ [see Fig. 4(b)].

TABLE I. Ratio of oxygen-to-copper (O/Cu) and oxygen-to-silver (O/Ag) in sputter-deposited Cu and Ag films, as determined from x-ray photoemission spectroscopy. Spectra were acquired after etching with Ar$^+$ ions, which removes surface contamination and the amorphous carbon capping layer. For Cu films, data for various deposition rates F are presented.

	O/Cu			O/Ag
F	0.015 nm/s	0.102 nm/s	0.535 nm/s	0.109 nm/s
~1 nm etching	0.246	0.143	0.091	0.111
~5 nm etching				0
~7 nm etching	0.014	0.012	0.006	

Finally, we return to a comparison among the stress evolution during Ag and Cu film growth. With the information on microstructure, microchemistry, and surface morphology presented above, we can relate the larger stress values measured in Cu films compared to Ag films to smaller grain size (i.e., higher GB number density), smaller surface roughness, and higher affinity to gas molecules from the growth atmosphere. Moreover, the biaxial modulus of the bulk Cu $Y_{Cu} = 200$ GPa is larger than bulk silver $Y_{Ag} = 130$ GPa; consequently, a comparable strain level would result in ~50% larger stress in Cu compared to Ag films.

D. Postdeposition stress evolution

Postdeposition stress measurements (see Fig. 7) show that all process parameters used in this work lead to a tensile stress rise when deposition is stopped. This is a typical behavior for films grown at conditions of high atomic mobility[15,57–59] and it is commonly referred to as "stress relaxation," relative to the compressive stress observed after formation of a continuous film. Experiments on stress evolution before continuous-layer formation[6,60,61] have shown that additional processes, including adatom-surface interactions and defect annihilation, are operative after deposition flux is turned off. Therefore, in the following, we will not use the term relaxation when presenting and discussing the evolution of $\sigma \times h_f$ as a function of time t after deposition stop. We remind the reader that T_S was kept constant during postdeposition stress monitoring and note that thermal stress from heating of the substrate during deposition has been corrected, as explained in Sec. II.

Figures 7(a)–7(c) present the postdeposition stress evolution of Ag films for deposition rates (a) 0.033 nm/s, (b) 0.149 nm/s, and (c) 1.27 nm/s and $T_h = 0.24$, 0.25, 0.27, and 0.31 (i.e., 298, 313, 338, 378 K), after correction for σ_{th}, as a function of time t. For all deposition rates, we find decreasing tensile stress rise with increasing values of T_h, e.g., for $F = 0.033$ nm/s, $\sigma \times h_f$ decreases from 3.0 to 1.0 N/m when increasing T_h from 0.24 to 0.31 [see Fig. 7(a)]. Conversely, the postdeposition tensile rise increases with increasing deposition rate, e.g., $\sigma \times h_f = 6.2$ N/m for $F = 1.27$ nm/s and $T_h = 0.24$ [compare Figs. 7(a) and 7(c)].

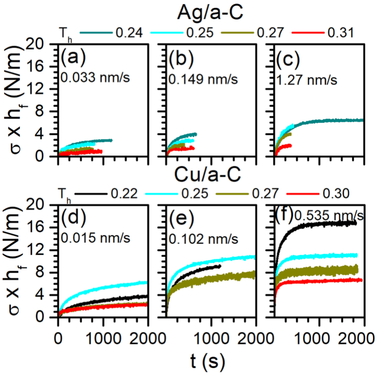

FIG. 7. Evolution of stress-thickness $\sigma \times h_f$ with time t after deposition completion of (a)–(c) Ag and (d)–(f) Cu thin films on amorphous carbon (a-C). For Ag, deposition rates (a) 0.033 nm/s, (b) 0.149 nm/s, and (c) 1.27 nm/s and homologous temperatures $T_h = 0.24, 0.25, 0.27$, and 0.31 (i.e., 298, 313, 338, 378 K) were used, for Cu, the deposition rates were (d) 0.015 nm/s, (e) 0.102 nm/s, and (f) 0.535 nm/s and $T_h = 0.22, 0.25, 0.27$, and 0.30 (i.e., 298, 338, 378, 413 K).

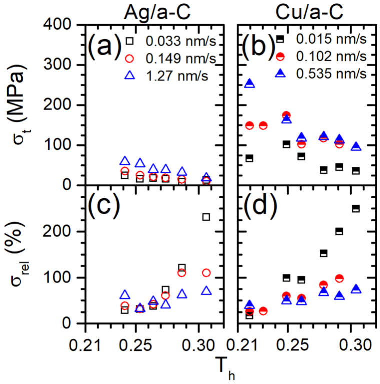

FIG. 8. Temperature dependence of [(a) and (b)] postdeposition tensile rise σ_t and [(c) and (d)] σ_t relative to the compressive stress formed during deposition (σ_{rel}) for Ag [(a) and (c)] and Cu [(b) and (d)] films on amorphous carbon (a-C) deposited with three different deposition rates F for Ag ($F = 0.033$ nm/s, 0.149 nm/s, 1.27 nm/s) and Cu ($F = 0.015$ nm/s, 0.102 nm/s, 0.535 nm/s), respectively. Ag and Cu films were deposited in the homologous temperature T_h range $0.24 - 0.31$ (i.e., substrate temperature $T_S = 298 - 378$ K) and $0.22 - 0.30$ (i.e., $T_S = 298 - 413$ K), respectively.

The same trend can be seen for the postdeposition stress evolution of Cu films for deposition rates (d) 0.015 nm/s, (e) 0.102 nm/s, and (f) 0.535 nm/s and a comparable T_h-range. The magnitude of the tensile stress rise decreases with increasing T_h, e.g., for $F = 0.015$ nm/s, $\sigma \times h_f$ decreases from 6.1 to 2.1 N/m when increasing T_h from 0.25 to 0.30 [see Fig. 7(d)]. The magnitude of the tensile rise at $T_h = 0.22$ is smaller than at 0.25 for $F \leq 0.102$ nm/s [see Figs. 7(d) and 7(e)]. With increasing deposition rate, the tensile rise becomes more pronounced for all values of T_h, e.g., $\sigma \times h_f$ increases from 6 to 11 N/m when increasing F from 0.015 to 0.535 nm/s at $T_h = 0.25$ [compare Figs. 7(d) and 7(f)].

Figures 8(a) and 8(b) give an overview of the postdeposition tensile stress rise σ_t for Ag and Cu, respectively, as extracted from Fig. 7 and highlights the larger values of σ_t in Cu films compared to Ag films. For a more complete picture of the relation between σ_t and compressive stress σ_c formed during film growth, we calculate the relative stress $\sigma_{rel} = \sigma_t/|\sigma_c|$, where $|\sigma_c|$ denotes the absolute value of σ_c. Figures 8(c) and 8(d) present σ_{rel} for Ag and Cu, respectively, as a function of T_h for different deposition rates F. For Ag, two regimes can be identified: (i) for $T_h < 0.27$, variations of T_h and F have little influence on σ_{rel}, with a tendency of higher σ_{rel} values at higher values of F; (ii) for $T_h > 0.27$, σ_{rel} increases with T_h and decreases with increasing F, for given T_h. It is also in this region where σ_{rel} exhibits values larger than 100% for the lowest deposition rate $F = 0.033$ nm/s, which shows that the measured tensile rise cannot purely be a relaxation process. A very similar trend can be found for the postdeposition stress evolution of Cu on a-C [Fig. 8(d)]. σ_{rel} increases with increasing T_h, and for $T_h > 0.27$, σ_{rel} exhibits values larger than 100% for $F = 0.015$ nm/s. The increase in σ_{rel} with increasing T_h becomes less pronounced at high F, while no $\sigma_{rel} > 100\%$ were measured for $F \geq 0.102$ nm/s in the range $0.27 < T_h < 0.31$.

In the literature, the following mechanisms have been associated with the postdeposition stress evolution: (i) thermal stress σ_{th}; (ii) grain growth; (iii) out-diffusion of atoms from GBs, as adatom supersaturation on the film surface decreases after deposition stop;[9,17,62] and (iv) reshaping of GB grooves.[20,21,30,63] All these mechanisms lead to tensile stress and are active for conditions of high mobility. Our postdeposition stress data have been corrected for the contribution due to σ_{th}, and hence thermal stress does not account for the trends observed in Fig. 8. Table S2 in the supplementary material gives an overview of ΔT_S and σ_{th} for Ag and Cu thin films, for selected F values. We note that the knowledge of σ_{th} is especially important for Ag films deposited at high values of F, where σ_{th} is responsible for 50% of the originally observed tensile rise.

Flötotto *et al.*[30] have shown in experiments for which the grain size is fixed using template layers that F has little influence on the magnitude of the postdeposition tensile rise σ_t, while increasing grain size—i.e., decreasing GB number density—leads to a smaller tensile rise. This is in agreement with the decrease in σ_t [Fig. 8(a)] we find with decreasing F and increasing T_h at $F = 0.033$ nm/s for Ag, for which EBSD results (Fig. 6) show that the grain size increases. For $F = 1.27$ nm/s, the grain size is nearly constant with T_h, while we still see a decreasing σ_t with increasing T_h; which may be related to the larger compressive stress formed during growth [e.g., compare $\sigma \times h_f = -2.9$ N/m for $T_h = 0.24$ at deposition-interrupt vs -1.0 N/m for $T_h = 0.31$ in Fig. 2(c)].

While the general trend toward larger tensile rise with increasing F also holds for the postdeposition stress evolution of Cu depicted in Fig. 8(b), this cannot be solely explained by the associated change of grain size. In particular, for depositions at $T_h = 0.22$, for which the grain size does not vary between 0.102 and 0.535 nm/s, an σ_t increase from 150 to 250 MPa is observed. Possible incorporation of residual gas species into the GB, as suggested in Sec. III C, may effectively hinder the out-diffusion of adatoms from the GBs, once the deposition is stopped, and thus decrease the tensile stress developing postdeposition.

The stress evolution during and postdeposition of Ag and Cu films is dissimilar in magnitude and is affected by changes of T_h and F to a substantially different degree, which is related to morphological and microchemical changes in the films. Nevertheless, the comparison of $\sigma_{rel} = \sigma_t/|\sigma_c|$ for Ag and Cu presented in Figs. 7(c) and 7(d), respectively, shows a coherent picture, indicating that the key processes governing the stress evolution are the same.

Figure 9 presents the postdeposition tensile rise $\sigma \times h_f$, normalized to $\sigma_t \times h_f$, with the final value σ_t presented in Fig. 8(b) for Cu films, showing an overall trend toward faster tensile rise with increasing F and T_h. While a constant $(\sigma \times h_f)/(\sigma_t \times h_f)$ value is reached within 200 s for the highest $T_h = 0.30$ (i.e., $T_S = 413$ K) and $F = 0.535$ nm/s, only ~85% is reached during the same time and for the same value of F at $T_h = 0.22$ (i.e., $T_S = 298$ K), and merely ~35% is reached for the lowest values $F = 0.015$ nm/s and $T_h = 0.22$. The F-dependence of the tensile rise kinetics for the Ag/a-C system shows the same trend, however, less pronounced (see Fig. S2 in the supplementary material).

Previous studies on postdeposition stress evolution [47,64] attribute tensile rise within hundreds of seconds to surface-diffusion based processes, while grain growth is a slower process involving bulk rearrangements. Flötotto *et al.*[30] found faster tensile rise with increasing F and for larger grain sizes. They explained this trend in light of different shapes of GB grooves during and after deposition: (i) during deposition, the driving force for adatom diffusion to the GB is large, allowing adatoms to overcome the accumulation of steps close to GB (i.e., Zeno effect[65]), which results in GB grooves that are more shallow than the equilibrium surface profile; (ii) while after deposition, the driving force for atom incorporation into GB decreases dramatically, the grooves deepen as adatoms attach to steps, and a shape closer to the equilibrium surface profile is attained.[21,63] This postdeposition deepening of GB grooves releases compressive stress and is more pronounced for high T_h, which is consistent with our data.

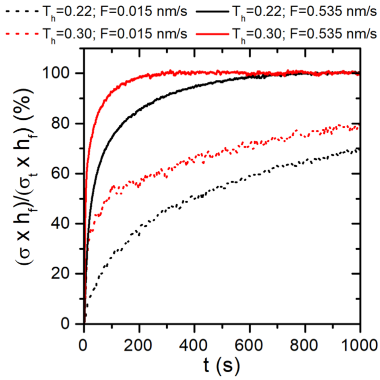

FIG. 9. Evolution of stress-thickness $(\sigma \times h_f)/(\sigma_t \times h_f)$, normalized to the maximum tensile rise σ_t presented in Figs. 7(d)–7(f), with time t after deposition of Cu thin films on amorphous carbon at homologous temperatures $T_h = 0.22$ (i.e., substrate temperature $T_S = 298$ K) and 0.30 (i.e., $T_S = 413$ K) as well as deposition rates $F = 0.015$ and 0.535 nm/s.

Earlier in the present section, we have discussed the influence of incorporation of adsorbed gas molecules on the magnitude of the tensile rise of Cu films at low values of T_h and F. The presence of such impurities in GBs may delay the out-diffusion of atoms postdeposition, resulting in the slow tensile rise seen for these deposition conditions. Moreover, during the discussion of the stress evolution in continuous Cu films deposited with $F = 0.015$ nm/s (see Sec. III C), we have identified grain growth as a potential explanation for the trend toward tensile stress formation in Cu films. If grain growth is active after deposition, its long time scale[64] may account for the much slower tensile rise seen for $F = 0.015$ nm/s in Fig. 9. The above discussed mechanisms (i.e., grain growth and impurity incorporation) are seemingly not relevant for Ag film stress generation and evolution, as mentioned in Sec. III C, which may explain the overall faster postdeposition stress evolution kinetics as compared to Cu.

IV. SUMMARY AND OUTLOOK

We have studied real-time stress evolution during and after growth of Ag and Cu films that are deposited by magnetron sputtering on amorphous carbon substrates, while systematically changing substrate temperature between 298 and 413 K (corresponding to homologous temperatures $0.22 - 0.31$) and deposition rate between 0.015 and 1.27 nm/s. All films show a compressive-tensile-compressive stress evolution as a function of film thickness. Increasing substrate temperature results in smaller compressive stress due to increasing grain size (i.e., lower grain-boundary length), and weaker deposition rate-dependence of the stress as adatom surface diffusion is promoted. With increasing deposition rate, less compressive stress is formed during the deposition of Ag. This is an indication that incorporation of atoms into grain boundaries is inhibited owing to the higher density of adatoms on the surface with increasing deposition rate, and consequently shorter diffusion lengths. This trend can also be seen for Cu films deposited with deposition rates > 0.102 nm/s, whereas for deposition rates < 0.102 nm/s, a tendency toward tensile stress formation is observed. From chemical microanalysis with x-ray photoelectron spectroscopy, we find increasing incorporation of oxygen from the background pressure with decreasing deposition rate, which inhibits atom incorporation into grain boundaries, and such that less compressive stress is formed. The grain-boundary number density determines the strength of the postdeposition tensile rise, while high substrate temperature and deposition rate promote the kinetics of the postdeposition stress evolution. This trend is especially pronounced for Cu, where the presence of gas molecules seemingly slows the diffusion out of grain-boundaries.

SUPPLEMENTARY MATERIAL

See the supplementary material for (i) calculation of the deposition rate-dependent thermal stress that builds up after the deposition is stopped; (ii) incremental compressive and tensile stress during the initial growth stages of Ag and Cu film growth; (iii) atomic force microscopy images that were used to analyze the surface morphology of Ag and Cu films; (iv) normalized stress-thickness vs time curves for Ag thin films after deposition stop; and (v) x-ray photoelectron spectroscopy measurements of Ag and Cu thin films.

ACKNOWLEDGMENTS

The authors wish to thank Dr. Hadi Bahsoun for performing the EBSD measurements and Ph. Guérin for his technical assistance during sample deposition. A.J. and G.A. acknowledge the financial support of the French Government program “Investissements d’Avenir” (LABEX INTERACTIFS, Reference No. ANR-11-LABX-0017-01). K.S. acknowledges Linköping University (“LiU Career Contract, Dnr-LiU-2015-01510, 2015-2020”) and the Swedish Research Council (Contract No. VR-2015-04630). A.J. and K.S. acknowledge financial support from the Åforsk Foundation (Contract No. ÅF 19-137). K.S. and N.P. acknowledge financial support from the Olle Engkvist Foundation (Contract No. SOEB 190-312) and the Wenner-Gren Foundations (Contract Nos. UPD2018-0071 and UPD2019-0007).

REFERENCES

[1] R. Koch, Surf. Coat. Technol. **204**, 1973 (2010).
[2] G. Abadias, L. Simonot, J. J. Colin, A. Michel, S. Camelio, and D. Babonneau, Appl. Phys. Lett. **107**, 183105 (2015).
[3] G. Abadias, E. Chason, J. Keckes, M. Sebastiani, G. B. Thompson, E. Barthel, G. L. Doll, C. E. Murray, C. H. Stoessel, and L. Martinu, J. Vac. Sci. Technol. A **36**, 020801 (2018).
[4] E. Chason and P. R. Guduru, J. Appl. Phys. **119**, 191101 (2016).
[5] C. W. Mays, J. S. Vermaak, and D. Kuhlmann-Wilsdorf, Surf. Sci. **12**, 134 (1968).
[6] J. A. Floro, S. J. Hearne, J. A. Hunter, P. Kotula, E. Chason, S. C. Seel, and C. V. Thompson, J. Appl. Phys. **89**, 4886 (2001).
[7] M. A. Phillips, V. Ramaswamy, B. M. Clemens, and W. D. Nix, J. Mater. Res. **15**, 2540 (2000).
[8] S. C. Seel, C. V. Thompson, S. J. Hearne, and J. A. Floro, J. Appl. Phys. **88**, 7079 (2000).
[9] E. Chason, J. W. Shin, S. J. Hearne, and L. B. Freund, J. Appl. Phys. **111**, 83520 (2012).
[10] W. D. Nix and B. M. Clemens, J. Mater. Res. **14**, 3467 (1999).
[11] L. B. Freund and E. Chason, J. Appl. Phys. **89**, 4866 (2001).
[12] E. Chason, M. Karlson, J. J. Colin, D. Magnfält, K. Sarakinos, and G. Abadias, J. Appl. Phys. **119**, 145307 (2016).
[13] S. Y. Grachev, F. D. Tichelaar, and G. C. A. M. Janssen, J. Appl. Phys. **97**, 073508 (2005).
[14] J. J. Colin, G. Abadias, A. Michel, and C. Jaouen, Acta Mater. **126**, 481 (2017).
[15] E. Chason, B. W. Sheldon, L. B. Freund, J. A. Floro, and S. J. Hearne, Phys. Rev. Lett. **88**, 156103 (2002).
[16] E. Chason, Thin Solid Films **526**, 1 (2012).
[17] A. Saedi and M. J. Rost, Nat. Commun. **7**, 10733 (2016).
[18] E. Chason, A. M. Engwall, Z. Rao, and T. Nishimura, J. Appl. Phys. **123**, 185305 (2018).
[19] P. Chaudhari, J. Vac. Sci. Technol. **9**, 520 (1972).
[20] E. Vasco and C. Polop, Phys. Rev. Lett. **119**, 256102 (2017).
[21] E. Vasco, E. G. Michel, and C. Polop, Phys. Rev. B **98**, 195428 (2018).
[22] A. M. Engwall, Z. Rao, and E. Chason, J. Electrochem. Soc. **164**, D828 (2017).
[23] A. L. Del Vecchio and F. Spaepen, J. Appl. Phys. **101**, 063518 (2007).
[24] T. Kaub, Z. Rao, E. Chason, and G. B. Thompson, Surf. Coat. Technol. **357**, 939 (2019).
[25] F. A. Doljack and R. W. Hoffman, Thin Solid Films **12**, 71 (1972).
[26] G. Thurner and R. Abermann, Thin Solid Films **192**, 277 (1990).
[27] E. Chason and A. F. Bower, J. Appl. Phys. **125**, 115304 (2019).
[28] X. Zhou, X. Yu, D. Jacobson, and G. B. Thompson, Appl. Surf. Sci. **469**, 537 (2019).
[29] M. Pletea, W. Brückner, H. Wendrock, and R. Kaltofen, J. Appl. Phys. **97**, 054908 (2005).
[30] D. Flötotto, Z. M. Wang, L. P. H. Jeurgens, and E. J. Mittemeijer, J. Appl. Phys. **118**, 055305 (2015).
[31] J. Leib and C. V. Thompson, Phys. Rev. B **82**, 121402 (2010).
[32] J. A. Floro, E. Chason, S. R. Lee, R. D. Twesten, R. Q. Hwang, and L. B. Freund, J. Electron. Mater. **26**, 969 (1997).
[33] A. Fillon, G. Abadias, A. Michel, and C. Jaouen, Thin Solid Films **519**, 1655 (2010).
[34] G. G. Stoney, Proc. R. Soc. Lond. A **82**, 172 (1909).
[35] D. Nečas and P. Klapetek, Open Phys. **10**, 181 (2012).
[36] R. C. Cammarata, T. M. Trimble, and D. J. Srolovitz, J. Mater. Res. **15**, 2468 (2000).
[37] R. Abermann and R. Koch, Thin Solid Films **129**, 71 (1985).
[38] T. Michely and J. Krug, *Islands, Mounds and Atoms* (Springer, Berlin, 2004).
[39] E. Ganz, K. Sattler, and J. Clarke, Surf. Sci. **219**, 33 (1989).
[40] G. M. Francis, I. M. Goldby, L. Kuipers, B. von Issendorff, and R. E. Palmer, J. Chem. Soc. Dalton. Trans. **5**, 665 (1996).
[41] J. Carrey and J.-L. Maurice, Phys. Rev. B **65**, 205401 (2002).
[42] J. M. Warrender and M. J. Aziz, Phys. Rev. B **76**, 045414 (2007).
[43] B. Lü, V. Elofsson, E. P. Münger, and K. Sarakinos, Appl. Phys. Lett. **105**, 163107 (2014).
[44] A. Jamnig, D. G. Sangiovanni, G. Abadias, and K. Sarakinos, Sci. Rep. **9**, 6640 (2019).
[45] B. Lü, E. P. Münger, and K. Sarakinos, J. Appl. Phys. **117**, 134304 (2015).
[46] T. Kaub, R. Anthony, and G. B. Thompson, J. Appl. Phys. **122**, 225302 (2017).
[47] F. Cemin, G. Abadias, T. Minea, C. Furgeaud, F. Brisset, D. Solas, and D. Lundin, Acta Mater. **141**, 120 (2017).
[48] F. Family and T. Vicsek, *Dynamics of Fractal Surfaces* (World Scientific Publishing Co. Pte. Ltd., Singapore, 1991).
[49] G. Palasantzas and J. Krim, Phys. Rev. Lett. **73**, 3564 (1994).
[50] B. W. Karr, I. Petrov, D. G. Cahill, and J. E. Greene, Appl. Phys. Lett. **70**, 1703 (1997).
[51] A. B. Mei, B. M. Howe, C. Zhang, M. Sardela, J. N. Eckstein, L. Hultman, A. Rockett, I. Petrov, and J. E. Greene, J. Vac. Sci. Technol. A **31**, 061516 (2013).
[52] F. Nita, C. Mastail, and G. Abadias, Phys. Rev. B **93**, 64107 (2016).
[53] H. Z. Yu and C. V. Thompson, Acta Mater. **67**, 189 (2014).
[54] H. Z. Yu and C. V. Thompson, J. Vac. Sci. Technol. A **33**, 021504 (2015).
[55] A. Michaelides, V. A. Ranea, P. L. de Andres, and D. A. King, Phys. Rev. Lett. **90**, 216102 (2003).
[56] H. Ibach, *Physics of Surfaces and Interfaces* (Springer-Verlag, Berlin, 2006).
[57] J. S. Tello, A. F. Bower, E. Chason, and B. W. Sheldon, Phys. Rev. Lett. **98**, 216104 (2007).
[58] J. S. Tello and A. F. Bower, J. Mech. Phys. Solids **56**, 2727 (2008).

[59] C.-W. Pao, S. M. Foiles, E. B. Webb, D. J. Srolovitz, and J. A. Floro, Phys. Rev. Lett. **99**, 036102 (2007).
[60] C. Friesen and C. V. Thompson, Phys. Rev. Lett. **89**, 126103 (2002).
[61] C. Friesen, S. C. Seel, and C. V. Thompson, J. Appl. Phys. **95**, 1011 (2004).
[62] J. W. Shin and E. Chason, Phys. Rev. Lett. **103**, 056102 (2009).
[63] H. Z. Yu and C. V. Thompson, Appl. Phys. Lett. **104**, 141913 (2014).
[64] H. Z. Yu, J. S. Leib, S. T. Boles, and C. V. Thompson, J. Appl. Phys. **115**, 043521 (2014).
[65] M. J. Rost, Phys. Rev. Lett. **99**, 266101 (2007).

Supplementary material: “The effect of kinetics on intrinsic stress generation and evolution in sputter-deposited films at conditions of high atomic mobility”

A. Jamnig[1,2,*], N. Pliatsikas[2], K. Sarakinos[2], and G. Abadias[1]

*Corresponding author, email: andreas.jamnig@univ-poitiers.fr ; andreas.jamnig@liu.se

[1]*Institut Pprime, Département Physique et Mécanique des Matériaux, UPR 3346 CNRS, Université de Poitiers, SP2MI, 11 Bvd M. et P. Curie, F86073 Poitiers Cedex 9, France*

[2]*Nanoscale Engineering Division, Department of Physics, Chemistry, and Biology, Linköping University, SE 581 83, Linköping, Sweden*

S1. THERMAL STRESS CALCULATION

The stress evolution of films deposited at conditions of high atomic mobility continues after deposition, and usually shows a tensile rise. One contributor to this tensile stress is the thermal stress $\sigma_{th} = Y \Delta\alpha_{th} \Delta T_S$, where Y is the film material biaxial modulus ($Y_{Ag} = 130\,GPa$ and $Y_{Cu} = 200\,GPa$), $\Delta\alpha_{th}$ is the difference in thermal expansion coefficients of substrate and film, and ΔT_S is the deposition-induced substrate temperature increase. Using thermocouples mounted in the vicinity of the substrate, we found that after deposition stop the substrate temperature T_S decreases exponentially, following $T_S(t) = T_S + \Delta T_S \times \exp(-t/\tau)$, where $\tau = 2470 \pm 3\,s$ is the decay time, which is independent of T_S. This leads to the build-up of thermal stress with $\sigma_{th}(t) = \sigma_{th} \times (1 - \exp(-t/\tau))$. Table S1 provides an overview of ΔT_S, σ_{th}, and the stress-thickness product $\sigma_{th} \times h_f$ for Ag ($h_{f,Ag} = 105\,nm$) and Cu ($h_{f,Cu} = 65\,nm$) films grown at $T_S = 298\,K$ for representative deposition rate (F) values (i.e., 0.033, 0.149 and $1.27\,nm/s$ for Ag, and 0.015, 0.102 and $0.535\,nm/s$ for Cu). According to Table S1, ΔT_S and thereby σ_{th} increase with increasing deposition rate for both film/substrate systems. Moreover, our measurements showed that increase of T_S above $298\,K$ does not affect ΔT_S. The σ_{th} values listed in Table S1 have been used to correct the post-growth stress evolution curves presented in Figs. 1, 7 and 9 in the manuscript and in Fig. S2 in the present document.

Table S1: Deposition rate (F)-dependent temperature increase ΔT_S during deposition of Ag and Cu thin films on amorphous carbon (a-C) and corresponding thermal stress σ_{th} and stress-thickness $\sigma_{th} \times h_f$ values that build up post-deposition.

	$F\ (nm/s)$	$\Delta T_S\ (K)$	$\sigma_{th}\ (MPa)$	$\sigma_{th} \times h_f\ (N/m)$
Ag/a-C	0.033	1.2	2.5	0.3
	0.149	2.8	5.8	0.6
	1.27	8.4	17.5	1.8
Cu/a-C	0.015	1.4	3.9	0.3
	0.102	2.0	5.6	0.4
	0.535	5.2	14.5	0.9

S2. INCREMENTAL STRESS PRIOR TO CONTINUOUS FILM FORMATION

Table S2 presents the initially-formed incremental compressive stress $\sigma_{c,init}$ and tensile stress $\sigma_{t,init}$ of Ag and Cu thin films deposited at various values of F and homologous temperatures $T_h = T_S/T_m$, where T_m is the melting temperature of Ag or Cu given in K. $\sigma_{c,init}$ (determined as slope in the film thickness range $h_f = 0 - 10\,nm$ in Figs. 2 and 3 in the main document) increases when increasing T_h, and the magnitude of $\sigma_{t,init}$ $(h_f = 10 - 65\,nm)$ decreases when increasing T_h. Conversely, increasing F results in a smaller initial compressive stress and a more pronounced $\sigma_{t,init}$.

Table S2: Incremental compressive $\sigma_{c,init}$ and tensile stress $\sigma_{t,init}$ during the initial growth stages of Ag and Cu thin films deposited on amorphous carbon (a-C). Films were deposited at homologous temperatures $T_h = 0.25, 0.30$, and 0.31, at deposition rates $F = 0.033$ and $1.27\,nm/s$ for Ag, and 0.015 and $0.535\,nm/s$ for Cu.

		$F\ (nm/s)$	
Ag/a-C		0.033	1.27
	T_h	$\sigma_{c,init}\ (MPa)$ / $\sigma_{t,init}\ (MPa)$	
	0.25	-21 / 150	0 / 160
	0.31	-74 / 19	-44 / 45
		$F\ (nm/s)$	
Cu/a-C		0.015	0.535
	T_h	$\sigma_{c,init}\ (MPa)$ / $\sigma_{t,init}\ (MPa)$	
	0.25	-51 / 200	-34 / 305
	0.30	-86 / 25	-51 / 90

S3. FILM SURFACE TOPOGRAPHY

Figure S1 presents images of the surface topography, acquired by atomic force microscopy (AFM), of Cu (film thickness $h_{f,Cu} = 65\,nm$) and Ag

($h_{f,Ag} = 105\ nm$) thin films deposited at representative values of F and T_h. Height-height-correlation functions that are presented in Fig. 5 in the manuscript were calculated from the images shown in Fig. S1. We find that the in-plane size of surface features increases with increasing T_h (for a given F value). Moreover, we observe that larger F (for a given T_h) results in a decrease of the height of the surface features (compare z-scales in Fig. S1).

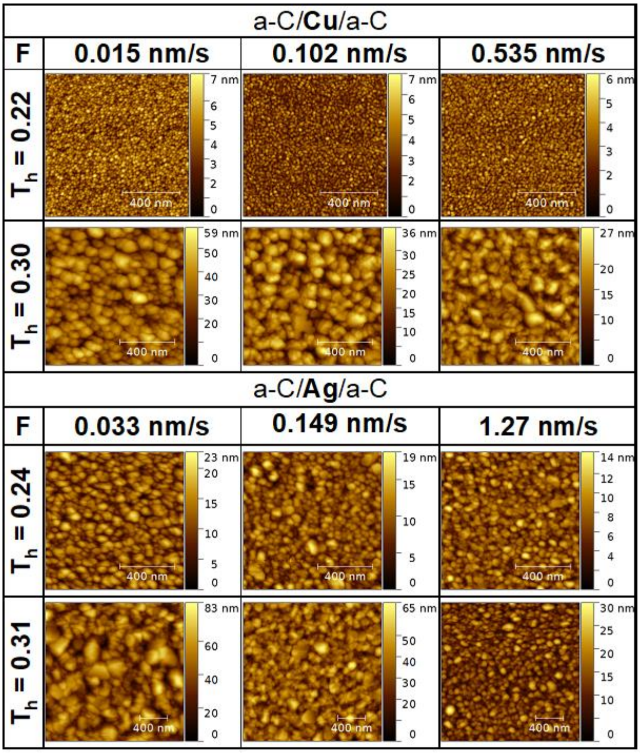

Fig. S1: Atomic force microscopy images obtained from amorphous carbon (a-C)/Ag/a-C/Si and a-C/Cu/a-C/Si deposited at various deposition rates F and homologous temperatures T_h values, as indicated in each panel. The Ag and Cu thin films are $105\ nm$ and $65\ nm$ thick, respectively.

S4. POST-DEPOSITION STRESS EVOLUTION

For a better understanding of the effect of F and T_h on the kinetics of the post-deposition tensile rise, Fig. S2 presents the tensile rise after deposition of Ag as function of time t, normalized to the maximum tensile rise presented in Fig. 7(a) and (c) in the main document, for $F = 0.033\ nm/s$ and $1.27\ nm/s$ as well as $T_h = 0.24$ and 0.31. We find trends toward faster tensile rise with increasing values of F and T_S, which is most pronounced in the first seconds after deposition stop.

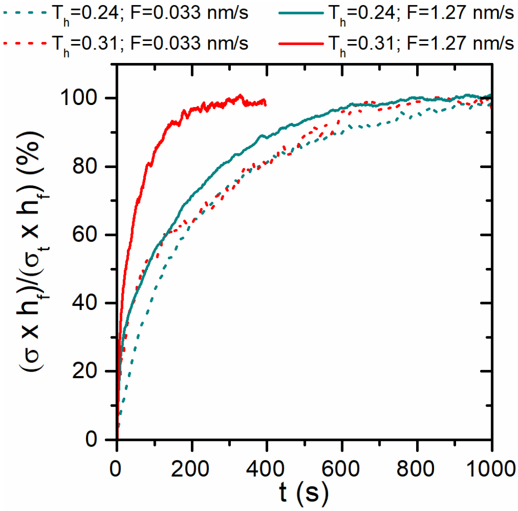

Fig. S2: Evolution of stress-thickness $(\sigma \times h_f)/(\sigma_t \times h_f)$, normalized to the maximum tensile rise σ_t presented in Figs. 7(a)-(c), with time t after deposition of Ag thin films on amorphous carbon for homologous temperatures $T_h = 0.24$ and 0.31, as well as deposition rates 0.033 and $1.27\ nm/s$. The curves are normalized to the maximum tensile rise presented in Figs. 7(a) and (c) in the manuscript.

S5 MICROCHEMICAL ANALYSIS

Figure S3 presents photoelectron spectra of Cu and Ag films deposited without additional heating and capped with a $6.5\ nm$ thick a-C film. For the analysis of the metals, Cu-2p and Ag-3d emission lines were used, respectively. We also studied the O-1s emission lines as fingerprint of possible contamination by gas molecules from the background pressure during deposition. The films were sputter-cleaned with $4\ keV$ Ar^+ ions to remove surface contamination. For Cu, spectra were acquired in the as-deposited state, and after etching of ~ 1 and $\sim 7\ nm$, while for Ag, spectra are presented for the as-deposited state and after $\sim 5\ nm$ etching.

For Cu (Fig. S3(a)-(f)), we find increasing intensity of Cu-2p with increasing etching depth, while the O-1s intensity decreases. In the as-deposited state, peaks at binding energies for $Cu(OH)_2$ and CuO indicate an oxidation state of Cu, which is most pronounced for films deposited with the lowest deposition rate $0.015\ nm/s$ (see also the satellite CuO peaks in Fig. S3(a)). With increasing etching time, oxygen is removed, but is still present after $\sim 7\ nm$ of etching. The quantitative analysis of these spectra is presented in Table 1 in the main document.

X-ray photoelectron spectroscopy for Ag was performed for one deposition rate $(0.109\ nm/s)$, and ion etching was performed until a depth of $\sim 5\ nm$, where oxygen has been completely removed (see Fig. S3(g) and (h)). For Ag, no oxide-compound formation could be uncovered from the Ag-3d line, and the oxygen content was below the detection limit of the O-1s signal.

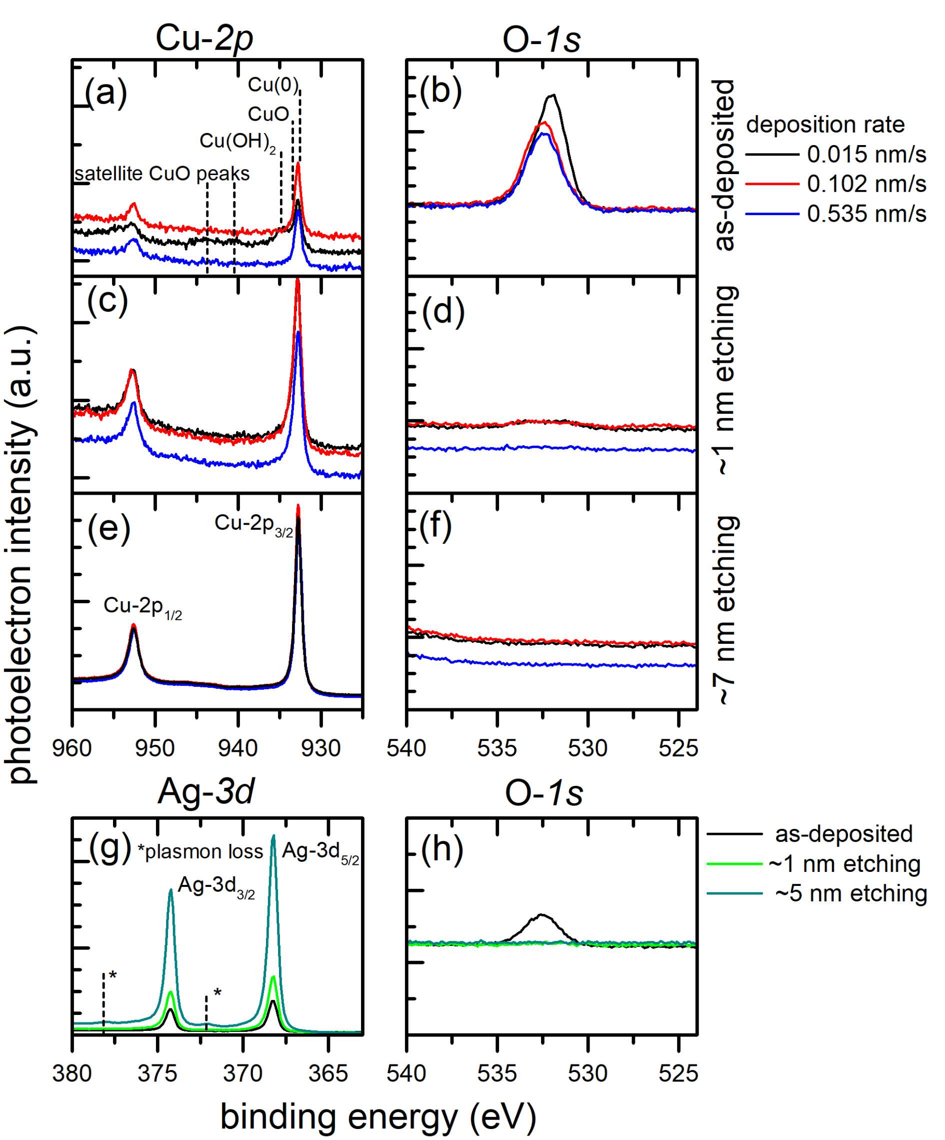

Fig. S3: X-ray photoelectron emission spectra of (a)-(f) Cu and (g)-(h) Ag thin films with an amorphous carbon capping layer. Cu films were deposited at $0.015, 0.102$, and $0.535\ nm/s$, Ag at $0.109\ nm/s$. The first column presents photoelectron emission lines of Cu-2p ((a), (c), (e)) and Ag-3d (g), the second column presents O-1s emission lines. (a) to (b) correspond to spectra before surface cleaning, while (c)-(d) and (e)-(f) display spectra after etching ~ 1 and $\sim 7\ nm$ with Ar$^+$ ions, respectively.

Paper III

3D-to-2D Morphology Manipulation of Sputter-Deposited Nanoscale Silver Films on Weakly-Interacting Substrates via Selective Nitrogen Deployment for Multifunctional Metal Contacts

Andreas Jamnig[1,2], Nikolaos Pliatsikas[1], Martin Konpan[1], Jun Lu[3], Thomas Kehagias[4], Alexios N. Kotanidis[5], Nikolaos Kalfagiannis[6], Dimitris V. Bellas[5], Elefterios Lidorikis[5,7], Janez Kovac[8], Gregory Abadias[2], Ivan Petrov[3,9], Joseph E. Greene[3,9,10], and Kostas Sarakinos[1,*]

*Corresponding author

[1]Nanoscale Engineering Division, Department of Physics, Chemistry, and Biology, Linköping University, SE 581 83, Linköping, Sweden

[2]Institut Pprime, Département Physique et Mécanique des Matériaux, UPR 3346 CNRS, Université de Poitiers, SP2MI, 11 Bvd. M. et P. Curie, TSA 41123, F86073 Poitiers Cedex 9, France

[3]Thin Film Physics Division, Department of Physics, Chemistry, and Biology, Linköping University, SE-581 83 Linköping, Sweden

[4]Aristotle University of Thessaloniki, Department of Physics, GR-54124 Thessaloniki, Greece

[5]University of Ioannina, Department of Materials Science and Engineering, Ioannina, 45110, Greece

[6]Nottingham Trent University, School of Science and Technology, NG11 8NS, Nottingham, UK

[7]University Research Center of Ioannina (URCI), Institute of Materials Science and Computing, 45110 Ioannina, Greece

[8]Department of Surface Engineering and Optoelectronics, Jozef Stefan Institute, SI-1000 Ljubljana, Slovenia

[9]Materials Science and Physics Departments, University of Illinois, Urbana, Illinois, 61801, USA

[10]Department of Materials Science and Engineering, National Taiwan University of Science and Technology, Taipei 10607, Taiwan

ACS Applied Nano Materials 3 (2020), acsanm.0c00736.

https://dx.doi.org/10.1021/acsanm.0c00736

ACS APPLIED NANO MATERIALS

www.acsanm.org Article

3D-to-2D Morphology Manipulation of Sputter-Deposited Nanoscale Silver Films on Weakly Interacting Substrates via Selective Nitrogen Deployment for Multifunctional Metal Contacts

Andreas Jamnig, Nikolaos Pliatsikas, Martin Konpan, Jun Lu, Thomas Kehagias, Alexios N. Kotanidis, Nikolaos Kalfagiannis, Dimitris V. Bellas, Elefterios Lidorikis, Janez Kovac, Gregory Abadias, Ivan Petrov, Joseph E. Greene, and Kostas Sarakinos*

Cite This: *ACS Appl. Nano Mater.* 2020, 3, 4728–4738 Read Online

ACCESS | Metrics & More | Article Recommendations | Supporting Information

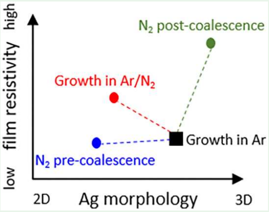

ABSTRACT: The ability to reverse the inherent tendency of noble metals to grow in an uncontrolled three-dimensional (3D) fashion on weakly interacting substrates, including two-dimensional (2D) materials and oxides, is essential for the fabrication of high-quality multifunctional metal contacts in key enabling devices. In this study, we show that this can be effectively achieved by deploying nitrogen (N_2) gas with high temporal precision during magnetron sputtering of nanoscale silver (Ag) islands and layers on silicon dioxide (SiO_2) substrates. We employ real-time *in situ* film growth monitoring using spectroscopic ellipsometry, along with optical modeling in the framework of the finite-difference time-domain method, and establish that localized surface plasmon resonance (LSPR) from nanoscale Ag islands can be used to gauge the evolution of surface morphology of discontinuous layers up to a SiO_2 substrate area coverage of ~70%. Such analysis, in combination with data on the evolution of room-temperature resistivity of electrically conductive layers, reveals that presence of N_2 in the sputtering gas atmosphere throughout all film-formation stages: (i) promotes 2D growth and smooth film surfaces and (ii) leads to an increase of the continuous-layer electrical resistivity by ~30% compared to Ag films grown in a pure argon (Ar) ambient atmosphere. Detailed *ex situ* nanoscale structural analyses suggest that N_2 favors 2D morphology by suppressing island coalescence rates during initial growth stages, while it causes interruption of local epitaxial growth on Ag crystals. Using these insights, we deposit Ag layers by deploying N_2 selectively, either during the early precoalescence growth stages or after coalescence completion. We show that early N_2 deployment leads to 2D morphology without affecting the Ag-layer resistivity, while postcoalescence introduction of N_2 in the gas atmosphere further promotes formation of three-dimensional (3D) nanostructures and roughness at the film growth front. In a broader context this study generates knowledge that is relevant for the development of (i) single-step growth manipulation strategies based on selective deployment of surfactant species and (ii) real-time methodologies for tracking film and nanostructure morphological evolution using LSPR.

KEYWORDS: *silver, nitrogen, thin film, growth manipulation, FDTD calculations, in situ growth monitoring*

1. INTRODUCTION

Vapor-based growth of thin noble-metal films with two-dimensional (2D) morphology on weakly interacting 2D material and oxide substrates is essential for the fabrication of multifunctional metal contacts in a wide array of devices, including photodetectors,[1,2] long-range surface plasmon resonance biosensors,[3] and tunnel field-effect transistors for ultralight-weight mobile and wearable electronics.[4,5] Noble-metal films typically exhibit a pronounced and uncontrolled three-dimensional (3D) morphology on weakly interacting substrates,[4,6] which manifests itself by discontinuous layer formation during the initial film growth stages and rough surfaces upon formation of a continuous layer. From the viewpoint of thermodynamics, this growth behavior is explained by the fact that the adsorption energy of noble-metal atoms on weakly interacting surfaces is significantly smaller than the bulk metal binding energy,[4,6] which provides the driving force for minimizing the metal/substrate contact area.

Film growth via vapor condensation is a far-from-equilibrium process, and hence, morphological evolution depends, primarily, on kinetic rates of atomic-scale structure-forming mechanisms.[7−10] The kinetic pathways leading to 3D morphologies in metal-on-metal homoepitaxial systems are well established in the literature.[10] This understanding has

Received: March 16, 2020
Accepted: April 23, 2020
Published: April 23, 2020

Scheme 1. Schematic Representation of the Vacuum Chamber Used for Magnetron-Sputter Deposition of Nanoscale Ag Islands and Continuous Layers on SiO_2 Substrates[a]

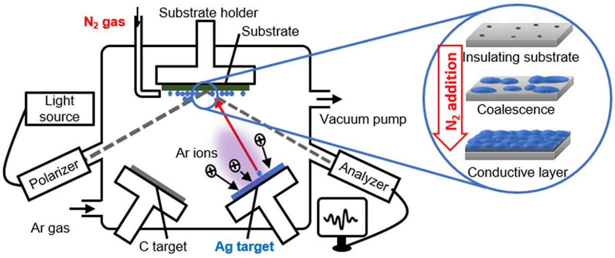

[a]The chamber is equipped with a spectroscopic ellipsometer for *in situ* and real-time monitoring of film growth. Nitrogen (N_2) is introduced to the sputtering atmosphere with high temporal precision to selectively target key film-formation stages and promote 2D growth morphology, without compromising the electrical conductivity of the Ag layers.

facilitated the development of growth manipulation strategies, in which minority metal[11−17] and gaseous[18,19] species (also termed surfactants) are deposited simultaneously with the film-forming species, thereby modifying atomic-scale kinetics and allowing navigation between 3D and 2D morphologies. Numerous studies on surfactant effects for semiconductor epitaxial film growth[20−23] and metal-on-metal heteroepitaxial systems[24−26] are also available in the literature.

The mechanisms that govern morphological evolution of metal films on weakly interacting substrates are different than those in strongly interacting homo- and heteroepitaxial systems.[6,27−31] As a result, established knowledge for surfactant-based growth manipulation is not directly applicable to the case of noble-metal-film deposition on, e.g., oxides and 2D materials. Despite this, empirical studies exist in which less-noble-metal surfactants and seed layers[32−37] as well as gaseous surfactants (nitrogen (N_2) and oxygen (O_2))[38−44] have been used to suppress 3D morphology of silver (Ag) and copper (Cu) films on oxide substrates. The presence of surfactants at the film growth front, however, is often accompanied by changes in other physical properties of the noble-metal layers (e.g., electronic, optical, and transport properties),[33,38,39] which, if not reversed or mitigated, render surfactant-based approaches largely inapplicable for metal-contact synthesis. Hence, a fundamental understanding of the surfactant effects on various film-growth stages (i.e., island nucleation, island growth, island coalescence, and hole filling) is required for designing knowledge-based, efficient, and noninvasive growth manipulation strategies.

In the present work, we investigate the effects of N_2 on the growth of magnetron-sputtered nanoscale Ag islands and layers on silicon dioxide (SiO_2) substrates, with the purpose of exploring the viability of surfactant-based approaches for metal-contact fabrication, as conceptualized in Scheme 1. Ag/SiO_2 is an archetypal weakly interacting film/substrate system which exhibits pronounced 3D morphological evolution.[45−48] Furthermore, N_2 does not chemisorb on Ag surfaces, and no thermodynamically stable Ag−N compounds exist,[49] which enables us to focus on the effect of N_2 on surface atomic-scale growth processes. By employing spectroscopic ellipsometry for real-time *in situ* film growth monitoring, along with finite-difference time-domain (FDTD) calculations, we show that addition of N_2 to the sputtering gas atmosphere, throughout all film-growth stages, promotes in-plane nanoscale island growth and 2D film morphology, while it leads to an increase in the electrical resistivity of continuous layers, relative to Ag films grown in pure Ar. Moreover, we find—by means of detailed *ex situ* microstructural analyses—that 2D morphology is promoted because N_2 suppresses the coalescence rate of nanoscale Ag islands, while the electrical resistivity increase is attributed to N_2-induced grain refinement.

On the basis of the above insights highlighted in the previous paragraph, we design and implement a deposition protocol in which N_2 is introduced during Ag film growth with high temporal precision for influencing selected film-formation stages. We show that when N_2 is deployed only during island nucleation, growth, and coalescence, after which N_2 supply is turned off, such that deposition commences in an Ar/N_2 atmosphere and is completed in pure Ar atmosphere, 3D morphology is suppressed without compromising the Ag-layer electrical resistivity. In the opposite case, when deposition commences in an Ar atmosphere and N_2 is introduced after island coalescence has been largely completed, the tendency for 3D morphological evolution is dramatically enhanced. The overall results of this study provide the scientific foundation for designing advanced growth manipulation strategies based on selective deposition of surfactants to promote 2D growth without affecting the film physical properties. Such approaches can also be the basis of single-step room-temperature processes for enhancing 3D morphology and tuning the size of supported nanoparticles. Moreover, the combination of FDTD calculations and experiments highlights a path toward real-time methodologies for tracking metal film and nanostructure morphological evolution by using LSPR.

2. RESEARCH METHODOLOGY

2.1. Film Growth. Ag films are grown by direct-current magnetron sputtering (dcMS), at a constant current mode of 20 mA, on Si(001) substrates with an ~530 nm thick thermally grown SiO_2 overlayer. No intentional heating is applied on the substrate, and all depositions are performed in a multisource, ultrahigh-vacuum (UHV) chamber with a base pressure below 10^{-10} Torr (~10^{-8} Pa). The Ag target (purity 99.99 at. %; diameter 7.6 cm; thickness 6 mm) is placed 7.5 cm away from the substrate and at a 45° angle with respect to the substrate surface normal.

Ag depositions are performed in Ar and Ar/N_2 mixtures at a total working pressure p_{total} of 10 mTorr (1.33 Pa). For samples grown in Ar/N$_2$ atmospheres, initial tests at various N$_2$ partial pressures p_{N2} showed that increasing p_{N2} from $0.05p_{total}$ to $0.1p_{total}$ affected film growth (as evidenced from *in situ* ellipsometry data by using the methodologies described in section 2.2), while no appreciable difference was observed for further p_{N2} increase up to $0.15p_{total}$. Hence, on the basis of results of those initial tests, in this article we focus on experiments performed at $p_{N2} = 0.1p_{total}$. It should be pointed out that additional effects on film properties for p_{N2} values well outside the range considered here (i.e., substantially larger than $0.15p_{total}$) cannot be ruled out; see for example the studies by Lee et al.[50] and Wang et al.[51] on the growth of Cu−O films in Ar−O$_2$−N$_2$ gas mixtures, in which it was found that N$_2$ partial pressures above ∼30% of the total working pressure affect profoundly the plasma chemistry and film electron transport properties.

Film morphological evolution, microstructure, and chemical composition are analyzed by using the *in situ* and *ex situ* tools and methodologies described in sections 2.2 and 2.3, respectively. Prior to exposing the samples to atmosphere for *ex situ* analyses, and immediately after Ag deposition, samples are capped with a 3 nm thick amorphous carbon (a-C) layer to avoid surface contamination and changes in film morphology upon atmospheric exposure. The a-C capping layers are sputter-deposited at a rate of 0.01 nm/s in the same UHV chamber from a graphite target (purity 99.99 at. %; diameter 7.6 cm; thickness 6 mm) in pure Ar discharge at 10 mTorr. The graphite target is operated with dcMS at a constant current mode of 50 mA, 7.5 cm away from the substrate, and at an angle of 45° with the substrate surface normal.

2.2. *In Situ* Film Growth Monitoring. Spectroscopic ellipsometry is employed to monitor the change in film optoelectronic properties during deposition and, thereby, provide real-time insights into film morphological evolution. Ellipsometric angles Ψ and Δ are acquired every ∼2 s at 67 incident-light photon energies in the range 1.6−3.2 eV, at an angle of incidence of ∼70° from the substrate normal, by using a J.A. Woollam Inc. M-88 instrument. The acquired data are fitted to a three-phase model consisting of substrate, film, and vacuum. The substrate is modeled as a 625 μm thick Si slab with a SiO$_2$ overlayer, the thickness of which (∼530 nm) is confirmed by measuring the optical response of the substrate prior to deposition. Reference data for the substrate layers are taken from Herzinger et al.[52] The optical response of the film is described by different dispersion models, depending on the film growth stage (i.e., nominal film thickness Θ), as detailed below.

During initial growth stages, the film surface primarily features isolated Ag islands that support LSPR.[46,53] Being a resonant effect, LSPR can be described by adapting the Lorentz oscillator model[46,53] to express the complex dielectric function of the layer $\tilde{\epsilon}(\omega)$ as

$$\tilde{\epsilon}(\omega) = \frac{f\omega^2}{{\omega_0}^2 - \omega^2 - i\Gamma\omega} \tag{1}$$

In eq 1, f and ω_0 are the oscillator strength and resonance frequency, respectively, and Γ represents the damping rate of the plasmon resonance. It should be emphasized here that eq 1 describes the effective LSPR of the nanoscale Ag islands/air complex system, which is considered a homogeneous layer. Moreover, the single Lorentz model does not account for dipole−dipole interactions; i.e., the optical response of early growth-stage Ag layers can be accurately modeled by eq 1 as long as the distance between islands is large enough to render island−island interactions ineffective.[46,53]

The optical response of electrically conductive Ag films is described by the Drude free electron theory, which is extensively used for ideal metals.[54] In this case, $\tilde{\epsilon}_D(\omega)$ is given by the expression

$$\tilde{\epsilon}_D(\omega) = \epsilon_\infty - \frac{{\omega_p}^2}{\omega^2 + i\Gamma_D\omega} \tag{2}$$

In eq 2, ϵ_∞ is a constant that accounts for the effect of interband transitions occurring at frequencies higher than the ones considered here, Γ_D is the free-electron damping constant, and $\omega_p = \sqrt{ne^2/\varepsilon_0 m_e}$ is the free-electron plasma frequency, where n is the free-electron density, ε_0 is the permittivity of free space, and m_e is the free-electron effective mass. From eq 2, the room-temperature film resistivity is calculated as[54]

$$\rho = \frac{\Gamma_D}{\epsilon_0 {\omega_p}^2} \tag{3}$$

In addition to optical properties, analysis of the ellipsometric data provides the film thickness h_f as a function of deposition time t. Based upon h_f values of continuous layers, a deposition rate $F \cong 0.1$ nm/s is obtained, irrespective of the growth conditions. This allows the nominal film thickness, $\Theta = F \times t$, to be determined to be a function of the deposition time. Here, Θ is expressed in monolayers (ML), in which 1 ML corresponds to the distance between adjacent Ag (111) atomic planes (0.236 nm). We note that h_f is also determined by *ex situ* X-ray reflectometry measurements, as detailed in section 2.3.

2.3. *Ex Situ* Characterization. Crystal structure, coherence length, and film texture are determined by X-ray diffractometry (XRD) in Bragg−Brentano geometry by using a Panalytical X'pert Pro diffractometer. Film thickness, density, and roughness are determined by X-ray reflectometry (XRR), performed in a Panalytical Empyrean diffractometer. For both techniques, a copper Kα source (wavelength 0.15418 nm) in line focus is used (operated with 45 kV and 40 mA), with a parallel beam mirror and parallel plate collimator in incident and diffracted/reflected beam path, respectively. The diffracted/reflected X-ray signal is processed with a X'Celerator/PIXcel-3D detector (Malvern Pananalytical) operated in scanning line mode. Moreover, a nickel filter is used in XRD measurements for removing the copper Kβ radiation.

Film morphology during initial growth stages is analyzed by plan-view transmission electron microscopy (TEM) as a function of nominal film thickness Θ. Plan-view specimens are prepared by depositing a-C-capped Ag films, grown in both Ar and Ar/N$_2$ atmospheres, on electron-transparent SiO$_2$ grids, stabilized by a Formvar foil. The TEM specimens are imaged in bright- and dark-field modes by using a FEI G2 TF20UT transmission electron microscope operated at 200 kV with 0.19 nm resolution. Selected area electron diffraction (SAED) patterns are also recorded to obtain information about the film crystal structure.

The microstructure and growth morphology of Ar- and Ar/N$_2$-grown continuous Ag layers are examined by cross-sectional TEM (XTEM). Specimens are prepared by mechanical polishing, followed by Ar$^+$ ion milling in a Gatan

PIPS TEM; high-resolution TEM (HRTEM) and SAED data are acquired in a Jeol 2011 UHR electron microscope, operated at 200 kV, with a point resolution of 0.194 nm and a spherical aberration of 0.5 mm.

Film chemical composition is determined by X-ray photoelectron spectroscopy (XPS). XPS measurements are performed in a Kratos AXIS Ultra DLD UHV system (base pressure ~ 3 × 10^{-10} Torr), equipped with a monochromated aluminum Kα X-ray beam, a hemispherical sector analyzer, and a multichannel detector. A 20 eV pass energy, resulting in full width at half-maximum (FWHM) of <500 meV for the Ag-$3d_{5/2}$ peak, is used to record core-level spectra. Measurements are performed as a function of the sample depth by etching the surface with a 4 keV Ar^+ ion beam. Charge-induced shifts of the binding energy are corrected with respect to the Ar-2p peak, which originates from Ar implanted in the film during the Ar^+ ion sputtering process. The Kratos Vision software and its sensitivity factor database are used for elemental analysis.

Compositional depth profiles are also acquired using time-of-flight secondary ion-mass spectrometry (ToF-SIMS) in a ToF.SIMS 5 instrument (ION-TOF; Münster, Germany) with a base pressure of 7.5 × 10^{-10} Torr. A 1 keV cesium ion (Cs^+) beam produces a 400 × 400 μm^2 crater at a rate of ~0.3 nm/s. SIMS spectra are acquired while scanning a 1 pA 30 keV bismuth ion (Bi^+) beam over sample areas of 100 × 100 μm^2. SIMS spectra are recorded every 1 s.

2.4. Finite-Difference Time-Domain Calculations.

Along with the ellipsometric analyses, we perform optical calculations based on the finite-difference time-domain (FDTD) method[55,56] to evaluate the LSPR positions and compare them with the experimentally determined Lorentz-oscillator energy ($\hbar\omega_0$) values (see eq 1). We use surface morphology data (i.e., island size and number density) obtained from *ex situ* plan-view TEM measurements (see section 2.3 for details) to compute the total reflectivity of the nanoscale Ag islands in the near-infrared, visible, and ultraviolet spectral range and thereby extract the LSPR position from the maximum of the corresponding spectra reflectivity curves. More information about the use of plan-view TEM data for FDTD calculations is given in the Supporting Information.

3. RESULTS AND DISCUSSION

3.1. Film Morphological Evolution.

The room-temperature resistivities of percolated Ag films grown in pure Ar and Ar/N_2 mixtures are plotted in Figure 1 as a function of the nominal thickness Θ. The data are extracted from *in situ* spectroscopic ellipsometry analysis, as explained in section 2.2. Both ρ vs Θ curves exhibit a sharp initial drop until they reach a steady-state value ρ^{ss}. We have previously shown[57] that the Θ value at which ρ^{ss} is established marks the completion of the hole-filling process and the formation of a continuous film. The data in Figure 1 show that addition of N_2 in the growth atmosphere results in the thickness of continuous film formation Θ_{cont} to decrease to 51 ML from 78 ML for the Ag film grown in pure Ar. Thus, the presence of N_2 promotes 2D growth. Furthermore, Ag growth in N_2-containing atmosphere yields a steady-state resistivity ρ^{ss} = 1.4 × 10^{-5} Ω·cm, which is larger than the corresponding value 1.1 × 10^{-5} Ω·cm for films grown in pure Ar.

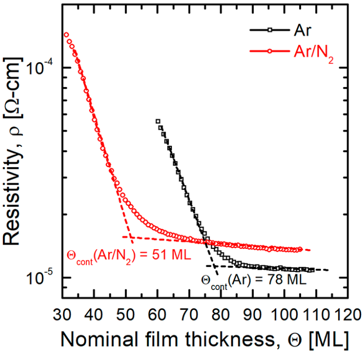

Figure 1. Resistivity (ρ) vs nominal thickness (Θ) curves extracted from *in situ*, real-time spectroscopic ellipsometry measurements (see section 2.2) of magnetron sputter-deposited Ag layers on SiO_2/Si substrates in Ar (hollow black squares) and Ar/N_2 (hollow red circles) atmospheres. The nominal thickness Θ_{cont} at which the film becomes continuous is 51 and 78 ML for films grown in Ar/N_2 and pure Ar, respectively.

To correlate early film growth stages with the morphological evolution trends extracted from Figure 1, we perform plan-view TEM investigations for a-C/Ag/SiO_2 samples grown in Ar and Ar/N_2 atmospheres. Typical micrographs, for Θ = 2, 8, 21, and 42 ML, are displayed in Figure 2 (top and bottom panel for Ar- and Ar/N_2-grown samples, respectively). Irrespective of the composition of the sputtering gas atmosphere, the plan-view TEM data show the expected overall film morphological evolution as a function of Θ: the initially formed isolated nanoscale islands increase in size, until they start impinging upon another, and coalesce. Further vapor deposition leads to island sizes that hinder coalescence completion, which results in the formation of an interconnected island network and eventually (for the film grown in Ar/N_2 atmosphere at Θ = 42 ML) in a nearly continuous layer.

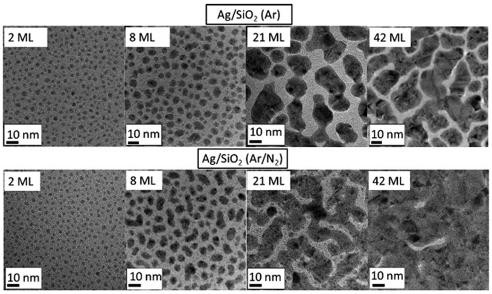

Figure 2. Typical bright-field plan-view TEM micrographs of discontinuous magnetron sputter-deposited Ag films on SiO_2/Si substrates in Ar (top row) and Ar/N_2 (bottom row) atmospheres at nominal thicknesses Θ = 2, 8, 21, and 42 ML.

For Θ = 2 ML, both Ar- and Ar/N_2-grown film surfaces feature nearly spherical islands with sizes in the range ~1−2 nm. Moreover, the presence of N_2 in the growth atmosphere results in a slight increase of the island number density. By analyzing data from multiple images, we find island densities of (3.97 ± 0.45) × 10^{16} and (4.13 ± 0.40) × 10^{16} m^{-2} for films deposited in Ar and Ar/N_2 atmospheres, respectively. This change by only ~5% is rather marginal, relative to multifold increases in homoepitaxial growth experiments performed at the presence of surfactant gases.[10,18] Hence, we conclude that N_2, at the partial pressures used in this study, does not have a significant effect on Ag adspecies surface diffusion rates during nucleation and early film-growth stages.

More pronounced differences in the film morphology are observed at larger nominal thicknesses. For Θ = 8 ML, deposition in Ar atmosphere yields mostly spherical islands with sizes between ~2 and ~7 nm. Addition of N_2 leads, instead, to a film surface that hosts, predominantly, polycrystalline elongated island clusters with sizes ~5−10 nm. Experimental and theoretical studies on the growth of metals on weakly interacting substrates[45,58−61] have attributed the formation of elongated cluster shapes to a decrease in the rate of island coalescence. On the basis of these studies, we conclude that the presence of N_2 in the gas atmosphere causes suppression of coalescence-induced cluster reshaping, promoting in-plane island growth and 2D growth morphology. In a recent study of vapor-based growth of Ag nanoparticles on ZnO in Ar/N_2 gas mixtures, Yun et al.[44] suggested that atomic nitrogen incorporation onto nanoparticle facets lowers their surface energy and thereby the thermodynamic driving force for coalescence. This mechanism may also be relevant for explaining the results in Figure 2, but further research is required to understand the atomistic pathways by which N_2 suppresses the coalescence rate of nanoscale Ag islands.

At a nominal thickness Θ = 21 ML, the plan-view TEM micrograph that corresponds to the Ar-grown sample shows the existence of isolated island clusters at various stages of coalescence, which cover ~60% of the substrate surface. For the same amount of deposited material, the Ar/N_2-grown sample surface consists of interconnected islands and the substrate area coverage is ~70%. Moreover, the presence of N_2 causes the appearance of smaller islands, with sizes ~1 nm, both in between and on the top of the elongated Ag clusters. The existence of these small islands is a signature of repeated nucleation, i.e., interruption of local epitaxial growth and nucleation of new islands with different crystallographic orientation.[9,27]

An almost continuous film with only a small fraction of the substrate surface exposed is obtained at Θ = 42 ML, when deposition is performed in an Ar/N_2 atmosphere. In contrast, the Ag layer is still discontinuous (substrate area coverage ~80%) in pure Ar atmosphere for the same nominal thickness. The overall results presented in Figure 2 are qualitatively consistent and confirm the trends observed in Figure 1, i.e., N_2 addition to the growth atmosphere promotes 2D film morphological evolution.

Discontinuous Ag layers that consist of isolated islands and/or island clusters, i.e., films for $\Theta \leq 21$ ML according to the results presented in Figure 2, can give rise to LSPR.[46,49] Using data from multiple images (like those presented in Figure 2) as input, we performed FDTD calculations and estimated the expected LSPR energies for Ar- and Ar/N_2-grown films, as explained in section 2.4 and in the Supporting Information. Representative experimental (TEM) and simulated plan-view morphologies along with the corresponding calculated reflectivity spectra for Θ = 2 ML (film deposited in Ar atmosphere) are displayed in Figures 3a, 3b, and 3c, respectively. Additional data for Ar- and Ar/N_2-grown films at Θ = 2 and 8 ML are presented in the Supporting Information. The theoretical LSPR position corresponds to the wavelength at which the reflectivity curve exhibits its maximum value, as marked by the vertical dotted line in Figure 3c.

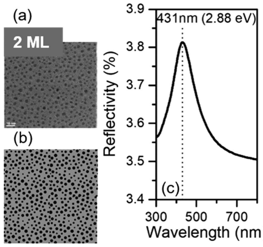

Figure 3. (a) Plan-view TEM image (105 × 105 nm^2), (b) simulated random Ag island distribution, and (c) calculated reflectivity spectrum for an Ar-grown Ag film at Θ = 2 ML. The vertical dotted line in (c) marks the wavelength at which the maximum of the reflectivity curve occurs and corresponds to the theoretical LSPR position.

Figure 4a presents the FDTD-predicted LSPR position (full symbols) along with the Lorentz-model resonance energy $\hbar\omega_0$ (hollow symbols), obtained from *in situ* ellipsometric analyses, as a function of Θ. Irrespective of the composition of the sputtering atmosphere, both calculated and experimentally obtained resonance energy values exhibit qualitatively consistent trends vs Θ (i.e., red-shift), while they are in fairly good quantitative agreement. This agreement confirms that the

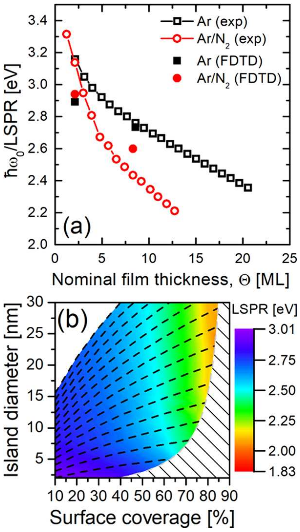

Figure 4. (a) Lorentz resonance energy $\hbar\omega_0$ (hollow symbols; extracted from *in situ*, real-time spectroscopic ellipsometry) and calculated LSPR (full symbols; obtained using the finite difference time-domain method) vs nominal thickness (Θ) of discontinuous magnetron-sputter-deposited Ag layers on SiO_2/Si substrates in pure Ar (squares) and Ar/N_2 (circles) atmospheres. (b) Color-coded map of FDTD-calculated LSPR position of hemispherical periodic island arrays of various substrate coverages and island diameters. The black dashed lines indicate the iso-population point of the size-coverage parameter space.

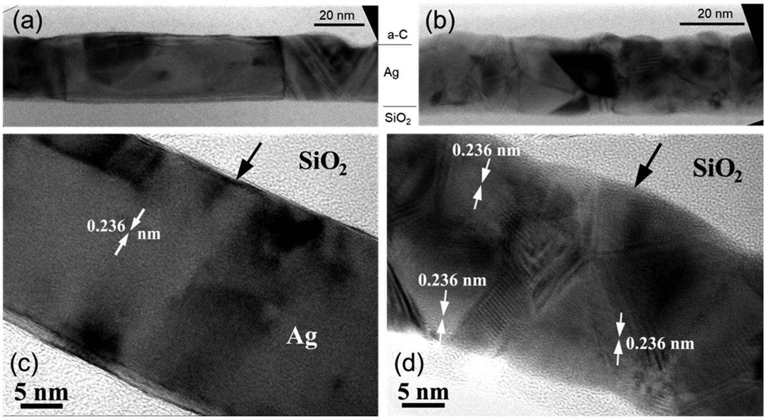

Figure 5. Cross-sectional TEM (XTEM) micrographs of continuous magnetron-sputter-deposited Ag films on SiO_2/Si in (a) Ar and (b) Ar/N_2 atmospheres. Panels c and d display corresponding HRTEM images from panels a and b, illustrating a (111)-oriented large crystal in the Ar-grown Ag film and multiple twinned grains in Ar/N_2-grown Ag film, respectively. Moiré fringes arise due to overlapping of slightly disoriented adjacent Ag grains. In both images, the 0.236 nm interplanar spacing of the (111) planes and the growth direction are denoted by the white and black arrows, respectively.

Lorentz model is an accurate description of the effective resonant response of the nanoscale Ag islands on the surface of the substrate during the initial film-growth stages.

Upon vapor deposition up to ~2 ML, the LSPR/$\hbar\omega_0$ vs Θ curves for both Ar- and Ar/N_2-grown films are essentially identical, indicating no significant difference in the film morphology, which is consistent with plan-view TEM results for $\Theta = 2$ ML in Figure 2. The systematic shift of the FDTD-calculated LSPR positions to lower values relative to the ellipsometry-derived $\hbar\omega_0$ at $\Theta = 2$ ML can be attributed to (i) the use of a correction factor to the electron scattering time in the FDTD calculations (see the Supporting Information), which may successfully capture the major effects of plasmon damping, but overestimates the plasmon broadening and underestimates the plasmon blue-shift;[62−64] (ii) the fact that classical electromagnetism, used in FDTD, cannot account for nonlocalities, including blue-shift and quenching of the plasmon resonance of very small particle sizes;[62−64] and (iii) the low sample reflectivity at the initial growth stages (i.e., small Θ values).

For $\Theta > 2$ ML, N_2 addition to the sputtering atmosphere leads to a steeper decline of the LSPR/$\hbar\omega_0$ vs Θ curve compared to the Ar-deposited film. The red-shift in the LSPR/$\hbar\omega_0$ position has been attributed in the literature to changes in island size and/or in inter-island separation;[46,53] i.e., it reflects changes of surface areal coverage with continued deposition. To better understand the correlation among the data in Figure 4a and early stage film morphological evolution, we calculate (using FDTD) the LSPR positions for various periodic and close-packed hemispherical island arrays as a function of the substrate surface coverage (in the range 10 to 90%) for two scenarios: (i) the island number density (i.e., number of islands/m^2) is kept constant, and the surface coverage is varied by changing the island volume (i.e., diameter); (ii) the island diameter is kept constant, and the surface coverage is varied by changing the island number density. The results of these calculations are shown in Figure 4b, whereby the contour plot is a color-coded map which depicts the LSPR evolution for the scenarios i and ii above. The island iso-population points are indicated by black dashed lines, while the gray-line-shaded region denotes surfaces on which islands are separated by <1 nm, and other nonlocal effects make the FDTD calculations inaccurate[64] (more details on the calculations can be found in the Supporting Information). From the data in Figure 4b, it becomes evident that an LSPR red-shift of a magnitude that is consistent with the experimental results in Figure 4a requires a significant increase of the areal coverage that is caused by a concurrent increase/decrease of island size/island−island separation. Hence, the steeper LSPR/$\hbar\omega_0$ vs Θ curve slope for the Ar/N_2 grown sample (relative to the Ar-deposited one) indicates that the presence of N_2 promotes in-plane vs out-of-plane island growth, in agreement with the morphology evidenced by the plan-view TEM data for $\Theta = 8$ and 21 ML in Figure 2. Moreover, by combining the results in Figures 1−4a, we conclude that film morphological evolution, as manifested by changes in Θ_{cont} at later growth stages, is largely set during the initial film-formation stages of island growth and coalescence.

3.2. Continuous Film Microstructure and Structure-Forming Process.

The effect of adding N_2 to the sputtering atmosphere on the microstructure and chemical composition of continuous layers is also investigated. XRD analyses for ~25 nm thick Ar- and Ar/N_2-grown Ag samples are presented in Figure S4. The XRD pattern of the Ag film grown in pure Ar atmosphere shows 111 preferred orientation with a full width at half-maximum (FWHM) of 0.44°. The XRD pattern of the Ar/N_2-deposited layer exhibits no indication of strong texture formation, a much lower (111) peak intensity, and a wider FWHM of 0.88°. The latter is an indication that presence of N_2 causes the formation of a finer grain structure compared to films deposited in pure Ar.

Typical XTEM micrographs for Ar- and Ar/N_2-grown samples are shown in Figures 5a and 5b, respectively. The micrograph of the Ag layer grown in a pure Ar atmosphere (Figure 5a) reveals a microstructure composed of columnar grains with in-plane sizes up to 100 nm, which extend throughout the entire film growth direction. The projected film thickness, obtained from multiple positions, is found to be 27.5 ± 1.8 nm, and no discontinuities are observed, which is consistent with data in Figure 1 showing that a continuous layer is obtained at 78 ML (∼18 nm). The absence of discontinuities is also the case for the film grown in an Ar/N_2 atmosphere (Figure 5b). However, the grains of the Ar/N_2-deposited layer have more globular shapes and smaller sizes in the range 10−20 nm, and they are irregularly stacked along the growth direction. This morphology yields a similar to the Ar-grown layer mean projected thickness of 26.8 nm, but a larger statistical spread of ±3.6 nm.

The polycrystalline nature of both Ar- and Ar/N_2-grown films, evidenced by the XRD data in Figure S4, is also confirmed by the ring-type SAED patterns presented in Figure S5. Moreover, the SAED patterns—recorded under the same size selected area aperture—reveal an apparently lower number of reflections in the Ar-grown Ag film, which indicates the occurrence of larger Ag crystals compared to the film deposited in Ar/N_2 gas mixtures. Concerning preferred growth orientation, HRTEM imaging shows that large Ag grains in Ar-grown films are $\langle 111 \rangle$ oriented; namely, their $\{111\}$ crystal planes are normal to the $[100]$ growth direction of the Si substrate (Figure 5c). This crystallographic texture becomes considerably less pronounced for Ar/N_2-grown films because of the random orientation of the smaller Ag crystals (Figure 5d), which is consistent with XRD analysis.

XPS analyses of Ar- and Ar/N_2-grown films, after sputter-etching ∼3 nm of surface layers (see Figure S6 for spectra), show the existence of all Ag-related peaks (Ag-3s, Ag-3p, Ag-3d, Ag-4s, and Ag-4p). In addition, Ag-3d core-level high-resolution scans (also presented in Figure S6) reveal that only Ag−Ag bonds form in both films. Hence, no evidence of Ag−N compound formation is found in the XPS data, despite the presence of N_2 with a $p_{N2}/p_{\mathrm{total}}$ ratio of 10% in the sputtering atmosphere. This is consistent with previous XPS studies by Depla and De Gryse.[49] Moreover, N-1s high-resolution scans (not shown here) reveal traces of nitrogen (N) in the Ar/N_2-grown sample: on the surface of the a-C/Ag/SiO_2 stack (C−N, C═N, and C≡N bonds) and in the vicinity of the Ag/SiO_2 interface (Si−N bonds). However, the XPS detection limit for N and other light elements is below 1 at. %, while in our films the N-1s peak cannot be easily resolved, since its binding energy coincides with the Ag-3d plasmon-loss satellite peak.[49,65] Hence, ToF-SIMS measurements are performed to unequivocally confirm or refute N incorporation in the Ag/N_2-grown film, as explained in the following.

The ToF-SIMS technique exhibits sensitivity in the part-per-million range, but accurate quantitative concentration determination for dopants (i.e., low content elements as N in our case) is often nontrivial due to matrix effects related to different degrees of ionization for emitted secondary ions, while the use of reference samples is required. Hence, here we focus on qualitative analysis of the film composition. In our measurements, the most significant signals in negative ion spectra stem from CN^- ions at 26 Da—which we relate with N and are detected in both Ar and Ar/N_2-grown layers—and Ag^- ions at 107 Da. We attribute the presence of N in the sample deposited in pure Ar atmosphere to contamination from atmospheric exposure of (i) the substrate prior to film growth and (ii) the sample in the time between growth and SIMS measurements. Figure 6 plots the CN^--to-Ag^- signal intensity ratio as a function of the sputtering depth (i.e., the product of the sputtering rate and the sputtering time) for Ag films grown in pure Ar (black squares) and mixed Ar/N_2 (red circles) atmospheres. The position of the film surface and the approximate position of the film/substrate interface (which corresponds to the film thickness of 25 nm according to the XRR results shown in section 3.3) are marked with blue dashed vertical lines. For both deposition conditions, the signal ratio exhibits a qualitatively similar evolution; i.e., it initially decreases when moving away from the surface into the bulk of the film and then shows a peak near the film/substrate interface. However, the CN^--to-Ag^- signal ratio obtained for the Ar/N_2-grown film is systematically larger by up to 2 orders of magnitude than that for the Ar-deposited Ag layer, in the thickness range 10−25 nm. This shows that presence of N_2 in the growth atmosphere leads to incorporation N in the sample, primarily at the Ag/SiO_2 interface as indicated by the XPS results. The absence of N in the bulk of the Ag layer may be attributed to the weak Ag−N interaction, which has been suggested to lead to N−N recombination into N_2 and desorption from the film surface.[66,67] Accumulation of N at the film/substrate interface has also been reported by Yun et al.[44] for Ag/ZnO heterostructures synthesized by magnetron sputtering in Ar/N_2 gas mixtures.

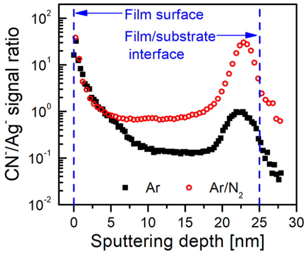

Figure 6. Ratio of CN^- to Ag^- ion signal vs sputtering depth as measured by ToF-SIMS for magnetron sputter-deposited Ag layers on SiO_2/Si substrates in pure Ar (black squares) and Ar/N_2 (red circles) atmospheres. The position of the film surface and the approximate position of the film/substrate interface are indicated by dashed vertical lines.

The occurrence of repeated nucleation in Ag films grown in mixed Ar/N_2 atmospheres is consistent with the fine-grained structure evidenced in the XRD and XTEM results in Figure S4 and Figure 5, respectively. This type of morphology can also explain the larger steady-state resistivity ρ^{ss} for the Ar/N_2- vs Ar-deposited films shown in Figure 1; a finer-grained structure implies a larger number density of grain boundaries, which scatter charge carriers and reduce their mean-free path. Repeated nucleation has been ascribed in the literature to intense energetic bombardment during growth and/or to surfactant and impurity adsorption at the film growth front.[9,27] In our case, combined SIMS and XPS data support temporary N adsorption during Ag film growth in Ar/N_2 atmospheres, which may lead to interruption of local epitaxy and grain refinement.[9,27,68]

3.3. Growth Manipulation by Selective N_2 Deployment. The results presented in sections 3.1 and 3.2 show that N_2 has different effects on island nucleation, growth, and coalescence. These effects can be leveraged separately or combined to design versatile manipulation strategies for metal-contact fabrication in which N_2 is introduced to the sputtering atmosphere with high temporal precision to selectively target film-growth stages and mechanisms. In this section we explore the viability of this approach by using the following N_2 deployment schemes: (i) N_2 is introduced at the early film-growth stages for 20 s (which corresponds to a value $\Theta \approx 8$ ML) and, subsequently, is pumped out from the deposition chamber, while deposition continues and is completed in a pure Ar atmosphere. (ii) Deposition commences in a pure Ar atmosphere, and after 20 s (again $\Theta \approx 8$ ML) N_2 is introduced during the remainder of growth.

The effect of the two N_2 deployment schemes on Ag-film morphological evolution is shown in Figure 7, which consists of plots of film resistivity ρ as a function of the nominal thickness Θ for the following conditions: (i) deposition in Ar/N_2 atmosphere for 20 s followed by growth in Ar (blue triangles; denoted as [Ar/N_2(20 s) + Ar]) and (ii) deposition in pure Ar atmosphere for 20 s followed by growth in Ar/N_2 (inverse green triangles; denoted as [Ar(20 s) + Ar/N_2]). The ρ vs Θ curves for the Ar- and Ar/N_2-grown films, originally plotted in Figure 1, are also reproduced in Figure 7 for reference.

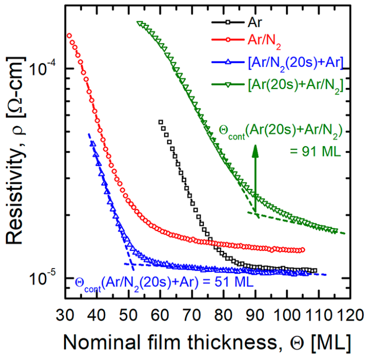

Figure 7. Resistivity (ρ) vs nominal film thickness (Θ) curves, extracted from *in situ*, real-time spectroscopic ellipsometry measurements (see section 2.2), of magnetron sputter-deposited Ag films on SiO_2/Si substrates in (i) an Ar/N_2 atmosphere for 20 s followed by growth in pure Ar (hollow blue triangles; denoted as [Ar/N_2(20 s) + Ar]) and (ii) an Ar atmosphere for 20 s followed by growth in Ar/N_2 (hollow inverse green triangles; denoted as [Ar(20 s) + Ar/N_2]). The ρ vs Θ curves for the Ar-grown (hollow black squares) and Ar/N_2-grown (hollow read circles) films, originally presented in Figure 1, are reproduced for reference. The continuous film formation thicknesses Θ_{cont} for the [Ar/N_2(20 s) + Ar] and the [Ar(20 s) + Ar/N_2] samples are indicated in the figure.

The presence of N_2 during the first 20 s of film deposition ([Ar/N_2(20 s) + Ar]) yields a Θ_{cont} value equal to that of continuous growth in mixed Ar/N_2 atmospheres (= 51 ML), i.e., 2D morphology is promoted, relative to the film grown in pure Ar for which Θ_{cont} = 78 ML. This is explained considering the findings in Figure 2, where it is seen that N_2 impedes coalescence completion, which happens primarily during the first ≈20 ML of deposition. Concurrently, the Ag-layer conductivity is not compromised ($\rho^{ss} \approx 1.1 \times 10^{-5}$ Ω·cm), since N_2 is not present during postcoalescence growth stages to cause substantial grain refinement.

Deployment of N_2 after the first 20 s of deposition ([Ar(20 s) + Ar/N_2]) results in Θ_{cont} = 91 ML; i.e., a more pronounced 3D morphology is obtained compared to the Ar-deposited Ag layer. Moreover, the steady-state resistivity value increases to $\rho^{ss} = 1.7 \times 10^{-5}$ Ω·cm, which is substantially larger in comparison to the values for both Ar/N_2-deposited ($\rho^{ss} \approx 1.4 \times 10^{-5}$ Ω·cm) and Ar-deposited ($\rho^{ss} = 1.1 \times 10^{-5}$ Ω·cm) films. Under the [Ar(20 s) + Ar/N_2] deposition scheme, N_2 is deployed on a pronounced 3D film-growth front which has been formed by extensive and uninterrupted island coalescence during the early growth stages. The effect of N_2 is then to interrupt local epitaxial growth and cause grain refinement on the rough postcoalescence film surface. This leads to higher resistivity than that for Ar-deposited samples. The fact that the film deposited under the [Ar(20 s) + Ar/N_2] condition exhibits a larger Θ_{cont} value than the Ar-grown film indicates that interruption of epitaxial growth on a rough surface also impedes the hole-filling process and promotes further 3D growth.

To confirm the morphological trends observed in Figure 7, we perform *ex situ* XRR measurements on a-C/Ag/SiO_2/Si stacks in which the Ag layers were grown at the same conditions are those listed in Figure 7. Analysis of the reflectivity curves (Figure 8; black circles represent experimental data and red solid lines represent calculated curves) shows that Ag films with thicknesses in the range 22–25 nm are deposited in all cases, which is in very good agreement with the thicknesses obtained from spectroscopic ellipsometry and XTEM. We also extract the roughness $w_{a\text{-}C/Ag}$ of the a-C/Ag interface (i.e., the Ag film roughness) and find that the Ar/N_2-grown film exhibits the smallest value of $w_{a\text{-}C/Ag}$ = 1.5 nm. Slightly larger roughness ($w_{a\text{-}C/Ag}$ = 1.7 nm) is obtained for films grown at the condition [Ar/N_2(20 s) + Ar], while $w_{a\text{-}C/Ag}$ increases to 1.9 nm for the Ar-deposited sample. The largest

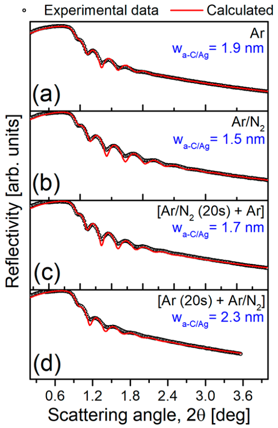

Figure 8. X-ray reflectivity curves (hollow black circles for experimental data and red solid lines for calculated curves) of a-C/Ag/SiO_2/Si stacks in which Ag films are magnetron sputter-deposited in gas compositions: (a) Ar; (b) Ar/N_2; (c) deposition in Ar/N_2 for 20 s followed by growth in Ar (denoted as [Ar/N_2(20 s) + Ar]); and (d) deposition in Ar atmosphere for 20 s followed by growth in Ar/N_2 (denoted as [Ar(20 s) + Ar/N_2]). The roughness of the a-C/Ag interface $w_{a\text{-}C/Ag}$ is also provided for each case in the figure.

value $w_{a\text{-}C/Ag}$ = 2.3 nm is obtained for the film synthesized under the condition [Ar(20 s) + Ar/N_2]. The XRR roughness data described above are consistent with the results from the ρ vs Θ curves shown in Figure 7; i.e., early N_2 deployment promotes 2D growth morphology, while the presence of N_2 during postcoalescence growth stages yields roughness buildup at the film growth front. Moreover, we find that the mass density of the Ag layers is very close to the bulk value of 10.5 g cm^{-3} at all deposition conditions.

4. CONCLUSION

The ability to grow noble-metal films with two-dimensional (2D) morphologies on weakly interacting substrates, including 2D materials and oxides, is essential for the fabrication of high-performance enabling devices. The use of less-noble-metal and gaseous surfactants is a known strategy for manipulating the growth of noble metal layers, but the mechanisms by which surfactant atoms affect the complex structure-forming processes are not understood.

In the present work, we combine *in situ* film growth monitoring, *ex situ* characterization, and optical modeling in the framework of the finite-difference time-domain (FDTD) method to study the effect of nitrogen (N_2) gas surfactant on growth evolution of nanoscale silver (Ag) islands and films on silicon dioxide (SiO_2) substrates, with the purpose of exploring the viability of surfactant-based approaches for metal-contact synthesis. We show that N_2 presence during the early film-growth stages suppresses the rate of island coalescence, which favors 2D morphology and formation of flat films. Furthermore, for later growth stages beyond coalescence, N_2 causes interruption of crystal growth, which leads to grain refinement and increases the resistivity of continuous layers. FDTD calculations confirm that monitoring of the localized surface plasmon resonance (LSPR) via spectroscopic ellipsometry can be a powerful tool to track and control in real time the early stage morphological evolution of ultrathin metal films and supported nanostructures on weakly interacting substrates.

Using the insights presented above, we design and implement growth manipulation experiments in which N_2 is deployed selectively during specific growth stages. Early deployment only during the initial growth stages leads to decrease of coalescence rate and roughness development at the film growth front, without compromising the film electrical resistivity. On the contrary, postcoalescence N_2 deployment leads to pronounced increase in film roughness. This knowledge opens the way for growth strategies in which surfactant species will be deployed with high temporal and spatial precision to target critical film formation stages and manipulate growth morphologies, without altering the film physical properties. Moreover, targeted surfactant deployment can be used to tune the size of supported 3D nanostructures without the need to employ elevated growth temperatures and postdeposition annealing steps.

■ ASSOCIATED CONTENT

Supporting Information

The Supporting Information is available free of charge at https://pubs.acs.org/doi/10.1021/acsanm.0c00736.

> Description of the finite-difference time-domain method that was used to calculate the optical response of silver clusters; images and analysis of early stages of silver film growth obtained from plan-view transmission electron microscopy; determination of localized surface plasmon resonance position from computed total film reflectivity of periodic cluster spatial distributions; X-ray diffractograms and selected area electron diffractograms of continuous Ar- and Ar/N_2-grown silver films; X-ray photoemission spectra of Ar- and Ar/N_2-grown silver films (PDF)

■ AUTHOR INFORMATION

Corresponding Author

Kostas Sarakinos – *Nanoscale Engineering Division, Department of Physics, Chemistry, and Biology, Linköping University, SE 581 83 Linköping, Sweden;* orcid.org/0000-0003-2864-9509; Email: kostas.sarakinos@liu.se

Authors

Andreas Jamnig – *Nanoscale Engineering Division, Department of Physics, Chemistry, and Biology, Linköping University, SE 581 83 Linköping, Sweden; Institut Pprime, Département Physique et Mécanique des Matériaux, UPR 3346 CNRS, Université de Poitiers, F86073 Cedex 9 Poitiers, France;* orcid.org/0000-0003-2765-2271

Nikolaos Pliatsikas – *Nanoscale Engineering Division, Department of Physics, Chemistry, and Biology, Linköping University, SE 581 83 Linköping, Sweden;* orcid.org/0000-0002-5098-6950

Martin Konpan – *Nanoscale Engineering Division, Department of Physics, Chemistry, and Biology, Linköping University, SE 581 83 Linköping, Sweden*

Jun Lu – *Thin Film Physics Division, Department of Physics, Chemistry, and Biology, Linköping University, SE-581 83 Linköping, Sweden*

Thomas Kehagias – *Department of Physics, Aristotle University of Thessaloniki, GR-54124 Thessaloniki, Greece*

Alexios N. Kotanidis – *Department of Materials Science and Engineering, University of Ioannina, Ioannina 45110, Greece*

Nikolaos Kalfagiannis – *School of Science and Technology, Nottingham Trent University, NG11 8NS Nottingham, U.K.;* orcid.org/0000-0002-4030-5525

Dimitris V. Bellas – *Department of Materials Science and Engineering, University of Ioannina, Ioannina 45110, Greece*

Elefterios Lidorikis – *Department of Materials Science and Engineering, University of Ioannina, Ioannina 45110, Greece; Institute of Materials Science and Computing, University Research Center of Ioannina (URCI), 45110 Ioannina, Greece;* orcid.org/0000-0002-9552-9366

Janez Kovac – *Department of Surface Engineering and Optoelectronics, Jozef Stefan Institute, SI-1000 Ljubljana, Slovenia*

Gregory Abadias – *Institut Pprime, Département Physique et Mécanique des Matériaux, UPR 3346 CNRS, Université de Poitiers, F86073 Cedex 9 Poitiers, France;* orcid.org/0000-0001-6801-9937

Ivan Petrov – *Thin Film Physics Division, Department of Physics, Chemistry, and Biology, Linköping University, SE-581 83 Linköping, Sweden; Materials Science and Physics Departments, University of Illinois, Urbana, Illinois 61801, United States*

Joseph E. Greene – *Thin Film Physics Division, Department of Physics, Chemistry, and Biology, Linköping University, SE-581 83 Linköping, Sweden; Materials Science and Physics Departments, University of Illinois, Urbana, Illinois 61801, United States; Department of Materials Science and*

Engineering, National Taiwan University of Science and Technology, Taipei 10607, Taiwan

Complete contact information is available at:
https://pubs.acs.org/10.1021/acsanm.0c00736

Notes

The authors declare no competing financial interest.

■ ACKNOWLEDGMENTS

A.J. and G.A. acknowledge the financial support of the French Government program "Investissements d'Avenir" (LABEX INTERACTIFS, reference ANR-11-LABX-0017-01). K.S. acknowledges financial support from Linköping University ("LiU Career Contract Dnr-LiU-2015-01510, 2015-2020") and the Swedish Research Council (Contract VR-2015-04630). A.J. and K.S. acknowledge financial support from the ÅForsk foundation (Contracts ÅF 19-137 and ÅF 19-746). K.S. and N.P. acknowledge financial support from the Olle Engkvist Foundation (Contract SOEB 190-312) and the Wenner-Gren Foundation (Contracts UPD2018-0071 and UPD2019-0007). J.K. acknowledges financial support from Slovenian Research Agency (Contract BI-US/18-20-08). T.K. acknowledges financial support by the project "INNOVATION-EL" (MIS 5002772), implemented under the Action "Reinforcement of the Research and Innovation Infrastructure", funded by the Operational Program "Competitiveness, Entrepreneurship and Innovation" (NSRF 2014-2020) and cofinanced by Greece and the European Union (European Regional Development Fund).

■ REFERENCES

(1) Echtermeyer, T. J.; Milana, S.; Sassi, U.; Eiden, A.; Wu, M.; Lidorikis, E.; Ferrari, A. C. Surface Plasmon Polariton Graphene Photodetectors. *Nano Lett.* **2016**, *16* (1), 8−20.

(2) Mueller, T.; Xia, F.; Avouris, P. Graphene Photodetectors for High-Speed Optical Communications. *Nat. Photonics* **2010**, *4* (5), 297−301.

(3) Xu, Y.; Hsieh, C.-Y.; Wu, L.; Ang, L. K. Two-Dimensional Transition Metal Dichalcogenides Mediated Long Range Surface Plasmon Resonance Biosensors. *J. Phys. D: Appl. Phys.* **2019**, *52* (6), 065101.

(4) Liu, X.; Han, Y.; Evans, J. W.; Engstfeld, A. K.; Behm, R. J.; Tringides, M. C.; Hupalo, M.; Lin, H.-Q.; Huang, L.; Ho, K.-M.; Appy, D.; Thiel, P. A.; Wang, C.-Z. Growth Morphology and Properties of Metals on Graphene. *Prog. Surf. Sci.* **2015**, *90* (4), 397−443.

(5) Gong, C.; Huang, C.; Miller, J.; Cheng, L.; Hao, Y.; Cobden, D.; Kim, J.; Ruoff, R. S.; Wallace, R. M.; Cho, K.; Xu, X.; Chabal, Y. J. Metal Contacts on Physical Vapor Deposited Monolayer MoS2. *ACS Nano* **2013**, *7* (12), 11350−11357.

(6) Campbell, C. T. Metal Films and Particles on Oxide Surfaces: Structural, Electronic and Chemisorptive Properties. *J. Chem. Soc., Faraday Trans.* **1996**, *92* (9), 1435.

(7) Ohring, M. *Materials Science of Thin Films*; Academic Press: San Diego, 1991.

(8) Martin, P. M. *Handbook of Deposition Technologies for Films and Coatings*, 3rd ed.; Martin, P. M., Ed.; William Andrew: Amsterdam, 2010.

(9) Petrov, I.; Barna, P. B.; Hultman, L.; Greene, J. E. Microstructural Evolution during Film Growth. *J. Vac. Sci. Technol., A* **2003**, *21* (5), S117−S128.

(10) Michely, T.; Krug, J. *Islands, Mounds and Atoms*; Springer Series in Surface Sciences 42; Springer: Berlin, 2004.

(11) Vrijmoeth, J.; van der Vegt, H. A.; Meyer, J. A.; Vlieg, E.; Behm, R. J. Surfactant-Induced Layer-by-Layer Growth of Ag on Ag(111): Origins and Side Effects. *Phys. Rev. Lett.* **1994**, *72* (24), 3843−3846.

(12) Oppo, S.; Fiorentini, V.; Scheffler, M. Theory of Adsorption and Surfactant Effect of Sb on Ag(111). *Phys. Rev. Lett.* **1993**, *71* (15), 2437−2440.

(13) van der Vegt, H. A.; van Pinxteren, H. M.; Lohmeier, M.; Vlieg, E.; Thornton, J. M. C. Surfactant-Induced Layer-by-Layer Growth of Ag on Ag(111). *Phys. Rev. Lett.* **1992**, *68* (22), 3335−3338.

(14) van der Vegt, H. A.; Breeman, M.; Ferrer, S.; Etgens, V. H.; Torrelles, X.; Fajardo, P.; Vlieg, E. Indium-Induced Lowering of the Schwoebel Barrier in the Homoepitaxial Growth of Cu(100). *Phys. Rev. B: Condens. Matter Mater. Phys.* **1995**, *51* (20), 14806−14809.

(15) Breeman, M.; Barkema, G. T.; Langelaar, M. H.; Boerma, D. O. Computer Simulation of Metal-on-Metal Epitaxy. *Thin Solid Films* **1996**, *272* (2), 195−207.

(16) van der Vegt, H. A.; Alvarez, J.; Torrelles, X.; Ferrer, S.; Vlieg, E. Indium-Induced Layer-by-Layer Growth and Suppression of Twin Formation in the Homoepitaxial Growth of Cu(111). *Phys. Rev. B: Condens. Matter Mater. Phys.* **1995**, *52* (24), 17443−17448.

(17) Camarero, J.; Ferrón, J.; Cros, V.; Gómez, L.; Vázquez de Parga, A. L.; Gallego, J. M.; Prieto, J. E.; de Miguel, J. J.; Miranda, R. Atomistic Mechanism of Surfactant-Assisted Epitaxial Growth. *Phys. Rev. Lett.* **1998**, *81* (4), 850−853.

(18) Esch, S.; Hohage, M.; Michely, T.; Comsa, G. Origin of Oxygen Induced Layer-by-Layer Growth in Homoepitaxy on Pt(111). *Phys. Rev. Lett.* **1994**, *72* (4), 518−521.

(19) Poelsema, B.; Kunkel, R.; Nagel, N.; Becker, A. F.; Rosenfeld, G.; Verheij, L. K.; Comsa, G. New Phenomena in Homoepitaxial Growth of Metals. *Appl. Phys. A: Solids Surf.* **1991**, *53* (5), 369−376.

(20) Hoegen, M. H.; Pietsch, H. Homoepitaxy of Si(111) Is Surface Defect Mediated. *Surf. Sci.* **1994**, *321* (1−2), L129−L136.

(21) Voigtländer, B.; Zinner, A. Influence of Surfactants on the Growth-Kinetics of Si on Si(111). *Surf. Sci. Lett.* **1993**, *292* (1−2), L775−L780.

(22) Horn-von Hoegen, M.; Falta, J.; Copel, M.; Tromp, R. M. Surfactants in Si(111) Homoepitaxy. *Appl. Phys. Lett.* **1995**, *66* (4), 487−489.

(23) Kandel, D.; Kaxiras, E. The Surfactant Effect in Semiconductor Thin-Film Growth. In *Solid State Physics*; Ehrenreich, H., Spaepen, F., Eds.; Academic Press: New York, 2000; Vol. *54*, pp 219−262.

(24) Camarero, J.; Graf, T.; de Miguel, J. J.; Miranda, R.; Kuch, W.; Zharnikov, M.; Dittschar, A.; Schneider, C. M.; Kirschner, J. Surfactant-Mediated Modification of the Magnetic Properties of Co/Cu(111) Thin Films and Superlattices. *Phys. Rev. Lett.* **1996**, *76* (23), 4428−4431.

(25) Scheuch, V.; Potthast, K.; Voigtländer, B.; Bonzel, H. P. Investigation of the Growth of Co on Cu(111) and Sb/Cu(111) Using Photoelectron Forward Scattering. *Surf. Sci.* **1994**, *318* (1−2), 115−128.

(26) Wolter, H.; Schmidt, M.; Wandelt, K. Surfactant Induced Layer-by-Layer Growth of Cu on Ru(0001) as Revealed by Oscillatory Work Function Changes. *Surf. Sci.* **1993**, *298* (1), 173−186.

(27) Barna, P. B.; Adamik, M. Fundamental Structure Forming Phenomena of Polycrystalline Films and the Structure Zone Models. *Thin Solid Films* **1998**, *317* (1−2), 27−33.

(28) Lü, B.; Almyras, G. A.; Gervilla, V.; Greene, J. E.; Sarakinos, K. Formation and Morphological Evolution of Self-Similar 3D Nanostructures on Weakly Interacting Substrates. *Phys. Rev. Mater.* **2018**, *2* (6), 063401.

(29) Gervilla, V.; Almyras, G. A.; Thunström, F.; Greene, J. E.; Sarakinos, K. Dynamics of 3D-Island Growth on Weakly-Interacting Substrates. *Appl. Surf. Sci.* **2019**, *488*, 383−390.

(30) Sarakinos, K. A Review on Morphological Evolution of Thin Metal Films on Weakly-Interacting Substrates. *Thin Solid Films* **2019**, *688*, 137312.

(31) Hershberger, M. T.; Hupalo, M.; Thiel, P. A.; Wang, C. Z.; Ho, K. M.; Tringides, M. C. Nonclassical "Explosive" Nucleation in Pb/

Si(111) at Low Temperatures. *Phys. Rev. Lett.* **2014**, *113* (23), 236101.

(32) Anders, A.; Byon, E.; Kim, D.-H.; Fukuda, K.; Lim, S. H. N. Smoothing of Ultrathin Silver Films by Transition Metal Seeding. *Solid State Commun.* **2006**, *140* (5), 225−229.

(33) Gu, D.; Zhang, C.; Wu, Y. K.; Guo, L. J. Ultrasmooth and Thermally Stable Silver-Based Thin Films with Subnanometer Roughness by Aluminum Doping. *ACS Nano* **2014**, *8* (10), 10343.

(34) Ciesielski, A.; Skowronski, L.; Górecka, E.; Kierdaszuk, J.; Szoplik, T. Growth Model and Structure Evolution of Ag Layers Deposited on Ge Films. *Beilstein J. Nanotechnol.* **2018**, *9*, 66−76.

(35) Liu, H.; Wang, B.; Leong, E. S. P.; Yang, P.; Zong, Y.; Si, G.; Teng, J.; Maier, S. A. Enhanced Surface Plasmon Resonance on a Smooth Silver Film with a Seed Growth Layer. *ACS Nano* **2010**, *4* (6), 3139−3146.

(36) Furgeaud, C.; Simonot, L.; Michel, A.; Mastail, C.; Abadias, G. Impact of Ge Alloying on the Early Growth Stages, Microstructure and Stress Evolution of Sputter-Deposited Cu-Ge Thin Films. *Acta Mater.* **2018**, *159*, 286−295.

(37) Bulír, J.; Novotný, M.; Lynnykova, A.; Lančok, J.; Bodnár, M.; Škereň, M.; Martin-Palma, R. J.; Jen, Y.-J.; Lakhtakia, A. Preparation of Nanostructured Ultrathin Silver Layer. *Proc. SPIE* **2010**, 77660Q.

(38) Zhao, G.; Wang, W.; Bae, T.-S.; Lee, S.-G.; Mun, C.; Lee, S.; Yu, H.; Lee, G.-H.; Song, M.; Yun, J. Stable Ultrathin Partially Oxidized Copper Film Electrode for Highly Efficient Flexible Solar Cells. *Nat. Commun.* **2015**, *6* (1), 8830.

(39) Wang, W.; Song, M.; Bae, T.-S.; Park, Y. H.; Kang, Y.-C.; Lee, S.-G.; Kim, S.-Y.; Kim, D. H.; Lee, S.; Min, G.; Lee, G.-H.; Kang, J.-W.; Yun, J. Transparent Ultrathin Oxygen-Doped Silver Electrodes for Flexible Organic Solar Cells. *Adv. Funct. Mater.* **2014**, *24* (11), 1551−1561.

(40) Riveiro, J. M.; Normile, P. S.; Andrés, J. P.; González, J. A.; De Toro, J. A.; Muñoz, T.; Muñiz, P. Oxygen-Assisted Control of Surface Morphology in Nonepitaxial Sputter Growth of Ag. *Appl. Phys. Lett.* **2006**, *89* (20), 201902.

(41) Birnbaum, A. J.; Thompson, C. V.; Steuben, J. C.; Iliopoulos, A. P.; Michopoulos, J. G. Oxygen-Induced Giant Grain Growth in Ag Films. *Appl. Phys. Lett.* **2017**, *111* (16), 163107.

(42) Bulíř, J.; Novotný, M.; Lančok, J.; Fekete, L.; Drahokoupil, J.; Musil, J. Nucleation of Ultrathin Silver Layer by Magnetron Sputtering in Ar/N2 Plasma. *Surf. Coat. Technol.* **2013**, *228*, S86−S90.

(43) Ko, R. H. H.; Khalatpour, A.; Clark, J. K. D.; Kherani, N. P. Ultrasmooth Ultrathin Ag Films by AlN Seeding and Ar/N 2 Sputtering for Transparent Conductive and Heating Applications. *APL Mater.* **2018**, *6* (12), 121112.

(44) Yun, J.; Chung, H.-S.; Lee, S.-G.; Bae, J.-S.; Hong, T. E.; Takahashi, K.; Yu, S. M.; Park, J.; Guo, Q.; Lee, G.-H.; Han, S. Z.; Ikoma, Y.; Choi, E.-A. An Unexpected Surfactant Role of Immiscible Nitrogen in the Structural Development of Silver Nanoparticles: An Experimental and Numerical Investigation. *Nanoscale* **2020**, *12* (3), 1749−1758.

(45) Warrender, J. M.; Aziz, M. J. Effect of Deposition Rate on Morphology Evolution of Metal-on-Insulator Films Grown by Pulsed Laser Deposition. *Phys. Rev. B: Condens. Matter Mater. Phys.* **2007**, *76* (4), 045414.

(46) Oates, T. W. H.; Mücklich, A. Evolution of Plasmon Resonances during Plasma Deposition of Silver Nanoparticles. *Nanotechnology* **2005**, *16* (11), 2606−2611.

(47) Jamnig, A.; Sangiovanni, D. G.; Abadias, G.; Sarakinos, K. Atomic-Scale Diffusion Rates during Growth of Thin Metal Films on Weakly-Interacting Substrates. *Sci. Rep.* **2019**, *9* (1), 6640.

(48) Jamnig, A.; Pliatsikas, N.; Sarakinos, K.; Abadias, G. The Effect of Kinetics on Intrinsic Stress Generation and Evolution in Sputter-Deposited Films at Conditions of High Atomic Mobility. *J. Appl. Phys.* **2020**, *127* (4), 045302.

(49) Depla, D.; De Gryse, R. Target Voltage Measurements during DC Sputtering of Silver in a Nitrogen/Argon Plasma. *Vacuum* **2003**, *69* (4), 529−536.

(50) Lee, Y. S.; Heo, J.; Winkler, M. T.; Siah, S. C.; Kim, S. B.; Gordon, R. G.; Buonassisi, T. Nitrogen-Doped Cuprous Oxide as a p-Type Hole-Transporting Layer in Thin-Film Solar Cells. *J. Mater. Chem. A* **2013**, *1* (48), 15416.

(51) Wang, Y.; Ghanbaja, J.; Horwat, D.; Yu, L.; Pierson, J. F. Nitrogen Chemical State in N-Doped Cu 2 O Thin Films. *Appl. Phys. Lett.* **2017**, *110* (13), 131902.

(52) Herzinger, C. M.; Johs, B.; McGahan, W. A.; Woollam, J. A.; Paulson, W. Ellipsometric Determination of Optical Constants for Silicon and Thermally Grown Silicon Dioxide via a Multi-Sample, Multi-Wavelength, Multi-Angle Investigation. *J. Appl. Phys.* **1998**, *83* (6), 3323−3336.

(53) Oates, T. W. H.; Wormeester, H.; Arwin, H. Characterization of Plasmonic Effects in Thin Films and Metamaterials Using Spectroscopic Ellipsometry. *Prog. Surf. Sci.* **2011**, *86* (11−12), 328−376.

(54) Wooten, F. *Optical Properties of Solids*; Academic Press: New York, 1972.

(55) Taflove, A.; Hagness, S. C. *Computational Electrodynamics: The Finite-Difference Time-Domain Method*, 3rd ed.; 2005.

(56) Lidorikis, E.; Egusa, S.; Joannopoulos, J. D. Effective Medium Properties and Photonic Crystal Superstructures of Metallic Nanoparticle Arrays. *J. Appl. Phys.* **2007**, *101* (5), 054304.

(57) Elofsson, V.; Lü, B.; Magnfält, D.; Münger, E. P.; Sarakinos, K. Unravelling the Physical Mechanisms That Determine Microstructural Evolution of Ultrathin Volmer-Weber Films. *J. Appl. Phys.* **2014**, *116* (4), 044302.

(58) Jensen, P. Growth of Nanostructures by Cluster Deposition: Experiments and Simple Models. *Rev. Mod. Phys.* **1999**, *71* (5), 1695−1735.

(59) Carrey, J.; Maurice, J.-L. Transition from Droplet Growth to Percolation: Monte Carlo Simulations and an Analytical Model. *Phys. Rev. B: Condens. Matter Mater. Phys.* **2001**, *63* (24), 245408.

(60) Carrey, J.; Maurice, J.-L. Scaling Laws near Percolation during Three-Dimensional Cluster Growth: A Monte Carlo Study. *Phys. Rev. B: Condens. Matter Mater. Phys.* **2002**, *65* (20), 205401.

(61) Lü, B.; Münger, E. P.; Sarakinos, K. Coalescence-Controlled and Coalescence-Free Growth Regimes during Deposition of Pulsed Metal Vapor Fluxes on Insulating Surfaces. *J. Appl. Phys.* **2015**, *117* (13), 134304.

(62) Kreibig, U.; Vollmer, M. *Optical Properties of Metal Clusters*; Springer Series in Materials Science; Springer: Berlin, 1995; Vol. 25.

(63) Scholl, J. A.; Koh, A. L.; Dionne, J. A. Quantum Plasmon Resonances of Individual Metallic Nanoparticles. *Nature* **2012**, *483* (7390), 421−427.

(64) Iati, M. A.; Lidorikis, E.; Saija, R. Modeling of Enhanced Electromagnetic Fields in Plasmonic Nanostructures. In *Handbook of Enhanced Spectroscopy*; de la Chapelle, M. L., Gucciardi, P. G., Lidgi-Guigui, N., Eds.; Taylor & Francis: Boca Raton, FL, 2016.

(65) Leiro, J.; Minni, E.; Suoninen, E. Study of Plasmon Structure in XPS Spectra of Silver and Gold. *J. Phys. F: Met. Phys.* **1983**, *13* (1), 215−221.

(66) Ueta, H.; Gleeson, M. A.; Kleyn, A. W. Scattering of Hyperthermal Nitrogen Atoms from the Ag(111) Surface †. *J. Phys. Chem. A* **2009**, *113* (52), 15092−15099.

(67) Carter, R. N.; Murphy, M. J.; Hodgson, A. On the Recombinative Desorption of N2 from Ag(111). *Surf. Sci.* **1997**, *387* (1−3), 102−111.

(68) Hultman, L.; Bareño, J.; Flink, A.; Söderberg, H.; Larsson, K.; Petrova, V.; Odén, M.; Greene, J. E.; Petrov, I. Interface Structure in Superhard TiN-SiN Nanolaminates and Nanocomposites: Film Growth Experiments and Ab Initio Calculations. *Phys. Rev. B: Condens. Matter Mater. Phys.* **2007**, *75* (15), 155437.

Supporting information: "3D-to-2D Morphology Manipulation of Sputter-Deposited Nanoscale Silver Films on Weakly-Interacting Substrates via Selective Nitrogen Deployment for Multifunctional Metal Contacts"

Andreas Jamnig[1,2], Nikolaos Pliatsikas[1], Martin Konpan[1], Jun Lu[3], Thomas Kehagias[4], Alexios N. Kotanidis[5], Nikolaos Kalfagiannis[6], Dimitris V. Bellas[5], Elefterios Lidorikis[5,7], Janez Kovac[8], Gregory Abadias[2], Ivan Petrov[3,9], Joseph E. Greene[3,9,10], and Kostas Sarakinos[1,]*

[1]Nanoscale Engineering Division, Department of Physics, Chemistry, and Biology, Linköping University, SE 581 83, Linköping, Sweden

[2]Institut Pprime, Département Physique et Mécanique des Matériaux, UPR 3346 CNRS, Université de Poitiers, SP2MI, 11 Bvd. M. et P. Curie, TSA 41123, F86073 Poitiers Cedex 9, France

[3]Thin Film Physics Division, Department of Physics, Chemistry, and Biology, Linköping University, SE-581 83 Linköping, Sweden

[4]Aristotle University of Thessaloniki, Department of Physics, GR-54124 Thessaloniki, Greece

[5]University of Ioannina, Department of Materials Science and Engineering, Ioannina, 45110, Greece

[6]Nottingham Trent University, School of Science and Technology, NG11 8NS, Nottingham, UK

[7]University Research Center of Ioannina (URCI), Institute of Materials Science and Computing, 45110 Ioannina, Greece

[8]Department of Surface Engineering and Optoelectronics, Jozef Stefan Institute, SI-1000 Ljubljana, Slovenia

[9]Materials Science and Physics Departments, University of Illinois, Urbana, Illinois, 61801, USA

[10]Department of Materials Science and Engineering, National Taiwan University of Science and Technology, Taipei 10607, Taiwan

S1. Finite-difference time-domain calculations

We use the finite-difference time-domain (FDTD) method to calculate the optical responses of assemblies of discrete nanoscale silver (Ag) islands, formed during the initial stages of film growth, on silicon dioxide (SiO_2) substrates. The calculations are performed by dividing the film/substrate system into domains and, subsequently, the Maxwell's equations (see Eqs.(S1)) are time-integrated on the computational grid[1–3]:

$$\nabla \times E = -\mu \partial_t H \quad \text{(S1a)}$$

$$\nabla \times H = \varepsilon_0 \partial_t E + \partial_t P_0 + \sum_{j=1}^{N} \partial_t P_j \text{ (S1b)}$$

In Eq.(S1a), E denotes the electric field, μ is the relative permittivity, and H represents the magnetic field. In Eq.(S2b), ε_0 is the permittivity of free space, and P_0 and P_j stand for the polarization of the free and bound electrons, respectively, in each material.

The polarizations P_0 and P_j are connected to the Drude free-electron and the Lorentz oscillator models, respectively, through the differential equations:

$$\partial_t^2 P_0 + \tau^{-1} \partial_t P_0 = \omega_p^2 \varepsilon_0 E \text{ (S2a)}$$

$$\partial_t^2 P_j + \Gamma_j \partial_t P_j + \omega_{0j} P_j = f_j \omega_{0j}^2 \varepsilon_0 E \text{ (S2b)}$$

Equations (S2) imply the dielectric function is expressed by the Drude-Lorentz model as:

$$\tilde{\epsilon}(\omega) = \epsilon_\infty - \frac{\omega_p^2 \tau}{\omega^2 \tau + i\omega} + \sum_{j=1}^{N} \frac{f_j \omega^2}{\omega_{0j}^2 - \omega^2 - i\Gamma_j \omega} \text{ (S3)}$$

In Eq.(S3), ϵ_∞ is the value of the high photon-energy dielectric function, ω_p and τ are the free electron plasma frequency and relaxation time, respectively, and ω_{0j}, f_j, and Γ_j denote oscillator resonance frequency, strength, and damping rate, respectively.

The SiO$_2$ substrate is described as dielectric material with a real and constant refractive index $n = \sqrt{\epsilon} = 1.45$. For the Ag layer, we calculate the polarization by fitting the Drude-Lorentz model (Eq.(S3)) to the bulk dielectric function of Ag taken from Ref.(4)[4]. Since we describe the optical response of assemblies of nanoscale islands, we account for the effect of the island size on the free-electron relaxation time τ_r by correcting the bulk Ag free-electron relaxation time τ_{bulk} for the surface scattering contribution according to[5]:

$$\tau_r^{-1} = \tau_{bulk}^{-1} + \frac{v_F}{r} \text{ (S4)},$$

where r is the island radius and v_F is the Fermi velocity (i.e., $1.39 \times 10^6\ ms^{-1}$)[2].

The polarization for each material is then introduced to Eqs.(S1), which is solved concurrently with the E and H fields using an in-house 3D FDTD simulator[2]. In doing so, we obtain the electromagnetic fields and fluxes at every point in the computational grid in the time domain. By performing Fourier transformation, we compute the latter quantities in the frequency domain, from which we extract the reflectivity of the simulated structure[2].

We perform FDTD calculations for nanoscale Ag islands with sizes obtained from plan-view transmission electron microscopy (TEM) data (see Section 3.1. and Fig.2 in the main manuscript). Using such data, we calculate the Ag island size distributions for Ar and Ar/N_2-grown films at coverages $\Theta = 2$ and $8\ ML$ (see Fig.S1) and we extract the total surface coverage.

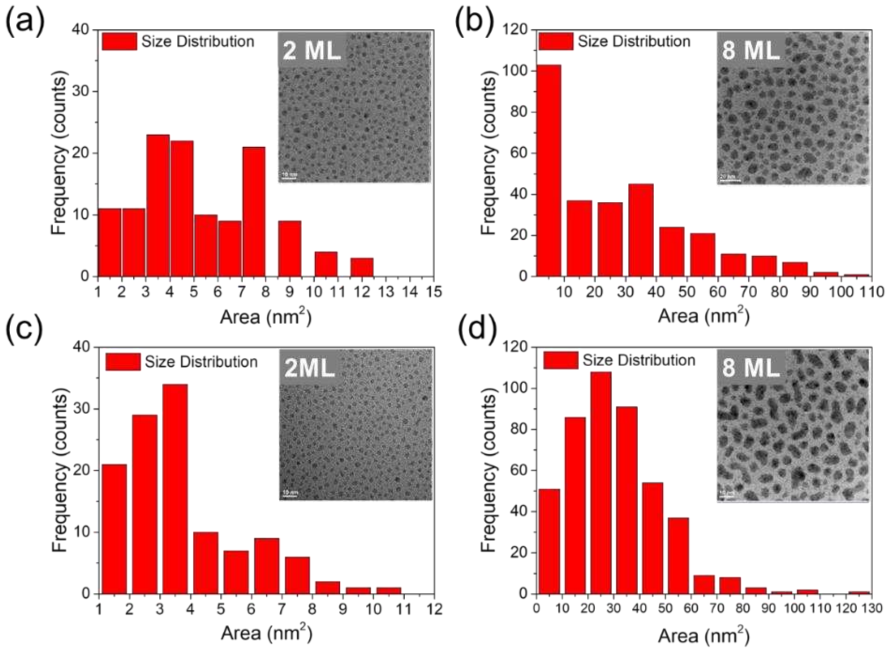

Figure S1. Nanoscale Ag island size distributions for: (a) Ar-grown films at $\Theta = 2\ ML$; (b) Ar-grown films at $\Theta = 8\ ML$; (c) Ar/N$_2$-grown films at $\Theta = 2\ ML$; and (d) Ar/N$_2$-grown films at $\Theta = 8\ ML$. The insets present representative plan-view TEM micrographs from which the size distributions were calculated; they image surface areas of (a),(c),(d) $105 \times 105\ nm^2$ and (b) $145 \times 145\ nm^2$.

We then compute the total film reflectivity for each of the conditions shown in Fig.S1, by performing calculation for multiple random island spatial distributions (denoted as D1 through D5), as shown in Fig.S2. From the peaks with the highest intensity in each reflectivity curve, we determine the position of localized surface plasmon resonance that is plotted in Fig.4(a) in the main manuscript.

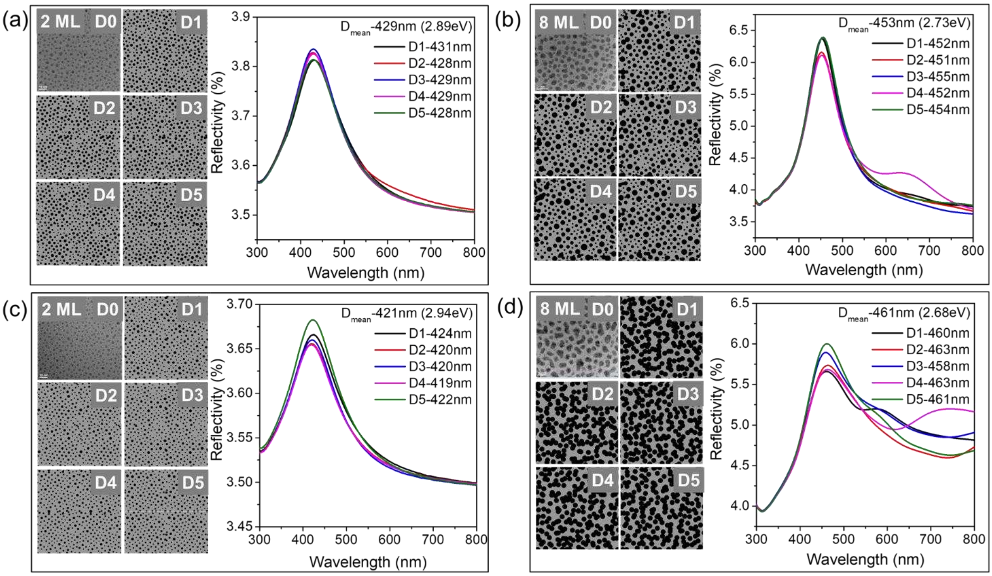

Figure S2. Plan-view TEM images (denoted as D0), simulated random Ag island distributions with island size distributions comparable to D0 (denoted as D1 through D5), and calculated reflectivity spectra for (a) Ar-grown films for $\Theta = 2\,ML$; (b) Ar-grown films for $\Theta = 8\,ML$; (c) Ar/N$_2$-grown films for $\Theta = 2\,ML$; and (d) Ar/N$_2$-grown films for $\Theta = 8\,ML$. The wavelength at which the reflectivity curves exhibit their maximum values corresponds to theoretical LSPR positions, which are provided for each simulated distribution (D1 through D5) along with the mean LSPR value denoted as D$_{mean}$.

To better understand the early-stage film morphological evolution, we calculate, using FDTD, the localized surface plasmon resonance (LSPR) positions for various periodic and close-packed hemispherical island arrays. The simulations describe the optical response as function of surface coverage in the range 10 to 90% for two scenarios: (i) the island number density (i.e., number of islands/m^2) is kept constant and the surface coverage is varied by varying the island volume (i.e., diameter) (Fig.S3(a)); and (ii) the island diameter is kept constant and the surface coverage is varied by varying the island number density (Fig.S3(b)). In both cases we run simulations for a different range of initial diameters varying from 2 to $15\ nm$. The results of these calculations are used in Fig.4(b) of the main manuscript.

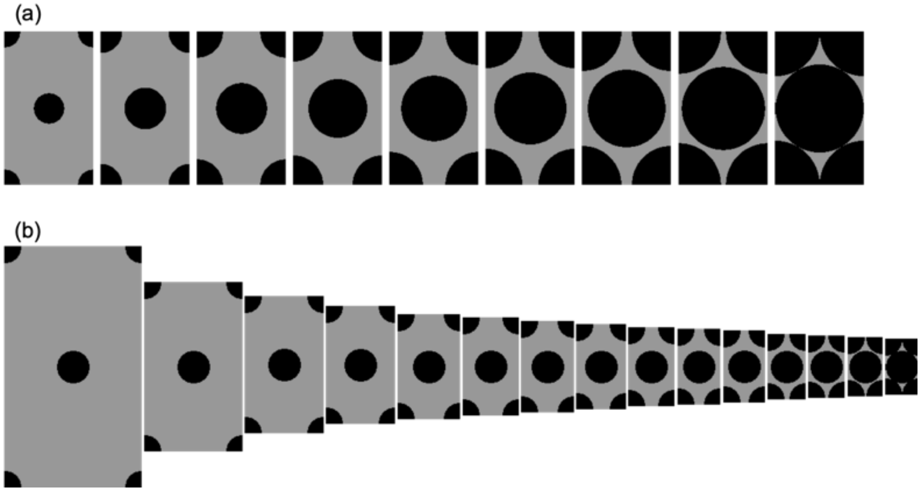

Figure S3. Indicative snapshots of the hexagonal closed pack FDTD unit cells of: (a) a case where the island surface density is preserved while increasing the island volume. The initial particle diameter in this case is $10\ nm$. (b) maintaining the island diameter (in this case $10\ nm$) while increasing the island surface density.

S2. Microstructural and microchemical analysis of continuous films

The microstructure of $\sim 25\ \mathrm{nm}$-thick magnetron-sputter-deposited Ag films on SiO_2/Si substrates is analyzed using x-ray diffractometry (XRD) in Bragg-Brentano configuration. XRD patterns are presented in Fig.S4 for Ar- and Ar/N_2-grown films. The expected 2θ positions of the (111) and (200) reflections for bulk and unstrained Ag[6] are indicated by dashed vertical lines. A detailed discussion with regards to the XRD data can be found in Section 3.2 of the manuscript.

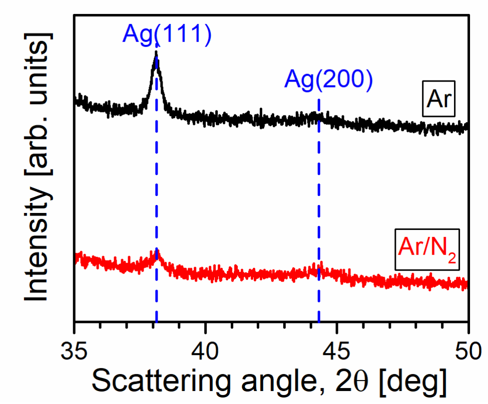

Figure S4. Bragg-Brentano x-ray diffraction patterns of $\sim 25\ \mathrm{nm}$-thick magnetron-sputter-deposited Ag films on SiO_2/Si substrates in Ar (black solid line) and Ar/N2 (red solid line) atmospheres. The vertical blue dashed lines indicate the position of the (111) and (200) reflections in bulk, unstrained Ag[6].

Figure S5 illustrates the selected area electron diffraction (SAED) patterns from Ar-grown and Ar/N_2-grown Ag films, taken along the [011] projection direction of the Si substrate.

Ring-type SAED patterns are typical of the polycrystalline nature of the Ag films. Since both patterns were recorded under the same selected area aperture of $20\ \mu\mathrm{m}$, the apparently lower number of reflections in the Ar-grown Ag film (Fig.S5(a)) implies the presence of larger Ag crystals compared to the Ar/N_2-grown Ag film (Fig.S5(b)). Figure S5(c) presents the Si substrate SAED pattern, where the growth direction is marked with an arrow.

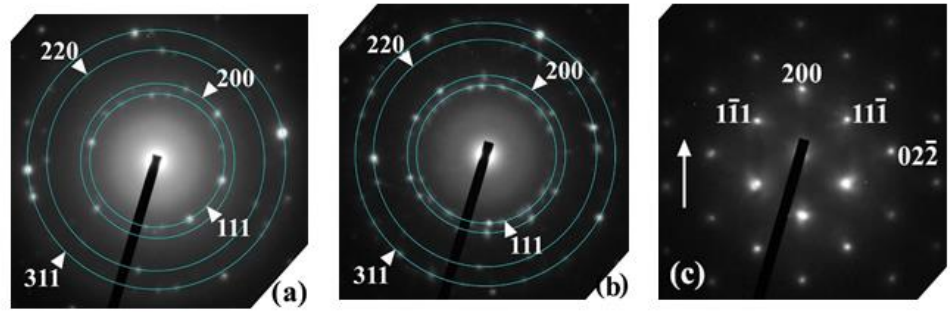

Figure S5. SAED patterns of (a) the Ar-grown and (b) the Ar/N_2-grown Ag film oriented along the [011] zone axis of the Si substrate, shown in (c) (the arrow indicates the growth direction). The Ag reflections are denoted by circles, indicating the polycrystalline nature of the films. The higher number of reflections in each ring suggests smaller crystals in the Ar/N_2-grown Ag film.

X-ray photoelectron spectroscopy was performed on Ar- and Ar/N_2-grown films. Sputter-etching was performed to remove surface layers ($\sim 3\ \mathrm{nm}$). For both films, XPS spectra presented in Fig.S6 show all Ag related peaks (Ag-*3s*, Ag-*3p*, Ag-*3d*, Ag-*4s*, and Ag-*4p*). The inset in Fig.S6 presents Ag-*3d* core-level high-resolution scans, which indicate that only Ag-Ag bonds form in both films. Ag-*3d* plasmon-loss satellite peaks, that limit the detectability of light elements, are marked with an arrow and a dashed rectangle in Fig.S6.

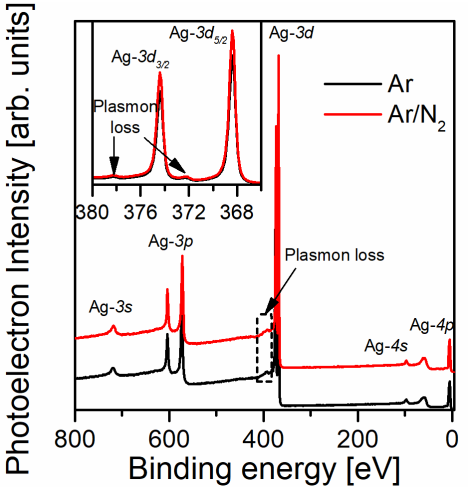

Figure S6. Wide-scan x-ray photoelectron spectra of magnetron-sputter-deposited Ag layers on SiO_2/Si substrates in pure Ar (black solid line) and Ar/N_2 (red solid line) atmospheres. The inset presents core-level high resolution scans around the Ag-*3d* binding energy position. The arrows show the position of Ag plasmon-loss peaks.

AUTHOR INFORMATION

***Corresponding author**, email: kostas.sarakinos@liu.se

Author contributions. The manuscript was written through contribution of all authors. All authors have given approval to the final version of the manuscript.

Notes. The authors declare no competing financial interest.

References

(1) Jackson, J. D. *Classical Electrodynamic*, 13th ed.; John Wiley & Sons Inc.: New York.

(2) Lidorikis, E.; Egusa, S.; Joannopoulos, J. D. Effective Medium Properties and Photonic Crystal Superstructures of Metallic Nanoparticle Arrays. *J. Appl. Phys.* **2007**, *101* (5), 054304. https://doi.org/10.1063/1.2709863.

(3) Taflove, A.; Hagness, S. C. *Computational Electrodynamics : The Finite-Difference Time-Domain Method*, 3rd ed.; Boston, MA, 2005.

(4) *Handbook of Optical Constants of Solids*, Vol. 3.; Palik, E. D., Ed.; Academic Press: New York, 1998.

(5) Kreibig, U.; Fragstein, C. v. The Limitation of Electron Mean Free Path in Small Silver Particles. *Zeitschrift für Phys.* **1969**, *224* (4), 307–323. https://doi.org/10.1007/BF01393059.

(6) ICDD Powder Diffraction File No. 00-004-0787.

Paper IV

Manipulation of thin silver film growth on weakly-interacting silicon dioxide substrates using oxygen as a surfactant

Nikolaos Pliatsikas[1], Andreas Jamnig[1,2], Martin Konpan[1], Andreas Delimitis[3], Gregory Abadias[2], and Kostas Sarakinos[1,*]

*Corresponding author

[1]Nanoscale Engineering Division, Department of Physics, Chemistry and Biology, Linköping University, Linköping, SE 581 83, Sweden

[2]Institut Pprime, Département Physique et Mécanique des Matériaux, UPR 3346 CNRS, Université de Poitiers, SP2MI, 11 Bvd M. et P. Curie, F86073 Poitiers Cedex 9, France

[3]Department of Mechanical and Structural Engineering and Materials Science, University of Stavanger, N-4036 Stavanger, Norway

Journal of Vacuum Science & Technology A 38 (2020), 043406

https://doi.org/10.1116/6.0000244

JVST A
Journal of Vacuum Science & Technology A

Manipulation of thin silver film growth on weakly interacting silicon dioxide substrates using oxygen as a surfactant

Cite as: J. Vac. Sci. Technol. A **38**, 043406 (2020); https://doi.org/10.1116/6.0000244
Submitted: 06 April 2020 . Accepted: 14 May 2020 . Published Online: 05 June 2020

Nikolaos Pliatsikas, Andreas Jamnig, Martin Konpan, Andreas Delimitis, Gregory Abadias, and Kostas Sarakinos

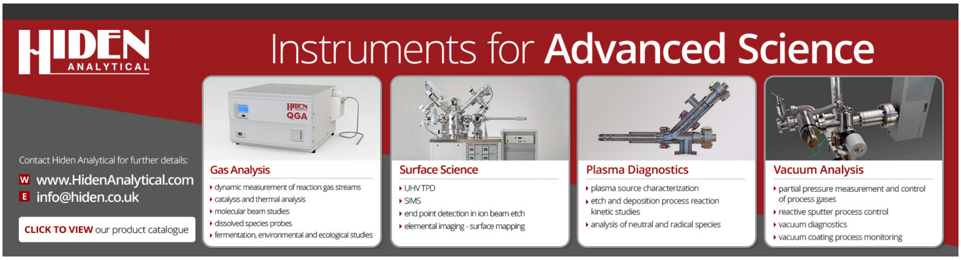

JVST A
Journal of Vacuum Science & Technology A

ARTICLE

avs.scitation.org/journal/jva

Manipulation of thin silver film growth on weakly interacting silicon dioxide substrates using oxygen as a surfactant

Cite as: J. Vac. Sci. Technol. A **38**, 043406 (2020); doi: 10.1116/6.0000244
Submitted: 6 April 2020 · Accepted: 14 May 2020 ·
Published Online: 5 June 2020

Nikolaos Pliatsikas,[1] Andreas Jamnig,[1,2] Martin Konpan,[1] Andreas Delimitis,[3] Gregory Abadias,[2] and Kostas Sarakinos[1,a)]

AFFILIATIONS

[1]Nanoscale Engineering Division, Department of Physics, Chemistry and Biology, Linköping University, Linköping SE 581 83, Sweden
[2]Institut Pprime, Département Physique et Mécanique des Matériaux, UPR 3346 CNRS, Université de Poitiers, SP2MI, 11 Bvd M. et P. Curie, F86073 Poitiers Cedex 9, France
[3]Department of Mechanical and Structural Engineering and Materials Science, University of Stavanger, N-4036 Stavanger, Norway

Note: This paper is part of the 2020 Special Topic Collection Festschrift Honoring Dr. Steve Rossnagel.
[a)]**Electronic mail:** kostas.sarakinos@liu.se

ABSTRACT

The authors study the morphological evolution of magnetron-sputtered thin silver (Ag) films that are deposited on weakly interacting silicon dioxide (SiO_2) substrates in an oxygen-containing (O_2) gas atmosphere. *In situ* and real-time monitoring of electrically conductive layers, along with *ex situ* microstructural analyses, shows that the presence of O_2, throughout all film-formation stages, leads to a more pronounced two-dimensional (2D) morphology, smoother film surfaces, and larger continuous-layer electrical resistivities, as compared to Ag films grown in pure argon (Ar) ambient. In addition, the authors' data demonstrate that 2D morphology can be promoted, without compromising the Ag-layer electrical conductivity, if O_2 is deployed with high temporal precision to target film formation stages before the formation of a percolated layer. Detailed real-space imaging of discontinuous films, augmented by *in situ* growth monitoring data, suggests that O_2 favors 2D morphology by affecting the kinetics of initial film-formation stages and most notably by decreasing the rate of island coalescence completion. Furthermore, compositional and bonding analyses show that O_2 does not change the chemical nature of the Ag layers and no atomic oxygen is detected in the films, i.e., O_2 acts as a surfactant. The overall results of this study are relevant for developing noninvasive surfactant-based strategies for manipulating noble-metal-layer growth on technologically relevant weakly interacting substrates, including graphene and other 2D crystals.

I. INTRODUCTION

Growth of thin noble-metal films with two-dimensional (2D) morphology on weakly interacting 2D-material and oxide substrates is a crucial step in the fabrication of multifunctional contacts in a wide array of key enabling devices.[1–7] Achieving such morphology, so that the metal-layer fully wets the underlying substrate, entails a great scientific challenge: the adsorption energy of noble-metal atoms on weakly interacting surfaces is significantly smaller than the bulk-metal binding energy,[4,7] thereby providing the driving force toward a pronounced and uncontrolled three-dimensional (3D) growth.

Vapor-based film deposition is a far-from-equilibrium process in which morphology is predominantly determined by the kinetic rates of atomic-scale structure-forming processes during early growth stages.[8–11] The kinetic pathways leading to 3D morphologies in homo- and heteroepitaxial film/substrate systems are well established in the literature.[11] This understanding has enabled the development of growth manipulation strategies in which *surfactants* (i.e., minority metal or gaseous species) are deployed and temporarily adsorbed at the film growth front to allow navigation between 2D and 3D morphologies.[12–26]

The atomistic mechanisms that govern morphological evolution of metal films on weakly interacting substrates are different from those in strongly interacting epitaxial systems.[7,27–29] As such, established knowledge for surfactant-based growth manipulation is not directly applicable to the case of noble-metal film deposition on 2D materials and oxides. Despite the latter, there are empirical studies in which less-noble-metal surfactants and seed layers,[30–35] as well as gaseous surfactants,[36–41] have been used to suppress the 3D morphology of silver and copper films on oxide substrates.

Recently, we have contributed to the fundamental understanding of the mechanisms that govern surfactant-modified film growth on weakly interacting substrates by studying the effect of nitrogen (N_2) gas on the morphological evolution of silver (Ag) films on silicon dioxide (SiO_2).[42] Our results showed that N_2 affects the various film-formation stages in a complex manner: when N_2 is present during island nucleation and coalescence, 2D growth morphology is promoted, while the opposite is observed when N_2 is deployed after island coalescence is completed, so that the stage of hole-filling is primarily affected.

The goal of the present work is to understand the role of chemical affinity between noble-metal and gas surfactant species on various film-formation stages and the overall film morphological evolution on weakly interacting substrates. To this purpose, we study the growth of magnetron-sputtered Ag films on SiO_2 substrates in an oxygen-containing (O_2) gas atmosphere. We use *in situ* and real-time spectroscopic ellipsometry to monitor the evolution of optoelectronic properties of electrically conductive layers, and in combination with *ex situ* microstructural analysis, we establish that the presence of O_2 throughout all film-formation stages leads to a more pronounced 2D morphology, smoother film surfaces, but larger continuous-layer electrical resistivities, relative to Ag films grown in a pure argon (Ar) atmosphere. These trends are qualitatively consistent with the effect of N_2 on Ag-layer morphology.[42,43] However, an ∼10 times smaller O_2 partial pressure is required for the surfactant effect to manifest itself, which can be explained by the higher reactivity of O_2 toward Ag, as compared to that of N_2.[44–46] In addition, our *in situ* and real-time data demonstrate that the detrimental effect of O_2 on Ag-layer conductivity can be mitigated, while promoting 2D morphology, if O_2 is deployed in a way that targets initial film-growth stages before the formation of a percolated layer. Detailed *ex situ* real-space imaging, combined with data from *in situ* and real-time monitoring of discontinuous metal-layer growth, suggests that O_2 favors 2D morphology by affecting the kinetics of initial film-formation stages—most notably by decreasing the rate of island coalescence completion. Moreover, compositional and bonding analyses show that the presence of O_2 in the gas atmosphere does not affect the chemical nature of the metal layer in which only Ag-Ag bonds are present, while no atomic oxygen is detected in the bulk of the film, thereby showing that O_2 acts as a surfactant.

II. EXPERIMENTAL STRATEGY AND PROCEDURES

A. Film synthesis

Thin Ag films are synthesized by direct current magnetron sputtering (dcMS) at a constant current of 20 mA, resulting in a deposition rate of ∼0.11 nm/s. All depositions are carried out in a multisource ultrahigh vacuum chamber (base pressure of $\sim 10^{-8}$ Pa) on Czochralski-grown n-type Si(100) wafers, covered with a ∼530 nm-thick thermally grown SiO_2 layer. No intentional substrate heating is used during depositions. The magnetron source, equipped with a Ag target (diameter 7.62 cm, purity 99.99%), is placed 7.5 cm from the substrate and at an angle of 45° with respect to the substrate surface normal.

Ar (purity 99.999%) is used as a sputtering gas. Films are deposited either in pure Ar atmosphere or in Ar/O_2 mixtures (O_2 purity 99.999%) at a total working pressure p_{total} of 1.3 Pa. For samples grown in Ar/O_2 atmospheres, initial tests at different O_2 partial pressures p_{O_2} showed no appreciable difference in the film morphological evolution for $\frac{p_{O_2}}{p_{total}} > 0.01$. Hence, in the remainder of the article, we focus on experiments performed for $p_{O_2} = 0.01 \times p_{total}$. It should be pointed out that the partial pressures refer to values measured in the absence of plasma. Moreover, the Ar introduction point is at the chamber wall halfway between the substrate holder and the magnetrons, while O_2 is introduced through an orifice in the vicinity of the substrate. A schematic illustration of the chamber layout, including the spectroscopic ellipsometer used for *in situ* film growth monitoring (see Sec. II B) and the gas introduction points, is shown in Fig. 1.

We have recently studied[42] the growth of magnetron sputter-deposited Ag layers on SiO_2 in mixed Ar/N_2 gas atmospheres, and we established that N_2 affects the various film-formation stages in distinctly different ways. In order to explore whether the latter is also the case when O_2 is used to manipulate growth, we deploy O_2 using the following schemes: (1) O_2 is present together with Ar throughout the entire deposition process; (2) O_2 is introduced at the early film-growth stages so that the growth surface is exposed to the presence of surfactant for a time t_E ranging between 2 and 20 s. Subsequently, O_2 is pumped out from the deposition chamber, while deposition continues and is completed in pure Ar atmosphere; and (3) deposition commences in pure Ar ambient,

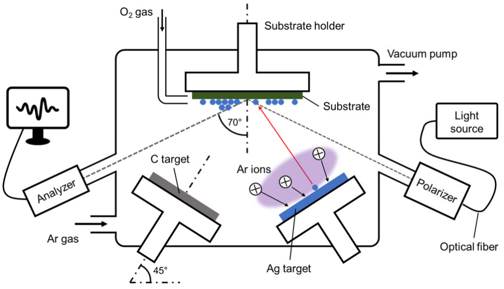

FIG. 1. Schematic illustration of the deposition chamber, including the Ar and O_2 gas introduction points and the spectroscopic ellipsometer used for *in situ* film growth monitoring.

and after a delay time t_D ranging from 2 to 20 s, O_2 is introduced for the remainder of the growth.

The film morphological evolution, microstructure, and chemical composition are analyzed using the *in situ* and *ex situ* tools and methodologies described in Sec. II B. Prior to exposing the samples to atmosphere for *ex situ* analyses, and immediately after Ag deposition, samples are capped with a 3 nm-thick amorphous carbon (a-C) layer to avoid surface contamination and changes in film morphology upon atmospheric exposure. The a-C capping layers are sputter-deposited at a rate of 0.01 nm/s from a graphite (C) target (purity 99.99 at. %; diameter 7.6 cm; thickness 6 mm) in pure Ar at 1.3 Pa. The C target is operated in dcMS at a constant current mode of 50 mA, 7.5 cm away from the substrate, and at an angle of 45° with the substrate surface normal.

B. *In situ* film growth monitoring and *ex situ* film characterization

Spectroscopic ellipsometry is employed *in situ* and in real-time to monitor the change of film optoelectronic properties during deposition and, thereby, draw conclusions about the film morphological evolution. Data are collected every ~2 s in the range of 1.6–3.2 eV, at an angle of incidence of ~70° from the substrate normal, using a rotating analyzer ellipsometer. The acquired data are fitted to a three-phase model consisting of vacuum, a metal-layer, and a substrate. The substrate optical properties are described by a semi-infinite 625 μm Si slab with a top layer of SiO_2, the thickness of which is determined by measuring the optical response of the substrate prior to deposition. Optical constants for the Si and SiO_2 layers are taken from Ref. 47 and Ref. 48. The optical response of the film is described using the Drude–Lorentz dispersion model, as detailed below.

During initial growth stages, the film surface primarily features isolated Ag islands that give rise to localized surface plasmon resonance (LSPR),[49,50] which can be described by adapting the Lorentz oscillator model[49,50] to express the complex dielectric function of the layer $\tilde{\epsilon}(\omega)$ as

$$\tilde{\epsilon}(\omega) = \frac{f\omega^2}{\omega_o^2 - \omega^2 - i\Gamma\omega}. \quad (1)$$

In Eq. (1), f and ω_o are the oscillator strength and resonance frequency, respectively, and Γ represents the damping rate of the plasmon resonance. More details on the implementation and relevance of the Lorentz oscillator model for describing the optical response of discontinuous Ag layers can be found in our previous work.[42]

The optical response of electrically conductive Ag films is described by the Drude free electron theory,[51] according to which the dielectric function $\tilde{\epsilon}_D(\omega)$ is given by the expression

$$\tilde{\epsilon}_D(\omega) = \epsilon_\infty - \frac{\omega_p^2}{\omega^2 + i\Gamma_D\omega}. \quad (2)$$

In Eq. (2), ϵ_∞ is a constant that accounts for the effect of interband transitions occurring at frequencies higher than the ones considered here, Γ_D is the free-electron damping constant, and $\omega_p = \sqrt{ne^2/\varepsilon_0 m_e}$ is the free-electron plasma energy, where n is the free-electron density, e is the electric charge, m_e is the free-electron effective mass, and ε_0 is the permittivity of free space. From Eq. (2), the room-temperature film resistivity is calculated as[51]

$$\rho = \frac{\Gamma_D}{\epsilon_0 \omega_p^2}. \quad (3)$$

Besides the optical properties, the analysis of the ellipsometric data enables us to calculate the film height h_f as a function of deposition time t. Using the continuous-layer h_f value, the film deposition rate F is extracted ($F \approx 0.11$ nm/s at all conditions used in this work), from which the nominal film thickness Θ (i.e., the amount of deposited material) at any given time during growth t is calculated as $\Theta = F \times t$. Throughout the article, Θ is expressed in monolayers (ML), whereby one ML corresponds to the amount of atoms per unit area that is required to increase the film thickness by an amount equal to the Ag (111) interplanar spacing (0.235 nm), which is the most common out-of-plane growth orientation for physical vapor deposited face-centered-cubic (fcc) metal films.

In situ characterization is complemented by *ex situ* imaging of discontinuous film surfaces using a field emission gun scanning electron microscope (SEM) at an operating voltage of 4 kV and a working distance of 3 mm. SEM images are analyzed using the ImageJ software package[52] to determine the fraction of the substrate covered by the film, as well as the island size and shape distribution.

Real-space imaging is combined with x-ray reflectometry (XRR) to obtain film roughness w, thickness h_f, and mass density ρ_m. The optics for XRR are a 1/32° divergence slit and a Goebel mirror for the incident beam, while a parallel plate collimator and a nickel filter are used for the reflected beam path. Reflectivity data are modeled using the X'Pert reflectivity software package. The crystal structure is determined from x-ray diffractometry (XRD) in Bragg–Brentano geometry using a Goebel mirror for the incident beam. For both XRR and XRD measurements, a copper K_α source (wavelength of 0.15418 nm) in line focus is used.

Film chemical composition and bonding properties are determined by x-ray photoelectron spectroscopy (XPS). XPS measurements are carried using an AXIS Ultra spectrometer in a UHV system (base pressure of $\sim 10^{-8}$ Pa), equipped with a monochromated aluminum K_α x-ray beam, a hemispherical sector analyzer, and a multichannel detector. A 20 eV pass energy resulting in full width at half maximum (FWHM) for the Ag-$3d_{5/2}$ peak of less than 500 meV is used in order to obtain information from the core-level spectra. Photoelectron spectra are collected as a function of the sample depth using 4 keV Ar^+ ion-beam etching. Charge-induced shifts of the binding energy are corrected using the Ar-$2p$ peak that originates from Ar^+ ion sputtering. XPS data are analyzed with Kratos Vision software and the quantitative analysis use the relative sensitivity factors contained within the Vision Software.

III. RESULTS AND DISCUSSION

Representative room-temperature resistivities ρ of conductive Ag layers grown in Ar and Ar/O_2 mixtures (for various O_2 deployment schemes described in Sec. II A) are plotted as a function of nominal film thickness Θ in Fig. 2. For clarity, the plot is divided into two panels. Both panels depict curves that were recorded during film growth in pure Ar (squares) and Ar/O_2 mixtures, whereby O_2 is present throughout the entire deposition (stars). Moreover, Fig. 2(a) presents data from experiments in which the growth surface is exposed to O_2 for times $t_E = 2$ and 20 s, and Fig. 2(b) shows ρ vs Θ curves in which O_2 is introduced in the gas ambient after delay times $t_D = 2$ and 20 s (the corresponding 2 and 20 s curves are represented with circles and diamonds, respectively). All curves show a sharp decrease in ρ with increasing Θ after which a steady-state resistivity value ρ^{SS} is reached. The nominal film thickness at which ρ^{SS} is established marks to the formation of continuous layer (this Θ value is hereinafter denoted as Θ_{cont}) as we have previously shown.[42,53–55]

The data in both panels in Fig. 2 show that the addition of O_2 in the growth atmosphere results in Θ_{cont} to decrease from ≈81 ML for film grown in pure Ar to ≈51 ML, i.e., the presence of O_2 promotes 2D growth. Furthermore, Ag growth in an O_2-containing atmosphere yields a steady-state resistivity of $\rho^{SS} \approx 1.3 \times 10^{-5}\,\Omega\,\mathrm{cm}$, which is larger than the corresponding value of $\approx 1.1 \times 10^{-5}\,\Omega\,\mathrm{cm}$ for the film grown in pure Ar.

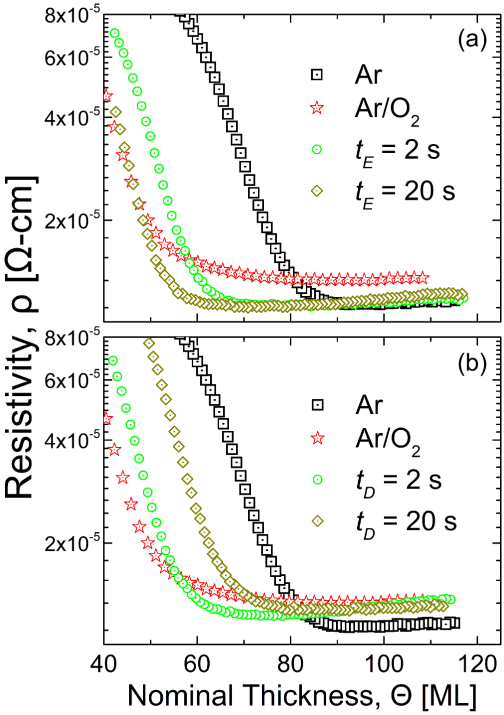

FIG. 2. Resistivity (ρ) vs nominal thickness (Θ) for (a) O_2 deployment at the early film-growth stages for exposure times $t_E = 2$ and 20 s; (b) O_2 deployment at late film-growth stages for delay times $t_D = 2$ and 20 s. Both panels display curves recorded during growth of samples in pure Ar and mixed Ar/O_2 ambient, whereby in the latter case, the surfactant gas is continuously present until deposition completion.

Figure 2(a) reveals that the addition of O_2 in the gas atmosphere during the early growth stages for time t_E as short as 2 s is sufficient for decreasing Θ_{cont} from ≈81 ML (Ar-deposited layer) to ≈61 ML. By further increasing t_E to 20 s, the continuous-layer formation thickness decreases to $\Theta_{cont} \approx 54$ ML Moreover, $\rho^{SS} \approx 1.1 \times 10^{-5}\,\Omega\,\mathrm{cm}$ for both t_E values presented in Fig. 2(a), which is smaller than the value of $\rho^{SS} \approx 1.3 \times 10^{-5}\,\Omega\,\mathrm{cm}$ for the sample grown under continuous presence of O_2, and nearly identical to resistivity obtained during Ag deposition in pure Ar atmosphere. These trends with respect to both Θ_{cont} and ρ^{SS} are qualitatively consistent with our previous observations for the effect of N_2 on Ag-layer morphological evolution of Ref. 42, in which we have demonstrated that early-stage-introduction of N_2 also promotes 2D growth without compromising noble-metal-layer resistivity. Hence, the results in both the present study and in Ref. 42 underscore that effective and noninvasive surfactant-based growth manipulation strategies can be developed by targeting and selectively modifying early film-formation stages.

Delayed O_2 deployment [see Fig. 2(b)] with $t_D = 2$ s yields $\Theta_{cont} \approx 57$ ML that is slightly larger than the value of ≈51 ML for the Ar/O_2-grown sample. This value increases further to ≈66 ML for $t_D = 20$ s. Concurrently, ρ^{SS} takes values in the range of $\sim 1.2 \times 10^{-5}$ to $\sim 1.3 \times 10^{-5}\,\Omega\,\mathrm{cm}$, which is comparable to the steady-state resistivity of the Ar/O_2 grown layer and only slightly higher than the value obtained for films grown in Ar atmosphere. The trends in Fig. 2(b) are opposite than those found when N_2 is used to modify film growth,[42] for which late surfactant gas introduction leads to increase in Θ_{cont} and ρ^{SS} above the values for layers grown in pure Ar atmosphere, i.e., 3D morphological evolution is promoted. This indicates that O_2 is more effective in promoting 2D morphology than N_2, since its presence in the gas atmosphere is the only prerequisite for yielding a smaller Θ_{cont}, relative to films grown in pure Ar.

Multiple studies[42,49,53–56] have shown that ρ vs Θ curves obtained from analysis of *in situ* spectroscopy ellipsometry data provide a physically correct picture of the morphological evolution of electrically conductive layers. To confirm that this is the case also for the Ag films in the present study, we perform XRR measurements on a-C/Ag/SiO_2/Si stacks, in which continuous Ag layers are grown in Ar and Ar/O_2 atmospheres. The XRR curves are plotted in Fig. 3, whereby circles represent experimental data and solid lines represent the calculated curves, from which the morphology-related quantities of the stack layers are extracted, including the Ag film thickness h_f, the a-C/Ag interface roughness $w_{a-C/Ag}$ (i.e., Ag-layer roughness), and the Ag-layer mass density ρ_m (the values for these quantities are also provided in Fig. 3 next to each corresponding reflectivity curve). The analysis shows that $h_f \approx 25$ nm for both Ag-layer synthesis conditions, which is in very good agreement with the thicknesses obtained from spectroscopic ellipsometry. Moreover, ρ_m is very close to the bulk Ag mass density ($10.49\,\mathrm{g/cm^3}$)[57] as expected for magnetron-sputter-deposited high mobility (i.e., low melting point) metal films.[58,59] We also find that $w_{a-C/Ag} = 1.8$ nm

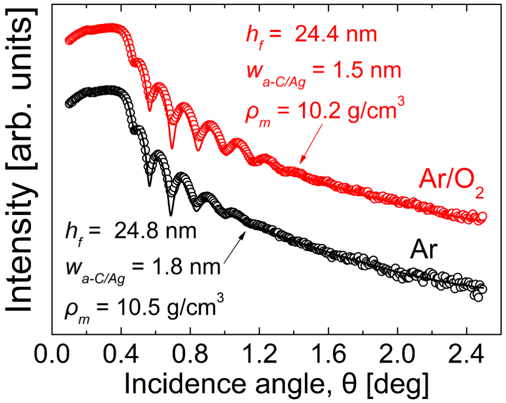

FIG. 3. XRR measurements from a-C/Ag/SiO_2/Si stacks in which Ag layer is grown in Ar (circles) and Ar/O_2-(circles) atmospheres. The solid lines represent the calculated curves from which the film thickness h_f, the a-C/Ag interface roughness $w_{a-C/Ag}$, and the mass density ρ_m are calculated. The values for these quantities for both stacks are also provided in the figure.

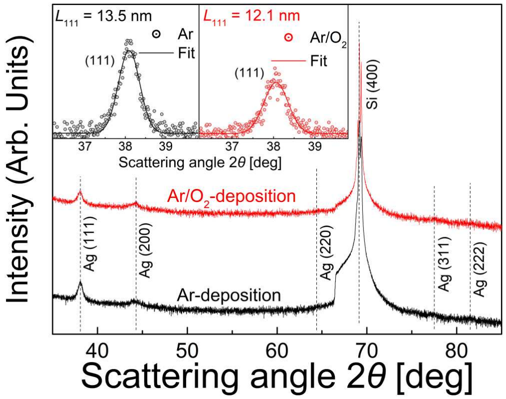

FIG. 4. Bragg–Brentano XRD patterns recorded from a-C/Ag/SiO_2/Si stacks in which ∼25 nm-thick Ag layers are grown in Ar (bottom solid line) and Ar/O_2 (top solid line) atmospheres. The vertical dashed lines mark the angular position of XRD reflections in unstrained Ag powder and Si(100) crystal. The inset shows a magnified section of the XRD patterns around the Ag(111) reflections for both samples in which experimental data (circles) are fitted by Gaussian functions (solid lines). From the Gaussian fit, the reflection full width at half-maximum is extracted, from which the size of the 111 crystallographic grains L_{111} along the film growth direction is estimated.

for the Ar-grown film, while addition of O_2 to the sputtering atmosphere leads to $w_{a-C/Ag} = 1.5\,\text{nm}$. Hence, the results from the XRR analysis confirm that the presence of O_2 is associated with reduction of roughness at the film growth front, i.e., 2D morphology is promoted.

In order to establish the effect of the sputtering atmosphere composition on the crystal structure of continuous Ag layers, we investigate the a-C/Ag/SiO_2/Si stacks grown at the conditions reported in Fig. 3 by means of XRD. The corresponding Bragg–Brentano XRD patterns are shown in Fig. 4 (bottom and top solid lines for Ar- and Ar/O_2-grown Ag films, respectively), in which the angular positions of scattering-intensity maxima in unstrained reference Ag powder and Si(100) single crystal are marked by vertical dashed lines. The sample grown in Ar atmosphere exhibits a strong 111 reflection, and a much weaker 200 peak (integrated intensity ratio $\frac{I_{111}}{I_{200}} = 8.0$), while no other Ag-related diffraction maxima are observed. This indicates that the Ag layer exhibits an [111] out-of-plane texture, as expected for fcc metals. Addition of O_2 leads to a more random texture evidenced by the change of 111 and 200 reflection intensities $\left(\frac{I_{111}}{I_{200}} = 3.4\right)$ in the corresponding XRD pattern. Moreover, no diffraction peaks originating from phases other than metallic Ag (e.g., AgO, Ag_2O) are detected in Fig. 4.

We further analyze the XRD data in Fig. 4 by fitting the 111 reflections with Gaussian functions (see inset in Fig. 4) from which we calculate a full width at half-maximum (FWHM) of 0.621° and 0.695° for Ar and Ar/O_2-grown samples, respectively. These FWHM values are then used in Scherrer's formula[60,61] to estimate the size of the 111 crystallites, L_{111}, along the growth direction. We find that the addition of O_2 to the sputtering gas leads to a small decrease in L_{111} from 13.5 to 12.1 nm, i.e., our XRD data indicate that O_2 causes grain refinement. The latter can explain the increase of steady-state resistivity seen in Fig. 2 when O_2 is present in the sputtering atmosphere throughout the entire film deposition; decrease of grain size corresponds to an increase in the grain boundary area where scattering of charge carriers (electrons) takes place.

The *in situ* analysis data presented in Fig. 2 indicate that O_2 affects the various film-formation stages in a complex fashion. In order to better understand the effect of O_2 on the initial growth stages and its correlation with the overall film morphological evolution, we perform SEM analysis on discontinuous layers. Images recorded from a-C/Ag/SiO_2/Si stacks, whereby the Ag layer is grown in Ar and Ar/O_2 ambient, are shown in Figs. 5(a) and 5(b), respectively. For both deposition conditions, data for $\Theta = 8$, 13, and 21 ML are presented. For $\Theta = 8$ ML, both samples exhibit similar surface topography, featuring nearly spherical islands with similar size and number density. Increase of Θ to 13 ML leads to larger islands, but with different shapes depending on the composition of the gas atmosphere; the Ar-grown sample still exhibits nearly spherical islands, while islands for the Ar/O_2-grown layer become more irregularly shaped. The differences between the two growth conditions become more pronounced for $\Theta = 21$ ML, where islands for the sample deposited in Ar/O_2 ambient are more interconnected and elongated, and the substrate areal coverage is larger, as compared to the Ar-grown sample.

The data and trends presented in Figs. 5(a) and 5(b) are better visualized and quantified by extracting the island size and shape

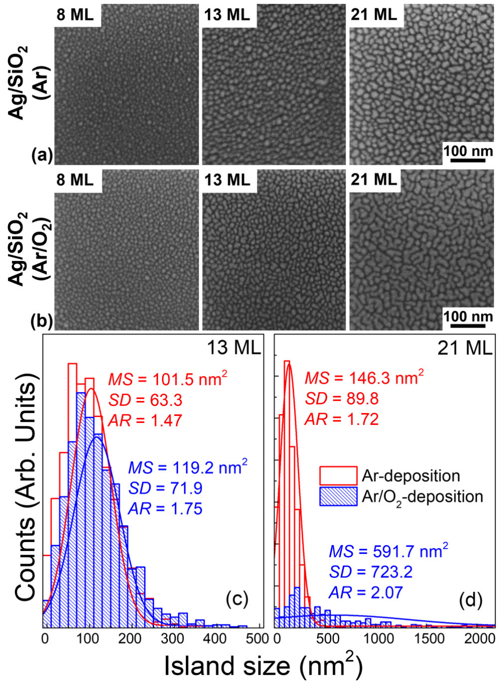

FIG. 5. SEM images of Ag layers grown in (a) pure Ar and (b) Ar/O$_2$ atmospheres for $\Theta = 8$, 13, and 21 ML. Panels (c) and (d) present island size distribution plots and analysis from the data shown in panels (a) and (b) for $\Theta = 13$ and 21 ML, respectively. The solid and lines in (c) and (d) are generated by fitting the corresponding histogram data to Gaussian functions.

distributions, and calculating the island mean size (*MS*), island size standard deviation (*SD*), and the mean in-plane island aspect ratio (*AR*), for $\Theta = 13$ ML [Fig. 5(c)] and $\Theta = 21$ ML [Fig. 5(d)]. The results in Fig. 5(c) show similar bell-shaped island size distributions for both conditions with the histogram for Ar/O$_2$-grown sample (patterned bars) being shifted to slightly larger sizes as compared to the corresponding histogram for the Ag layer deposited in pure Ar ambient (hollow bars). This is also reflected in the calculated $MS \pm SD$ values that are 101.5 ± 63.3 nm^2 (Ar) and 119.2 ± 71.9 nm^2 (Ar/O$_2$). Moreover, the visual impression that the addition of O$_2$ in the gas atmosphere yields more elongated islands is also confirmed by the *AR* value of 1.75, relative to $AR = 1.47$ for the Ar-deposited sample (note that for spherical islands $AR = 1$). Increase of Θ to 21 ML [Fig. 5(d)] results in significant differences in the island size distributions, depending on the composition of the gas atmosphere. The sample grown in pure Ar still exhibits a bell-shaped histogram with $MS \pm SD = 146.3 \pm 89.8$ nm^2, while $AR = 1.72$. In stark contrast, the island sizes for the Ar/O$_2$-deposited sample are significantly larger and are distributed over a larger range ($MS \pm SD = 591.7 \pm 723.2$ nm^2), while the island shapes deviate more clearly from the spherical geometry ($AR = 2.07$). The overall results in Fig. 5 show that addition of O$_2$ in the gas atmosphere leads to larger and elongated islands for $\Theta > 8$ ML; this behavior has been associated in the literature[42,62–66] with incomplete island coalescence. The latter delays cluster reshaping and favors in-plane versus out-of-plane island growth, i.e., a 2D morphology is promoted.

In order to obtain information on the film morphology for $\Theta < 8$ ML and ascertain whether O$_2$ affects the precoalescence film-formation stages of island nucleation and growth, we study the evolution of optoelectronic properties of discontinuous layers using *in situ* spectroscopic ellipsometry. Such layers consist of isolated islands and/or island clusters and can give rise to LSPR.[49] We have recently shown[42] that the LSPR-related optical response can be effectively modeled by a Lorentz oscillator, while the evolution of the oscillator energy $\hbar\omega_0$ as a function of nominal thickness Θ reflects changes in the substrate areal coverage.

Figure 6 plots $\hbar\omega_0$ vs Θ curves from Ag films in which (1) the growth surface is exposed to O$_2$ for times $t_E = 2$ and 20 s [Fig. 6(a)]; and (2) O$_2$ is introduced in the gas ambient after delay times t_D of 2 and 20 s [Fig. 6(b)]. For reference, both panels display curves recorded during growth of samples in pure Ar (squares) and mixed Ar/O$_2$ (stars) ambient. All curves in Fig. 6 show that the value of $\hbar\omega_0$ redshifts (i.e., decreases) with increasing Θ. This behavior has been attributed to in-plane island growth with continued deposition that leads to a decrease in the substrate areal (surface) coverage and the island-island separation distance.[42,49] Moreover, both panels show that the addition of O$_2$ to the sputtering atmosphere leads to smaller $\hbar\omega_0$ values for a given Θ, while the Ar/O$_2$ $\hbar\omega_0$ vs Θ curve exhibits a larger declining slope as compared to its Ar counterpart. This is another indication that the presence of O$_2$ promotes in-plane island growth and 2D morphological evolution and shows that the decrease of Θ_{cont} (Fig. 2) and $w_{a-C/Ag}$ for continuous layers (Fig. 3) has its origin in initial film-formation stages of island nucleation, growth, and coalescence.

The data in Fig. 6(a) show that, even at a minimum exposure of the growing surface to O$_2$ for $t_E = 2$ s (which corresponds to $\Theta \approx 1$ ML), the $\hbar\omega_0$ vs Θ slope for Θ in the range of ≈2 to ≈5 ML is distinctly steeper than that of the corresponding Ar curve. Earlier simulations of 3D film growth[53,54] have estimated that the saturation island density—the latter denotes the point during growth until which island nucleation is the dominant structure-forming process—is established for $\Theta \approx 0.4$ ML, when adatoms are the only mobile species on the growing film surface and islands have hemispherical shapes. This value can be further increased when higher-order clusters (i.e., dimers and trimers) are mobile, as, e.g., during growth of high-mobility metals (including Ag) on weakly interacting substrates.[59] Hence, based on the differences in the slope of $\hbar\omega_0$ vs Θ curves for Ar- and Ar/O$_2$-grown ($t_E = 2$ s) films, it cannot be ruled out that O$_2$ promotes 2D growth morphology by (1) enhancing island densities and (2) favoring in-plane growth of individual islands through suppression of uphill atomic transport.[67] However, the main mechanism that affects morphology appears to be the decrease of island coalescence completion rate, as seen by the steeper $\hbar\omega_0$ vs Θ slope at $\Theta > 5$ ML for the Ar/O$_2$-deposited ($t_E = 2$ s) layer.

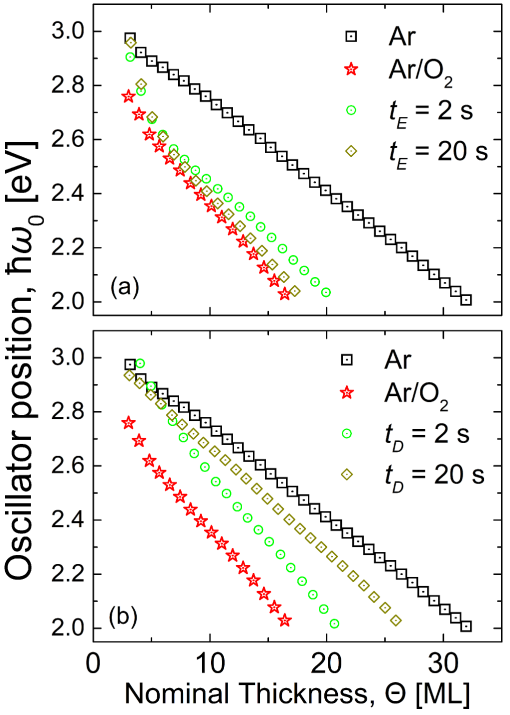

FIG. 6. Lorentz-model resonance energy ($\hbar\omega_0$) vs nominal thickness (Θ) for (a) O_2 deployment at the early film-growth stages for exposure times t_E between 2 and 20 s; (b) O_2 deployment at late film-growth stages for delay times t_D between 2 and 20 s. Both panels plot curves recorded during growth of samples in pure Ar and mixed Ar/O_2 ambient with continuous presence of surfactant gas until deposition completion.

This notion is also supported by the additional increase of the $\hbar\omega_0$ vs Θ curve slope when $t_E = 20$ s, which approaches asymptotically that of the Ar/O_2-grown sample.

When deposition commences in pure Ar atmosphere and O_2 is introduced after a delay time t_D, Fig. 6(b) shows that $\hbar\omega_0$ vs Θ curves are nearly identical to that of pure Ar for $\Theta \leq 5$ ML, above which the curve slope deviates from the Ar line and increases, approaching gradually that of the Ar/O_2 data, as t_D is decreased from 20 to 2 s. This is consistent with the results in Fig. 2 showing that Θ_{cont} increases with increasing t_D and again indicates that the effect of O_2 on the initial stages of film formation is very crucial for subsequent overall layer morphology.

To correlate the Ag-layer morphological evolution with changes in film chemistry and bonding properties, we perform XPS analyses on a-C/Ag/SiO_2/Si stacks sputter-deposited in Ar and Ar/O_2 gas atmospheres. Wide XPS scans (not shown here) of both as deposited and Ar^+-etched samples exhibit peaks matching the binding energies of all Ag-related electronic orbitals (Ag-3*s*, Ag-3*p*, Ag-3*d*, Ag-4*s*, and Ag-4*p*), irrespective of the presence or not of O_2 in the deposition chamber during Ag film growth. This is exemplified by the Ag-3*d* high-resolution scans for the Ar/O_2-grown sample presented in Fig. 7. We find that only Ag-Ag bonds form, while no Ag-O peak signature is detected (the expected binding energies for Ag_2O and AgO bonds are also marked in Fig. 7). High-resolution scans of the O-1*s* (Fig. 7 inset) reveal that O-related XPS peaks can be either identified as O-Si bonds[68] (which emanate from the substrate) or as surface contamination. Moreover, there is no evidence of O-Ag peaks at binding energies of 529.0 and 528.5 eV, which are correlated to Ag_2O and AgO bonds, respectively.[69,70] Hence, the results in Fig. 7 suggest that O_2 is only temporarily adsorbed at the film growth front, i.e., it acts as a surfactant. However, incorporation of small amounts of oxygen (<1 at. %, which is the typical XPS detection limit for light elements[71]) cannot be ruled out, most prominently at the film/substrate interface, in accordance with recent literature results.[42,44,72]

In comparison to our previous study on the effect of N_2 on Ag-layer morphological evolution,[42] we observe that for the same Ag vapor deposition rate, an ∼10 lower O_2 partial pressure is required for significantly affecting film growth. This can be attributed to the smaller dissociation energy of O_2 molecule (5.2 eV) compared to that of N_2 (9.8 eV),[73] which makes generation of reactive atomic species (O) by energetic plasma electrons and incorporation on the

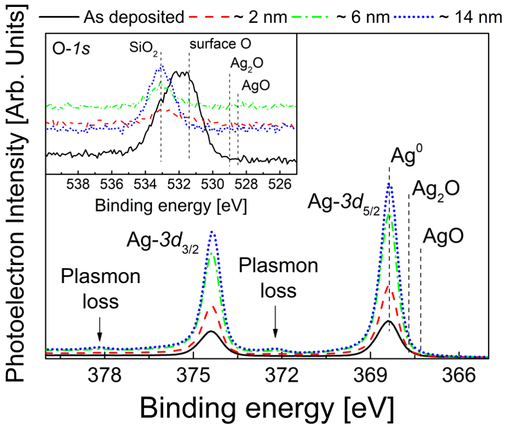

FIG. 7. Ag-3*d* core-level high-resolution XPS spectra of ∼25 nm-thick continuous Ag layers grown by magnetron sputtering on SiO_2/Si substrates in Ar/O_2 atmospheres. Spectra are recorded from as deposited samples, as well as from samples that have been etched by Ar^+ ions removing ∼2, ∼6, and ∼14 nm of material. The inset presents core-level high-resolution scans around the O-1*s* binding energy position. The arrows show the position of Ag plasmon-loss peaks.

growth front more likely. Atomic oxygen has been suggested to favor Ostwald over Smoluchowksi ripening (i.e., cluster diffusion) in the Ag/Ag(100) homoepitaxial system.[72,74,75] Concurrently, Ostwald ripening is a much slower process than cluster diffusion, and hence, it is only relevant for postdeposition coarsening. From the latter, it follows that in an oxygen-free system material will be, primarily, redistributed between islands during growth, while the presence of atomic oxygen will promote material redistribution postdeposition, i.e., coarsening during growth will be hindered. Furthermore, exposure of vicinal Ag surfaces to atomic oxygen has been shown to promote sidewall facet formation,[76] which is known to decrease the rate of material transport between the coalescing islands.[29,77] Moreover, atomic oxygen adsorption on the surface of Ag islands residing on SiO_2 surfaces has been suggested to lower the island surface and the island/substrate interface energies, which yields a smaller driving force for cluster reshaping.[78] The above-mentioned mechanisms are relevant for explaining the hindrance of coalescence completion in our film/substrate system, which is seemingly the process by which 2D growth morphology is promoted for Ag films in the presence of O_2.

IV. SUMMARY AND CONCLUSIONS

The ability to grow noble-metal films with 2D morphologies on weakly interacting substrates, including 2D materials and oxides, is essential for the fabrication of high-performance enabling devices. The weak film/substrate interaction provides the driving force toward uncontrolled and pronounced 3D morphological evolution. This tendency can be reversed by using minority less-noble-metal (e.g., transition metals) and gaseous species (both referred to also as surfactants). The mechanisms by which surfactants affect various film growth stages on weakly interacting substrates are far from being understood, while surfactant-based strategies should be designed in a way that does not compromise other physical properties (e.g., optoelectronic properties) of the noble-metal layers.

In the present work, we explore the way by which O_2 affects the complex formation stages and the overall morphological evolution of Ag layers deposited by magnetron sputtering on weakly interacting SiO_2 substrates. We combine real-time *in situ* growth monitoring and *ex situ* structural and chemical characterization and find that Ag layers grow flatter in the presence of O_2 due to incomplete island coalescence. However, O_2 causes the increase of Ag-layer electrical resistivity, relative to films grown in pure Ar atmosphere, unless the surfactant gas is only deployed during the initial stages of island nucleation, growth, and coalescence. The overall results are consistent with previous findings on the effect of N_2 on Ag-layer growth on SiO_2;[42,43] yet significantly smaller amounts of O_2 are required to affect morphology owing to its higher reactivity toward Ag compared to that of N_2. The knowledge generated herein provides critical insights into the development of noninvasive growth manipulation strategies in which 2D morphology can be promoted by deploying gaseous species, as well as other less-noble-metals, at the film growth with high temporal precision to target and selectively modify critical film formation stages.

ACKNOWLEDGMENTS

K.S. acknowledges financial support from Linköping University ("LiU Career Contract," No. Dnr-LiU-2015-01510, 2015–2020) and the Swedish Research Council (Contract No. VR-2015-04630). K.S. and N.P. acknowledge financial support from the Olle Engkvist Foundation (Contract No. SOEB 190-312) and the Wenner-Gren Foundations (Contract Nos. UPD2018-0071 and UPD2019-0007). A.J. and G.A. acknowledge financial support from the French Government Program "Investissements d'Avenir" (LABEX INTERACTIFS, Reference No. ANR-11-LABX-0017-01). A.J. and K.S. acknowledge financial support from the Åforsk Foundation (Contract No. ÅF 19-137). A.D. and K.S. acknowledge financial support through a mobility grant in the framework of the European Consortium of Innovative Universities (ECIU).

REFERENCES

[1] T. J. Echtermeyer, S. Milana, U. Sassi, A. Eiden, M. Wu, E. Lidorikis, and A. C. Ferrari, Nano Lett. **16**, 8 (2016).
[2] T. Mueller, F. Xia, and P. Avouris, Nat. Photonics **4**, 297 (2010).
[3] Y. Xu, C.-Y. Hsieh, L. Wu, and L. K. Ang, J. Phys. D Appl. Phys. **52**, 065101 (2019).
[4] X. Liu *et al.*, Prog. Surf. Sci. **90**, 397 (2015).
[5] C. Gong *et al.*, ACS Nano **7**, 11350 (2013).
[6] A. Sclafani and J.-M. Herrmann, J. Photochem. Photobiol. A Chem. **113**, 181 (1998).
[7] C. T. Campbell, J. Chem. Soc. Faraday Trans. **92**, 1435 (1996).
[8] M. Ohring, *The Materials Science of Thin Films* (Academic Press, San Diego, 1992).
[9] P. M. Martin, *Handbook of Deposition Technologies for Films and Coatings* (William Andrew, Amsterdam, 2010).
[10] I. Petrov, P. B. Barna, L. Hultman, and J. E. Greene, J. Vac. Sci. Technol. A **21**, S117 (2003).
[11] T. Michely and J. Krug, *Islands, Mounds and Atoms*, 1st ed. (Springer-Verlag, Berlin, 2004).
[12] J. Camarero, T. Graf, J. J. de Miguel, R. Miranda, W. Kuch, M. Zharnikov, A. Dittschar, C. M. Schneider, and J. Kirschner, Phys. Rev. Lett. **76**, 4428 (1996).
[13] V. Scheuch, K. Potthast, B. Voigtländer, and H. P. Bonzel, Surf. Sci. **318**, 115 (1994).
[14] H. Wolter, M. Schmidt, and K. Wandelt, Surf. Sci. **298**, 173 (1993).
[15] D. Kandel and E. Kaxiras, in *Solid State Physics*, edited by H. Ehrenreich and F. Spaepen (Academic, San Diego, 2000), Vol. 54, pp. 219–262.
[16] M. H. Hoegen and H. Pietsch, Surf. Sci. **321**, L129 (1994).
[17] B. Voigtländer and A. Zinner, Surf. Sci. Lett. **292**, L775 (1993).
[18] B. Poelsema, R. Kunkel, N. Nagel, A. F. Becker, G. Rosenfeld, L. K. Verheij, and G. Comsa, Appl. Phys. A Solids Surf. **53**, 369 (1991).
[19] M. Horn-von Hoegen, J. Falta, M. Copel, and R. M. Tromp, Appl. Phys. Lett. **66**, 487 (1995).
[20] H. A. van der Vegt, J. Alvarez, X. Torrelles, S. Ferrer, and E. Vlieg, Phys. Rev. B **52**, 17443 (1995).
[21] S. Oppo, V. Fiorentini, and M. Scheffler, Phys. Rev. Lett. **71**, 2437 (1993).
[22] S. Esch, M. Hohage, T. Michely, and G. Comsa, Phys. Rev. Lett. **72**, 518 (1994).
[23] H. A. van der Vegt, H. M. van Pinxteren, M. Lohmeier, E. Vlieg, and J. M. C. Thornton, Phys. Rev. Lett. **68**, 3335 (1992).
[24] J. Vrijmoeth, H. A. van der Vegt, J. A. Meyer, E. Vlieg, and R. J. Behm, Phys. Rev. Lett. **72**, 3843 (1994).
[25] J. Camarero, J. Ferrón, V. Cros, L. Gómez, A. L. Vázquez de Parga, J. M. Gallego, J. E. Prieto, J. J. de Miguel, and R. Miranda, Phys. Rev. Lett. **81**, 850 (1998).
[26] M. Breeman, G. T. Barkema, M. H. Langelaar, and D. O. Boerma, Thin Solid Films **272**, 195 (1996).
[27] B. Lü, G. A. Almyras, V. Gervilla, J. E. Greene, and K. Sarakinos, Phys. Rev. Mater. **2**, 063401 (2018).
[28] V. Gervilla, G. A. Almyras, F. Thunström, J. E. Greene, and K. Sarakinos, Appl. Surf. Sci. **488**, 383 (2019).

[29] V. Gervilla, G. A. Almyras, B. Lü, and K. Sarakinos, Sci. Rep. **10**, 2031 (2020).
[30] A. Anders, E. Byon, D.-H. Kim, K. Fukuda, and S. H. N. Lim, Solid State Commun. **140**, 225 (2006).
[31] D. Gu, C. Zhang, Y.-K. Wu, and L. J. Guo, ACS Nano **8**, 10343 (2014).
[32] V. J. Logeeswaran, N. P. Kobayashi, M. S. Islam, W. Wu, P. Chaturvedi, N. X. Fang, S. Y. Wang, and R. S. Williams, Nano Lett. **9**, 178 (2009).
[33] H. Liu, B. Wang, E. S. P. Leong, P. Yang, Y. Zong, G. Si, J. Teng, and S. A. Maier, ACS Nano **4**, 3139 (2010).
[34] C. Furgeaud, L. Simonot, A. Michel, C. Mastail, and G. Abadias, Acta Mater. **159**, 286 (2018).
[35] J. Bulír, M. Novotný, A. Lynnykova, J. Lančok, M. Bodnár, and M. Škereň, Proc. SPIE **7766**, 77660Q (2010).
[36] G. Zhao *et al.*, Nat. Commun. **6**, 8830 (2015).
[37] W. Wang *et al.*, Adv. Funct. Mater. **24**, 1551 (2014).
[38] J. M. Riveiro, P. S. Normile, J. P. Andrés, J. A. González, J. A. De Toro, T. Muñoz, and P. Muñiz, Appl. Phys. Lett. **89**, 201902 (2006).
[39] A. J. Birnbaum, C. V. Thompson, J. C. Steuben, A. P. Iliopoulos, and J. G. Michopoulos, Appl. Phys. Lett. **111**, 163107 (2017).
[40] J. Bulíř, M. Novotný, J. Lančok, L. Fekete, J. Drahokoupil, and J. Musil, Surf. Coatings Technol. **228**, S86 (2013).
[41] R. H. H. Ko, A. Khalatpour, J. K. D. Clark, and N. P. Kherani, APL Mater. **6**, 121112 (2018).
[42] A. Jamnig *et al.*, ACS Appl. Nano Mater. **3**, 4728 (2020).
[43] J. Yun *et al.*, Nanoscale **12**, 1749 (2020).
[44] J. F. Pierson, D. Wiederkehr, and A. Billard, Thin Solid Films **478**, 196 (2005).
[45] M. Kawamura, Y. Abe, and K. Sasaki, Thin Solid Films **515**, 540 (2006).
[46] R. N. Carter, M. J. Murphy, and A. Hodgson, Surf. Sci. **387**, 102 (1997).
[47] C. M. Herzinger, B. Johs, W. A. McGahan, J. A. Woollam, and W. Paulson, J. Appl. Phys. **83**, 3323 (1998).
[48] C. M. Herzinger, B. Johs, W. A. McGahan, and W. Paulson, Thin Solid Films **313–314**, 281 (1998).
[49] T. W. H. Oates and A. Mücklich, Nanotechnology **16**, 2606 (2005).
[50] T. W. H. Oates, H. Wormeester, and H. Arwin, Prog. Surf. Sci. **86**, 328 (2011).
[51] F. Wooten, *Optical Properties of Solids*, 1st ed. (Academic, New York, 1972).
[52] C. A. Schneider, W. S. Rasband, and K. W. Eliceiri, Nat. Methods **9**, 671 (2012).
[53] B. Lü, L. Souqui, V. Elofsson, and K. Sarakinos, Appl. Phys. Lett. **111**, 084101 (2017).
[54] B. Lü, V. Elofsson, E. P. Münger, and K. Sarakinos, Appl. Phys. Lett. **105**, 163107 (2014).
[55] V. Elofsson, B. Lü, D. Magnfält, E. P. Münger, and K. Sarakinos, J. Appl. Phys. **116**, 044302 (2014).
[56] P. Patsalas and S. Logothetidis, J. Appl. Phys. **93**, 989 (2003).
[57] A. M. James and M. P. Lord, *MacMillan's Chemical and Physical Data, Illustrate* (Macmillan, London, 1992).
[58] A. Jamnig, N. Pliatsikas, K. Sarakinos, and G. Abadias, J. Appl. Phys. **127**, 045302 (2020).
[59] A. Jamnig, D. G. Sangiovanni, G. Abadias, and K. Sarakinos, Sci. Rep. **9**, 6640 (2019).
[60] P. Scherrer, *Kolloidchem. Ein Lehrb.* (Springer, Berlin, 1912), pp. 387–409.
[61] A. L. Patterson, Phys. Rev. **56**, 978 (1939).
[62] J. M. Warrender and M. J. Aziz, Phys. Rev. B **76**, 045414 (2007).
[63] P. Jensen, Rev. Mod. Phys. **71**, 1695 (1999).
[64] J. Carrey and J.-L. Maurice, Phys. Rev. B **63**, 245408 (2001).
[65] J. Carrey and J.-L. Maurice, Phys. Rev. B **65**, 205401 (2002).
[66] B. Lü, E. P. Münger, and K. Sarakinos, J. Appl. Phys. **117**, 134304 (2015).
[67] D. McDougall, H. Hattab, M. T. Hershberger, M. Hupalo, M. Horn von Hoegen, P. A. Thiel, and M. C. Tringides, Carbon N. Y. **108**, 283 (2016).
[68] D. S. Jensen, S. S. Kanyal, N. Madaan, M. A. Vail, A. E. Dadson, M. H. Engelhard, and M. R. Linford, Surf. Sci. Spectra **20**, 36 (2013).
[69] J. F. Weaver and G. B. Hoflund, J. Phys. Chem. **98**, 8519 (1994).
[70] T. C. Kaspar, T. Droubay, S. A. Chambers, and P. S. Bagus, J. Phys. Chem. C **114**, 21562 (2010).
[71] A. G. Shard, Surf. Interface Anal. **46**, 175 (2014).
[72] A. R. Layson and P. A. Thiel, Surf. Sci. **472**, L151 (2001).
[73] Y.-R. Luo, *Comprehensive Handbook of Chemical Bond Energies*, 1st ed. (CRC, Boca Raton, 2007).
[74] A. R. Layson, J. W. Evans, and P. A. Thiel, Phys. Rev. B **65**, 193409 (2002).
[75] A. R. Layson, J. W. Evans, V. Fournée, and P. A. Thiel, J. Chem. Phys. **118**, 6467 (2003).
[76] J. S. Ozcomert, W. W. Pai, N. C. Bartelt, and J. E. Reutt-Robey, Phys. Rev. Lett. **72**, 258 (1994).
[77] N. Combe, P. Jensen, and A. Pimpinelli, Phys. Rev. Lett. **85**, 110 (2000).
[78] G. Zhao, E. Jeong, E.-A. Choi, S. M. Yu, J.-S. Bae, S.-G. Lee, S. Z. Han, G.-H. Lee, and J. Yun, Appl. Surf. Sci. **510**, 145515 (2020).

Paper V

On the effect of copper as wetting agent during growth of thin silver films on silicon dioxide substrates

A. Jamnig[1,2], N. Pliatiskas[1], G. Abadias[2], and K. Sarakinos[1,*]

*Corresponding author

[1]Nanoscale Engineering Division, Department of Physics, Chemistry, and Biology, Linköping University, SE 581 83, Linköping, Sweden

[2]Institut Pprime, Département Physique et Mécanique des Matériaux, UPR 3346 CNRS, Université de Poitiers, 11 Bvd M. et P. Curie, TSA 41123, F86073 Poitiers Cedex 9, France

(Submitted)

On the effect of copper as wetting agent during growth of thin silver films on silicon dioxide substrates

A. Jamnig[1,2], N. Pliatiskas[1], G. Abadias[2], and K. Sarakinos[1,*]
*Corresponding author, email: kostas.sarakinos@liu.se
[1]Nanoscale Engineering Division, Department of Physics, Chemistry, and Biology, Linköping University, SE 581 83, Linköping, Sweden
[2]Institut Pprime, Département Physique et Mécanique des Matériaux, UPR 3346 CNRS, Université de Poitiers, 11 Bvd M. et P. Curie, TSA 41123, F86073 Poitiers Cedex 9, France

Abstract

We study the effect of Cu incorporation on the morphological evolution and the optoelectronic properties of thin Ag films deposited by magnetron sputtering on weakly-interacting SiO_2 substrates. *In situ* and real time spectroscopic ellipsometry data show that by adding up to $4\,at.\%$ Cu throughout the entire film deposition process, wetting of the substrate by the metal layer is promoted, as evidenced by a decrease of the thickness at which the film becomes continuous from $19.5\,nm$ (pure Ag) to $15\,nm$ ($Ag_{96}Cu_4$). The *in situ* data are consistent with *ex situ* x-ray reflectometry analyses which show that Cu-containing films exhibit a root mean square roughness of $1.3\,nm$ compared to the value $1.8\,nm$ for pure Ag films, i.e., Cu leads to smoother film surfaces. These morphological changes are coupled with an increase in continuous-layer electrical resistivity from $1.0 \times 10^{-5}\,\Omega cm$ (Ag) to $1.25 \times 10^{-5}\,\Omega cm$ ($Ag_{96}Cu_4$). Scanning electron microscopic studies of discontinuous layers reveal that the presence of Cu at the film growth front promotes smooth surfaces (as compared to pure Ag films) by hindering the rate of island coalescence. To further understand the effect of Cu on film growth and electrical properties, in a second set of experiments, we deploy Cu with high temporal precision to target specific film-formation stages. The results show that longer presence of Cu in the vapor flux and the film growth front promote flat morphology. However, both a flat surface and a continuous-layer electrical resistivity that is equal to that of pure Ag films can only be achieved when Cu is deployed during the first $2.4\,nm$ of film deposition, during which morphological evolution is, primarily, governed by island coalescence. Our overall results highlight potential pathways for fabricating high-quality multifunctional metal contacts in a wide range of optoelectronic devices based on weakly-interacting oxides and van der Waals materials.

Keywords

Silver, thin films, weakly-interacting substrates, growth manipulation, *in situ* growth monitoring, island coalescence

1. INTRODUCTION

Thin noble-metal films deposited from the vapor phase on weakly-interacting oxides and van der Waals materials exhibit a pronounced and uncontrolled three-dimensional (3D) morphology.[1, 2] This is a major obstacle toward fabricating high-quality metal contacts and functional layers in a wide array of nanoelectronic,[3–6] energy-saving, and energy-conversion devices;[7–10] which necessitates the development of methodologies for controllably influencing film growth and achieving two-dimensional (2D) morphology, so that the metal layer wets uniformly the underlying substrate.

Vapor-based thin film deposition is typically characterized by high supersaturation ratios at the vapor/solid interface, which yield a large driving force for condensation, and thereby, lead to far-from-equilibrium growth. As such, film morphological evolution is primarily governed by kinetic rates of atomic-scale mechanisms (e.g., adatom diffusion, corner-crossing, step edge-crossing) that affect the key initial formation stages of island nucleation, growth, and coalescence.[11,12] Variation of the most common deposition process parameters, including substrate temperature and deposition rate, has been routinely used to modify growth kinetics and the resulting film morphology.[13] This strategy is, however, not effective for selectively targeting film-formation stages and processes, so that growth can be manipulated in an efficient manner.

Selective manipulation of structure-forming processes to promote 2D growth morphology has been demonstrated for epitaxial metal-on-metal [14–18] and semiconductor-on-semiconductor systems,[19,20] via deployment of minority metal and gaseous species (also referred to as surfactants) at the film surface. Concurrently, the atomistic mechanisms that control morphological evolution in weakly-interacting film/substrate systems are different than those in classical epitaxial growth theory,[12,21,22] such that conventional surfactant-based strategies are not directly applicable for manipulating growth of noble-metal films on oxides and van der Waals materials. Despite the latter, there are studies in which less-noble metal (e.g., Nb, Ti, Cr) [4,23,24] and gaseous species (e.g., N_2, O_2) [8–10,25,26] have been shown to suppress the tendency of Ag and Cu films to grow in a 3D fashion on various oxide substrates. This, however, comes at cost of affecting other metal-layer physical properties (e.g., conductivity); [8,10,25,27] which underscores the need to establish a fundamental understanding of the effect of surfactant (i.e., minority) species at various stages of thin noble-metal film growth on weakly-interacting substrates, in order to develop efficient and non-invasive morphology manipulation strategies.

We have recently contributed to the afore-mentioned understanding by sputter-depositing Ag films on SiO_2 substrates in mixed Ar-N_2 and Ar-O_2 gas atmospheres.[27,28] Our data showed that the presence of both N_2 and O_2 in the sputtering gas promotes 2D growth by decreasing the rates of island coalescence completion, while N_2 and O_2 are only incorporated in the film in trace amounts. Based on these insights, we demonstrated that morphology can be manipulated from 3D to 2D, without compromising the Ag layer electrical conductivity, if N_2 and O_2 are deployed with high temporal precision to selectively target the initial stages of island nucleation, growth, and coalescence.

In the present study, we explore the viability of the growth manipulation approach introduced in our recent works [27,28] using less-noble metals, instead of gaseous species, for promoting 2D morphology during deposition of Ag on SiO_2. We choose Cu as wetting agent, since it exhibits a less pronounced tendency for 3D growth than Ag,[13] and it is relatively insensitive (i.e., inert) to interaction with impurities and the substrate material, compared to other metals (e.g., Al and group 4, 5, and 6 transition metals) that have been used in the literature for promoting 2D growth morphology.[25,29] Moreover, Cu is immiscible to Ag,[30–32] which allows to selectively study its effect on surface growth kinetics without modifying the intrinsic bulk chemistry of the metal layer.

We monitor the evolution of the optoelectronic properties of percolated films *in situ* and in real time, and show that by increasing the Cu content in the metal layer up to $4\ at.\%$ the thickness at which the film becomes continuous decreases from $19.5\ nm$ (pure Ag) to $15.0\ nm$ ($Ag_{96}Cu_4$), while further increase of the Cu content up to $13\ at.\%$ does not have an appreciable effect on the value of the continuous film formation thickness. The *in situ* analysis is complemented by *ex situ* film characterization, which shows that Cu leads to flatter film morphologies—the film surface roughness decreases from 1.8 to $1.3\ nm$ upon increasing Cu content from 0 to $4\ at.\%$—i.e., 2D growth is promoted. Concurrently, the presence of Cu in the metal layer causes the film resistivity to increase monotonously from $1.0 \times 10^{-5}\ \Omega cm$ (pure Ag) to $1.25 \times 10^{-5}\ \Omega cm$ ($Ag_{96}Cu_4$) and $1.8 \times 10^{-5}\ \Omega cm$ ($Ag_{87}Cu_{13}$). Additional *ex situ* analyses of morphology of discontinuous films reveals that the decrease of the continuous-layer roughness with Cu addition has its origin in the initial film growth stages, whereby the presence of Cu delays reshaping of coalescing island clusters and promotes in-plane island growth.

To gain a better understanding of the effect of Cu on the overall film morphological evolution and electrical properties, we introduce Cu in the vapor flux during well-defined times. We find that the thickness of continuous film formation decreases with increasing time during which Cu is present in the deposition flux. However, by deploying Cu at the film growth front only during the first $20\ s$ of deposition—corresponding to a nominal film thickness of $2.4\ nm$ at which growth is primarily controlled by island coalescence—2D morphology can be promoted without compromising the metal-layer electrical conductivity. These findings, along with our previous results on the effect of N_2 [27] and O_2 [28] on Ag morphological evolution on SiO_2, pave the way toward a holistic platform for manipulating growth of noble-metal layers on weakly-interacting substrates in an efficient and non-invasive fashion.

2. FILM GROWTH AND CHARACTERIZATION

Thin films are synthesized by pulsed magnetron sputtering in an ultra-high vacuum (UHV) chamber (base pressure $\sim 10^{-8}\,Pa$) on Si(100) substrates (thickness $525\,\mu m$), which are covered with $\sim 530\,nm$ thermally grown SiO2 layer. Experiments are performed using spatially separated magnetron sources equipped with elemental Ag and Cu targets (purity $99.99\,at.\%$, diameter $76\,mm$, thickness $6\,mm$), which are placed $7.5\,cm$ away from the substrate at an angle of $45°$ with respect to the substrate normal. Ar is used as working gas at a pressure of $1.3\,Pa$. Power is applied to the magnetrons in the form of unipolar square voltage pulses with a width of $50\,\mu s$ and a frequency of $1\,kHz$, using MELEC SPIK 3000A pulsing units fed by ADL GS30 DC Power Supplies. A voltage pulse amplitude of $V_T^{Ag} = 485\,V$ is used for operating the Ag-equipped magnetron, while V_T^{Cu} is altered from 225 to $400\,V$, in order to vary the Ag-to-Cu vapor arrival ratio on the substrate and the Cu content in the film. Moreover, the V_T^{Ag} signal is used to trigger the pulsing unit supplying power to the Cu-equipped magnetron, such that the voltage pulses on both magnetrons are synchronous. To investigate the effect of Cu addition on different film growth stages, three deposition schemes are employed: (i) co-deposition of Ag and Cu throughout all film formation stages; (ii) co-deposition for a total time t_E during which the film growth front is exposed to Cu vapor flux, followed by deposition of pure Ag until growth completion; and (iii) initial deposition of pure Ag until power is applied to the Cu target after delay time t_D, so that growth is completed in the presence of both Ag and Cu vapor fluxes. Between each deposition run, the targets are sputter-cleaned for $10\,min$ to eliminate cross-contamination of the magnetron sources.

Film growth is monitored *in situ* and in real time using a M-88 spectroscopic ellipsometer (J.A. Woollam Inc.). Ellipsometric angles Ψ and Δ are acquired at a rate of $0.5\,s^{-1}$, at an incidence angle of $\sim 70°$ with respect to the substrate normal, and incident-light photon energies between 1.6 and $3.2\,eV$. The optical response of the substrate is measured and modelled prior to film growth as Si substrate, covered with a SiO2 layer with its thickness ($\sim 530\,nm$) as fitting parameter. Reference data for Si and SiO2 are taken from Herzinger *et al.*[33]

The optical response of percolated and continuous metal layers is described by the Drude free-electron model,[34] according to which the complex dielectric function $\tilde{\varepsilon}_D(\omega)$ reads

$$\tilde{\varepsilon}_D(\omega) = \varepsilon_\infty - \frac{\omega_p^2}{\omega^2 + i\Gamma_D\omega}. \qquad (1)$$

In Eq. (2), the parameter ε_∞ accounts for interband transitions occurring at higher values of ω than measured with the ellipsometer, Γ_D is the free-electron damping rate, and ω_p is the free-electron plasma frequency. From these fitting parameters, the electron scattering time $\tau = \hbar/\Gamma_D$ and the room-temperature resistivity $\rho = \Gamma_D/(\varepsilon_0\omega_p^2)$ can be calculated, where ε_0 is the vacuum permittivity.

An additional fitting parameter in the analysis of the ellipsometric data is the film height h_f, from which we extract the film deposition rate F by calculating the steady-state slope of h_f vs. deposition time t curves ($F = 0.120\ nm/s$ for Ag; $F = 0.120$ to $0.136\ nm/s$ for Ag-Cu films in the V_T^{Cu} range 225 to $400\ V$). Based on F, we then calculate the nominal film thickness $\Theta = Ft$, which represents the number of deposited atoms at each stage of film growth.

Ellipsometric measurements are complemented by *ex situ* chemical, morphological, and structural analyses. Prior to removal from the deposition chamber, all samples that are used for *ex situ* characterization are capped with $3\,nm$ thick layer of amorphous carbon (a-C), to avoid contamination and changes of the surface morphology upon atmospheric exposure. The capping layer is deposited by direct current magnetron sputtering from an elemental graphite target (purity $99.99\,at.\%$, diameter $76\,mm$, thickness $6\,mm$), by applying a constant voltage of $460\,V$ at an Ar working pressure of $1.3\,Pa$. The magnetron is placed $7.5\,cm$ away from the substrate at an angle of $45°$ with respect to the substrate normal.

Film thickness, mass density, and a-C/metal-layer interface roughness in a-C/Ag-Cu/SiO$_2$/Si stacks are determined from x-ray reflectometry (XRR), performed in a Panalytical X'pert Pro diffractometer, equipped with a copper K$_\alpha$ source (wavelength $0.15418\,nm$) in line focus (operated with $45\,kV$ and $40\,mA$), where a parallel beam mirror and a parallel-plate collimator are used in the incident and the reflected beam path, respectively. The reflected x-ray signal is processed with a X'Celerator/PIXcel-3D detector (Malvern Panalytical) operated in scanning line mode.

The crystal structure of Ag and Ag-Cu films is studied by x-ray diffractometry (XRD) in $\theta - 2\theta$ geometry, performed in the same instrument as the one used for XRR measurements. A nickel filter is used for removing copper K$_\beta$ radiation. For crystallographic analysis, the texture coefficient $TC(hkl) = \left(I_{hkl}/I_{0,hkl}\right)/\left(\frac{1}{N}\sum_N I_{hkl}/I_{0,hkl}\right)$ is calculated, where I_{hkl} is the experimentally recorded diffraction intensity of (hkl) planes, $I_{0,hkl}$ are the corresponding (hkl) intensities in reference Ag powder diffraction pattern,[35] and N is the number of diffraction peaks used for calculating the texture coefficient.

Film morphology is studied by scanning electron microscopy (SEM) performed in a LEO 1550 Gemini microscope, with $5\,kV$ acceleration voltage, and $3\,mm$ working distance utilizing the InLens detector. The ImageJ software package[36] is used to quantify island number densities, size distribution, and shape, as well as substrate area coverage, by analyzing SEM images of a series of non-continuous films with $\Theta = 2.4, 3.6,$ and $6.0\,nm$.

The Ag-to-Cu ratio is determined by performing energy-dispersive x-ray spectroscopy (EDS) measurements on $200\,nm$ thick AgCu films, in the same instrument as the SEM analysis, with $20\,kV$ acceleration voltage and $8.5\,mm$ working distance. Additional chemical composition analyses, including bonding configuration and spatial distribution of Cu in layers grown at various V_T^{Cu} values, are carried out by means of x-ray photoelectron spectroscopy (XPS) measurements on $25.0\,nm$ thick Ag-Cu films. Photoelectron spectra are collected using a Kratos AXIS Ultra DLD UHV system (base pressure $\sim 4 \times 10^{-8}\,Pa$). Emission of photoelectrons is triggered by monochromated aluminum K$_\alpha$ x-rays, and their energies and intensities are measured using a hemispherical sector analyzer and a multichannel detector, in which core-level spectra are recorded with a $20\,eV$ pass energy. Depth compositional profiles are acquired by etching the surface with a $4\,keV$ Ar$^+$ ion beam, and ion-induced charging of the sample is corrected with respect to the Ar-*2p* peak, to account for shifts in the binding energy. Elemental analysis is performed with the Kratos Vision software and its sensitivity factor database.

3. RESULTS AND DISCUSSION

3.1 CONTINUOUS FILM MORPHOLOGY, CHEMISTRY AND MICROSTRUCTURE

Figure 1 presents the evolution of room-temperature resistivity ρ vs. nominal film thickness Θ for Ag$_{100-x}$Cu$_x$ films in the x range 0 to $13\ at.\%$. For all ρ vs. Θ curves, ρ decreases initially by approximately an order of magnitude, after which decrease a steady-state resistivity ρ^{SS} is reached. The initial drop in resistivity indicates that the film is percolated (i.e., interconnected array of islands exists over the entire sample area), and the Θ value for which ρ^{SS} is reached corresponds to the continuous film formation thickness Θ_{cont}.[37]

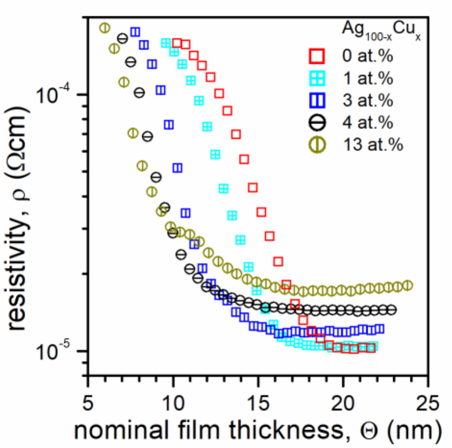

Figure 1: Resistivity (ρ) vs. nominal thickness (Θ) curves extracted from in situ, real-time spectroscopic ellipsometry measurements, of magnetron-sputter-deposited Ag and Ag$_{100-x}$Cu$_x$ layers on SiO$_2$/Si substrates with increasing Cu content x in the film.

The data show that the increase of Cu content from 0 to $13\ at.\%$ results in a decrease of Θ_{cont} from 19.5 to $15.0\,nm$ (i.e., a decrease by 23%). This indicates that Cu promotes wetting and 2D growth morphology. Concurrently, Cu incorporation leads to increase of resistivity from 1.0×10^{-5} to $1.8 \times 10^{-5}\,\Omega cm$. This can be attributed to the larger room-temperature resistivity/shorter electron scattering time of bulk Cu ($1.678\,\mu\Omega cm$ / $36.0\,fs$), compared to bulk Ag ($1.587\,\mu\Omega cm$ / $36.8\,fs$).[38,39] To better illustrate the effect of Cu on film morphology, we plot in Fig. 2(a) Θ_{cont} vs. x extracted from multiple sets of data similar to those in Fig. 1. Θ_{cont} decreases sharply from 19.5 to $15.0\,nm$ in x range 0 to $4\ at.\%$ after which it saturates. An additional effect of the alloying with Cu is a linear increase in ρ^{SS} vs. x, which is presented in Fig. 2(b).

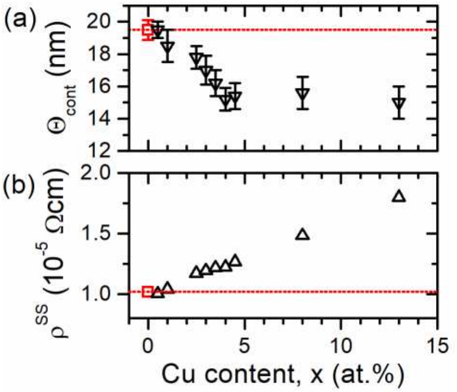

Figure 2: Evolution of (a) the continuous film formation thickness Θ_{cont}, (b) steady-state resistivity ρ^{SS} of $Ag_{100-x}Cu_x$ films with increasing Cu content x in the film. Error bars correspond to the standard error from determining Θ_{cont} from resistivity vs. thickness plots presented in Fig. 1. The dotted lines represent the respective reference values for pure Ag films.

Based on the trends shown in Figs. 1 and 2(a), the remainder of the manuscript focuses on detailed comparison among Ag and $Ag_{96}Cu_4$ layers by employing *ex situ* techniques to study their morphology, microstructure, and bonding properties. Figure 3 presents XRR data recorded from a-C/$Ag_{100-x}Cu_x$/SiO_2/Si stacks with $x = 0$ and $4\ at.\%$, in which we have adjusted the metal-layer deposition time to obtain a nominal thickness of $\Theta = 30\ nm$. Experimental data are represented by symbols, while calculated reflectivity curves, fitted to the measured data, are drawn as solid lines. From the fit we find that Ag and $Ag_{96}Cu_4$ layers have thicknesses (heights) $h_f = 29.1$ and $29.9\ nm$, respectively, which confirms the deposition rate established from spectroscopic ellipsometry.

Furthermore, we see that both films have a mass density $\rho_m = 10.16\ g/cm^3$, which is close to the bulk density of Ag (i.e., $10.49\ g/cm^3$).[40] The latter is consistent with the *in situ* data in Fig. 1, showing that, for all Cu contents, the metal layers are continuous for $\Theta > 19\ nm$. Moreover, the Cu-containing film exhibits a smaller a-C/metal-layer interface root-mean-square roughness ($w_{a-C/Ag96Cu4} = 1.3\ nm$) compared to the pure Ag film ($w_{a-C/Ag} = 1.8\ nm$), which is consistent with the conclusion from Figs 1 and 2(a) that addition of Cu promotes 2D growth morphology and flatter film surfaces.

X-ray diffractograms of $50\ nm$ thick Ag and $Ag_{96}Cu_4$ films are presented in Fig. 4, where the positions of diffraction peaks of unstrained Ag[35], Cu[41] and Si(001)[42] are indicated by vertical lines in the graph. Both films have the face-centered cubic crystal structure of Ag, as evidenced by the

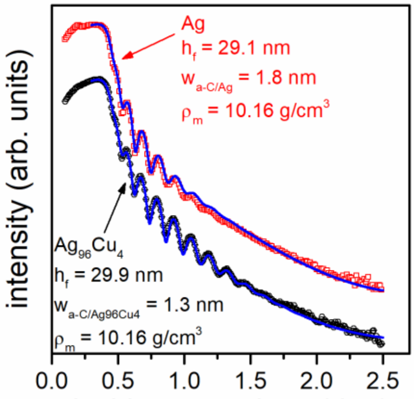

Figure 3: X-ray reflectivity measurements of a-C/Ag/SiO_2/Si (red symbols) and a-C/$Ag_{96}Cu_4$/SiO_2/Si stacks (black symbols). The solid lines represent calculated reflectivity curves for fitting each data set, from which the metal-layer thickness h_f, mass density ρ_m, and a-C/Ag-Cu interface roughness ($w_{a-C/Ag}$ and $w_{a-C/Ag96Cu4}$) are determined .

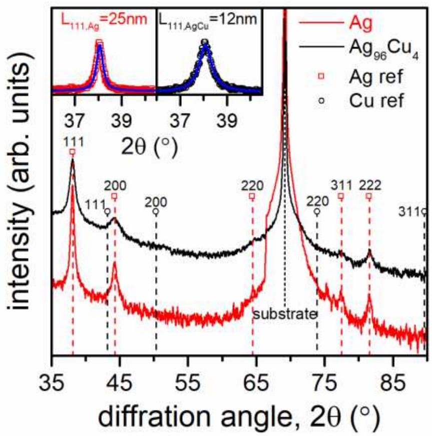

Figure 4: X-ray diffractograms of $50\ nm$ thick Ag and $Ag_{96}Cu_4$ films deposited on SiO_2/Si substrates. Peak positions of unstrained Ag[35], Cu[41] and Si[42] are indicated by vertical lines. The inserts show the (111) peak of Ag (left) and $Ag_{96}Cu_4$ (right) after baseline correction (symbols), and the Pseudo Voigt model fitted to the experimental data (lines). From the fit, the peak full width at half maximum, and thereby, the out-of-plane crystallite size L_{111} are determined.

presence of diffraction peaks corresponding to the (111), (200), (220), (311), and (222) crystallographic planes in the measured $\theta - 2\theta$ range. Texture analysis of the five observed diffraction peaks shows that $TC(111) = 2.1$ and 2.2 for Ag and AgCu films, respectively, indicating that both films exhibit a strong 111 crystallographic texture, which does not change by Cu addition. Moreover, no indication of formation of crystalline Cu domains that are detectable with XRD can be found in the $Ag_{96}Cu_4$ diffractogram.

The inserts in Fig. 4 show the (111) XRD lines of both films after base line correction (symbols), with solid lines corresponding to the best-fit of the experimental data using the Pseudo-Voigt function.[43,44] From the fit, we determine full-width at half-maximum (FWHM) values of $\sim 0.33°$ and $\sim 0.66°$ for Ag and $Ag_{96}Cu_4$, respectively. Applying Scherrer's equation,[45] we calculate the out-of-plane size L_{111} of coherently diffracting domains in the film (i.e., crystallite size), which approximates the average grain size. Crystallites in the $Ag_{96}Cu_4$ film ($L_{111,AgCu} \cong 12\ nm$) are smaller than in Ag ($L_{111,Ag} \cong 25\ nm$); smaller grain sizes imply a larger grain boundary number density in the film, which favors charge-carrier scattering. Hence, the analysis presented in Fig. 4, in combination with the smaller bulk conductivity of Cu vs. Ag,[38,39] is consistent with the larger resistivity in continuous $Ag_{96}Cu_4$ films compared to Ag (see Fig. 2(b)).

The results of XPS analyses, performed on an a-C/$Ag_{96}Cu_4$/SiO_2/Si stack (metal layer thickness $25\ nm$), are presented in Fig. 5. High-resolution core-level Ag-*3d* and Cu-*2p* scans recorded for the as-received stack and after etching of 2, 6, 14 and $24\ nm$ of the stack surface are plotted in Figs. 5(a) and (b), respectively. Ag-*3d* data reveal the presence of the two doublets (*3/2* and *5/2*) at the expected positions (374.2 and $368.2\ eV$, respectively) [46] for Ag-Ag bonds. The peaks are symmetric, which means that no chemical interaction of Ag with Cu or other elements takes place. Cu-*2p* data in Fig. 5(b) show well defined Cu peaks (Cu-$2p_{1/2}$ at $952.5\ eV$ and Cu-$2p_{3/2}$ at $933\ eV$) [47,48] corresponding to Cu-Cu bonds for all spectra. Concurrently the as-received scan shows clear peaks that correspond to Cu-O ($933.6\ eV$) and Cu-OH ($934.8\ eV$) [47]—as well as Cu-O satellite peaks—which can be attributed to contamination upon atmospheric exposure. Similarly, the scan after $24\,nm$ etching shows a shoulder in the Cu-2p$_{3/2}$ peak that matches the position of Cu-O and Cu-OH bonds, which can be contributed to the interaction of Cu with the SiO$_2$ substrate.

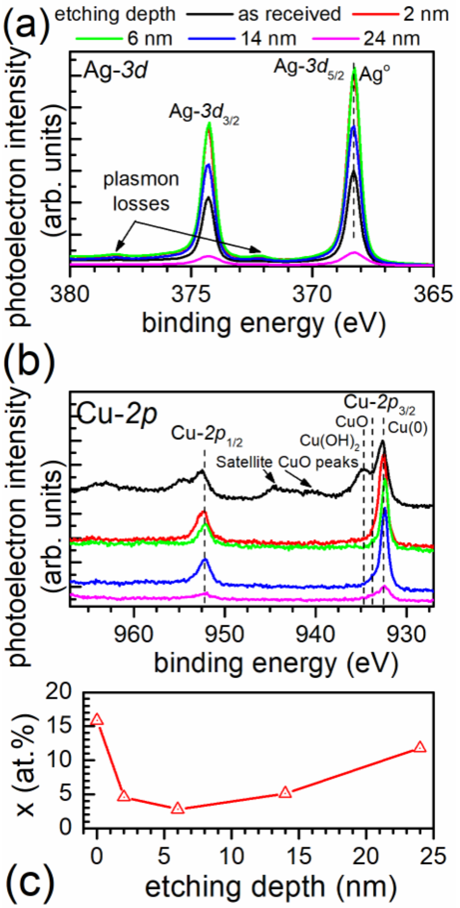

Figure 5: (a) Ag-3d and (b) Cu-2p core level high resolution x-ray photoelectron spectra of a-C-capped $25\,nm$ thick Ag$_{96}$Cu$_4$ thin films in the as-received state and after ion-beam etching of 2, 6, 14 and $24\,nm$. Ag plasmon loss peaks and positions for Cu-O binding states, as well as satellite peak positions are indicated. (c) Evolution of the atomic concentration x of Cu in the Ag$_{96}$Cu$_4$ film as function of ion-etching depth.

Figure 5(c) presents the evolution of the Cu atomic concentration x as function of the etching depth. Cu is detected throughout the film thickness, however, we find higher concentration of Cu close to the surface ($x = 16\,at.\%$) and toward the SiO$_2$ substrate ($x = 12\,at.\%$), as compared to intermediate etching depths (i.e., $2\,nm$ to $14\,nm$), where $x \cong 5\,at.\%$. As Ag and Cu arrival rates are constant during the deposition process, the data in Fig. 5(c) indicate Cu segregation toward the SiO$_2$ substrate and the surface layer. Similar compositional profiles have been reported for the miscible Ag-Al system by Zhang *et al.*,[29] who observed that Al segregates toward the film surface due to its tendency to form as aluminum-oxide. The latter may also explain the behavior of Cu which exhibits higher affinity toward oxygen as compared to Ag.[49] Another factor is the immiscibility of the Ag-Cu binary system which provides an additional driving force for phase separation.[31,32]

3.2 GROWTH MECHANISMS AND ATOMIC-SCALE PROCESSES

To correlate the structural and morphological features of continuous metal layers established in Section 3.1 with initial film formation stages, we perform SEM analyses on a-C/Ag$_{100-x}$Cu$_x$/SiO$_2$/Si stacks ($x = 0$ and $4\,at.\%$) in which the metal layers have nominal thicknesses $\Theta = 2.4$, 3.6, and $6.0\,nm$. SEM images for pure Ag films ($x = 0$) are presented in Fig. 6(a) through (c). At $\Theta = 2.4nm$, the surface hosts isolated spherical

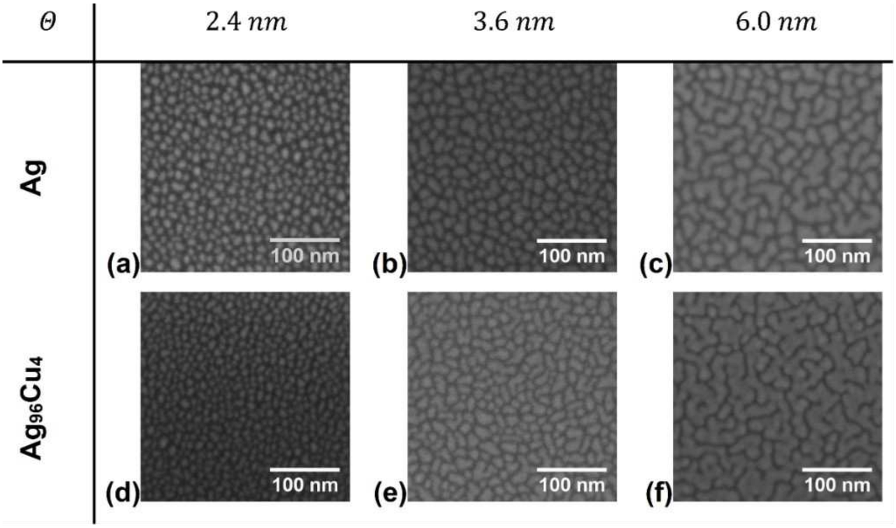

Figure 6: Scanning electron microscopy images of Ag ((a), (b), (c)) and $Ag_{96}Cu_4$ films ((d), (e), (f)) with nominal thicknesses $2.4\ nm$ ((a),(d)), $3.6\ nm$ ((b), (e)), and $6.0\ nm$ ((c), (f)).

islands/clusters, the size of which increases when increasing Θ to 3.6 and $6.0\ nm$. The size increase of islands/clusters with increasing Θ is accompanied by a gradual transition from spherical to more elongated shapes. This type of morphological evolution is typical in weakly-interacting film/substrate systems. Nanometer-size islands at the initial growth stages exhibit relatively short coalescence completion times (t_{coal}) so that, upon impingement, material is redistributed rapidly over the coalescing cluster and equilibrium shape (i.e., hemisphere) is re-established. With continued vapor deposition and coalescence completion events, the island size increases and eventually t_{coal} becomes longer than the time between successive island impingement events (t_{imp}). When the condition $t_{coal} > t_{imp}$ is fulfilled, coalescence is not completed (i.e., the island equilibrium shape is not retained), and the film surface is predominately populated by elongated clusters.[12,13,37,50,51]

Addition of Cu does not change the overall morphological evolution (see Figs. 6(d) through (f)). However, islands are more elongated at $\Theta = 3.6\ nm$ as compared to pure Ag films, while at $\Theta = 6.0\ nm$, the $Ag_{96}Cu_4$ film covers a larger fraction of the substrate, and is percolated. These findings indicate that Cu addition hinders material redistribution during coalescence (i.e., t_{coal} becomes longer), which promotes in-plane vs. out-of-plane island growth at the early stages of film formation, and ultimately, yields a decrease in continuous formation thickness and smaller surface roughness, as shown in Figs. 1 through 3. The slower material redistribution during coalescence may be attributed to solute drag, i.e., the decrease of grain boundary diffusivity due to the presence of Cu in the Ag lattice,[52–54] resulting in incompletely coalesced islands with elongated shapes.

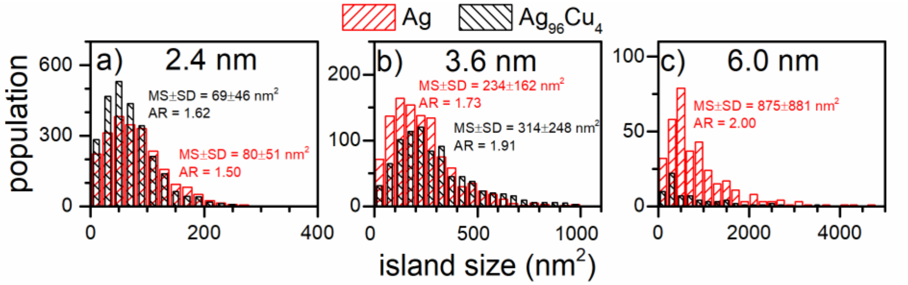

Figure 7: Island/cluster size distributions for non-continuous Ag and $Ag_{96}Cu_4$ films with nominal thicknesses of (a) $2.4\ nm$, (b) $3.6\ nm$ and (c) $6.0\ nm$. Mean islands size (MS), standard deviation (SD), and mean aspect ratio (AR) of islands are given for films that consist mainly of isolated islands. In (c) island sizes $> 5000\ nm^2$ are not presented for Ag (one island with $10\,000\ nm^2$) and $Ag_{96}Cu_4$ films (eight islands ranging $7\,000$ to $22\,000\ nm^2$, one island with $180\,000\ nm^2$). Data are obtained by analyzing scanning electron micrographs with an area of $850 \times 550\ nm^2$.

To quantify the trends observed in Fig. 6, we analyze SEM data to extract the evolution of the island size distribution for Ag and $Ag_{96}Cu_4$ films for nominal film thicknesses $\Theta = 2.4$, 3.6, and $6.0\ nm$, and we determine mean island size (MS) and standard deviation (SD). For island shape analysis, islands are approximated by ellipses, and the aspect ratio (AR), i.e., the ratio of major to minor ellipse axis, is calculated. The results are presented in Fig. 7, whereby the data presented therein are obtained from images with smaller magnification than those presented in Fig. 6 for better statistics.

Figure 7(a) displays data for both films with $\Theta = 2.4\ nm$ and shows that the island size distributions are bell-shaped, with the distribution for the $Ag_{96}Cu_4$ film (black bars) shifted toward lower island sizes relative to that for the Ag film (red bars). This is also seen in the $MS \pm SD$ values which are $69 \pm 46\ nm^2$ and $80 \pm 51\ nm^2$ for $Ag_{96}Cu_4$ and Ag films, respectively. Concurrently, the mean in-plane AR of islands is 1.62 for $Ag_{96}Cu_4$, which is higher than the value 1.50 for Ag, indicating that islands are more elongated, and suggests that t_{coal} is increased due to the presence of Cu.

Increasing Θ to $3.6\ nm$ shifts the overall island size distributions to larger values, as seen in Fig. 7(b) and reflected in the $MS \pm SD$ values for the $Ag_{96}Cu_4$ film ($314 \pm 248\ nm^2$) vs. that for Ag ($234 \pm 162\ nm^2$). Moreover, AR values increase compared to $\Theta = 2.4\ nm$, and remain larger for $Ag_{96}Cu_4$ (1.91) than for Ag (1.73), indicating more pronounced in-plane growth of islands.

At $\Theta = 6.0\ nm$, we find $MS \pm SD = 875 \pm 881\ nm^2$ for Ag, with $AR = 2.00$ (see Fig. 7(c)). The comparatively large value of SD shows that island sizes do not follow normal distribution and is consistent with the formation of large structures on the surface seen in Fig.6(c). For the $Ag_{96}Cu_4$ film, few very large islands are detected, that are highly interconnected, including one island with size $\sim 180\,000\ nm^2$ (not represented in Fig. 7(c)), which covers $\sim 40\%$ of the observed substrate surface. This distribution is consistent with the percolated morphology of the $Ag_{96}Cu_4$ film at $\Theta = 6.0\ nm$ in

Fig. 6(f)). From the island size distributions in Fig. 7, we can establish that increasing AR values can be used as indication for incomplete coalescence, which leads to elongated island shapes, and percolated film structures. While, initially, island sizes for $Ag_{96}Cu_4$ are smaller than for Ag, the larger AR values indicate that addition of Cu expedites percolation and favors 2D growth morphology.

The SEM data are further quantified by calculating the substrate area coverage and the number density of islands/clusters as function of the nominal film thickness. The substrate coverage for Ag films (Fig. 8(a)) increases from 39 to 64%, when increasing Θ from 2.4 to $6.0\,nm$. For $Ag_{96}Cu_4$ films, this increase is more pronounced, and the coverage increases from 38 to $70\,\%$ in the same thickness range. This trend confirms that deposition of Cu along with Ag vapor favors in-plane island growth and promotes 2D morphology.

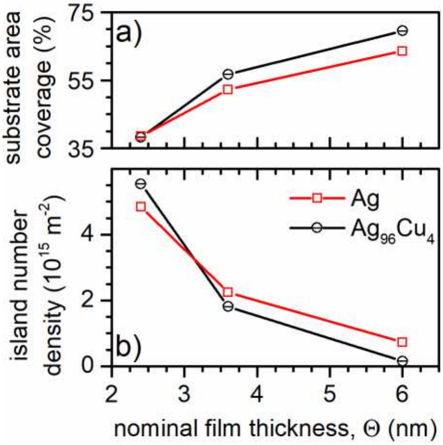

Figure 8: Evolution of (a) coverage and (b) island number density as a function of nominal film thickness of Ag and $Ag_{96}Cu_4$ films. Data obtained by analyzing scanning electron micrographs with an area of $850 \times 550\,nm^2$.

The increase in coverage is accompanied by a decrease in the island/cluster number density, presented in Fig. 8(b), from 4.8×10^{15} to $7 \times 10^{14}\,m^{-2}$ for Ag films. While the island/cluster number density is larger at $\Theta = 2.4\,nm$ when Cu is present during the deposition ($5.5 \times 10^{15}\,m^{-2}$), smaller values than that for Ag films are found for $\Theta \geq 3.6\,nm$ (e.g., $2 \times 10^{14}\,m^{-2}$ for $\Theta = 6.0\,nm$). This may be explained in light of previous studies which have suggested that Cu effectively decreases diffusion length of Ag on SiO_2, thereby increasing nucleation probability and island density.[55] However, simulations by Elofsson *et al.* [37] have estimated that saturation island density (i.e., the point at which island nucleation and growth rates are equal) occurs at $\Theta \cong 0.1\,nm$ for the case of perfectly hemispherical islands, i.e., the morphology established for $\Theta = 2.4\,nm$ in our SEM data is primarily governed by island coalescence. Hence, even though possible influence of Cu on surface diffusion and nucleation dynamics cannot be ruled out, we conclude that the morphological evolution in our films is primarily governed by the effect of Cu on island coalescence; which is consistent with recent studies on growth of Ag on SiO_2 and ZnO in nitrogen- and oxygen-containing gas atmospheres.[25,27, 28,56]

3.3. SELECTIVE COPPER DEPLOYMENT

We showed in Section 3.2 that Cu promotes 2D growth by increasing coalescence completion time, resulting in earlier onset of island interconnectivity. These morphological changes are accompanied by an increase in the electrical resistivity of continuous layers (see Section 3.1). Hence, two additional series of deposition experiments are conducted, aiming to study the effect of Cu on specific stages of the Ag film formation, and gauge the ability of Cu to change growth morphology, without compromising the film electrical properties, when released with high temporal precision: (i) in a first series, Cu is co-deposited with Ag for an exposure time t_E after which Cu supply is stopped and growth continues with Ag vapor until deposition is completed; (ii) in a second series, deposition starts with Ag vapor and Cu vapor is added after a delay time $t_D$until deposition completion. We note that one set of deposition parameters is chosen for both experimental series, corresponding to the instantaneous Ag and Cu arrival rates for which $Ag_{96}Cu_4$ is grown. Hence, the global film composition changes depending on t_E and t_D.

Figure 9(a) presents the evolution of Θ_{cont} with increasing values of t_E. The conditions $t_E = 0\,s$ and $t_E = 180\,s$ correspond to deposition of pure Ag and co-deposition of Ag and Cu yielding a $Ag_{96}Cu_4$ film, respectively, and are marked by horizontal dotted lines. For $t_E = 20\,s$, $\Theta_{cont} = 14.7 \pm 1.0\,nm$, which is very close to the value obtained for co-deposition (i.e., $15.0\,nm$) and lower than that of pure Ag (i.e., $19.5\,nm$). With increasing values of t_E, the Θ_{cont} value remains at $\sim 14.5\,nm$ and does not evolve further. The evolution of the resistivity ρ vs nominal film thickness Θ for Ag, co-deposited $Ag_{96}Cu_4$ films and $Ag_{100-x}Cu_x$ films with $t_E = 20\,s$ and $40\,s$ is presented in Fig. 9(b). From these curves, we find that the steady-state resistivity ρ^{SS} of the $20\,s$ exposure sample is the same as in the pure Ag film, while it approaches the value of the co-deposited film when increasing t_E to $40\,s$. Exposure to Cu for $20\,s$ can therefore decrease Θ_{cont}, while retaining the film resistivity from pure Ag films. For the $t_E = 20\,s$ experiment, the mean Cu content in a $22.5\,nm$ thick film is estimated to be $x = 0.4\,at.\%$. For comparable values of x in a co-deposited sample, the shift of Θ_{cont} can be expected to be minimal, e.g., we find $\Theta_{cont} = 18\,nm$ for $x = 1\,at.\%$ in Fig. 2(a) compared to $19.5\,nm$ for pure Ag. Thus, from ellipsometric data, we can conclude that addition of Cu during the first $20\,s$ of deposition (i.e., $\Theta \cong 2.4\,nm$) is sufficient to hinder coalescence completion.

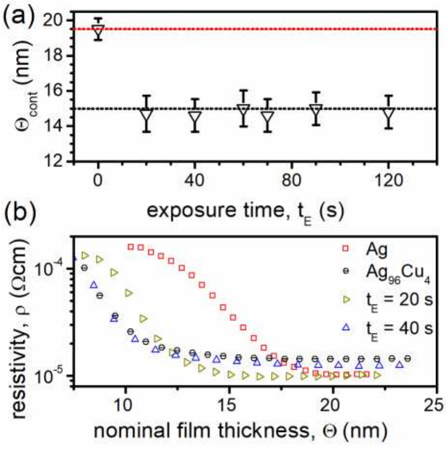

Figure 9: (a) Evolution of the continuous film formation thickness Θ_{cont} of $Ag_{100-x}Cu_x$ films with increasing exposure time t_E to Cu. Error bars correspond to the standard error from determining Θ_{cont} from resistivity ρ vs. nominal film thickness Θ plots. Horizontal dotted lines mark Θ_{cont} for Ag (red) and co-deposited $Ag_{96}Cu_4$ film (black). (b) Evolution of ρ vs. Θ for Ag, $Ag_{96}Cu_4$ co-deposition (also presented in Fig. 1) and $Ag_{100-x}Cu_x$ with exposure times $t_E = 20\,s$ and $40\,s$.

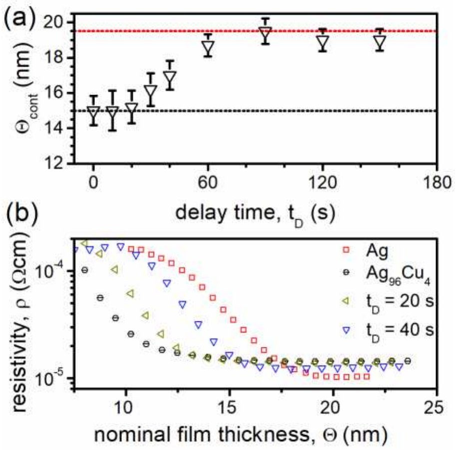

Figure 10: (a) Evolution of the continuous film formation thickness Θ_{cont} of $Ag_{100-x}Cu_x$ films with increasing delay time t_D of the Cu deposition. Error bars correspond to the standard error from determining Θ_{cont} from resistivity ρ vs. nominal thickness Θ plots. Horizontal dotted lines mark Θ_{cont} for Ag (red) and co-deposited $Ag_{96}Cu_4$ film (black). (b) Evolution of ρ vs. Θ for Ag, $Ag_{96}Cu_4$ co-deposition (also presented in Fig. 1) and $Ag_{100-x}Cu_x$ with delay times $t_D = 20\,s$ and $40\,s$.

The evolution of Θ_{cont} with increasing values of t_D is presented in Fig. 10(a), where $t_D = 0\,s$ corresponds to co-deposition of Ag and Cu (Θ_{cont} is marked by black horizontal dotted line). For $t_D \leq 20\,s$, Θ_{cont} remains at the value for co-deposition, i.e., $\sim 15.0\,nm$. Increasing t_D in the range 20 to $60\,s$ leads to a monotonic increase in Θ_{cont}, and the value close to pure Ag deposition (i.e., $19.5\,nm$) is reached for $t_D \geq 60\,s$. Figure 10(b) presents ρ vs. Θ curves of Ag and $Ag_{96}Cu_4$ films as well as $Ag_{100-x}Cu_x$ films deposited with $t_D = 20\,s$ and $40\,s$. While a low value of $\Theta_{cont} \cong 15.2\,nm$ is reached for the shorter delay time, which is close to $Ag_{96}Cu_4$, ρ^{SS} is larger compared to pure Ag films. Increasing of t_D to $40\,s$ leads to $\Theta_{cont} \cong 17.0\,nm$, which is lower than pure Ag, but ρ^{SS} still remains larger compared to Ag.

In summary, the results from experiments in which Cu deposition is controlled via the exposure and delay times t_E and t_D, respectively, show that Θ_{cont} decreases (i.e., 2D growth morphology is promoted) with longer presence of Cu in the deposition flux and the film growth front, which is, e.g., facilitated by smaller t_D values. However, both smaller-than-pure-Ag Θ_{cont} values and ρ^{SS} that is identical to that of Ag films cannot be achieved, unless Cu is deployed during the initial growth stages to affect island coalescence.

4. SUMMARY AND OUTLOOK

The tendency of thin noble-metal films to grow in an uncontrolled three-dimensional fashion on weakly-interacting substrates, including oxides and van der Waals materials, can be reversed by deploying gaseous and/or less-noble metallic minority species at the film growth front. In this work, we investigate the effect Cu as wetting agent on the growth evolution of magnetron sputter-deposition of Ag films on SiO_2 substrates, which is an archetypal weakly-interacting film/substrate system. We show, by combining *in situ* and real-time spectroscopic ellipsometry with *ex situ* x-ray reflectometry, that the thickness at which a continuous film is formed can be decreased by 23% (i.e., from 19.5 to $15.0\,nm$) by steadily adding $4\,at.\%$ Cu to the Ag film, while the root-mean-square surface roughness decreases by $28\,\%$ (from 1.8 to $1.3\,nm$). The addition of Cu is also accompanied by a 25% increase in film resistivity (from 1×10^{-5} to

$1.25 \times 10^{-5}\,\Omega cm$). Studies of the morphology of discontinuous layers using scanning electron microscopy reveal that Cu promotes two-dimensional growth and flat surface morphology by delaying island reshaping during coalescence. Moreover, we perform experiments in which Cu is deployed at the film growth front with high temporal precision to selectively target specific film-growth stages. By introducing Cu only during the first $20\,s$ of deposition, so that island coalescence is targeted, we are able to promote 2D morphology without compromising the Ag-layer electrical conductivity. Our overall results expand the understanding with regards to the effect of minority species on film morphological evolution on weakly-interacting substrates and provide the foundation for developing tailor-made strategies for non-invasive growth manipulation.

ACKNOWLEDGEMENTS

AJ and GA acknowledge the financial support of the French Government program "Investissements d'Avenir" (LABEX INTERACTIFS, reference ANR-11-LABX-0017-01). KS acknowledges financial support from Linköping University ("LiU Career Contract, Dnr-LiU-2015-01510, 2015-2020") and the Swedish research council (contract VR-2015-04630). AJ and KS acknowledge financial support from the ÅForsk foundation (contracts ÅF 19-137 and ÅF 19-746). KS and NP acknowledge financial support from the Olle Engkvist foundation (contract SOEB 190-312) and the Wenner-Gren foundations (contracts UPD2018-0071 and UPD2019-0007).

REFERENCES

[1] C.T. Campbell, Metal films and particles on oxide surfaces: structural, electronic and chemisorptive properties, J. Chem. Soc. Faraday Trans. 92 (1996) 1435. https://doi.org/10.1039/ft9969201435.

[2] X. Liu, Y. Han, J.W. Evans, A.K. Engstfeld, R.J. Behm, M.C. Tringides, M. Hupalo, H.-Q. Lin, L. Huang, K.-M. Ho, D. Appy, P.A. Thiel, C.-Z. Wang, Growth morphology and properties of metals on graphene, Prog. Surf. Sci. 90 (2015) 397–443. https://doi.org/10.1016/j.progsurf.2015.07.001.

[3] C. Gong, C. Huang, J. Miller, L. Cheng, Y. Hao, D. Cobden, J. Kim, R.S. Ruoff, R.M. Wallace, K. Cho, X. Xu, Y.J. Chabal, Metal contacts on physical vapor deposited monolayer MoS2, ACS Nano. 7 (2013) 11350–11357. https://doi.org/10.1021/nn4052138.

[4] J. Yun, Ultrathin Metal films for Transparent Electrodes of Flexible Optoelectronic Devices, Adv. Funct. Mater. 27 (2017) 1606641. https://doi.org/10.1002/adfm.201606641.

[5] I. Lee, J.-L. Lee, Transparent electrode of nanoscale metal film for optoelectronic devices, J. Photonics Energy. 5 (2015) 057609. https://doi.org/10.1117/1.JPE.5.057609.

[6] D. Gu, C. Zhang, Y.K. Wu, L.J. Guo, Ultrasmooth and thermally stable silver-based thin films with subnanometer roughness by aluminum doping, ACS Nano. 8 (2014). https://doi.org/10.1021/nn503577c.

[7] K. Kato, H. Omoto, T. Tomioka, A. Takamatsu, Visible and near infrared light absorbance of Ag thin films deposited on ZnO under layers by magnetron sputtering, Sol. Energy Mater. Sol. Cells. (2011). https://doi.org/10.1016/j.solmat.2011.04.005.

[8] G. Zhao, S.M. Kim, S.-G. Lee, T.-S. Bae, C. Mun, S. Lee, H. Yu, G.-H. Lee, H.-S. Lee, M. Song, J. Yun, Bendable Solar Cells from Stable, Flexible, and Transparent Conducting Electrodes Fabricated Using a Nitrogen-Doped Ultrathin Copper Film, Adv. Funct. Mater. 26 (2016) 4180–4191. https://doi.org/10.1002/adfm.201600392.

[9] G. Zhao, W. Shen, E. Jeong, S.-G. Lee, H.-S. Chung, T.-S. Bae, J.-S. Bae, G.-H. Lee, J. Tang, J. Yun, Nitrogen-Mediated Growth of Silver Nanocrystals to Form UltraThin, High-Purity Silver-Film Electrodes with Broad band Transparency for Solar Cells, ACS Appl. Mater. Interfaces. 10 (2018) 40901–40910. https://doi.org/10.1021/acsami.8b13377.

[10] W. Wang, M. Song, T.-S. Bae, Y.H. Park, Y.-C. Kang, S.-G. Lee, S.-Y. Kim, D.H. Kim, S. Lee, G. Min, G.-H. Lee, J.-W. Kang, J. Yun, Transparent Ultrathin Oxygen-Doped Silver Electrodes for Flexible Organic Solar Cells, Adv. Funct. Mater. 24 (2014) 1551–1561. https://doi.org/10.1002/adfm.201301359.

[11] T. Michely, J. Krug, Islands, Mounds and Atoms, Springer Berlin Heidelberg, Berlin, Heidelberg, 2004. http://link.springer.com/10.1007/978-3-642-18672-1.

[12] V. Gervilla, G.A. Almyras, F. Thunström, J.E. Greene, K. Sarakinos, Dynamics of 3D-island growth on weakly-interacting substrates, Appl. Surf. Sci. 488 (2019) 383–390. https://doi.org/10.1016/j.apsusc.2019.05.208.

[13] A. Jamnig, D.G. Sangiovanni, G. Abadias, K. Sarakinos, Atomic-scale diffusion rates during growth of thin metal films on weakly-interacting substrates, Sci. Rep. 9 (2019) 6640. https://doi.org/10.1038/s41598-019-43107-8.

[14] H.A. van der Vegt, H.M. van Pinxteren, M. Lohmeier, E. Vlieg, J.M.C. Thornton, Surfactant-induced layer-by-layer growth of Ag on Ag(111), Phys. Rev. Lett. 68 (1992) 3335–3338. https://doi.org/10.1103/PhysRevLett.68.3335.

[15] H.A. van der Vegt, M. Breeman, S. Ferrer, V.H. Etgens, X. Torrelles, P. Fajardo, E. Vlieg, Indium-induced lowering of the Schwoebel barrier in the homoepitaxial growth of Cu(100), Phys. Rev. B. 51 (1995) 14806–14809. https://doi.org/10.1103/PhysRevB.51.14806.

[16] J. Vrijmoeth, H.A. van der Vegt, J.A. Meyer, E. Vlieg, R.J. Behm, Surfactant-Induced Layer-by-Layer Growth of Ag on Ag(111): Origins and Side Effects, Phys. Rev. Lett. 72 (1994) 3843–3846. https://doi.org/10.1103/PhysRevLett.72.3843.

[17] S. Esch, M. Hohage, T. Michely, G. Comsa, Origin of oxygen induced layer-by-layer growth in homoepitaxy on Pt(111), Phys. Rev. Lett. 72 (1994) 518–521. https://doi.org/10.1103/PhysRevLett.72.518.

[18] B. Poelsema, R. Kunkel, N. Nagel, A.F. Becker, G. Rosenfeld, L.K. Verheij, G. Comsa, New phenomena in homoepitaxial growth of metals, Appl. Phys. A Solids Surfaces. 53 (1991) 369–376. https://doi.org/10.1007/BF00348149.

[19] B. Voigtländer, A. Zinner, Influence of surfactants on the growth-kinetics of Si on Si(111), Surf. Sci. Lett. 292 (1993) L775–L780. https://doi.org/10.1016/0167-2584(93)90833-5.

[20] M. Horn-von Hoegen, J. Falta, M. Copel, R.M. Tromp, Surfactants in Si(111) homoepitaxy, Appl. Phys. Lett. 66 (1995) 487–489. https://doi.org/10.1063/1.114065.

[21] K. Sarakinos, A review on morphological evolution of thin metal films on weakly-interacting substrates, Thin Solid Films. 688 (2019) 137312. https://doi.org/10.1016/j.tsf.2019.05.031.

[22] B. Lü, G.A. Almyras, V. Gervilla, J.E. Greene, K. Sarakinos, Formation and morphological evolution of self-similar 3D nanostructures on weakly interacting substrates, Phys. Rev. Mater. 2 (2018) 063401. https://doi.org/10.1103/PhysRevMaterials.2.063401.

[23] A. Anders, E. Byon, D.-H. Kim, K. Fukuda, S.H.N. Lim, Smoothing of ultrathin silver films by transition metal seeding, Solid State Commun. 140 (2006) 225–229. https://doi.org/10.1016/j.ssc.2006.08.027.

[24] K. Fukuda, S.H.N. Lim, A. Anders, Coalescence of magnetron-sputtered silver islands affected by transition metal seeding (Ni, Cr, Nb, Zr, Mo, W, Ta) and other parameters, Thin Solid Films. 516 (2008) 4546–4552. https://doi.org/10.1016/j.tsf.2007.05.080.

[25] G. Zhao, E. Jeong, E.-A. Choi, S.M. Yu, J.-S. Bae, S.-G. Lee, S.Z. Han, G.-H. Lee, J. Yun, Strategy for improving Ag wetting on oxides: Coalescence dynamics versus nucleation density, Appl. Surf. Sci. 510 (2020) 145515. https://doi.org/10.1016/j.apsusc.2020.145515.

[26] J.M. Riveiro, P.S. Normile, J.P. Andrés, J.A. González, J.A. De Toro, T. Muñoz, P. Muñiz, Oxygen-assisted control of surface morphology in nonepitaxial sputter growth of Ag, Appl. Phys. Lett. 89 (2006) 201902. https://doi.org/10.1063/1.2388140.

[27] A. Jamnig, N. Pliatsikas, M. Konpan, J. Lu, T. Kehagias, A.N. Kotanidis, N. Kalfagiannis, D. V. Bellas, E. Lidorikis, J. Kovac, G. Abadias, I. Petrov, J.E. Greene, K. Sarakinos, 3D-to-2D Morphology Manipulation of Sputter-Deposited Nanoscale Silver Films on Weakly Interacting Substrates via Selective Nitrogen Deployment for Multifunctional Metal Contacts, ACS Appl. Nano Mater. 3 (2020) 4728–4738. https://doi.org/10.1021/acsanm.0c00736.

[28] N. Pliatsikas, A. Jamnig, M. Konpan, A. Delimitis, G. Abadias, K. Sarakinos, Manipulation of thin silver film growth on weakly interacting silicon dioxide substrates using oxygen as a surfactant, J. Vac. Sci. Technol. A Vacuum, Surfaces Film. 38 (2020) 043406. https://doi.org/10.1116/6.0000244.

[29] C. Zhang, N. Kinsey, L. Chen, C. Ji, M. Xu, M. Ferrera, X. Pan, V.M. Shalaev, A. Boltasseva, L.J. Guo, High-Performance Doped Silver Films: Overcoming Fundamental Material Limits for Nanophotonic Applications, Adv. Mater. 29 (2017) 1605177. https://doi.org/10.1002/adma.201605177.

[30] T. Kaub, R. Anthony, G.B. Thompson, Intrinsic stress response of low and high mobility solute additions to Cu thin films, J. Appl. Phys. 122 (2017) 225302. https://doi.org/10.1063/1.5008269.

[31] V. Elofsson, G.A. Almyras, B. Lü, R.D. Boyd, K. Sarakinos, Atomic arrangement in immiscible Ag–Cu alloys synthesized far-from-equilibrium, Acta Mater. 110 (2016) 114–121. https://doi.org/10.1016/j.actamat.2016.03.023.

[32] V. Elofsson, G.A. Almyras, B. Lü, M. Garbrecht, R.D. Boyd, K. Sarakinos, Structure formation in Ag-X (X = Au, Cu) alloys synthesized far-from-equilibrium, J. Appl. Phys. 123 (2018) 165301. https://doi.org/10.1063/1.5018907.

[33] C.M. Herzinger, B. Johs, W.A. McGahan, J.A. Woollam, W. Paulson, Ellipsometric determination of optical constants for silicon and thermally grown silicon dioxide via a multi-sample, multi-wavelength, multi-angle investigation, J. Appl. Phys. 83 (1998) 3323–3336. https://doi.org/10.1063/1.367101.

[34] F. Wooten, Optical Properties of Solids, Academic Press, New York, 1972.

[35] ICDD powder diffraction file no. 00-004-0787; silver, (n.d.).

[36] C.T. Rueden, J. Schindelin, M.C. Hiner, B.E. DeZonia, A.E. Walter, E.T. Arena, K.W. Eliceiri, ImageJ2: ImageJ for the next generation of scientific image data, BMC Bioinformatics. 18 (2017) 529. https://doi.org/10.1186/s12859-017-1934-z.

[37] V. Elofsson, B. Lü, D. Magnfält, E.P. Münger, K. Sarakinos, Unravelling the physical mechanisms that determine microstructural evolution of ultrathin Volmer-Weber films, J. Appl. Phys. 116 (2014) 044302. https://doi.org/10.1063/1.4890522.

[38] W.M. Haynes, CRC Handbook of chemistry and physics: a ready-reference book for chemical and physical data, ed. 58, CRC Press, Cleveland, Ohio, 1977.

[39] D. Gall, Electron mean free path in elemental metals, J. Appl. Phys. 119 (2016) 085101. https://doi.org/10.1063/1.4942216.

[40] A.M. James, M.P. Lord, Macmillan's chemical and physical data, Macmillan, London, 1992. https://doi.org/10.1016/0307-4412(93)90067-A.

[41] ICDD powder diffraction file no. 01-070-3038; copper, (n.d.).

[42] ICDD powder diffraction file no. 00-027-1402; silicon, (n.d.).

[43] A.. Hindeleh, D.. Johnson, Crystallinity and crystallite size measurement in cellulose fibres: 1. Ramie and Fortisan, Polymer (Guildf). 13 (1972) 423–430. https://doi.org/10.1016/0032-3861(72)90107-3.

[44] T. de Keijser, E.J. Mittemeijer, H.C.F. Rozendaal, The determination of crystallite-size and lattice-strain parameters in conjunction with the profile-refinement method for the determination of crystal structures, J. Appl. Crystallogr. 16 (1983) 309–316. https://doi.org/10.1107/S0021889883010493.

[45] A.L. Patterson, The Scherrer Formula for X-Ray Particle Size Determination, Phys. Rev. 56 (1939) 978–982. https://doi.org/10.1103/PhysRev.56.978.

[46] Y. Liu, R.G. Jordan, S.L. Qiu, Electronic structures of ordered Ag-Mg alloys, Phys. Rev. B. 49 (1994) 4478–4484. https://doi.org/10.1103/PhysRevB.49.4478.

[47] M.C. Biesinger, Advanced analysis of copper X-ray photoelectron spectra, Surf. Interface Anal. 49 (2017) 1325–1334. https://doi.org/10.1002/sia.6239.

[48] A.C. Miller, G.W. Simmons, Copper by XPS, Surf. Sci. Spectra. 2 (1993) 55–60. https://doi.org/10.1116/1.1247725.

[49] A. Michaelides, V.A. Ranea, P.L. de Andres, D.A. King, General Model for Water Monomer Adsorption on Close-Packed Transition and Noble Metal Surfaces, Phys. Rev. Lett. 90 (2003) 216102. https://doi.org/10.1103/PhysRevLett.90.216102.

[50] J. Carrey, J.-L. Maurice, Transition from droplet growth to percolation: Monte Carlo simulations and an analytical model, Phys. Rev. B. 63 (2001) 245408. https://doi.org/10.1103/PhysRevB.63.245408.

[51] B. Lü, V. Elofsson, E.P. Münger, K. Sarakinos, Dynamic competition between island growth and coalescence in metal-on-insulator deposition, Appl. Phys. Lett. 105 (2014) 163107. https://doi.org/10.1063/1.4900575.

[52] C.O. Jeong, N.S. Roh, S.G. Kim, H.S. Park, C.W. Kim, D.S. Sakong, J.H. Seok, K.H. Chung, W.H. Lee, D. Gan, P.S. Ho, B.S. Cho, B.J. Kang, H.J. Yang, Y.K. Ko, J.G. Lee, Feasibility of an Ag-alloy film as a thin-film transistor liquid-crystal display source/drain material, J. Electron. Mater. 31 (2002) 610–614. https://doi.org/10.1007/s11664-002-0132-5.

[53] F. Misják, P.B. Barna, G. Radnóczi, Growth of nanocomposite in eutectic Cu–Ag films, Thin Solid Films. 518 (2010) 4247–4251. https://doi.org/10.1016/j.tsf.2009.12.095.

[54] F.A. Nichols, Coalescence of Two Spheres by Surface Diffusion, J. Appl. Phys. 37 (1966) 2805–2808. https://doi.org/10.1063/1.1782127.

[55] H.-J. Kim, K.-W. Seo, H.-K. Kim, Y.-J. Noh, S.-I. Na, Ag-Pd-Cu alloy inserted transparent indium tin oxide electrodes for organic solar cells, J. Vac. Sci. Technol. A Vacuum, Surfaces, Film. 32 (2014) 051507. https://doi.org/10.1116/1.4891560.

[56] G. Zhao, W. Shen, E. Jeong, S.-G. Lee, S.M. Yu, T.-S. Bae, G.-H. Lee, S.Z. Han, J. Tang, E.-A. Choi, J. Yun, Ultrathin Silver Film Electrodes with Ultralow Optical and Electrical Losses for Flexible Organic Photovoltaics, ACS Appl. Mater. Interfaces. 10 (2018) 27510–27520. https://doi.org/10.1021/acsami.8b08578.

Paper VI

The effect of nitrogen on the stress and morphology evolution during growth of thin silver films

A. Jamnig[1,2], N. Pliatsikas[2], H. Bahsoun[1], K. Sarakinos[2], P. Barna[3], G. Radnóczi[3], and G. Abadias[1,*]

*Corresponding author

[1]Institut Pprime, Département Physique et Mécanique des Matériaux, UPR 3346 CNRS, Université de Poitiers, 11 Bvd M. et P. Curie, TSA 41123, 86073 Poitiers Cedex 9, France

[2]Nanoscale Engineering Division, Department of Physics, Chemistry, and Biology, Linköping University, SE 581 83, Linköping, Sweden

[3]Centre for Energy Research of the Hungarian Academy of Sciences, Institute for Technical Physics and Materials Science, H1121 Budapest, Konkoly-Thege M. u. 29-33, Hungary

(Manuscript in final preparation)

The effect of nitrogen on the stress and morphology evolution during growth of thin silver films

A. Jamnig[1,2], N. Pliatsikas[2], H. Bahsoun[1], K. Sarakinos[2], P. Barna[3], G. Radnóczi[3], and G. Abadias[1,*]

*Corresponding author, email: gregory.abadias@univ-poitiers.fr

[1]Institut Pprime, Département Physique et Mécanique des Matériaux, UPR 3346 CNRS, Université de Poitiers, 11 Bvd M. et P. Curie, TSA 41123, 86073 Poitiers Cedex 9, France

[2]Nanoscale Engineering Division, Department of Physics, Chemistry, and Biology, Linköping University, SE 581 83, Linköping, Sweden

[3]Centre for Energy Research, Institute for Technical Physics and Materials Science, H1121 Budapest, Konkoly-Thege M. u. 29-33, Hungary

Abstract

We present a systematic study on the stress generation and evolution in thin Ag films grown by magnetron sputtering in mixed Ar-N_2 gas atmospheres (N_2-to-total pressure ratios $p_{N_2}/p_{tot} = 0\%$ to 25%) on silicon substrates covered with native oxide. *In situ* and real-time wafer curvature measurements for $p_{N_2}/p_{tot} = 0\%$ (i.e., growth in pure Ar) show a compressive-tensile-compressive (C-T-C) stress evolution with increasing film thickness, whereby a steady-state stress is reached in the second compressive regime. When N_2 is added to the working gas, the first compressive regime is no longer detectable, while no steady state is reached in the second compressive regime, which is followed by a further transition to tensile stress, i.e., an overall T-C-T evolution is observed. Moreover, we find that by increasing p_{N_2}/p_{tot} from 3% to 25%, the stress in the compressive regime increases, while the thickness of the C-T transition decreases from 310 to $40\,nm$. *In situ* stress measurements are complemented by *ex situ* chemical and microstructural analyses. These analyses show that the presence of N_2 in the gas atmosphere leads to a larger number density of grain boundaries relative to films grown in Ar atmosphere at thicknesses that correspond to the compressive stress regime, which can explain the larger stress magnitude. As films grow thicker ($> 100\,nm$), abnormal grain growth is observed in Ar-N_2-grown films in which (100) out-of-plane orientation crystals prevail and grain boundaries are eliminated, triggering the C-T transition. We argue that the grain growth process is driven by strain energy minimization in the various crystals. Despite the extensive grain growth, roughness emerges in the form of surface undulations with a nearly constant wavelength of $\sim 50\,nm$. We attribute this phenomenon to limited Ag adspecies mobility and mound formation caused by the presence of N_2 at the film growth front. The overall results of our study provide critical insights for controlling stress in films grown in complex gas compositions.

1. INTRODUCTION

Mechanical stresses are crucial for the reliability and functionality of devices based on thin films.[1] In vapor deposited thin films, the stress magnitude and type (i.e., whether the stress is tensile or compressive) depend on the structure and chemistry of grains, grain boundaries (GB), as well as on the film/substrate interface.[1–3] Moreover, stress evolution is intimately linked with the structure-forming processes which govern film growth.[4]

Films which are deposited at conditions of high atomic mobility and exhibit a pronounced three-dimensional (3D) growth morphology (e.g., noble-metal films grown on weakly-interacting van der Waals materials and oxides)[5] are characterized by a compressive-tensile-compressive (C-T-C) stress evolution as function of film thickness.[4,6,7] The initial compressive stress is caused by the Laplace-pressure which yields a smaller-than-equilibrium lattice constant as isolated islands grow in size and become immobile.[8] Formation of GBs following the impingement and incomplete coalescence of islands leads to tensile stress.[9,10] With further deposition and formation of a continuous layer, strain energy is stored in GBs due to insertion of excess diffusing adatoms, leading to compressive stress, which reaches a steady state if there is a continuous adatom flux into the GBs.[4]

Noble-metal films deposited on weakly-interacting substrates are key constituents in a wide range of modern optoelectronic devices.[11–15] In such devices, metal-layer growth manipulation, so that two-dimensional (2D) morphology is promoted, is paramount for performance enhancement. One way of achieving such morphology is by using seed layers at the film/substrate interface[16–18] or by deploying minority species at the film growth front [19–22] to control the rates of atomic-scale processes that govern structure formation. In a recent study,[23] we showed that 2D morphology of magnetron sputter-deposited Ag on SiO_2 for thicknesses below $\sim 20\,nm$ can be promoted by introducing N_2 in the growth atmosphere so that island coalescence completion is delayed.

In the present work, we study the effect of N_2 on stress generation and evolution in the Ag/Si film/substrate system, and study microstructure and morphology with focus on films with thicknesses above $20\,nm$. We perform *in situ* and real-time stress measurements, using the substrate curvature technique, for films deposited in Ar-N_2 mixed atmospheres, whereby the ratio of N_2-to-total pressure p_{N_2}/p_{tot} is varied from 0 to 25%. Our data show that for $p_{N_2}/p_{tot} = 0\%$ (i.e., pure Ar atmosphere) a C-T-C stress evolution vs. film thickness is observed, where the final compressive regime exhibits a steady state. Presence of N_2 changes the stress vs. thickness evolution to T-C-T, where by the thickness of the C-T transition decreases from 310 to $40\,nm$ when p_{N_2}/p_{tot} is increased from 3% to 25%. Moreover, the stress magnitude in the compressive regime that is common for all growth conditions increases, which is in accordance with increasing number density of GBs in this thickness range, observed in *ex situ* cross-sectional transmission electron microscopy (XTEM). Concurrently, abnormal grain growth is observed in thicker ($> 100\,nm$) Ar-N_2 deposited films, during which a (100) preferred crystal orientation develops. We attribute the CT stress transition to GB elimination in course of this grain growth process, and we argue that it is driven by strain energy minimization. From *ex situ* surface imaging with atomic force microscopy and XTEM, we find that surface undulations with a nearly constant wavelength of $\sim 50\,nm$ form when N_2 is present during deposition, that are not correlated with grain size. We attribute the formation of these undulations to N_2-induced reduced adatom surface mobility.

2. FILM GROWTH AND CHARACTERIZATION

Ag films are deposited by direct current magnetron sputtering in mixed Ar-N_2 atmospheres (gas purities 99.9999%), in a multi-source high-vacuum chamber (base pressure $\sim 8 \times 10^{-6}\,Pa$) at a total working pressure $p_{tot} = 0.7\,Pa$. The ratio of N_2-to-total pressure p_{N2}/p_{tot} is varied between 0% and 25% by increasing the N_2 mass flow rate from 0 to $8\,sccm$ and decreasing the Ar mass flow rate from 42 to $35\,sccm$. The deposition rate of Ag is set to $0.11 \pm 0.01\,nm/s$ by applying $25\,W$ to a Ag target (purity 99.99%, diameter $7.62\,cm$) with a target-to-substrate-normal angle of $25°$ and target-to-substrate distance of $180\,mm$. Films are deposited without intentional heating on Si(100) substrates, covered with native oxide, with substrate thickness $h_s = 100 \pm 2\,\mu m$ for *in situ* stress measurements and $h_s = 675 \pm 20\,\mu m$ for *ex situ* characterization. In the case of samples used for *ex situ* analyses, a $6\,nm$ thick amorphous carbon (a-C) capping layer is sputter-deposited in Ar atmosphere ($p_{tot} = 0.36\,Pa$) from a graphite target (purity 99.995%, applied power $100\,W$, deposition rate $\sim 0.01\,nm/s$) immediately after Ag film growth. This capping layer minimizes the interaction between film and atmospheric ambient and suppresses post-deposition changes of the film morphology. For *ex situ* analyses, samples with Ag layer thicknesses in the range 20 to $500\,nm$ are used.

Stress is measured by means of the substrate curvature method. The evolution of the substrate curvature change $\Delta\kappa$ during deposition is monitored *in situ* and in real-time using a magnification inferred curvature setup by tracing the relative displacement of light points in a 3x3 matrix, which are reflected on a strained substrate. In this setup, the angle between optical beam and substrate-normal is $70°$, which induces a positive magnification of the reflected light spots in one dimension (i.e., round light spots appear elliptic in camera), increasing the relative displacement in this dimension and thus improving the sensitivity compared to setups that work with near-normal incidence.[24] The stress-film thickness product $\sigma \times h_f$ is then calculated from $\Delta(\sigma \times h_f) = \frac{1}{6} Y_s h_s^2 \Delta\kappa$,[25] where $Y_s = 180.5\,GPa$ is the Si(100) substrate biaxial modulus. The first derivative of the stress-thickness product is also plotted, giving information which corresponds to the incremental stress $\sigma_{incr} = d(\sigma \times h_f)/d\,(h_f)$; this differentiation is computationally approximated with the centered difference formula.[26]

In situ characterization is complemented by *ex situ* analyses. Mass density, surface roughness, film thicknesses, and deposition rates are determined from x-ray reflectometry (XRR, performed in an XRD 3000 Seifert diffractometer, line focus Cu source, Ge (220) monochromator selecting K$_{\alpha1}$ Cu radiation, scintillation detector) on a-C/Ag/Si stacks with Ag layer thicknesses h_f between 20 and $90\,nm$. Representative curves and a brief discussion are presented in Fig.S1 in the supplementary material file.[27] Microstructural analysis is performed by x-ray diffractometry (XRD) in Bragg-Brentano geometry (D8 Bruker AXS diffractometer, divergent-beam Cu K$_{\alpha1}$ radiation, LynxEye detector). From the integral intensities I_{hkl} of diffraction peaks of (hkl) crystallographic planes in the film, the texture coefficient

$$TC(hkl) = \frac{I_{hkl}/I_{0,hkl}}{\frac{1}{N}\sum_N I_{hkl}/I_{0,hkl}} \qquad (1)$$

is calculated, where $I_{0,hkl}$ are the intensities of the (hkl) crystallographic planes in a powder pattern,[28] and N is the number of considered diffraction peaks (see Figs.S2 and S3 in the supplementary material file for diffractograms).[27]

The surface morphology and topography of a-C/Ag/Si samples are imaged by atomic force microscopy (AFM) with a Nanoscope III Multimode Digital Instruments AFM operating in tapping mode. The acquired images are analyzed with the Gwyddion software package;[29] the height-height correlation function

$$g(\vec{r}) = \langle [h(\vec{x} + \vec{r}) - h(\vec{x})]^2 \rangle \qquad (2)$$

is determined for various working gas compositions and film thicknesses. In Eq 2, $h(\vec{x})$ is the surface height at a position $\vec{x} = (x, y)$ on the surface, $\vec{r}$ is a displacement vector, and $\langle \dots \rangle$ denotes the statistical average over the entire surface. From $g(\vec{r})$ vs. $\vec{r}$ plots, the roughness scaling exponent α, lateral feature size d, and root-mean-square surface roughness $w = \langle [h(\vec{x}) - \bar{h}]^2 \rangle^{1/2}$ are computed, where $\bar{h}$ is the average surface height.

Lateral grain size D and crystal orientation are analyzed via electron backscatter diffraction (EBSD) with a FEI-Helios Nanolab G3 Dual Beam microscope operated at $15\,kV$ with $11\,nA$, and a step size of $25\,nm$. The acquired maps are treated with the OIM Analysis™ software, using Neighbor Confidence Index Correlation (minimum Confidence Index 0.05) and Grain Dilatation cleanup (tolerance angle $2°$, minimum grain size 3 points).

The microstructure of the thin films is investigated by cross-sectional transmission electron microscopy (XTEM). Thin cross sections of films are prepared by focused ion milling (with Ga ions of $30\,keV$, reduced to $10\,keV$ at the end to polish the surface). The thin sections are transferred to the electron microscope immediately after preparation to avoid the growth of AgS$_2$ crystals on their surface.[30] A Philips CM 20 electron microscope, operated at $200\,kV$ and a JEOL 3010 microscope operated at $300\,kV$ are used for XTEM measurements. Bright field and selected area electron diffraction (SAED) patterns are recorded on imaging plates and on digital camera, accordingly.

Chemical analysis is performed with x-ray photoelectron spectroscopy (XPS), conducted in a Kratos AXIS Ultra DLD UHV system (base pressure $5 \times 10^{-8}\,Pa$). A monochromatic Al-K$_\alpha$ x-ray beam is used for the measurements, and the instrument is equipped with a hemispherical sector analyzer, and a multichannel detector with $20\,eV$ pass energy. Surface-cleaning and depth-etching are performed using a $4\,keV$ Ar$^+$ ion-beam, and the shift of the Ar-*2p* peak is used for correcting charge-induced shifts of the binding energies caused by the Ar$^+$ ions. Elemental analysis is performed with the Kratos Vision software and its sensitivity factor database.

3. RESULTS AND DISCUSSION

3.1. STRESS EVOLUTION DURING FILM GROWTH

The evolution of the stress-film thickness product $\sigma \times h_f$ vs. h_f for Ag films deposited for various gas atmospheres is presented in Figs.1(a)-(b), and the corresponding incremental stress σ_{incr} vs. h_f curves are shown in Figs.1(c)-(d). Panels (a) and (c) present data for $h_f \leq 1100\,nm$, while panels (b) and (d) magnify the thickness range 0 to $40\,nm$. For deposition in pure Ar ($p_{N2}/p_{tot} = 0\%$, curve A), a C-T-C stress evolution is seen, which is typical for metals deposited under high atomic mobility conditions.[2] Compressive stress is observed for $h_f \leq 2\,nm$ (Fig.1(b)), with an incremental value of $\sim -20\,MPa$ (Fig.1(d)). For h_f values between ~ 2 and $\sim 13\,nm$, tensile stress is formed in (i.e., $\sigma_{incr} > 0\,MPa$), and a T-C stress transition occurs at $h_f \cong 13\,n$. The position of this transition corresponds to the continuous film formation thickness h_{cont}. [31] Further deposition results in steady-state compressive stress evidenced by the constant slope of the $\sigma \times h_f$ vs. h_f curve with a value of $\sim -65\,MPa$ (see Fig.1(a)). This is also reflected in the σ_{incr} value that is constant for $h_f \geq \sim 100\,nm$ (see Fig.1(c)).

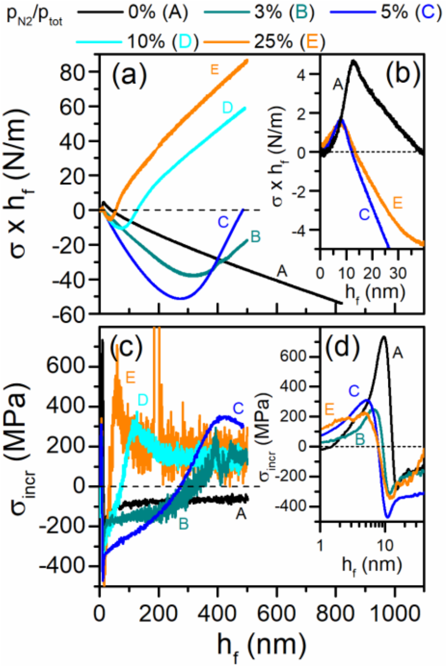

Figure 1: Evolution of (a)-(b) the stress-film thickness product $\sigma \times h_f$ and (c)-(d) incremental stress σ_{incr} with film thickness h_f of sputter-deposited Ag films deposited at nitrogen partial pressures p_{N2}/p_{tot} (A) 0%, (B) 3%, (C) 5%, (D) 10%, and (E) 25%. Data stems from in situ substrate curvature measurements.

Addition of N$_2$ to the gas atmosphere affects all stages of stress evolution. Opposite to growth in pure Ar, no compressive stress is observed at the initial growth stages (Fig.1(d)), e.g., $\sigma_{incr} = \sim 100\,MPa$ for $h_f = 1\,nm$ and $p_{N2}/p_{tot} = 5\%$ (curve C) and 25% (curve E). This is an indication that impingement between islands, which leads to tensile stress formation, starts earlier compared to films deposited in Ar ambient, as discussed further in Section 3.3. Transition from tensile to compressive stress is observed for all deposition atmospheres (at h_{cont}), but presence of N$_2$ leads to a decrease of h_{cont} (from $\sim 13\,nm$ for $p_{N2}/p_{tot} = 0\%$ to $\sim 7\,nm$ for $p_{N2}/p_{tot} = 25\%$), i.e., N$_2$

promotes 2D growth morphology in accordance with our previous work.[23] The magnitude of the incremental compressive stress for $h > h_{cont}$ increases with increasing p_{N2}/p_{tot} from 0% to 5% (e.g., compare slopes of curves A, B and C at $h_f = 100\,nm$ in Fig.1(a)). This is not the case for $p_{N2}/p_{tot} > 5\%$, as σ_{incr} is governed a tensile stress component (e.g., compare slopes of curves C and E in Fig.1(b)). Further increase of thickness does not lead to a steady-state compressive stress, but instead a transition from compressive to tensile stress is observed, whereby the transition thickness h_{trans} decreases with increasing N2 content (Fig.1(a)), e.g., $h_{trans} = 310\,nm$ for $p_{N2}/p_{tot} = 3\%$ and $40\,nm$ for $p_{N2}/p_{tot} = 25\%$. For clarity the evolution of h_{cont} and h_{trans} as function of p_{N2}/p_{tot} is also presented in Figs.2(a) and (b), respectively.

3.2. FILM MICROSTRUCTURE, MORPHOLOGY AND CHEMISTRY

To understand the origin of stress evolution presented in Section 3.1., we study the film microstructure, morphology, and microchemistry. XRR measurements on $90\,nm$ thick Ag films that are deposited at $p_{N2}/p_{tot} = 0\%$ and 25% are presented in Fig.S1 in the supplementary material file.[27] They confirm that both films are dense, with mass densities ρ_m corresponding to the value of bulk silver $\rho_m = 10.5\ g/cm^3$.[32] Additionally, surface roughnesses w_{Ag} are determined, that show that Ar-N2-grown Ag films ($w_{Ag} = 2.5\,nm$ for $p_{N2}/p_{tot} = 25\%$) are smoother than Ar-grown films ($w_{Ag} = 3.2\,nm$).

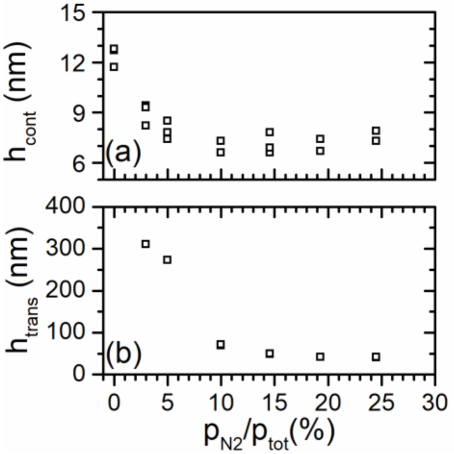

Figure 2: Evolution of (a) continuous film formation thickness h_{cont} and (b) compressive-to-tensile stress transition thickness h_{trans} of sputter-deposited Ag films with nitrogen partial pressure p_{N2}/p_{tot}. Data stems from in situ substrate curvature measurements presented in Fig.1.

XRD measurements are performed on $208\,nm$ thick Ag films that are deposited in the p_{N2}/p_{tot} range 0% to 25%, and reveal all expected fcc Ag peaks (see Fig.S2(a) in the supplementary material file),[27] indicating that Ag grows as a polycrystalline film. Peak intensities are analyzed to determine the texture coefficient $TC(hkl)$ (see Section 2). Figure 3(a) plots $TC(hkl)$ vs. p_{N2}/p_{tot}, whereby the horizontal dashed line indicates the value of the texture coefficient for the powder reference Ag sample which exhibits a random crystallographic orientation. Ag films deposited in pure Ar atmosphere ($p_{N2}/p_{tot} = 0\%$) have a (111) preferred orientation, grains with (200) orientation are diffracting with intensity comparable to a powder sample, while all other orientations are under-represented. With increasing N2 content, grains with (200) orientation become more numerous and a $(111) + (200)$ mixed preferred orientation is found. We note that the strongest (200) orientation is observed for $p_{N2}/p_{tot} = 5\%$, which is the film with the highest compressive stress at this film thickness (see Fig.1(a)). The texture develops toward more random orientation when increasing p_{N2}/p_{tot} above 5%, which is evidenced by the decrease of the $TC(200)$ and increase of all $TC(hkl)$ with $h + k + l > 3$.

As seen in Figs.3(a) and S2, (111) and (200) are the dominant crystallographic orientations for all N$_2$ contents. Hence, we study the texture evolution vs. film thickness ($h_f = 20$ to $500\,nm$) by focusing on these two orientations only (corresponding diffraction patterns are presented in Fig.S3 in the supplementary material file).[27] $TC(111)$ and $TC(200)$ are plotted as function of h_f in Figs.3(b) and (c), respectively, for $p_{N2}/p_{tot} = 0\%, 5\%,$ and 10%. The data show that for $h_f = 20\,nm$, i.e., shortly after continuous film formation for all p_{N2}/p_{tot} values, $TC(111) = {\sim}3$, independent of the N$_2$ content in the gas atmosphere (Fig.3(b)). This value remains constant with increasing film thickness for Ag films deposited in pure Ar atmosphere, while it decreases to unity as h_f increases from 20 to $90\,nm$ for films deposited at $p_{N2}/p_{tot} = 5\%$ and 10%. Concurrently, Fig.3(c) shows that $TC(200) = 1$ for $p_{N2}/p_{tot} = 0\%$, independent of h_f. At $p_{N2}/p_{tot} = 5\%$, $TC(200)$increases from 2 to 3 in the h_f range 20 to $90\,nm$, while the same thickness range $TC(200)$ decreases from 3 to 2.5 for $p_{N2}/p_{tot} = 10\%$. For all conditions presented in Figs.3(b) and (c), no change in the texture coefficient is found for $h_f > 90\,nm$, i.e., the texture analysis presented in Fig.3(a) is representative of continuous films.

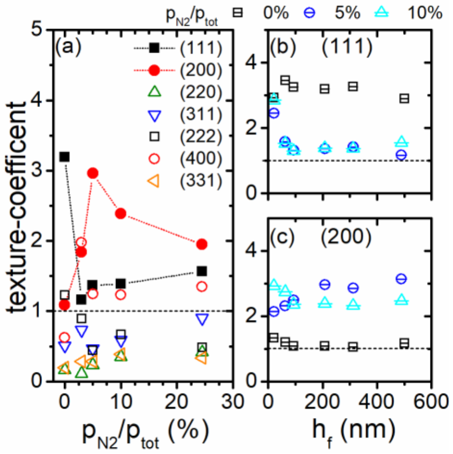

Figure 3: (a) Evolution of texture-coefficients of seven grain orientations as function of nitrogen partial pressure p_{N2}/p_{tot} of $208\,nm$ thick Ag films; lines are guides for the eye. Evolution of the texture coefficient of (b) (111) and (c) (200) grain orientations as function of film thickness h_f of Ag films deposited with $p_{N2}/p_{tot} = 0\%$, 5%, and 10%. Data stems from x-ray diffractograms presented in Figs. S2 and S3 in the supplementary material file.[27]

The effect of gas atmosphere on Ag surface morphology and topography is investigated by AFM. Using AFM images, the height-height-correlation functions $g(r)$ are calculated (see Fig.S4 in the supplementary material file [27] for $g(r)$ data for $p_{N2}/p_{tot} = 0\%$, 5%, and 10% at various film thicknesses), from which the root-mean-square surface roughness w, the lateral feature size d and the roughness scaling exponent α are computed. Figure 4(a) presents the evolution of w in the h_f range 20 to $500\,nm$. Overall, w increases with increasing h_f for all N$_2$ contents in the gas atmosphere. For $h_f = 20\,nm$, i.e., shortly after continuous-layer formation, w for Ag films deposited in pure Ar equals $1.23\,nm$, while it decreases down to $0.62\,nm$ for $p_{N2}/p_{tot} = 10\%$. This trend is consistent with the data presented in Figs.1 and 2, showing that N2 causes h_{cont} to decrease, and underscores the effectiveness of N2 in promoting 2D growth morphology, in accordance with our previous study.[23] However, this effect is only seen for $h_f < 100\,nm$, as for larger film thicknesses, w values of films deposited at $p_{N2}/p_{tot} = 0\%$ and 10% are comparable (e.g., $w = {\sim}3.0\,nm$ for $h_f = 208\,nm$), while films deposited at $p_{N2}/p_{tot} = 5\%$ are rougher ($w = 3.8\,nm$ for $h_f = 208\,nm$). This finding highlights that N2 affects film growth stages in a complex, non-trivial manner. We will return to this aspect later in the present section.

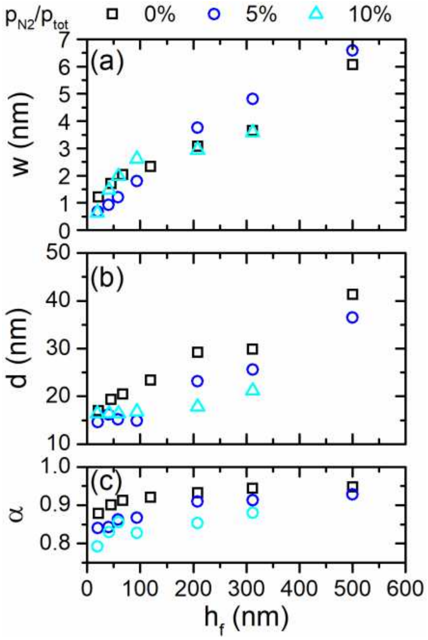

Figure 4: Evolution of root-mean-square surface roughness w, (b) lateral feature size d, and (c) roughness scaling exponent α with film thickness h_f of Ag films sputter-deposited in nitrogen partial pressure $p_{N2}/p_{tot} = 0\%$, 5%, and 10%. Data stems from analysis of height-height-correlation functions of atomic force microscopy measurements of the surfaces of respective films, presented in Fig.S4 in the supplementary material file.[27]

Figure 4(b) shows that evolution of the lateral feature size d vs. film thickness. For $h_f = 20\,nm$, $d = 16\,nm$ for all gas atmospheres. This value increases monotonically for thicker Ag films deposited in pure Ar gas ambient (e.g., $d = 30\,nm$ for $h_f = 300\,nm$), but remains constant for Ag films with $h_f < 100\,nm$ deposited in Ar-N2. For film thicknesses larger than $100\,nm$, d increases again. This increase is more pronounced for films deposited with $p_{N2}/p_{tot} = 5\%$, compared to films deposited with $p_{N2}/p_{tot} = 10\%$, leading to a general trend toward lower values of d with increasing values of p_{N2}/p_{tot}, e.g., for $h_f = 300\,nm$ $d = 26\,nm$ and $d = 21\,nm$ for $p_{N2}/p_{tot} = 5\%$ and 10%, respectively.

Figure 4(c) presents the roughness scaling exponent α, which is > 0.8 for all deposition conditions and film thicknesses, which indicates that surface morphology is more dependent on the out-of-plane than in-plane island growth. This is a typical behavior for films deposited at conditions of high atomic mobility,[33] i.e., a 3D surface morphology is formed. With increasing p_{N2}/p_{tot}, we find a systematic decrease of α, which is sign for weaker out-of-plane/stronger in-plane growth, i.e., 2D growth morphology is promoted as also evidenced by the h_{cont} and w vs. p_{N2}/p_{tot} data presented in Figs.2(b) and 4(a), respectively.

Additional information with regards to in-plane film morphology and texture is obtained from EBSD measurements. EBSD maps of $208\,nm$ thick Ag films deposited with $p_{N2}/p_{tot} = 0\%$, 5% and 10%, are shown in Figs.5(a), (b), and (c), respectively, From these maps, we determine the lateral grain size D and grain orientation (represented by colors indicated in inverse pole figure in Fig.5). For Ag films deposited in pure Ar ambient gas (Fig.5(a)), we find mainly (111)-oriented grains with an average grain size $D = 207 \pm 120\,nm$, i.e., D is comparable to the film thickness. With addition of N_2 to the working gas, no preferred orientation can be seen in the EBSD maps, and D increases to $265 \pm 139\,nm$ and $374 \pm 163\,nm$ for $p_{N2}/p_{tot} = 5\%$ (Fig.5(b)) and 10% (Fig.5(c)), respectively. For $p_{N2}/p_{tot} = 5\%$, the increase in D stems from the presence of a few grains with sizes larger than $700\,nm$, which are surrounded by grains which have sizes that are comparable to those of films deposited at $p_{N2}/p_{tot} = 0\%$. The fraction of large grains increases when increasing p_{N2}/p_{tot} to 10%, where the film consists mainly of large grains with $D > h_f$.

Figures 5(d)-(f) are AFM images of the films the EBSD maps of which are presented in Figs.5(a)-(c) (note that the data point for film of thickness $208\,nm$ for the analysis presented in Fig.4 is based on Figs. 5(d)-(f)). For films deposited in Ar ambient, the lateral feature size d and grain size D correspond well (compare Figs.5(d) and (a)). The size of surface features decreases with increasing values of p_{N2}/p_{tot} (see also Fig.4(b)), concurrently, D increases with increasing values of p_{N2}/p_{tot}. We find that the large grain size in films deposited in Ar-N_2 atmosphere is not discernable in the AFM surface morphology.

For a better understanding of the grain size evolution during film growth, XTEM is performed on 100 and $500\,nm$ thick Ag films deposited at $p_{N2}/p_{tot} = 0\%$ and 5%, and a $100\,nm$ thick film deposited at $p_{N2}/p_{tot} = 10\%$. Figure 6 displays representative micrographs, in which it is seen that Ag films deposited in Ar gas exhibit a columnar grain structure at $h_f = 100\,nm$, with continuous grains from the substrate to the surface, and lateral grain sizes ranging 100 to $200\,nm$.

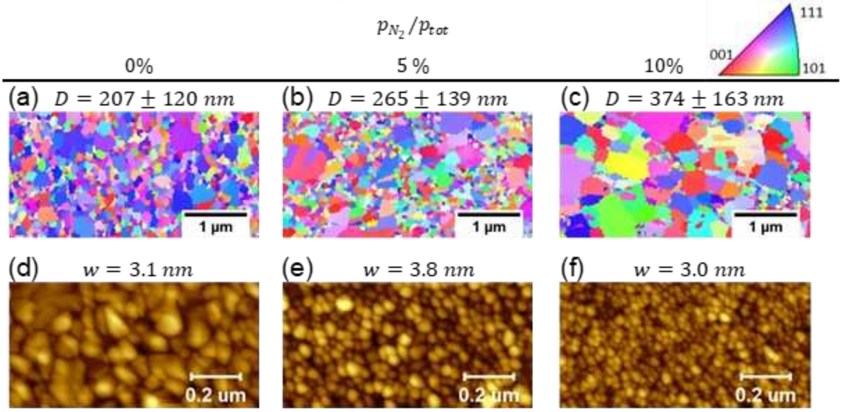

Figure 5: (a)-(c) Electron backscatter diffraction maps and (d)-(f) atomic force microscopy images of $208\,nm$ thick Ag films deposited in nitrogen partial pressure p_{N2}/p_{tot} (a),(d) 0%, (b),(e) 5%, and (c),(f) 10%. Respective average lateral grain size D and root-mean-square surface roughness w values are indicated above the images. The grain orientation in (a)-(c) is represented via colors indicated by the inverse pole figure, the height-scale in (d)-(f) is represented via color ranging from black ($0\,nm$) to gold ($23\,nm$).

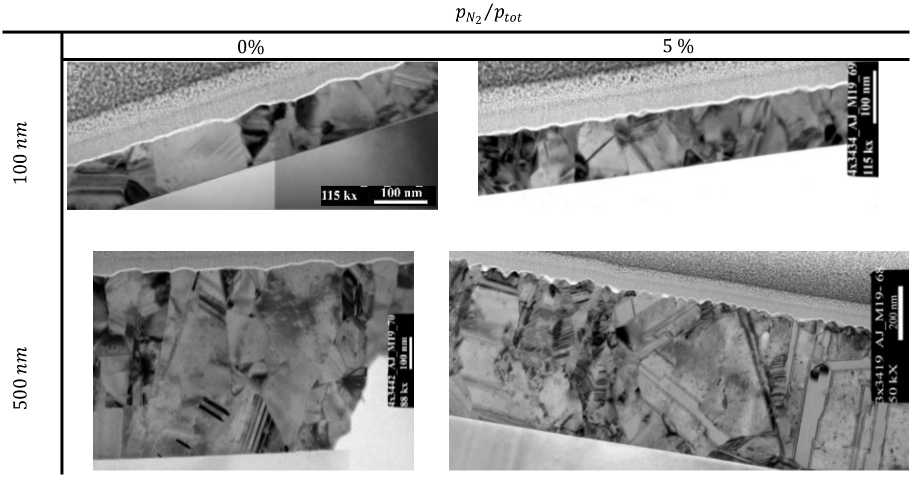

Figure 6: Film morphology of $\mathbf{100}$ and $\mathbf{500}\,nm$ thick Ag films deposited in nitrogen partial pressure $p_{N2}/p_{tot} = 0\%$ and 5% as determined with cross-sectional transmission electron microscopy.

After deposition of a $500\,nm$ thick film, V-shaped grains are present. We also observe that for both thicknesses the surface roughness correlates well with GB triple-junctions (i.e., GB grooves). For $h_f = 100\,nm$ and $p_{N2}/p_{tot} = 5\%$, the film exhibits primarily columnar grains that span the whole film thickness with lateral grain size $\sim 100\,nm$. However, there are also smaller grains visible close to the substrate that that have been overgrown. Increase of h_f to $500\,nm$ yields an inhomogeneous grain structure that comprises of large grains for which $D \cong h_f$, and areas with smaller globular grains with $D \cong 200\,nm$. This bimodal grain size distribution compares well with the distribution obtained for $208\,nm$ thick films from EBSD (see Fig.5(b)), i.e., inhomogeneous grain growth starts to occur in the thickness range 100 to $200\,n$. Grain structure and morphology for a $100\,nm$ thick film grown at $p_{N2}/p_{tot} = 10\%$ presented in Fig.7(a) are comparable to the film grown at $p_{N2}/p_{tot} = 5\%$, while surface features are more pronounced, in accordance with w values presented in Fig.4(a).

An additional feature observed for films deposited in N2-containing atmospheres is that the surface morphology does not correlate with the in-plane grain structure. This is more clearly shown in the higher magnification XTEM micrograph in Fig.7(b) ($h_f = 100\,nm$, $p_{N2}/p_{tot} = 10\%$), which shows a single grain with coherent twin boundaries (vertical lines). Even though no GB is within the image, several surface undulations are present, with a period of $\sim 50\,nm$. This is consistent with the results in Fig.5, where no connection between surface features and EBSD-determined grain size was found.

Chemical analysis is performed with XPS on $90\,nm$ thick samples grown with $p_{N2}/p_{tot} = 0\%$, 10%, and 25%. Spectra are acquired after surface etching to remove surface contamination from the atmosphere,

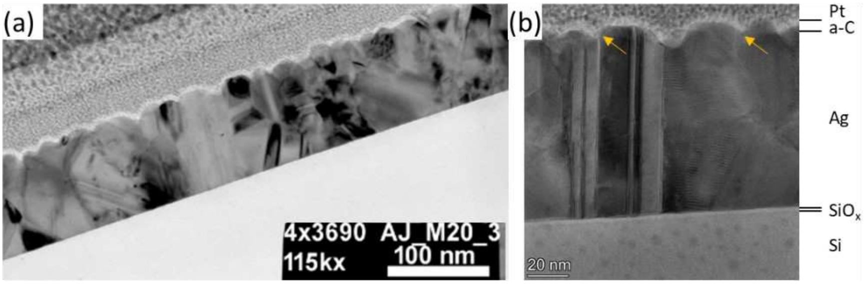

Figure 7: (a) Film morphology of $\mathbf{100}\,nm$ thick Ag film deposited in nitrogen partial pressure $p_{N2}/p_{tot} = \mathbf{10}\%$ as determined with cross-sectional transmission electron microscopy (XTEM). (b) High resolution XTEM micrograph of the same film. Visible are from bottom to top the Si substrate, native oxide (SiO$_x$) layer, Ag film, amorphous carbon (a-C) capping layer, and Pt protection layer. The vertical lines are coherent twin boundaries; arrows show positions where the surface undulations are not related to high-angle grain boundaries.

and as function of etching depth to obtain information about the compositional differences at the surface and film/substrate interface. Depth profiles of the chemical composition are presented in Fig.S5 in the supplementary material file.[27] Neither nitrogen nor other contamination are detected in the bulk of the Ag film deposited in pure Ar gas ambient, while nitrogen concentrations of 5.4 and $6.4\,at.\%$ are found in films grown with $p_{N2}/p_{tot} = 10\%$ and 25%, respectively. Concurrently, Ag-*3d* (binding energy for *3d$_{5/2}$* is $368.3\,eV$)[34] and N-*1s* peaks (binding energy $397\,eV$)[35] are not shifted in the bulk of the film, i.e., no chemical bonding between the two species exists. For the $p_{N2}/p_{tot} = 25\%$ sample, Si-N bonding is observed at the film/substrate interface, indicating the formation of a silicon-nitrogen compound (see Fig.S6 in the supplementary material file).[27] We note that the detection limit of nitrogen in Ag-based films is below $\sim 1\,at.\%$, and the N-*1s* peak is difficult to distinguish due to overlapping with Ag-*3d* plasmon loss peak.[36,37] Hence, even though incorporation of nitrogen $< 1\,at.\%$ cannot be detected, such small concentrations may still influence the film morphological and stress evolution.

3.3 STRESS-FORMING MECHANISMS

In this section, we use the microstructural and morphology data presented in Section 3.2 to explain the origin of the stress evolution seen in Section 3.1, as function of the composition of the gas atmosphere.

We start with the stress evolution at the early growth stages ($h_f < 2\,nm$) which shows (Fig.1) that, opposite to film grown in pure Ar, no compressive stress is formed upon N$_2$ addition. As explained in Section 1, the initial compressive stress forms due to the Laplace pressure when islands become immobile on the substrate. Our XPS data show the formation of a nitrogen-containing interlayer at the film/substrate interface. Such an interlayer may further reduce the interaction strength between Ag islands and substrates (there are no thermodynamically predicted Ag-N bonds), which would allow Ag islands to remain mobile until they impinge with each other. Another effect of N$_2$ is that it promotes 2D growth morphology, as seen by the decrease of h_{cont} as a function of p_{N2}/p_{tot} in Fig.1. In our recent study,[23] we showed that this is because N_2 hinders coalescence completion and island reshaping. Under these conditions, in-plane island expansion is favored over out-of-plane growth, so that island impingement occurs very early during growth, i.e., compressive stress formation occurs outside the h_f-range that can be captured by the curvature measurements.

The next notable feature in the stress evolution is the magnitude of the incremental compressive stress after the formation of a continuous layer (the latter is signified by the T-C stress transition). This magnitude increases with increasing p_{N2}/p_{tot} up to 5% (compare slopes of curves A, B and C at $h_f = 100\,nm$ in Fig.1(a)). XTEM micrographs show that the grain size in $100\,nm$ thick films decreases with increasing p_{N2}/p_{tot} (compare $p_{N2}/p_{tot} = 0\%$ to 5% in Fig.6), i.e., the number density of GBs at the surface increases. Compressive stress in continuous films is associated with adatom-GB interaction and GB densification via adatom insertion. Concurrently, the higher compressive stress magnitude can be explained with smaller lateral grain size in films that are deposited in N_2-containing atmosphere.

The morphology of films grown in N_2-containing atmospheres exhibits drastic changes as a function of films thickness, i.e., grain growth occurs for $h_f > 100\,nm$, as seen in the EBSD (Fig.5) and XTEM (Fig.6) data. Grain growth eliminates GBs which can explain the tendency for tensile stress formation and hence the C-T transition observed after h_{cont} in Fig.1. With increasing N_2 content, grain growth is enhanced and happens at smaller thicknesses, which can explain the shift of h_{trans} to lower values as function of p_{N2}/p_{tot} in Fig.2(b).

The evolution of the surface topography of films grown in atmospheres with high N_2 partial pressures ($p_{N2}/p_{tot} > 5\%$) is another indication for the effect of N_2 on growth of Ag films. For $p_{N2}/p_{tot} = 10\%$, the surface feature size $d \cong 17\,nm$ for film thicknesses between 20 and $208\,nm$ (Fig.4(b)), while the surface roughness w increases from 0.62 to $3.0\,nm$ (Fig.4(a)), i.e., in-plane growth is stopped, and all arriving adatoms add to out-of-plane mound growth. This indicates that the diffusion length of adatoms is shorter than d, and the insertion of adatoms into GBs, which is considered the main contribution to compressive stress formation in continuous films, should be inactive. When $h_f < h_{trans}$, adatoms are able to reach GBs because the lateral grain size is smaller than the average diffusion length, but as the grain size increases due to abnormal grain growth, the adatom flux into GBs decreases. The lack of this compressive stress component, which is signature for the stress evolution of thin films deposited at conditions of high atomic mobilities, in combination with tensile stress formation due to abnormal grain growth can explain the compressive-to-tensile stress turnaround seen in Ag films deposited with N_2 in the working gas. Limited surface self-diffusion due to presence of gaseous minority species is also reported by Yu and Thompson[38] for the Ni-O_2 system, which have a stronger interaction than Ag-N_2.

We remark that the observed increased roughening of the Ag-N_2 film and formation of surface undulation within single grains (see Fig.7) are reminiscent of roughening in epitaxial semi-conductor films via Asaro-Tiller-Grinfeld instabilities.[39–41] These instabilities are formed on the surfaces of strained crystals to elastically relax stress at the expense of the additionally created surface. Since these instabilities are seen for materials with low diffusivity, it can be argued that the surface and bulk diffusivity of Ag are decreased due to the presence of N_2 in the working gas. Additionally, single grains can be expected to be highly strained due to the presence and/or incorporation of N_2, in order for this stress-relaxation process to be activated. A macroscopic technique like substrate curvature measurements cannot resolve the stress-state of single crystals, when investigating a polycrystalline film, and the performed measurements can therefore not give further input to this subject.

Finally, we discuss the tensile steady-state stress of $\sim 150\ MPa$ which is found for all films deposited with N_2, after a tensile stress maximum that is N_2-dependent (between 300 and $500\ MPa$, see Fig. 1(c)). These values compare well to yield stress values of Ag thin films with grains containing nano-twins. For low fraction of nanotwins, Ott *et al.*[42] find yield stress values of $\sim 260\ MPa$, which increases to $\sim 510\ MPa$ for films containing only nano-twinned grains with lateral grain sizes 150 to $300\ nm$. XTEM measurements of $500\ nm$ thick films deposited with $p_{N2}/p_{tot} = 5\%$ presented in Fig.6 show regions with small grains with high defect-concentrations, which can contribute to supporting the high tensile stress of $300\ MPa$ that was measured for this film. For a film that has passed the tensile incremental stress peak and reached the tensile steady-state stress, these small grains are not present any more (due to abnormal grain growth), and the film can only support $\sim 150\ MPa$ tensile incremental stress before yielding. The similar stress levels for all Ag-N_2 films indicate that grain size and defect density for these films are similar, and that the abnormal grain growth process has concluded, which is supported by the EBSD map of $208\ nm$ thick Ag films deposited with $p_{N2}/p_{tot} = 10\%$ presented in Fig.5(c), which show few small grains. We conclude therefore that the tensile steady-state stress measured for Ag films deposited with N_2 in the working gas represents the yield stress of these films. We remark that the substrate-curvature technique measures the stress averaged over the whole film, which is polycrystalline in the present study. The effect of single grains on the macroscopic stress-state is not trivial and would need further investigation.

3.4 STRUCTURE-FORMING MECHANISMS

Changes in the grain structure and morphology, as well as in surface topography have direct implication for stress generation and evolution, as discussed Section 3.3. In the present section, we discuss the atomic-scale processes that are responsible for these changes.

Grain growth is an energy minimization process, that leads to a uniform increase in grain size. The bimodal grain size distribution in Ar-N_2-grown Ag films seen from EBSD (Fig.5) and

XTEM (Fig.6) measurements corresponds rather to abnormal grain growth, which can be induced by impurities. Impurity-driven abnormal grain growth in thin films has been attributed to a strain-energy minimization by increasing the size and volume fraction of grains with soft crystallographic orientations.[43,44] In face-centered-cubic metals, these are, e.g., the [100] and [110] directions, while the energetically and kinetically favored [111] direction is the stiffest. Two effects have to be considered: (i) for the same concentration of impurities in the grains with different orientations, more stress is formed in a grain with high stiffness (i.e., more strain energy has to be stored), and (ii) low stiffness-orientations have lower yield stress, i.e., the maximum storable strain-energy is lower, and addition of impurities into a yielded grain does not lead to additional stress, but increase dislocation and defect densities. Consequently, (i) impurity species will be incorporated into (100)/(110) terminated grains, and (ii) at stress-levels that result in local yielding, this effect will be enhanced.

The texture evolution with p_{N2}/p_{tot} for 0% and 5% presented in Fig.3(a) shows that (200) grains are preferentially formed in films with N_2 in the working gas, while (111) preferred orientation prevails for Ag films grown in Ar. For $p_{N2}/p_{tot} = 5\%$, the (200) texture becomes stronger with increasing film thickness between 20 and $208\,nm$ (compare $TC(200)$ values in Fig.3(c)), while $TC(111)$ decreases from 2.5 to ~ 1 in the same thickness range (Fig.3(b)). These trends suggest that (200) grains grow in expense of (111) grains, as film thickness increases, in accordance with strain-energy minimization-driven abnormal grain growth. For $p_{N2}/p_{tot} > 5\%$, no further increase of (200) texture is seen in Fig.3(a), and for $p_{N2}/p_{tot} = 10\%$, $TC(200)$ decreases in the thickness range between 20 and $100\,nm$ (Fig.3(c)) where abnormal grain growth is most active according to the local maximum of σ_{incr} presented in Fig.1(c). While (200) remains the most prominent texture, additional effects have to counteract further increase of (200) texture.

After continuous-layer formation, an arriving Ag atom interacts with a rough Ag surface, with mounds and GB-triple-junctions. The presence of N_2 at this stage of the film growth will change the surface self-diffusivity of these atoms after adsorption. Kawamura *et al.*[45] remark that the time for spontaneous desorption of N_2 might be long enough to alter Ag adatom diffusion, but not long enough for N_2 to be buried in the metal film during the deposition. For Ag films deposited in Ar ambient, the lateral size of surface features d and grain size D are comparable (see Figs.5(a) and (d)), while this is not the case for depositions with N_2 in the working gas, for which $d \ll D$ (see Figs.5(c) and (f)). This indicates that the average diffusion length of Ag adatoms on terraces is smaller than D when N_2 is present, resulting in long residence times of Ag adatoms and finally to nucleation of homoepitaxial Ag islands on top of large grains. For high values of p_{N2}/p_{tot}, the nitrogen population on the surface might be large, and Ag adatom surface diffusion therefore effectively stopped, i.e., they will interact with other adatoms and become immobile before arriving at energetically favorable sites. This can explain why the (200) texture does not become more pronounced for $p_{N2}/p_{tot} > 5\%$, where adatoms cannot diffuse freely anymore.

4. SUMMARY AND OUTLOOK

The addition of nitrogen during sputter-deposition of Ag thin films on SiO_2 substrates promotes two-dimensional growth morphology during early film formations stages, and has the potential to alter the otherwise uncontrolled three-dimensional film morphology in this weakly-interacting film/substrate system. In the present work, we investigate *in situ* and in real time the effect of N_2 on the mechanical stress-state of Ag films and discuss the stress changes with help of microstructural and chemical *ex situ* analysis. Upon formation of a continuous layer ($\sim 20\ nm$ thickness), more compressive stress is formed in Ar-N_2 sputter atmosphere compared to Ar ambient atmosphere, due to decreased grain size/increased grain-boundary number density. While Ar-deposited films show a compressive steady-state stress, a transition toward tensile stress is found for Ar-N_2-deposited Ag films with thicknesses $> 20\ nm$. We attribute these changes to (i) incorporation of N_2 into the Ag film resulting in strain-induced abnormal grain growth, and (ii) reduced surface self-diffusivity of Ag due to adsorbed N_2. The low mobility of Ag adatoms hinders adatom/grain-boundary interactions, and triggers strain-relief via formation of periodic surface undulations, which is an untypical behavior for metal films deposited at conditions of high mobility. The findings presented in this work further help understanding the effect of minority species during the growth of weakly-interacting film/substrate systems, and for the first time, reveal film-forming mechanisms of metal films at the verge of high-mobility and low-mobility growth regime.

ACKNOWLEDGEMENTS

AJ and GA acknowledge the financial support of the French Government program “Investissements d’Avenir” (LABEX INTERACTIFS, reference ANR-11-LABX-0017-01). This work has been partially supported by « Nouvelle Aquitaine » Region and by European Structural and Investment Funds (ERDF reference: P-2016-BAFE-94/95). AJ and KS acknowledge financial support from the Åforsk foundation (contract ÅF 19-137). KS acknowledges Linköping University (“LiU Career Contract, Dnr-LiU-2015-01510, 2015-2020”) and the Swedish research council (contract VR-2015-04630). KS and NP acknowledge financial support from the Olle Engkvist foundation (contract SOEB 190-312) and the Wenner-Gren foundations (contracts UPD2018-0071 and UPD2019-0007). RG acknowledges the financial support of the Hungarian National Research, Development and Innovation Office through the OTKA NN112156 project.

REFERENCES

[1] G. Abadias, E. Chason, J. Keckes, M. Sebastiani, G.B. Thompson, E. Barthel, G.L. Doll, C.E. Murray, C.H. Stoessel, L. Martinu, Review Article: Stress in thin films and coatings: Current status, challenges, and prospects, J. Vac. Sci. Technol. A Vacuum, Surfaces, Film. 36 (2018) 020801. https://doi.org/10.1116/1.5011790.

[2] R. Koch, Stress in Evaporated and Sputtered Thin Films – A Comparison, Surf. Coatings Technol. 204 (2010) 1973–1982. https://doi.org/10.1016/j.surfcoat.2009.09.047.

[3] C. Furgeaud, L. Simonot, A. Michel, C. Mastail, G. Abadias, Impact of Ge alloying on the early growth stages, microstructure and stress evolution of sputter-deposited Cu-Ge thin films, Acta Mater. 159 (2018) 286–295. https://doi.org/10.1016/j.actamat.2018.08.019.

[4] E. Chason, B.W. Sheldon, L.B. Freund, J.A. Floro, S.J. Hearne, Origin of Compressive Residual Stress in Polycrystalline Thin Films, Phys. Rev. Lett. 88 (2002) 156103. https://doi.org/10.1103/PhysRevLett.88.156103.

[5] K. Sarakinos, A review on morphological evolution of thin metal films on weakly-interacting substrates, Thin Solid Films. 688 (2019) 137312. https://doi.org/10.1016/j.tsf.2019.05.031.

[6] J.D. Wilcock, D.S. Campbell, J.C. Anderson, The internal stress in evaporated silver and gold films, Thin Solid Films. 3 (1969) 13–34. https://doi.org/10.1016/0040-6090(69)90108-4.

[7] A. Jamnig, N. Pliatsikas, K. Sarakinos, G. Abadias, The effect of kinetics on intrinsic stress generation and evolution in sputter-deposited films at conditions of high atomic mobility, J. Appl. Phys. 127 (2020) 045302. https://doi.org/10.1063/1.5130148.

[8] R.C. Cammarata, T.M. Trimble, D.J. Srolovitz, Surface stress model for intrinsic stresses in thin films, J. Mater. Res. 15 (2000) 2468–2474. https://doi.org/10.1557/JMR.2000.0354.

[9] S.C. Seel, C. V. Thompson, S.J. Hearne, J.A. Floro, Tensile stress evolution during deposition of Volmer–Weber thin films, J. Appl. Phys. 88 (2000) 7079–7088. https://doi.org/10.1063/1.1325379.

[10] W.D. Nix, B.M. Clemens, Crystallite coalescence: A mechanism for intrinsic tensile stresses in thin films, J. Mater. Res. 14 (1999) 3467–3473. https://doi.org/10.1557/JMR.1999.0468.

[11] T.J. Echtermeyer, S. Milana, U. Sassi, A. Eiden, M. Wu, E. Lidorikis, A.C. Ferrari, Surface Plasmon Polariton Graphene Photodetectors, Nano Lett. 16 (2016) 8–20. https://doi.org/10.1021/acs.nanolett.5b02051.

[12] T. Mueller, F. Xia, P. Avouris, Graphene photodetectors for high-speed optical communications, Nat. Photonics. 4 (2010) 297–301. https://doi.org/10.1038/nphoton.2010.40.

[13] Y. Xu, C.-Y. Hsieh, L. Wu, L.K. Ang, Two-dimensional transition metal dichalcogenides mediated long range surface plasmon resonance biosensors, J. Phys. D. Appl. Phys. 52 (2019) 065101. https://doi.org/10.1088/1361-6463/aaf0f7.

[14] C. Gong, C. Huang, J. Miller, L. Cheng, Y. Hao, D. Cobden, J. Kim, R.S. Ruoff, R.M. Wallace, K. Cho, X. Xu, Y.J. Chabal, Metal contacts on physical vapor deposited monolayer MoS2, ACS Nano. 7 (2013) 11350–11357. https://doi.org/10.1021/nn4052138.

[15] C.T. Campbell, Metal films and particles on oxide surfaces: structural, electronic and chemisorptive properties, J. Chem. Soc. Faraday Trans. 92 (1996) 1435. https://doi.org/10.1039/ft9969201435.

[16] K. Fukuda, S.H.N. Lim, A. Anders, Coalescence of magnetron-sputtered silver islands affected by transition metal seeding (Ni, Cr, Nb, Zr, Mo, W, Ta) and other parameters, Thin Solid Films. 516 (2008) 4546–4552. https://doi.org/10.1016/j.tsf.2007.05.080.

[17] A. Anders, E. Byon, D.-H. Kim, K. Fukuda, S.H.N. Lim, Smoothing of ultrathin silver films by transition metal seeding, Solid State Commun. 140 (2006) 225–229. https://doi.org/10.1016/j.ssc.2006.08.027.

[18] H.A. van der Vegt, H.M. van Pinxteren, M. Lohmeier, E. Vlieg, J.M.C. Thornton, Surfactant-induced layer-by-layer growth of Ag on Ag(111), Phys. Rev. Lett. 68 (1992) 3335–3338. https://doi.org/10.1103/PhysRevLett.68.3335.

[19] W. Wang, M. Song, T.-S. Bae, Y.H. Park, Y.-C. Kang, S.-G. Lee, S.-Y. Kim, D.H. Kim, S. Lee, G. Min, G.-H. Lee, J.-W. Kang, J. Yun, Transparent Ultrathin Oxygen-Doped Silver Electrodes for Flexible Organic Solar Cells, Adv. Funct. Mater. 24 (2014) 1551–1561. https://doi.org/10.1002/adfm.201301359.

[20] N. Pliatsikas, A. Jamnig, M. Konpan, A. Delimitis, G. Abadias, K. Sarakinos, Manipulation of thin silver film growth on weakly interacting silicon dioxide substrates using oxygen as a surfactant, J. Vac. Sci. Technol. A. 38 (2020) 043406. https://doi.org/10.1116/6.0000244.

[21] J. Yun, H.-S. Chung, S.-G. Lee, J.-S. Bae, T.E. Hong, K. Takahashi, S.M. Yu, J. Park, Q. Guo, G.-H. Lee, S.Z. Han, Y. Ikoma, E.-A. Choi, An unexpected surfactant role of immiscible nitrogen in the structural development of silver nanoparticles: an experimental and numerical investigation, Nanoscale. 12 (2020) 1749–1758. https://doi.org/10.1039/C9NR08076G.

[22] G. Zhao, E. Jeong, E.-A. Choi, S.M. Yu, J.-S. Bae, S.-G. Lee, S.Z. Han, G.-H. Lee, J. Yun, Strategy for improving Ag wetting on oxides: Coalescence dynamics versus nucleation density, Appl. Surf. Sci. 510 (2020) 145515. https://doi.org/10.1016/j.apsusc.2020.145515.

[23] A. Jamnig, N. Pliatsikas, M. Konpan, J. Lu, T. Kehagias, A.N. Kotanidis, N. Kalfagiannis, D. V. Bellas, E. Lidorikis, J. Kovac, G. Abadias, I. Petrov, J.E. Greene, K. Sarakinos, 3D-to-2D Morphology Manipulation of Sputter-Deposited Nanoscale Silver Films on Weakly Interacting Substrates via Selective Nitrogen Deployment for Multifunctional Metal Contacts, ACS Appl. Nano Mater. 3 (2020) 4728–4738. https://doi.org/10.1021/acsanm.0c00736.

[24] A. Arnoult, J.J. Colin, Method for Measuring the Curvature of a Reflective Surface and Associated Optical Device, WO/2018/215507, 2018. https://patentscope.wipo.int/search/en/detail.jsf?docId=WO2018215507&tab=PCT BIBLIO.

[25] G.G. Stoney, The Tension of Metallic Films Deposited by Electrolysis, Proc. R. Soc. London A. 82 (1909) 172–175. https://doi.org/10.1098/rspa.1909.0021.

[26] G. Lindfiled, J. Penny, Numerical Methods : Using MATLAB, 3rd ed., Elsevier Inc., Oxford, 2012.

[27] Supporting information, (n.d.).

[28] ICDD powder diffraction file no. 00-004-0787; silver, (n.d.).

[29] D. Nečas, P. Klapetek, Gwyddion: an open-source software for SPM data analysis, Open Phys. 10 (2012) 181–188. https://doi.org/10.2478/s11534-011-0096-2.

[30] M. Shen, D.-J. Liu, C.J. Jenks, J.W. Evans, P.A. Thiel, The effect of chalcogens (O, S) on coarsening of nanoislands on metal surfaces, Surf. Sci. 603 (2009) 1486–1491. https://doi.org/10.1016/j.susc.2008.11.045.

[31] G. Abadias, L. Simonot, J.J. Colin, A. Michel, S. Camelio, D. Babonneau, Volmer-Weber growth stages of polycrystalline metal films probed by in situ and real-time optical diagnostics, Appl. Phys. Lett. 107 (2015) 183105. https://doi.org/10.1063/1.4935034.

[32] D.R. Lide, ed., CRC Handbook of Chemistry and Physics: A Ready-Reference Book for Chemical and Physical Data, 88th ed., CRC Press, Boca Raton, Fl, 2008.
[33] P. Meakin, Fractals, scaling and growth far from equilibrium, Cambridge University Press, Cambridge, 1998.
[34] A.M. Ferraria, A.P. Carapeto, A.M. Botelho do Rego, X-ray photoelectron spectroscopy: Silver salts revisited, Vacuum. 86 (2012) 1988–1991. https://doi.org/10.1016/j.vacuum.2012.05.031.
[35] I. Kusunoki, T. Takaoka, Y. Igari, K. Ohtsuka, Nitridation of a Si(100) surface by 100–1000 eV N + 2 ion beams, J. Chem. Phys. 101 (1994) 8238–8245. https://doi.org/10.1063/1.468194.
[36] D. Depla, R. De Gryse, Target voltage measurements during DC sputtering of silver in a nitrogen/argon plasma, Vacuum. 69 (2003) 529–536. https://doi.org/10.1016/S0042-207X(02)00602-4.
[37] J. Leiro, E. Minni, E. Suoninen, Study of plasmon structure in XPS spectra of silver and gold, J. Phys. F Met. Phys. 13 (1983) 215–221. https://doi.org/10.1088/0305-4608/13/1/024.
[38] H.Z. Yu, C. V. Thompson, Stress engineering using low oxygen background pressures during Volmer–Weber growth of polycrystalline nickel films, J. Vac. Sci. Technol. A Vacuum, Surfaces, Film. 33 (2015) 021504. https://doi.org/10.1116/1.4902957.
[39] R.J. Asaro, W.A. Tiller, Interface morphology development during stress corrosion cracking: Part I. Via surface diffusion, Metall. Mater. Trans. B. 3 (1972) 1789–1796. https://doi.org/10.1007/BF02642562.
[40] D.J. Srolovitz, On the stability of surfaces of stressed solids, Acta Metall. 37 (1989) 621–625. https://doi.org/10.1016/0001-6160(89)90246-0.
[41] M.A. Grinfeld, The stress driven instability in elastic crystals: Mathematical models and physical manifestations, J. Nonlinear Sci. 3 (1993) 35–83. https://doi.org/10.1007/BF02429859.
[42] R.T. Ott, J. Geng, M.F. Besser, M.J. Kramer, Y.M. Wang, E.S. Park, R. LeSar, A.H. King, Optimization of strength and ductility in nanotwinned ultra-fine grained Ag: Twin density and grain orientations, Acta Mater. 96 (2015) 378–389. https://doi.org/10.1016/j.actamat.2015.06.030.
[43] A.J. Birnbaum, C. V. Thompson, J.C. Steuben, A.P. Iliopoulos, J.G. Michopoulos, Oxygen-induced giant grain growth in Ag films, Appl. Phys. Lett. 111 (2017) 163107. https://doi.org/10.1063/1.4998741.
[44] C. V. Thompson, R. Carel, Stress and grain growth in thin films, J. Mech. Phys. Solids. 44 (1996) 657–673. https://doi.org/10.1016/0022-5096(96)00022-1.
[45] M. Kawamura, Y. Abe, K. Sasaki, Sputter-deposition of Ag films in a nitrogen discharge, Thin Solid Films. 515 (2006) 540–542. https://doi.org/10.1016/j.tsf.2005.12.292.

Supplementary material to “The effect of nitrogen on the stress and morphology evolution during growth of thin silver films”

A. Jamnig[1,2], N. Pliatsikas[2], H. Bahsoun[1], K. Sarakinos[2], P. Barna[3], G. Radnóczi[3], and G. Abadias[1,*]
*Corresponding author, email: gregory.abadias@univ-poitiers.fr
[1]*Institut Pprime, Département Physique et Mécanique des Matériaux, UPR 3346 CNRS, Université de Poitiers, 11 Bvd M. et P. Curie, TSA 41123, 86073 Poitiers Cedex 9, France*
[2]*Nanoscale Engineering Division, Department of Physics, Chemistry, and Biology, Linköping University, SE 581 83, Linköping, Sweden*
[3]*Centre for Energy Research, Institute for Technical Physics and Materials Science, H1121 Budapest, Konkoly-Thege M. u. 29-33, Hungary*

This document presents experimental data from x-ray reflectometry (XRR), x-ray diffractometry (XRD), atomic force microscopy (AFM), and x-ray photoelectron spectroscopy (XPS) that are not included in the main manuscript. A short discussion of the presented data is given in the figure captions, in case of XRR and XPS data, the results are further discussed in the main manuscript. XRD and AFM data presented here are used to determine parameters that are presented and discussed in the main manuscript, i.e., diffraction peak integral intensities for texture analysis from XRD data, and the root-mean-square surface roughness w, the lateral feature size d, and the roughness scaling exponent α from AFM data.

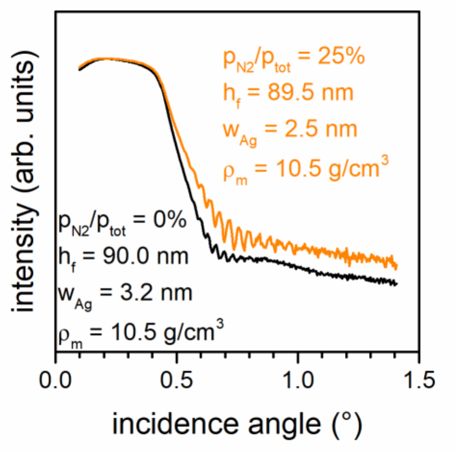

Figure S1: X-ray reflectometry measurements from Ag/SiO_2/Si stacks in which Ag is deposited at N_2-to-total-pressures $p_{N2}/p_{tot} = 0\%$ (black line) and 25% (orange line). Fitting the presented data to a mathematical model gives Ag layer thicknesses h_f, surface roughnesses w_{Ag}, and the mass densities ρ_m indicated in the figure. From the known deposition time $t = 900\,s$, the deposition rate is determined as h_f/t, and results in deposition rates 1.00 and $0.99\,nm/s$ for $p_{N2}/p_{tot} = 0\%$ and 25%, respectively. We note that the Ag-layer roughness is lower in the Ar-N_2-grown Ag film compared to the film deposited in pure Ar atmosphere, which is in agreement with experimental data presented in the main text. Both Ag films can be modelled with $\rho_m = 10.5\ g/cm^3$, i.e., ρ_m corresponds to the theoretical mass density of bulk Ag,[1] indicating that dense films are grown in both deposition conditions.

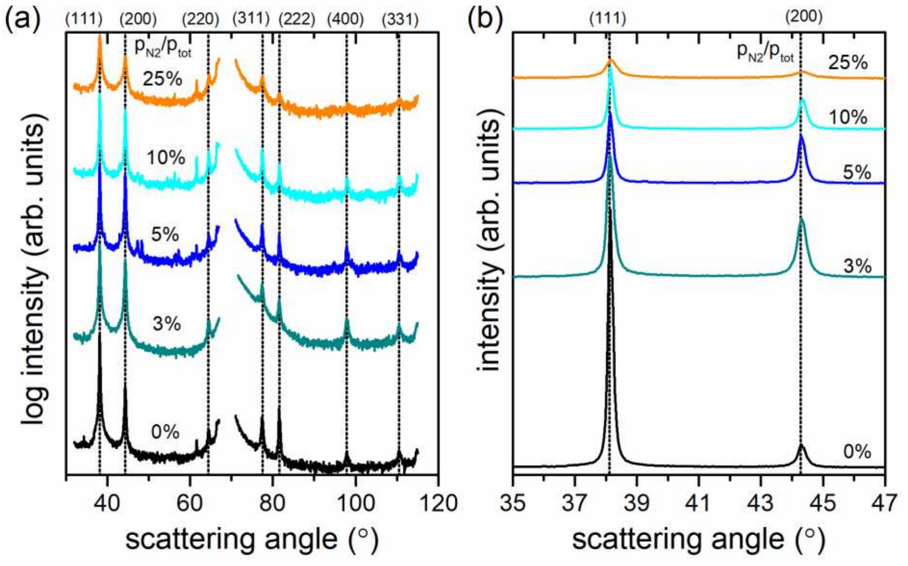

Figure S2: X-ray diffractograms of amorphous carbon/Ag/SiO_2/Si stacks with Ag film thickness $h_f = 208\,nm$ for N_2-to-total-pressures p_{N2}/p_{tot} ranging 0% to 25%. Vertical dashed lines represent the angular positions of x-ray diffraction peaks in unstrained Ag powder.[2] Data in (a) is plotted in logarithmic scale on the vertical axis, and missing data in the range $67°$ to $71°$ corresponds to the (100) reflection of the Si single crystal substrate. We find that all expected diffraction peaks are present in the diffractograms, i.e., polycrystalline Ag films form for all presented deposition conditions. Data in (b) is a magnification of the data in (a), showing the (111) and (200) peak intensity evolution. With increasing p_{N2}/p_{tot}, (111) peak intensity decreases. The (200) peak intensity increases in the range $p_{N2}/p_{tot} = 0\%$ to 3%, and decreases when p_{N2}/p_{tot} is further increased to 25%. Concurrently, peak broadening is observed. A discussion of the texture evolution with p_{N2}/p_{tot} can be found in the main document.

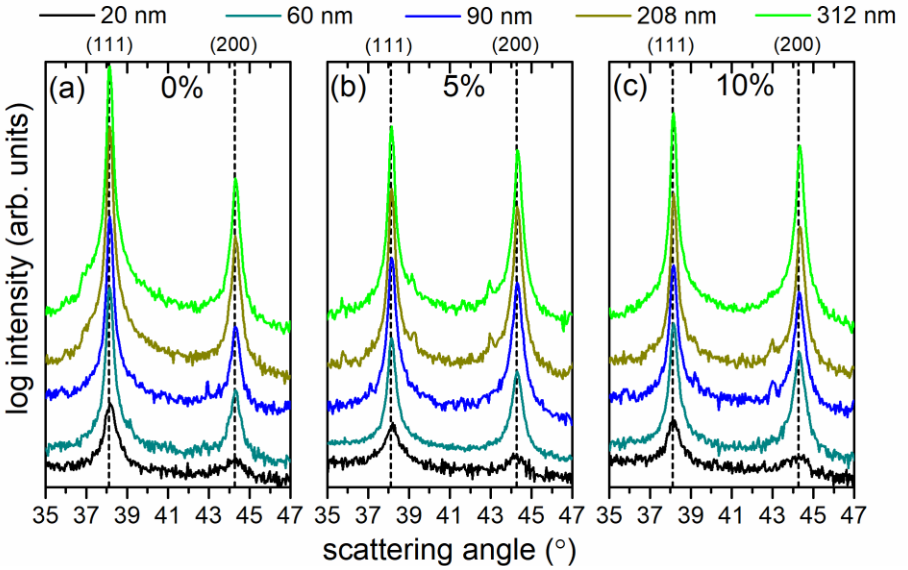

Figure S3: X-ray diffractograms of amorphous carbon /Ag/SiO_2/Si stacks with Ag film thicknesses ranging 20 to 300 nm for N_2-to-total-pressures p_{N2}/p_{tot} (a) 0%, (b) 5%, and (c) 10%. With increasing film thickness, intensities of (111) and (200) diffraction peaks increase. From the (111)-to-(200) peak intensity ratios, it can be found that Ag films deposited in pure Ar atmosphere have a stronger (111) preferred orientation than films deposited in N_2-containing atmosphere. A discussion of the texture evolution with film thickness can be found in the main document.

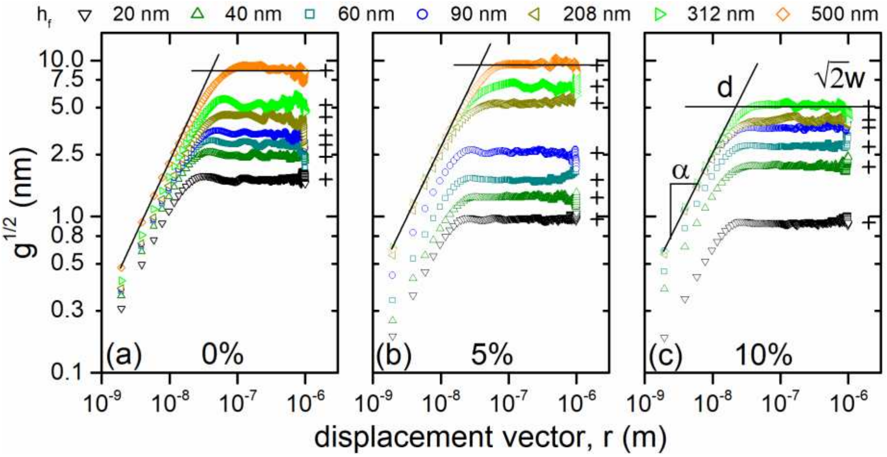

Figure S4: Square root of the height-height-correlation function $g(r)$ as function of the displacement vector r, for surfaces of amorphous carbon/Ag/SiO$_2$/Si stacks with Ag film thicknesses h_f ranging 20 to $500\ nm$ for N$_2$-to-total-pressures p_{N2}/p_{tot} (a) 0%, (b) 5%, and (c) 10%. From $g(r)$, the root-mean-square surface roughness w, the lateral feature size d, and the roughness scaling exponent α can be determined as described in the following: We find w from the relation $g^{1/2}(r \rightarrow \infty) = \sqrt{2}w$; for each film, the quantity $\sqrt{2}w$ is marked by the symbol $+$. For low values of r, $g^{1/2}(r \rightarrow 0) \sim r^{\alpha}$, where α describes the local surface slope of the surface. These two regimes are marked by lines for the films with highest thickness in the figure. The lateral feature size d can be determined at the intersection of these two boundary regimes. A discussion of the evolution of w, d, and α with film thickness can be found in the main document.

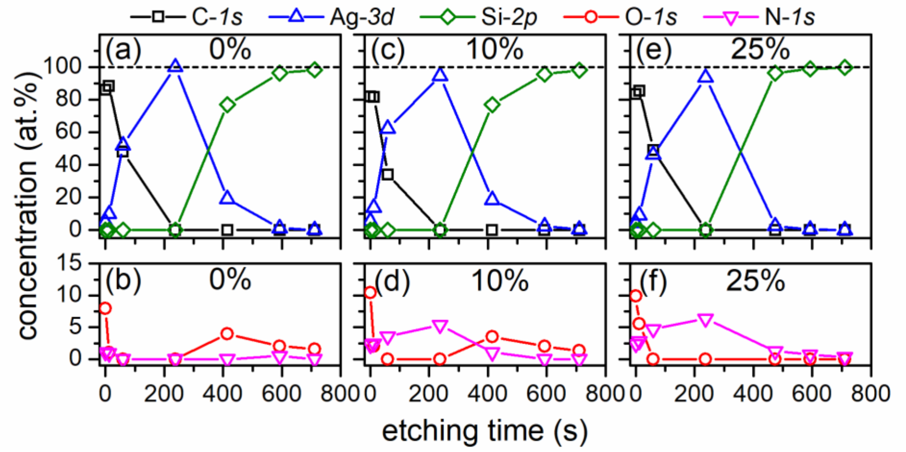

Figure S5: Film composition, as determined by x-ray photoelectron spectroscopy, of amorphous carbon (a-C)/Ag/SiO_2/Si stacks with Ag film thickness $h_f = 90\,nm$ deposited at N_2-to-total-pressures p_{N2}/p_{tot} (a),(b) 0% (c),(d) 10%, and (e),(f) 25%, as function of ion-etching time; C, Ag, and Si concentrations are presented in (a), (c), and (e), O and N concentrations are shown in (b), (d), and (f). Detected elements are marked with symbols, photoelectron peaks that are used for quantification are given in the legend, and lines are guides for the eye. In as-received films (etching time $0\,s$), C from the a-C capping layer is the most common element, while O-containing surface contaminations are also present; latter are removed after surface etching (see (b), (d), and (f)). After $235\,s$ etching, Ag is the only detectable element in the Ar-deposited Ag film (see (a) and (b)), while Ag and N are present in Ag films deposited in N_2-containing atmosphere (see (c) through (f)), N_2 concentrations in Ag films are determined from these data. With increasing etching time, the Si signal increases, while the Ag film is removed, and only the SiO_2/Si substrate remains. While Si-O bonding is seen for etching times $> 415\,s$ in Ag films deposited at $p_{N2}/p_{tot} = 0\%$ and 10%, Si-N bonds are detected in this etching time range in Ag films deposited at $p_{N2}/p_{tot} = 25\%$.

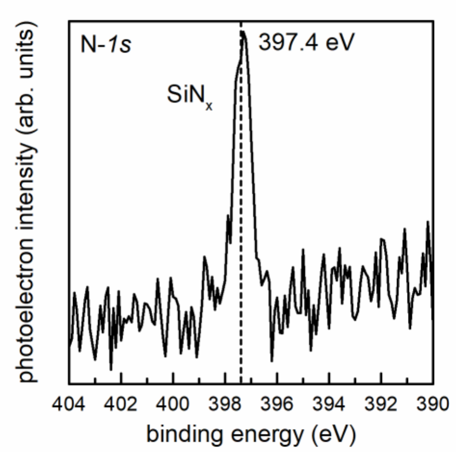

Figure S6: N-*1s* core-level high-resolution x-ray photoelectron spectroscopy spectrum after $474\ s$ ion-etching of amorphous carbon/Ag/SiO_2/Si stacks with Ag film thickness $h_f = 90\ nm$ deposited at N_2-to-total-pressures $p_{N2}/p_{tot} = 25\%$. The peak position is shifted by $0.4\ eV$ compared to the refence value $397\ eV$,[3] indicating the formation of a SiN_x compound.[4]

REFERENCES

[1] D.R. Lide, ed., CRC Handbook of Chemistry and Physics: A Ready-Reference Book for Chemical and Physical Data, 88th ed., CRC Press, Boca Raton, Fl, 2008.

[2] ICDD powder diffraction file no. 00-004-0787; silver, (n.d.).

[3] I. Kusunoki, T. Takaoka, Y. Igari, K. Ohtsuka, Nitridation of a Si(100) surface by 100–1000 eV N + 2 ion beams, J. Chem. Phys. 101 (1994) 8238–8245. https://doi.org/10.1063/1.468194.

[4] D.K. Rai, A.K. Panchal, D.S. Sutar, C.S. Solanki, K.R. Balasubramaniam, Mechanism for formation of ultra thin SiNx on a-Si - XPS and FTIR studies, in: 2015 IEEE 42nd Photovolt. Spec. Conf., IEEE, 2015: pp. 1–6. https://doi.org/10.1109/PVSC.2015.7355805.